LUND UNIVERSITY

Process based Modelling of Chemical and Physical Aerosol Properties Relevant for Climate and Health

Roldin, Pontus

2013

Citation for published version (APA):
Roldin, P. (2013). *Process based Modelling of Chemical and Physical Aerosol Properties Relevant for Climate and Health*. [Doctoral Thesis (compilation), Nuclear physics]. Division of Nuclear Physics, Department of Physics Box 118, SE-221 00 Lund.

Total number of authors:
1

LUND UNIVERSITY

PO Box 117
221 00 Lund
+46 46-222 00 00

Process based Modelling of Chemical and Physical Aerosol Properties Relevant for Climate and Health

Pontus Roldin

2013

LUND UNIVERSITY

Academic thesis which, for degree of Doctor of Philosophy in Engineering, by due permission of the Faculty of Engineering at Lund University will be publicly defended on Friday 31st May, 2013, at 13.15 in lecture hall Rydbergssalen at the Department of Physics, Sölvegatan 14, Lund. Faculty opponent is Dr. Hannele Korhonen, Finnish Meteorological Institute, Kuopio, Finland.

Organisation
LUND UNIVERSITY
Lund Institute of Technology
Division of Nuclear Physics
Department of Physics
Box 118, SE-221 00 Lund

Document name
Doctoral Dissertation

Date of issue
6 May 2013

CODEN
LUTFD2/(TFKF-1041)/1-67(2013)

Author(s)
Pontus Roldin

Sponsoring organization

Title and subtitle
Process based Modelling of Chemical and Physical Aerosol Properties Relevant for Climate and Health

Abstract

Atmospheric aerosol particles have substantial influence on climate and air quality. However, the anthropogenic influence on the atmospheric aerosol is still poorly known. This limits the understanding of past and future climate changes. Additionally, both epidemiological and toxicological studies indicate adverse health effects of inhaled aerosol particles. In order to study the effect of atmospheric processes on the particle properties relevant for climate and health, two models were developed and implemented.

The first is a 2D-Lagrangian model for Aerosol Dynamics, gas phase CHEMistry and radiative transfer (ADCHEM), which treats the dispersion in the vertical and horizontal direction perpendicular to air mass trajectories. The second model is a kinetic multilayer model for Aerosol Dynamics, gas and particle phase chemistry in laboratory CHAMber environments (ADCHAM). With ADCHAM it is possible to study process based formation and evaporation of secondary organic aerosol particles, and mass transfer limitations and reactions within the particle phase.

ADCHEM was used to quantify the anthropogenic influence from the city of Malmö (280 000 inhabitants) in southern Sweden. In Malmö and a few tens of kilometres downwind, the primary particle emissions have a large influence on the particle number concentration. However, more than 2 hours downwind Malmö, the anthropogenic particle mass contribution is dominated by secondary ammonium nitrate. To quantify the direct and indirect climate impact of urban aerosol emissions, the secondary aerosol formation which changes the optical and hygroscopic properties of the primary soot particles, needs to be addressed in future measurements and process modelling.

ADCHAM was used to simulate different laboratory chamber experiment, with focus on potential influential but poorly known processes for secondary organic aerosol properties, formation and evaporation rates in the atmosphere (i.e. oligomerization, organic salt formation, salting-out effects, oxidation of organic compounds in the particle phase and mass transfer limitations in the particle phase). The model results reveal that formation of small amounts of low-volatile and long lived oligomers, which accumulate in the particle surface layers, can effectively prevent the evaporation of more volatile compounds. This can significantly prolong the lifetime of SOA in the atmosphere.

Key words
aerosol particles, climate, aerosol dynamics, gas phase chemistry, kinetic multilayer model

Supplementary bibliographical information:

Language
English

Recipient's notes

Number of pages
274

Price

Security classification

Distribution by (name and address): Department of Physics, see address above.

I, the undersigned, being the copyright owner of the abstract of the above-mentioned dissertation, hereby grant to all reference sources permission to publish and disseminate the abstract of the above-mentioned dissertation.

Signature Pontus R **Date:** April 26, 2013

Process based Modelling of Chemical and Physical Aerosol Properties Relevant for Climate and Health

Pontus Roldin

2013

LUND UNIVERSITY

Division of Nuclear Physics
Department of Physics
Lund University
Box 118
SE-221 00 Lund, Sweden

Printed in Sweden by E-husets tryckeri, Lund 2013

ISBN 978-91-7473-535-2 (tryck)
ISBN 978-91-7473-536-9 (pdf)
ISRN LUTFD2/(TFKF-1041)/1-67(2013)

Papers

This dissertation thesis is based on the following papers, which are appended in the end.

I **Development and evaluation of the aerosol dynamics and gas phase chemistry model ADCHEM**
Roldin, P., Swietlicki, E., Schurgers, G., Arneth, A., Lehtinen, K. E. J., Boy, M., and Kulmala, M.
Atmospheric Chemistry and Physics, 11, 5867-5896, 2011a.

II **Aerosol ageing in an urban plume – implication for climate and health**
Roldin, P., Swietlicki, E., Massling, A., Kristensson, A., Löndahl, J., Eriksson, A., Pagels, J., and Gustafsson, S.
Atmospheric Chemistry and Physics, 11, 5897–5915, 2011b.

III **Modelling non-equilibrium secondary organic aerosol formation and evaporation with the aerosol dynamics, gas- and particle-phase chemistry kinetic multi-layer model ADCHAM**
Roldin, P., Eriksson, A. C., Nordin, E. Z., Hermansson, E., Mogensen, D., Rusanen, A., Boy, M., Swietlicki, E., Svenningsson, B., and Pagels, J.
Manuscript in preparation.

IV **Secondary organic aerosol formation from gasoline passenger vehicle emissions investigated in a smog chamber**
Nordin, E. Z., Eriksson, A. C., Roldin, P., Nilsson, P. T., Carlsson, J. E., Kajos, M. K., Hellén, H., Wittbom, C., Rissler, J., Löndahl, J., Swietlicki, E., Svenningsson, B., Bohgard, M., Kulmala, M., Hallquist, M., and Pagels, J.,
Atmos. Chem. Phys. Discuss., 12, 31725-31765, 2012.

The author's contribution to the papers

Paper I

I constructed the ADCHEM model code, did all model runs and evaluated the code. I analysed the model and measurement results and wrote the paper.

Paper II

I did all model runs with the ADCHEM model, analysed the model and measurement results and wrote the paper.

Paper III

I constructed the ADCHAM model code, did all model runs and evaluated the code. I analysed the model results and compared against previously published measurement data. I wrote the paper.

Paper IV

I performed model simulations on the experimental set-up before many of the experiments were conducted in order to optimize the experimental outcomes. I was also involved in the data analysis and modelled the gas phase chemistry and secondary aerosol formation in many of the experiments. I was proofreading the manuscript.

Related publications published in scientific journals

Gunthe S. S., King S. M., Rose D., Chen Q., Roldin P., Farmer D. K., Jimenez J. L., Artaxo P., Andreae M. O., Martin S. T. and Pöschl U.: Cloud condensation nuclei in pristine tropical rainforest air of Amazonia: size-resolved measurements and modeling of atmospheric aerosol composition and CCN activity. Atmos. Chem. Phys., 9, 7551-7575, 2009.

Pöschl U., Martin S. T., Sinha B., Chen Q., Gunthe S. S., Huffman J. A., Borrmann S., Farmer D. K., Garland R. M., Helas G., Jimenez J. L., King S. M., Manzi A., Mikhailov E., Pauliquevis T., Petters M. D., Prenni A. J., Roldin P., Rose D., Schneider J., Su H., Zorn S. R., Artaxo P. and Andreae M. O.: Rainforest aerosols as biogenic nuclei of clouds and precipitation in the Amazon, Science, 329, 1513-1516, 2010.

Reddington, C. L., Carslaw, K. S., Spracklen, D. V., Frontoso, M. G., Collins, L., Merikanto, J., Minikin, A., Hamburger, T., Coe, H., Kulmala, M., Aalto, P., Flentje, H., Plass-Dülmer, C., Birmili, W., Wiedensohler, A., Wehner, B., Tuch, T., Sonntag, A., O'Dowd, C. D., Jennings, S. G., Dupuy, R., Baltensperger, U., Weingartner, E., Hansson, H.-C., Tunved, P., Laj, P., Sellegri, K., Boulon, J., Putaud, J.-P., Gruening, C., Swietlicki, E., Roldin, P., Henzing, J. S., Moerman, M., Mihalopoulos, N., Kouvarakis, G., Ždímal, V., Zíková, N., Marinoni, A., Bonasoni, P., and Duchi, R.: Primary versus secondary contributions to particle number concentrations in the European boundary layer, Atmos. Chem. Phys., 11, 12007-12036, 2011.

Rizzo, L. V., Artaxo, P., Müller, T., Wiedensohler, A., Paixão, M., Cirino, G. G., Arana, A., Swietlicki, E., Roldin, P., Fors, E. O., Wiedemann, K. T., Leal, L. S. M., and Kulmala, M.: Long term measurements of aerosol optical properties at a primary forest site in Amazonia, Atmos. Chem. Phys., 13, 2391-2413, 2013.

Wiedensohler, A., Birmili, W., Nowak, A., Sonntag, A., Weinhold, K., Merkel, M., Wehner, B., Tuch, T., Pfeifer, S., Fiebig, M., Fjäraa, A. M., Asmi, E., Sellegri, K., Depuy, R., Venzac, H., Villani, P., Laj, P., Aalto, P., Ogren, J. A., Swietlicki, E., Williams, P., Roldin, P., Quincey, P., Hüglin, C., Fierz-Schmidhauser, R., Gysel, M., Weingartner, E., Riccobono, F., Santos, S., Grüning, C., Faloon, K., Beddows, D., Harrison, R., Monahan, C., Jennings, S. G., O'Dowd, C. D., Marinoni, A., Horn, H.-G., Keck, L., Jiang, J., Scheckman, J., McMurry, P. H., Deng, Z., Zhao, C. S., Moerman, M., Henzing, B., de Leeuw, G., Löschau, G., and Bastian, S.: Mobility particle size spectrometers: harmonization of technical standards and data structure to facilitate high quality long-term observations of atmospheric particle number size distributions, Atmos. Meas. Tech., 5, 657-685, 2012.

Symbols and abbreviations

σ_i	Surface tension of compound *i*
σ_a	Absorption coefficient
σ_s	Scattering coefficient
λ	Wavelength of light
γ_i	Activity coefficient of compound *i*
ε	Rate of dissipation of kinetic energy per mass
ρ_p	Particle density
ω	Single scattering albedo
a_w	Water activity
A_{cross}	Particle cross sectional area
C_{k_i}	Kelvin effect of compound *i*
$C_{\infty,i}$	Gas phase concentration of compound *i* far from the particle surface
$C_{s,i}$	Saturation concentration of compound *i* at the particle surface
D_i	Gas phase diffusion coefficient of compound *i*
D_p	Particle diameter
f_i	Correction factor in the transition regime for compound *i*
g	Asymmetry parameter
I_i	Particle molar growth rate due to condensation of compound *i*
K	Kinetic nucleation theory correlation coefficient
K_y	Eddy diffusivities (turbulent diffusivity) in the horizontal direction
K_z	Eddy diffusivities (turbulent diffusivity) in the vertical direction
LWC	Liquid water content
M_i	Molar mass of compound *i*
m_L	Refractive index
$PM_{2.5}$	Mass of particles with an aerodynamic diameter smaller than 2.5 μm
PM_{10}	Mass of particles with an aerodynamic diameter smaller than 10 μm
$p_{0,i}$	Pure liquid saturation vapour pressure of compound *i* over a flat surface
Q_a	Absorption efficiency
Q_s	Scattering efficiency
R	Universal gas constant
RH	Relative humidity
T	Temperature in Kelvin
x_i	Mole fraction of compounds *i* in the particle phase
x_w	Mole fraction of water in the particle phase

Contents

Populärvetenskaplig sammanfattning

Vid varje andetag fyller vi våra lungor med luft som innehåller miljontals små partiklar. Partiklarna tillsammans med gasen (luften) som omger dem kallas i naturvetenskapliga sammanhang för en aerosol. Många av aerosolpartiklarna är så små att de kan hållas svävande i luften flera veckor utan att falla ner till marken. Partiklarna i utomhusluften (atmosfären) kan oftast betraktas som små runda bollar (sfärer). Känner man en sfärs diameter kan man beskriva alla dess geometriska egenskaper (t ex dess volym och ytarea). Därför är det lämpligt att ange partiklars storlek utifrån deras diameter. De minsta partiklarna i atmosfären består enbart av ett fåtal ihopsatta gasmolekyler och har en diameter på cirka 1 miljarddels meter (1 nanometer). Den övre storleksgränsen för aerosolpartiklar går vid ungefär 0.1 millimeter. Detta är ungefär vid den gräns då partiklarna inte längre kan hållas svävande i luften och där vi med våra ögon börjar kunna uppfatta dem som enskilda partiklar.

Varför studerar vi aerosoler?

De flesta aerosolpartiklar påverkar klimatet på jorden genom att sprida och ändra riktningen på den inkomande solstrålningen. En del av solstrålarna som träffar partiklarna kommer därför att spridas tillbaka ut i rymden istället för att värma upp jordytan och dess atmosfär. Detta leder till en kylande effekt som sänker temperaturen på jorden. Ett viktigt undantag är de mörka sotpartiklar som bland annat släpps ut med avgaserna från dieselbilar eller vid ofullständig förbränning av ved. Dessa partiklar tar istället upp (absorberar) en stor del av solljuset som träffar dem och värmer därmed upp atmosfären runt dem. Utsläpp av dessa partiklar leder därför till en högre medeltemperatur på jorden.

Dessutom avgörs molnens egenskaper till stor del av partiklarna i atmosfären. Varje molndroppe bildas från en aerosolpartikel som tar upp vatten vid hög luftfuktighet. Genom våra partikelutsläpp ökar vi antalet aerosolpartiklar i atmosfären vilket gör att molnen som bildas bestå av fler, fast mindre molndroppar. Detta leder bland annat till att molnen blir ljusare och reflekterar mer solljus ut till rymden, vilket har en kylande effekt.

Totalt sett har aerosolpartiklarna i atmosfären med största sannolikhet en kylande effekt på klimatet. Hur stor denna effekt är vet man dock inte speciellt väl. Detta beror till stor del på den komplexa växelverkan mellan aerosoler och moln. Utan bättre kunskap om aerosolpartiklarnas kylande effekt kan vi inte med säkerhet uttala oss om hur stor växthusgasutsläppens klimatpåverkan är. Man kan säga att den kylande effekten av våra partikelutsläpp till viss del döljer den värmande effekten från växthusgaserna.

Aerosolpartiklar är dock inte bara viktiga för klimatet på jorden utan påverkar även vår hälsa. Många studier har visat att inandning av vissa typer av partiklar kan leda till lung- och hjärtsjukdomar. Vilka egenskaper som gör att vissa partiklar är mer farliga än andra vet man dock inte med säkerhet. För att förbättra luftkvaliten där vi bor finns det idag gränsvärden för hur höga partikelhalterna får vara i luften. I Sverige dör varje år uppskattningsvis cirka 5000 i förtid på grund av luftföroreningar.

Egenskaper hos partiklarna i atmosfären

Partiklarna i atmosfären kan vara helt flytande droppar, helt fasta eller däremellan (t ex. som honung eller tjära). I vilken av dessa former de befinner sig i kan ha stor betydelse för hur de påverkas av olika processer i atmosfären. Dessutom består partiklarna i atmosfären av hundratusentals olika kemiska ämnen av vilka enbart en bråkdel är kända. Aerosolernas kemiska egenskaper beror dels på dess ursprungliga källa och dels på vad de utsätts för (hur de åldras) i atmosfären. Exempel på viktiga direkta partikelkällor i atmosfären är väg-, båt- och flygtrafik, vedeldning, skogsbränder, vulkanutbrott, havsspray och uppvirvlade jord- och sandpartiklar.

Men de minsta, och till antalet ofta största andelen partiklar, bildas när vissa typer av gasmolekyler kolliderar med varandra. Trots omfattande forsking på området vet man fortfarande inte med säkerhet vilka dessa gasmolekyler är eller varför de kan klumpar ihop sig istället för att stötas bort från varandra. De nya partiklarna (med en diameter runt 1 nanometer) kan växa till större partiklar genom upptag av olika gaser. De flesta av gaserna är organiska ämnen som bildas genom kemiska reaktioner i atmosfären. Ursprunget till många av dessa organiska ämnen hittar vi i växtriket. Dessa ämnen kan man t ex känna doften av i en barrskog eller när man skalar en apelsin. Andra viktiga gaser kommer från bilavgaser och vedeldning.

Mätningar av partiklar och gaser

Idag finns i Europa ett nätverk med ett 20-tal olika mätsationer som kontinuerligt övervakar aerosolpartiklarnas kemiska och fysiska egenskaper med hjälp av standardiserade mätmetoder. En av dessa stationer ligger på Söderåsen i norra Skåne och drivs av aerosolgruppen på kärnfysik här i Lund. Under min tid som doktorand på kärnfysik har jag varit en del av en liten forskargrupp som har byggt upp och servat denna station samt analyserat mätdata. Dessutom har jag varit delaktig i uppbyggnaden av en liknande station i Brasiliens regnskog.

Mätresultaten från alla dessa stationer kvalitetsgranskas och skickas in till en databas som är tillgäng för klimatforskare. Syftet är att minska osäkerheten kring aerosolpartiklarnas klimatpåverkan bl. a. genom att förbättra dagens klimatmodeller.

Matematiska modeller för ökad förståelse och framtida projektioner

Denna avhandling handlar främst om hur man med hjälp av matematiska datormodeller kan beskriva aerosolernas egenskaper. Under min tid som doktorand på kärnfysik har jag utvecklat och använt två olika modeller.

Det övergripande syftet med dessa modeller är att öka förståelsen kring processer i atmosfären som påverkar partikelkoncentrationerna, partiklarnas optiska och kemiska egenskaper och deras förmåga att ta upp vatten och bilda molndroppar. Detta är viktigt för partiklarnas klimatpåverkan, hur effektivt de deponeras i våra lungor och deras hälsoeffekter i kroppen.

I atmosfären påverkas aerosolpartiklarna av processer som sker på molekylnivå och inom bråkdelen av en sekund, men även av globala cirkulationsmönster och klimatförändringar. För att minska osäkerheten kring partiklarnas klimatpåverkan krävs därför att man studerar processer som sker inom alla tänkbara rumsliga och tidsmässiga skalor. I denna avhandling ligger fokus kring att beskriva processer som sker på molekylärskala och mikrosekunder upp till den minsta skala som kan hanterars av globala klimatmodeller (runt 100 km och timmar till dagar). Ett av syftena med detta är att förbättra de globala klimatmodellernas förenklade beskrivningar av dessa småskaliga processer.

Den första modellen används för att beskriva hur partiklarna åldras i atmosfären. Med denna modell studerades bland annat hur utsläppen av partiklar och gaser i Malmö påverkar aerosolsammansättningen nedvinds staden. Modellen utvärderades med hjälp av mätningar av partiklar och gaser i Malmö och vid vår mätstation på Söderåsen i norra Skåne.

Den andra modellen är till för att användas vid avancerade laboratoriemätningar på partikelbildning och tillväxt. Simuleringar med denna modell låg bland annat till grund för designen och utvärderingen av experiment som syftar till att öka förståelsen kring vad som händer med bensinbilsavgaserna i atmosfären.

Introduction

1.1 The greenhouse effect

Without naturally occurring water vapour, carbon dioxide (CO_2) and other greenhouse gases in the atmosphere, the average global temperature of the earth would be approximately -18 °C. Fortunately, this is not the case and the pre-industrial levels of greenhouse gases raised the global mean temperature to about 13 °C. However, because of fossil fuel burning, the CO_2 levels in the atmosphere have increased with 40 % from 280 ppbv in 1750 to nearly 400 ppbv today. At the same time the global mean temperature at the surface of the earth has increased with about 0.8 °C. According to the Intergovernmental Panel on Climate Change (IPCC) it is very likely that there is a connection between human activities (such as burning of fossil fuels and land use changes) and the observed increase in the global mean temperature (IPCC, 2007). However, because of complex feedback mechanisms it is poorly known how sensitive the climate of the earth is to the anthropogenic emissions of e.g. greenhouse gases.

As an example, the emissions of CO_2 increase the mean temperature of the atmosphere. With an increased temperature, the atmosphere can hold more water vapour before water condenses and form clouds. Because water vapour is a strong greenhouse gas, the global temperature will increase more than what would be expected purely from the CO_2 increase. This is an example of a positive feedback mechanism. There are also negative feedback mechanisms which instead have a stabilizing effect on the earth's climate. Hence, in order to study the combined and complex effects of the anthropogenic emissions of greenhouse gases, aerosol particles and land use changes, global climate models are needed.

1.2 Atmospheric aerosols

In every breath we take we typically inhale millions of small aerosol particles. An aerosol is defined as solid or liquid particles suspended in a mixture of gases (usually air). Aerosol particles can be of natural or anthropogenic origin.

Important natural atmospheric aerosols and sources are windblown desert dust, volcanic eruptions, sea spray, natural forest fires and vegetation, while common anthropogenic sources are road and ship traffic, biomass burning and agriculture. Because of the wide diversity of sources, the diameters of aerosol particles range from one nanometre to about hundred micrometres. The lower limit is set by the smallest number of gas molecules required to form a stable molecular cluster, and the upper limit is set by the gravitational settling which prevents large particles from staying suspended in the air. Aerosol particles can be found everywhere in the troposphere, from remote areas such as the North Pole (e.g. Heintzenberg et al., 2006) and Amazonian rainforest (e.g. Martin et al., 2010), with concentrations of a few tens or hundreds of particles per cubic centimetre, to polluted urban regions with several tens to hundreds of thousands of particles per cubic centimetre (e.g. Mönkkönen et al., 2005).

Particles emitted into the atmosphere directly from a source (e.g. windblown dust) are referred to as primary particles, while secondary aerosol particles are formed by condensation (uptake of vapours onto the available particle surfaces). The smallest and by number often the largest concentrations of particles are formed by a mechanism where gas molecules collide and form small molecule clusters (so called homogeneous nucleation). These small new particles may then grow by condensation.

Anthropogenic influence is observed all over the world, even in the most pristine regions, like the polar regions (e.g. Stone et al., 2010) and the tropical rainforests (e.g. Rissler et al., 2004). Simulations show that the anthropogenic emissions have increased the particle concentrations in remote continental regions with 50-300 % (Andreae, 2007). However, the anthropogenic climate impact relative to the natural contribution is still poorly known.

1.3 Aerosols and climate

Aerosol particles influence the climate of earth by directly scattering and changing the direction of the incoming solar radiation (direct effect). Part of the solar radiation will be scattered back to space instead of heating the surface of the earth and the atmosphere. This gives a net cooling effect on the global climate. An important exception is the dark soot particles formed from incomplete combustion e.g. within a diesel engine or from wood combustion. These particles instead absorb a large fraction of the solar radiation which illuminates them, and heat the atmosphere around them. Therefore, soot particle emissions give a net heating effect on the global climate. In a recent assessment report by Bond et al. (2013) the anthropogenic soot climate radiative forcing (change in radiation balance of the earth and atmosphere) was estimated to be as large as +1.1 W/m^2. If this value is correct, soot is the single largest climate forcer after CO_2 (figure 1). However, although the soot emissions most likely are warming the climate, the magnitude is very uncertain. According to Bond et al. (2013) the 90 % uncertainty bound of the radiative forcing of soot is +0.17 to +2.1 W/m^2.

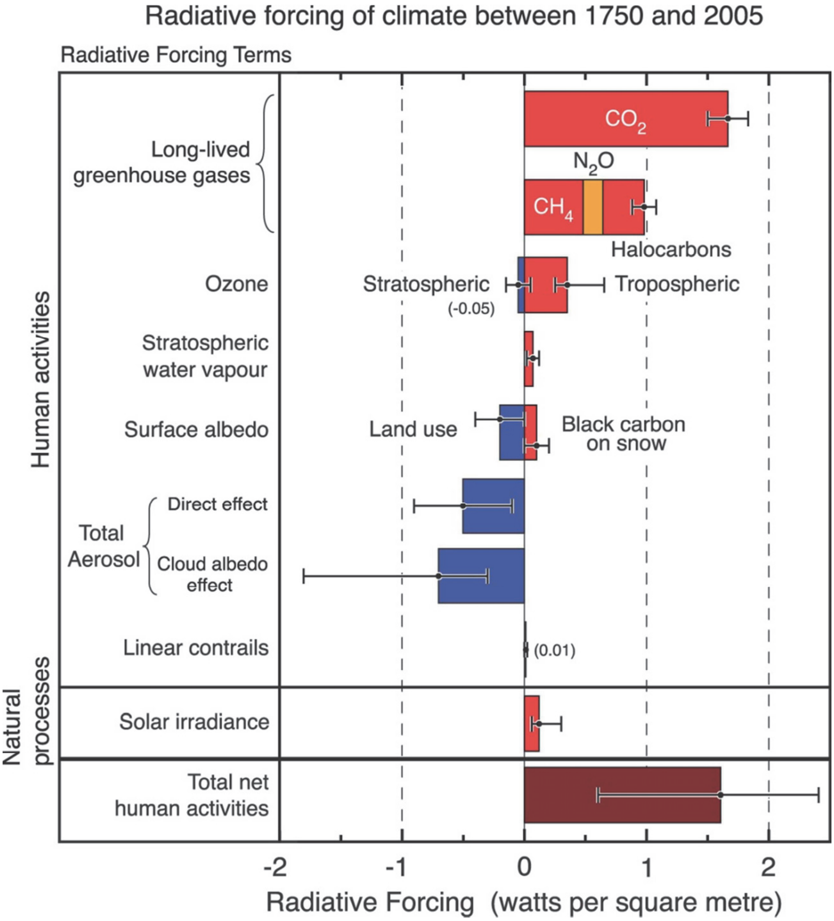

Figure 1. Summary of radiative forcing of climate change between 1750 and 2005 because of different anthropogenic activities. A positive forcing gives a warming of the climate while a negative forcing leads to a cooling. The error bars are 90 % confidence intervals (Reproduced from IPCC, 2007).

Aerosol particles also influence the global climate by changing the properties of the clouds (indirect effects). Without aerosol particles no cloud droplets would be formed at atmospheric conditions, and their number concentration, size and chemical composition influence the optical properties and lifetime of the clouds (e.g. Ramanathan et al., 2001, **Paper II**). If we emit more aerosol particles into the atmosphere, the clouds that are formed will contain more but smaller cloud droplets. These clouds are brighter and reflect more incoming sunlight back to space (cloud albedo effect) (Twomey, 1974). Smaller cloud droplets also inhibit precipitation and can thereby increase the lifetime of the clouds (Albrecht, 1989).

Today, it is virtually certain (i.e. > 99% probability) that anthropogenic emissions of aerosols have a net cooling effect on the global climate IPCC (2007). However, mostly because of the complex interactions between aerosols and clouds, the magnitude of this cooling is very uncertain (figure 1). IPCC, 2007 has stated that the radiative forcing caused by aerosols is the single largest source of uncertainty which limits the understanding of past and future climate changes.

1.4 Health effects of aerosol particles

Aerosol particles also influence the population health. This has been shown by several epidemiological studies (e.g. Dockery et al., 1993, Pope et al., 1995). The World Health Organization (WHO) has estimated that urban particle emissions causes 800 000 premature deaths annually in the world (World Health Organization, 2002), of which about 5 000 occur in Sweden (Forsberg et. al. 2005).

The adverse health effects which are dominated by cardiovascular and respiratory diseases, are primarily caused by particles deposited in the respiratory system (Löndahl, 2009). As for particle deposition in general (section 3.2), the most important mechanisms for deposition in the respiratory system are inertial impaction, diffusion, and gravitational settling. Because of the different deposition mechanisms and the complex geometry of the airways, the deposition pattern depends strongly on the particle size (ICRP Publication 66, 1995). For example, small particles (about 20 nm in diameter) are effectively deposited by diffusion, in the alveolar region of the lungs. In the lungs, particles trigger inflammations by the production of reactive oxygen species (Nel, 2005).

The physical and chemical particle properties responsible for the toxicity are still poorly understood. Air quality is regulated with respect to the total mass of particles below 10 µm in diameter (PM_{10}). However, it may very well be the submicron particles which are most relevant for the adverse health effects. These particles contribute relatively little to PM_{10}, but typical contribute to more than 99% of the total particle number concentration in urban regions. Many toxicological studies have shown that the particle surface area may be the single most relevant dose metrics for the health effects (e.g. Tran et al., 2000, Nygaard et al., 2004 and Schmid et al., 2009).

1.5 Strategies to reduce the uncertainties of aerosol impact on climate and air quality

Kulmala et al. (2011) identified 12 key subjects which primarily need to be studied in order to substantially decrease the uncertainty of the influence of aerosols on climate and air quality.

Among them, the flowing subjects are studied in this thesis:

- homogeneous nucleation,
- natural and anthropogenic particle emissions at urban, regional and global scales,
- the different anthropogenic and biogenic mass and number source contributions,
- secondary aerosol formation and gas-particle partitioning,
- influence of atmospheric ageing on the aerosol properties and
- the aerosol indirect effects.

These processes need to be studied experimentally and theoretically on all temporal and spatial scales (figure 2). This includes detailed process based models on the single particle scale (e.g. Shiraiwa et al., 2012, **Paper III**), laboratory chamber experiments (**Paper IV** and section 2.2**),** long-time measurements (section 2.1), local and regional scale Lagrangian modelling (e.g. Tunved et al., 2010, **Paper I** and **II**), regional and global Chemistry Transport Models (CTMs) (e.g. Simpson et al., 2003), global climate models (e.g. Makkonen et al., 2009) and earth system models (e.g. Hazeleger et al., 2012). The approximate temporal and spatial scales, and subjects covered in this thesis are marked with a rectangle in Figure 2.

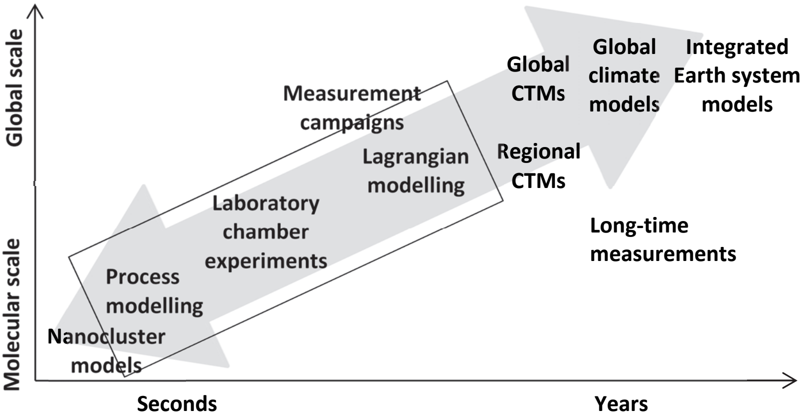

Figure 2. Schematic picture illustrating the different temporal and spatial scales of methods used in climate and air quality related aerosol research. Figure adopted from the original in Kulmala et al. (2011).

1.6 Main objectives of the thesis

Although, all methods presented in figure 2 are used extensively in current research, there is a lack of exchange of knowledge between the different research fields. This is partly because it is difficult to describe small scale processes in a computationally affordable way on a regional and global scale. However, there is also a lack of interdisciplinary exchange of knowledge between researchers working with different fields directly or indirectly related to aerosols and climate (e.g. particle physics and aerosol dynamics, particle phase chemistry, gas phase chemistry, meteorology, cloud microphysics and dynamics, dynamic vegetation processes, and the radiation balance of the earth), as well as between experimentalists and modellers within the same field.

The overall aims of this thesis were to:

1) develop theoretical models which combine the knowledge from experimental and theoretical studies within different research fields related to atmospheric aerosols (**Paper I** and **III**), and
2) evaluate and use these models in order to increase the knowledge about processes occurring on spatial and temporal scales which cannot be studied with regional and global chemistry transport models, or by measurements alone (**Paper II**-**IV**).

For this purpose, two different models were developed. The first model is an air mass trajectory model (Lagrangian model) for Aerosol Dynamics, gas and particle phase CHEMistry and radiative transfer (ADCHEM) **(Paper I)**. The second model is an Aerosol Dynamics, gas- and particle- phase chemistry, kinetic multi-layer model for laboratory CHAMber studies (ADCHAM) **(Paper III)**.

2 Measurements of particles

2.1 Long-time atmospheric observations

To better quantify the anthropogenic and natural influence on the aerosol properties, standardized and continuous measurements are needed. This is performed at 20 European Supersites for Atmospheric Aerosol Research (EUSAAR). One of these stations is the Vavihill field station in southern Sweden (56° 01' N, 13° 09' E, 172 m a.s.l.).

Figure 3 gives an example of the measured particle number size distribution during a new particle formation event 30th-31st of March, 2008 at the Vavihill field station. The new particles are formed by homogeneous nucleation during the morning and have grown by condensation to detectable size (3 nm in diameter) at around noon. The particles continue to grow until next day and reach a diameter of 70 nm, one day after the new particle formation event was first observed.

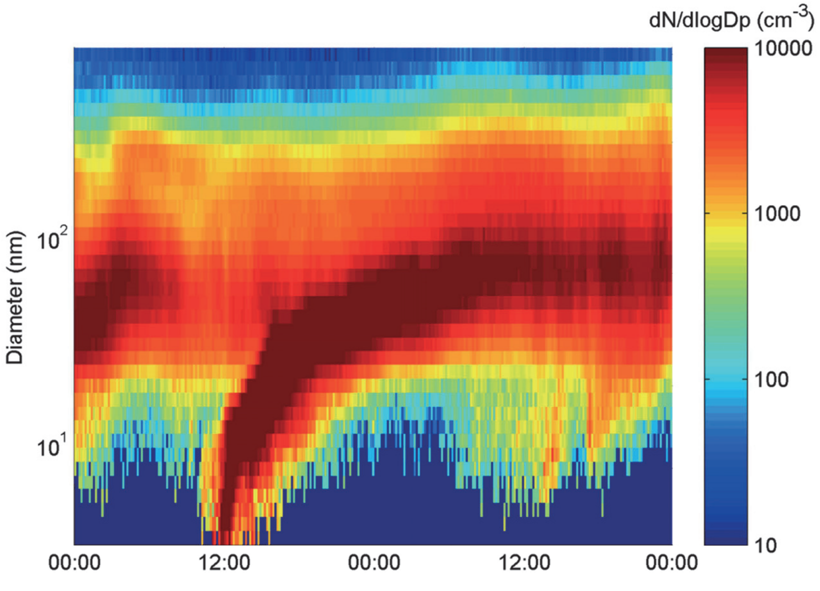

Figure 3. DMPS measurements during a new particle formation event the 30 th-31st of March, 2008 at Vavihill field station.

One way of evaluating a Lagrangian model is to follow an air mass traveling between two measurements stations, and use the data from the upwind station as input to the model and the downwind station as an evaluation point. This method was used in **Paper I** and **II,** where the measured particle number size distribution at the urban background station in Malmö (55° 36' N, 13° 00' E, 30 m a.s.l.) was used as input to the model. The measured particle number size distribution at the Vavihill background station (50 km downwind Malmö) was used to evaluate the model performance.

In more remote regions of the world (e.g. Amazonian rainforest, over oceans and the polar regions) there is still very little measurement data on the aerosol physical and chemical properties. Researchers from the aerosol group at the Division of Nuclear Physics at Lund University were part of the European integrated project on aerosol cloud climate air quality interactions (EUCAARI) (Kulmala et al., 2011). This project financed the development and maintenance of aerosol measurement sites in China, India, South Africa and Brazil. I was involved in the development, maintenance and evaluation of the data from one of those sites, which is positioned at a remote site in the Amazonian rainforest 60 km NNW from the city of Manaus (2.6° S, 60.2° W, 110 m a.s.l.) and 1600 km SW from the Atlantic Ocean. Since the start in February 2008 several studies have been published which describe the aerosol characteristics at this site (e.g. Gunthe et al., 2009, Pöschl et al., 2010, Alm, 2010 and Rizzo et al., 2013).

During the dry season, massive clear cutting and biomass burning in the Brazilian rainforest is conducted in order to clear land for agricultural use (Guyon et al., 2005). This anthropogenic land use has substantial impact of the aerosol properties over large areas of pristine rainforest, several hundred kilometres from the areas with intensive biomass burning.

Figure 4 shows the measured median particle number size distributions at the EUCAARI station in the Amazonian rainforest during the wet season (Feb-Jun) and dry season (Jul-Nov), respectively. The difference between the wet and dry season particle number size distributions is likely a good proxy of the contribution from long distance transported anthropogenic biomass burning aerosols. Although, other factors such as larger wet deposition losses during the wet season and influence from particle emissions in Manaus can also influence the concentrations.

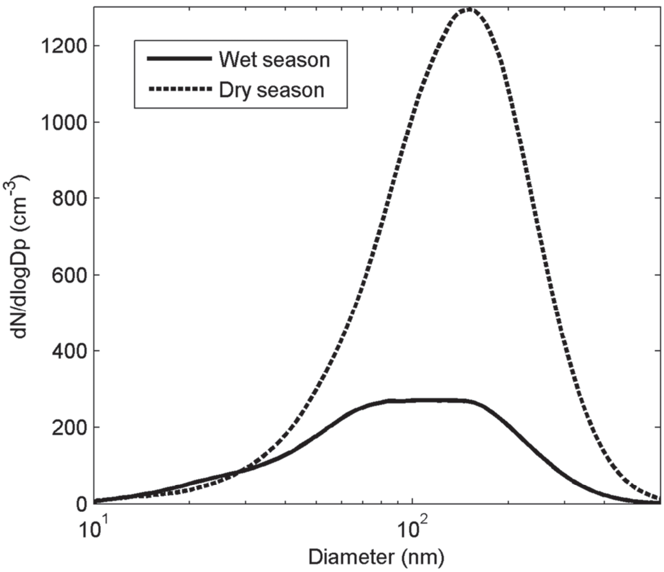

Figure 4. Measured median particle number size distributions from the EUCAARI station outside Manaus, during the wet season (Feb-Jun) and dry season (Jul-Nov). The data are from year 2008 and 2009.

2.2 Laboratory chamber experiments

A common problem with atmospheric measurements is that it is often hard to distinguish between different sources and atmospheric processes which affect the aerosol compositions. Hence, laboratory chamber experiments conducted during well controlled conditions (e.g. temperature, humidity and light intensity), are needed as a complement to atmospheric measurements.

One example is the CLOUD chamber at CERN in Zürich. CLOUD was built to study the effect of cosmic rays on aerosols, cloud droplets and ice particles. The well controlled and extremely clean environment in the stainless steel chamber of 26 m^3 enables the researchers to study specific homogeneous new particle formation mechanisms (Kirkby et al., 2011).

However, most chamber experiments reported in the literature deal with secondary organic aerosol (SOA) formation from different known precursors. These are gas phase compounds emitted from vegetation (e.g Hoffmann et al., 1997, Griffin et al., 1999 and Ng et al., 2008), or e.g. by gasoline cars (Odum et al., 1996, Ng et al., 2007, Hildebrandt et al., 2009 and **Paper IV**)). Parameterizations from these experiments are used in many chemistry transport models of today. In **Paper III** ADCHAM was used to study the SOA formation and properties during such experiments, and in **Paper IV** we performed experiments on the SOA formation from ageing gasoline car exhausts in a 6 m^3 Teflon chamber.

2.3 Particle number size distribution measurement techniques

Particle number size distributions are commonly measured with Scanning Mobility Particle Sizers (SMPS) or Differential Mobility Particle Sizers (DMPS). In these instruments the sampled particles are first charged with a bipolar diffusion charger. Here they gain a well-defined charge distribution (Wiedensohler, 2012). After this, the aerosol enters a Differential Mobility Analyser (DMA) where particles with a specific mobility diameter are selected, using an electrode with known voltage. Finally the particles are detected with a Condensation Particle Counter (CPC). By changing the voltage on the DMA electrode, particles with different electrical mobility can be selected with short time intervals. The particle number size distribution is derived from the measured electrical mobility distributions using the known charge distribution, and collection efficiency of the CPC.

In the SMPS system the voltage on the electrode is changed continuously according to an exponential function, while in a DMPS system the voltage is changed stepwise. This is the main difference between the two instrument types and is the reason why SMPS systems can measure a full particle number size distribution within about 1 minute, while a DMPS system typically requires about 10 minutes.

At the Vavihill field station the particle number size distribution measurements are performed with a Twin-DMPS. This instrument uses two DMAs instead of one to measure a full particle number size distribution. The first DMA is used to measure the small particles (at Vavihill between 3 and 21 nm) and the second DMA measures the larger particles (at Vavihill between 21 and 900 nm).

2.4 Measurements of the chemical particle composition

Although SMPS and DMPS systems give detailed information about the physical properties of the submicron particles, the instruments give no direct information of the chemical composition of the particles. Such information can instead be achieved either with filter samples, followed by off-line measurement techniques (e.g. Particle Induced X-ray Emission (PIXE) or Transmission Electron Microscopy (TEM)) (see for instance Martinsson et al., 2009 and Pöschl et al., 2010) or with on-line techniques (e.g. Time of Flight Aerosol Mass

Spectrometry (ToF-AMS) DeCarlo et al., 2006). One drawback with filter samples is that they generally have a low time resolution (usually days to weeks), and although they can give size resolved information (e.g. TEM), the analysing methods are generally very time consuming. Therefore, ToF-AMS which has a high time resolution (5 min) is a popular and frequently used instrument (see e.g. the overview article by Jimenez et al., 2009). The AMS can give size resolved information on the inorganic (nitrate, sulphate, ammonium and chloride) and organic compositions in the particles between about 50 and 1000 nm in diameter.

2.5 Combination of measurements and models

The combination of measurements and models often gives more valuable information than the measurements or models alone. The size resolved chemical and physical particle properties measured with a SMPS or DMPS system and AMS, enables us to calculate hygroscopic and optical properties of the aerosol particles (section 4 and 6). Together with an adiabatic cloud parcel model we can even estimate their ability to form cloud droplets during realistic atmospheric conditions (section 5 and 10.3).

At Vavihill the measured particle number size distributions (with the DMPS) is used as input to a Mie-theory model (section 6), which calculates the scattering and absorption coefficients (σ_s and σ_a), at different wavelengths of light (λ). The modelled scattering and absorption coefficients can then be compared with the measured scattering coefficients (from a 3-wavelength integrating Nephelometer) and absorption coefficients (from a soot photometer). This on-line closure gives direct information about the data quality of the instruments (figure 5). The agreement between the Mie-theory model and the Nephelometer measurements is usually best for the blue and green light. This is because the scattering coefficients at these wavelengths mainly are affected by the submicron particle concentrations and not the coarse mode particle concentrations (> 1 µm in diameter), which cannot be detected with the DMPS system.

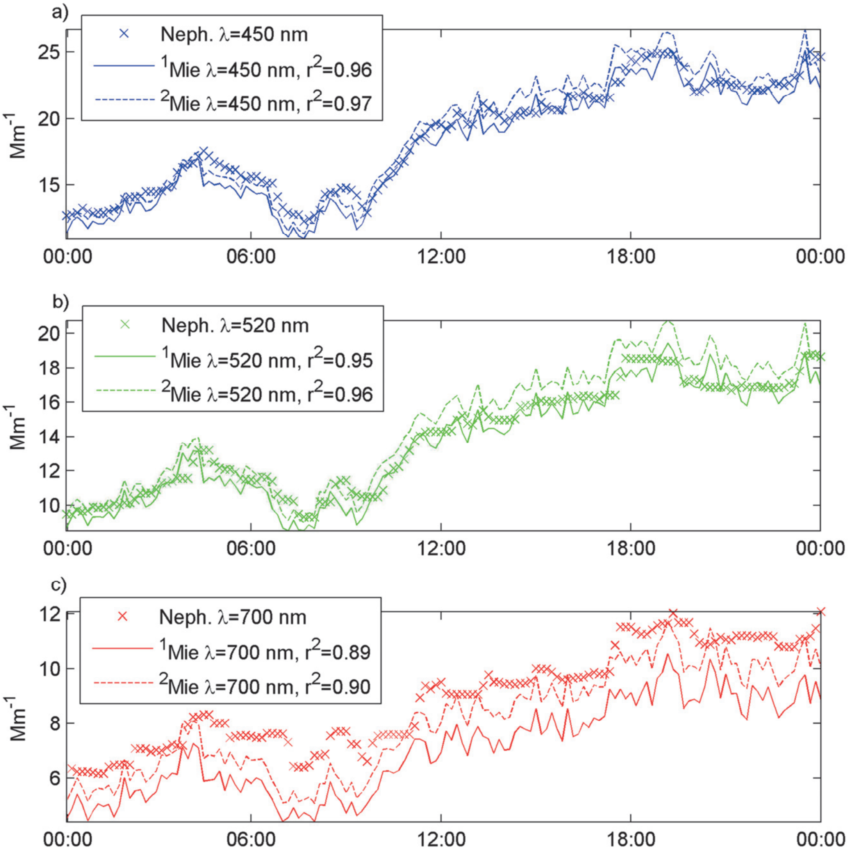

Figure 5. Comparison between measured and modelled particle scattering coefficients of blue light (λ=450 nm) **(a)**, green light (λ=520 nm) **(b)** and red light (λ=700 nm) **(c)**, at Vavihill the 6th of June, 2008. The model results are given for two different refractive indices, one for clean continental conditions (^1m_L=1.54-0.01i) and one for more polluted continental air masses (^2m_L=1.60-0.15i) (Ebert et al., 2004). The legend displays the squared correlation coefficients (r^2-values) between the modelled and measured scattering coefficients.

In all papers included in this thesis we combine the information from measurements and models in order to draw conclusions concerning different processes and aerosol properties relevant for climate and health.

3 Aerosol dynamics

In this section the most important aerosol dynamics processes in the atmosphere are described briefly and illustrated with a few examples. Readers interested in the governing equations and how they specifically are implemented in ADCHEM and ADCHAM are referred to **Paper I** and **III**.

3.1 Coagulation

Coagulation is the process where particles of same or different sizes collide and form larger particles. The probability of coagulation between two particles due to their Brownian motion (random motion because of the collision with gas phase molecules) depends on the diameters of the particles and the particle diffusion velocities. Particles with large diameters have low diffusion velocities but large particle surface areas to collide onto. Small particles on the other hand have high diffusion velocities but small surface areas. Therefore, the probability that either two small or two large particles will collide is much smaller than the probability that one small and one large particle will collide. Brownian coagulation is especially important in environments with a large number of small particles, (e.g. within a diesel engine, during new particle formation events or in a street canyon).

However, there are also other coagulation mechanisms which are important in the presence of large particles or cloud droplets (see Pruppacher and Klett, 1997). Large particles or cloud droplets with high fall velocities cause a substantial enhancement of the Brownian coagulation (so called convective Brownian coagulation). Additionally, the relative difference in sedimentation velocity between the aerosol particles and/or droplets enhances the coagulation rate (gravitational impaction).

Inside clouds, turbulence also enhances the coagulation rates because of: (1) velocity gradients which create relative particle motions (turbulent shear impaction) and (2) acceleration which (depending on their mass) give particles different relative velocities, (turbulent inertial impaction). Both the turbulent shear and inertial impaction depend on the rate of dissipation of kinetic energy per mass in clouds (ε). Observed values of ε inside different cloud types vary between 3 $cm^2\ s^{-3}$ in the least turbulent clouds (stratus) up to 2000 $cm^2\ s^{-3}$ in strong cumulonimbi (Pruppacher and Klett, 1997).

Figure 6 compares the coagulation rates of different coagulation mechanisms, between a particle with a diameter of 1 μm and other particles or droplets of different sizes. For all coagulation mechanisms except turbulent inertial impaction, the minimum coagulation rate is found for particles of equal size (in this case 1 μm in diameter). The figure also illustrates that Brownian coagulation is the only coagulation mechanism which is important for submicron particle sizes.

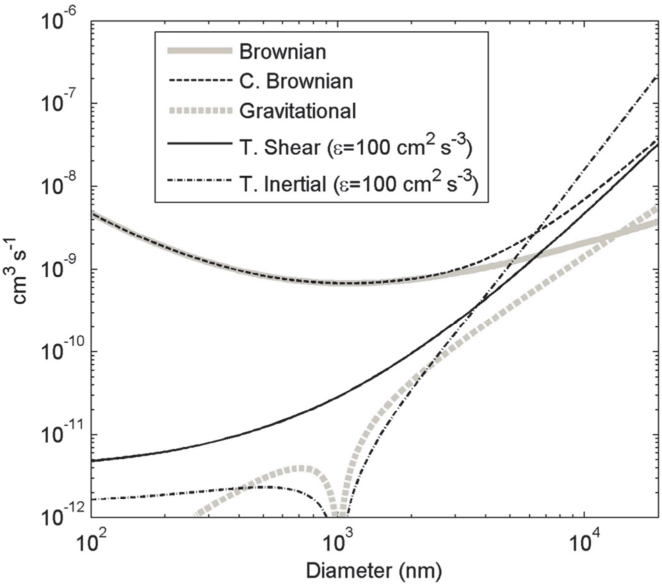

Figure 6. Coagulation rates of different coagulation mechanisms between a particle with a diameter of 1 μm, with other particles of different particles sizes (x-axis).

3.2 Dry deposition

The dry deposition (deposition without influence from clouds or precipitation) of particles onto different surfaces depends on impaction, interception, diffusion and gravitational settling. For the smallest particles (<0.1 μm in diameter) diffusion is the dominating mechanism, while for larger particles (>1 μm in diameter) gravitational settling is the main deposition loss mechanism in the atmosphere. Between 0.1 and 1 μm in diameter, there is a minimum in the dry deposition velocity because neither diffusion nor gravitational settling is an important loss mechanism. The dry deposition velocities of particles also depend on the surface structure (e.g. vegetation type) and the stability of the atmosphere. For instance a rough surface (e.g. a forest or city with large buildings) gives substantially larger dry deposition losses than a flat surface (e.g. grasslands).

During laboratory chamber experiments the deposition of particles to the chamber walls is largely governed by particle charge distribution and the chamber wall surface area to volume ratio (McMurry and Rader, 1985, Pierce et al., 2008 and **Paper III**). Particles in the air may be charged already when they are formed or when they collide with air ions. Air ions are e.g. formed during the decay of radon in the air. After some time in the atmosphere the particles approach a well-defined size dependent equilibrium charge distribution, with approximately equal amounts of positively and negatively charged particles. The same charge distribution is achieved in the bipolar diffusion charger of an SMPS or DMPS system (section 2.3).

Figure 7 shows: (a) the modelled fraction of particles with at least one positive or negative elemental charge and (b) the effective particle deposition losses to the chamber walls in the Teflon chamber in the aerosol lab at Lund University. The model results are given as a function of particle diameter and for different particle residence times within the chamber. Figure 7b also shows the initial wall loss rates for particles with no charge. The effective wall losses of the smallest particles rapidly decrease because the charged fraction is lost to the chamber walls. However, for the particles larger than 200 nm in diameter the effective wall deposition loss rates even increase over time. This is because the air volume within the chamber (flexible Teflon bag) decreases during the course of the experiment with about 0.8 m^3 $hour^{-1}$ which increases the chamber surface area to volume ratio.

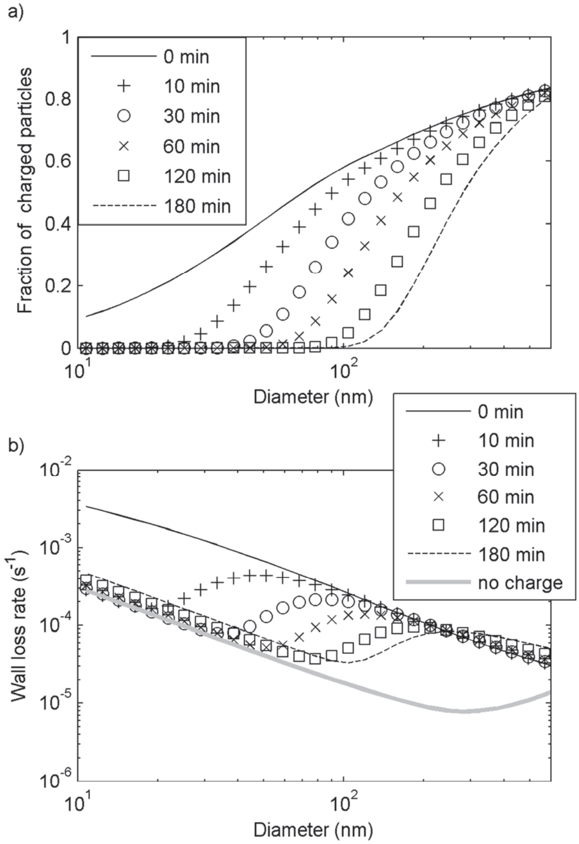

Figure 7. Modelled **(a)** fraction of particles with at least one positive or negative elemental charge and **(b)** the effective wall loss rates of particles of different sizes, in the Lund University Teflon chamber with an initial volume of 6 m^3, a volume loss rate of 0.8 m^3 hour^{-1}, a friction velocity of 0.05 m/s and an mean electrical field strength of 50 V/cm. At the start, the particles were at charge equilibrium.

3.3 Condensation and evaporation

Condensation is the process by which particles grow because of a net transport of gas molecules to the particles surfaces, while evaporation is the process by which particles shrink because of a net transport of molecules away from the particle surfaces. It is the concentration gradient of a compound i between the gas phase far from the particle surface ($C_{\infty,i}$ (moles m^{-3} air)) and the saturation concentration at the particle surface ($C_{s,i}$) which determine whether the particles will grow or shrink. At equilibrium between the particle and gas phase the concentration gradient between the gas phase and the particle surface is zero, and the particles neither grow nor shrink. Equation 1 gives the particle molar growth rate (I_i) of compound i. D_i is the gas phase diffusion coefficient of compound i, D_p is the particle diameter and f_i is a correction factor (Fuchs and Sutugin, 1971) for the so called transition regime.

$$I_i = 2D_i D_p f_i \left(C_{\infty,i} - C_{s,i}\right) \tag{1}$$

In the transition regime the diameter of the particles are comparable to the average travel distance of a gas molecule between collisions with other molecules (the mean free path). In air at room temperature and sea level pressure the mean free path is 65 nm. Hence, for submicron particles the gas around them does not behave as a homogeneous fluid (continuum regime).

For low volatile compounds with very low saturation concentrations (e.g. sulphuric acid) evaporation is usually a negligible process and the condensation growth is independent of the particle phase composition. However for most compounds, condensational growth requires that the compounds can dissolve in a water or organic particle phase, protonate or deprotonate, or form salts with other compounds in the particle phase.

If the condensable compound i is partitioning (dissolve) into the particle phase of a particle, the saturation concentration ($C_{s,i}$) can be derived from Raoult's law, corrected with activity coefficients (γ_i) which take into account the non-ideal interactions between the different compounds in the solution and the Kelvin effect (C_{k_i}) (eq. 2-3). $p_{0,i}$ in equation 2 is the pure-liquid saturation vapour pressure of compound i over a flat surface composed of only that compound. x_i is the mole fraction of compounds i in the particle phase which i dissolve in.

$$C_{s,i} = p_{0,i} \cdot x_i \cdot \gamma_i \cdot C_{k_i}/(RT) \tag{2}$$

$$C_{k_i} = e^{\left(\frac{4M_i\sigma_i}{RT\rho_p D_p}\right)} \tag{3}$$

T is the temperature in Kelvin, R is the universal gas constant (8.3145 J mol^{-1} K^{-1}), M_i is the molar mass of compound i, ρ_p is the density of the particle phase which the compound partition into and σ_i is the surface tension of compound i.

The Kelvin effect describes the relative increase in the vapour pressure because of the curvature of a particle surface. At a curved surface the intermolecular bonds between a molecule and its neighbour molecules are weaker. Hence, the molecules easier escape from curved surfaces than flat. Because the curvature increases with decreasing particle diameter, the saturation vapour pressure (of particles with identical composition) increases with decreasing particle size. This effect is mainly important for particles below 100 nm in diameter. For the smallest particles in the atmosphere (about 1 nm in diameter) the Kelvin effect is a strong barrier to overcome in order to grow. Therefore, these particles can only grow by certain very low volatile compounds (e.g. sulphuric acids or the least volatile organic compounds) (section 3.4 and **Paper III**).

Processes that decrease x_i (e.g. solid salt formation, other particle phase reactions and increased water content) allow the particles to grow faster (see section 4.2 and **Paper III**).

3.4 Homogeneous nucleation

Homogeneous nucleation is the process by which gas phase molecules form stable clusters with a diameter of around 1 nm. The molecules can either be formed of the same or different compounds. In the atmosphere it is still not clear: (1) which molecules that are involved in the formation of stable molecular clusters, (2) which molecules that are involved in the initial growth of these clusters, (3) the exact mechanism responsible of the cluster formation and the initial growth of these clusters, and (4) whether it is the formation or initial growth of these clusters that mainly limits the frequently observed homogeneous new particle formation in the atmosphere (figure 3).

The most recent observations in the atmosphere (Kulmala et al., 2013) indicate that sulphuric acid is one of the compounds in these 1-1.3 nm clusters, possibly stabilized by a strong base (e.g. amine). The slow initial growth between 1.2-1.7 nm may be explained by uptake of sulphuric acid. However, for particles larger than 2 nm, organic compounds must be involved to explain the observed growth rates.

For atmospheric model simulations, semi-empirical parameterizations of the formation rate (dN/dt (particles cm^{-3} s^{-1})) of clusters of e.g. 1.5 nm in diameter are commonly used. In these parameterizations the formation rate is often proportional to the sulphuric acid concentration to the power of 1 or 2 (eq. 4). The value of the exponent β depends on whether the clusters are believed to form from two colliding sulphuric acid molecules (kinetic nucleation theory (McMurry and Friedlander, 1979)), or from one sulphuric acid molecule that activates by heterogeneous reactions (Activation nucleation theory (Kulmala et al., 2006)). The correlation coefficient (K) in equation 4 is determined experimentally (e.g.

Paasonen et al., 2009). Unfortunately the value of K can vary substantially between different nucleation event days and at different geographical locations.

$$\frac{dN_{1.5nm}}{dt} = K[H_2SO_4]^{\beta} \qquad (4)$$

3.5 Wet deposition

Wet deposition can be divided into: (1) in cloud scavenging (rainout) and (2) below cloud scavenging (washout). Although the name implies that it is a deposition mechanism, the fundamental mechanisms which govern these processes are the different coagulation mechanisms described in section 3.1, condensation and evaporation which is described in section 3.3 and cloud dynamics (e.g. Cotton et al., 2011).

Below cloud scavenging is the process by which particles (and gases) are scavenged by precipitation. The wet deposition of particles depends on the size of the particles and the raindrops (snow crystals), but also on the intensity of the precipitation. During precipitation the wet deposition losses of particles and gases are generally substantially larger than the dry deposition losses.

Figure 8 shows the calculated below cloud scavenging particle deposition loss rate as a function of particle size, for a rain intensity of 1 and 10 mm hour^{-1}. The results were derived with an empirical parameterization from Hyytiälä in Finland (Laakso et al., 2003). As a comparison, figure 8 also displays the estimated effective dry deposition loss rates over a coniferous forest, during atmospheric stable conditions, a mixing height of 100 m and a wind speed of 1 m/s above the canopy. The dry deposition loss rates were calculated with the resistance model (Slinn, 1982 and Zhang et al., 2001), which is used in ADCHEM (**Paper I**).

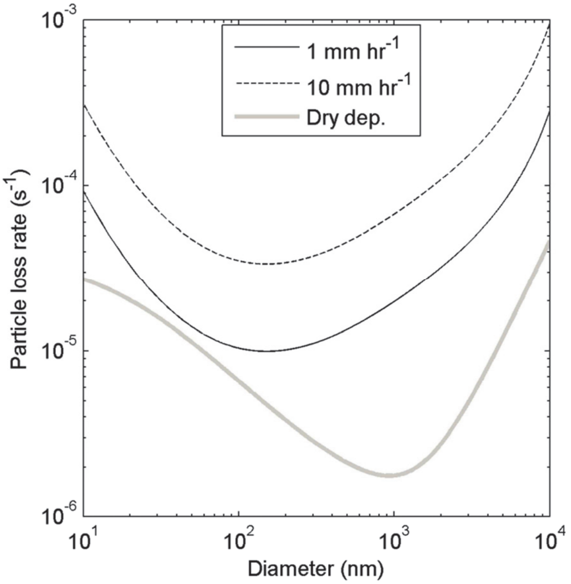

Figure 8. Below cloud scavenging, calculated with the empirical parameterization from Laakso et al. (2003), at rainfall intensities of 1 and 10 mm hour^{-1}. Given are also the calculated (with the resistance model by Slinn, 1982 and Zhang et al., 2001) effective dry deposition loss rates over an coniferous forest, during atmospheric stable conditions with a mixing height of 100 m and a wind speed of 1 m/s.

In cloud scavenging refers to the processes where particles are incorporated into the cloud droplets, either during the cloud droplet activation phase (nucleation scavenging) or by coagulation between the particles and cloud droplets (impaction scavenging) (Pruppacher and Klett, 1997 and section 5).

4 Particle phase chemistry

In order to model the gas-particle partitioning of e.g. hydrochloric acid, nitric acid and ammonia, the saturation concentrations above the particles or cloud droplet surfaces need to be determined (see section 3.3). This requires a thermodynamic model which can calculate:

1) the hydrogen ion concentration ($[H^+]$) (acidity) in the particle phase(s),
2) the dissociated and non-dissociated electrolyte and salt concentrations,
3) the non-ideal interactions (activity coefficients) of all compounds in the dissolved phase(s) and
4) the water content of the particle phase(s).

The problem is that all these properties depend on each other. Hence, an iterative approach is required, which starts with a first guess of the initial concentrations and activity coefficients. After this the model step by step calculates the properties in the list above and finally compares the new concentrations with the starting values (first guess). If the difference between any of these values is larger than a specified error tolerance the model starts from the beginning again.

Readers interested in the descriptions of how the models in this thesis calculate the different parameters in the list above are referred to **paper I** and **III**. Below a simplified example is given on how the thermodynamic model used in ADCHAM (**paper III**) can be used to estimate the water uptake of aerosol particles at different relative humidities (RH).

For known relative humidity (RH) the mole fraction of water in the particle phase (x_w) can be calculated with equation 5. a_w is the water activity which is equal to the RH for large particles with negligible surface curvature.

$$x_w = \frac{a_w}{\gamma_w}, \qquad a_w = \frac{p_{s,w/p_{0,w}}}{C_{k_w}} = \frac{RH}{C_{k_w}} \tag{5}$$

Figure 9 shows the modelled and measured solute mass fraction (dry particle mass / particle mass including water) for particles with a 1:1 molar ratio of malonic acid to ammonium sulphate ($(NH_4)_2SO_4$), at different a_w. The figure also shows the modelled solute mass fraction for pure ammonium sulphate (salt) and malonic acid (org.) particles. The water activity coefficient in equation 5 was derived with the activity coefficient model AIOMFAC

(Aerosol Inorganic-Organic Mixtures Functional groups Activity Coefficients) from Zuend et al. (2011).

The measurements in figure 9, which are from Choi and Chan (2002), show the gradual loss of water (increase of the solute mass fraction) from particles which first were allowed to equilibrate in an atmosphere at high RH. The model results and measurements are in good agreement all the way down to a water activity of approximately 0.45 (RH ≈ 45 %). At this a_w the mixed phase organic and inorganic salt particles suddenly lose a substantial fraction of the remaining water (seen as a sudden increase in the solute mass fraction in the measurements). This is probably because the dissolved ammonium and sulphate ions crystalize and form solid salts. However, the organic particle phase still contains small amount of water, at least down to a water activity of 0.1.

In the atmosphere the RH is usually larger than 45 %, and even at lower RH this sharp transition from a liquid to crystalline solid salt phase rarely exists. The reason for this is that atmospheric particles contain a much more complex mixture of organic and inorganic compounds with different hygroscopic properties.

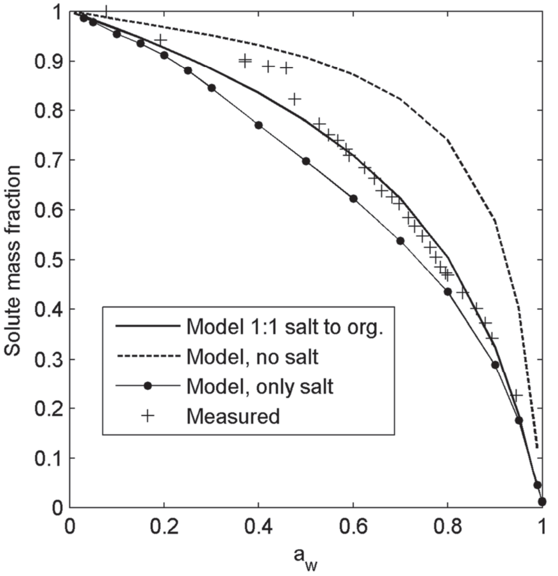

Figure 9. Comparison of modelled (AIOMFAC) and measured solute (malonic acid + ammonium sulphate) mass fractions, as a function of the water activity. The measurements were performed with electrodynamic balance (EDB) on evaporating particles with 1:1 molar ratio of malonic acid to ammonium sulphate (Choi and Chan, 2002).

4.1 Secondary organic aerosol (SOA) formation

The initial growth of stable molecule clusters during a nucleation event (figure 3) is a good example of observed secondary aerosol formation in the atmosphere. Even though sulphuric acid likely is involved in the homogeneous nucleation (section 3.4), the sulphuric acid vapour concentration is usually at least one order of magnitude too low to explain the observed particle growth rates (Kulmala et al., 2004).

Instead the growth of the nucleation mode particles is dominated by condensation of organic compounds (Kulmala et al., 2004 and 2013). However, modelling realistic SOA formation in the atmosphere is challenging because the SOA formation involves thousands of unknown compounds (Donahue et al., 2006). Furthermore it requires that the concentrations of the hydroxyl radical (OH), ozone ($O_{3)}$ and the nitrate radical (NO_3), which oxidize the organic compounds in the gas and particle phase (**Paper III**), can be modelled accurately.

Traditionally the SOA formation has been modelled as an equilibrium process using the partitioning theory from Pankow, 1994. The partitioning theory (which is based on Raoult's law) is usually used together with semi-empirical parameterizations on the SOA formation from known SOA precursors (e.g. light aromatic compounds and monoterpenes). The parameterizations are derived from laboratory chamber experiments (e.g. Odum et al., 1996, Pathak et al 2007 and **Paper IV**). They contain a number of representative model compounds (products) with different volatilities and relative mass contributions. Often not more than two products are required in order for the parameterization to capture the experimental data points (two-product models).

Lately the Volatility Basis Set (VBS) method (Donahue et al., 2006) which also builds on the partitioning theory has become a popular method (e.g. Lane et al., 2008, Shrivastava et al., 2008 and Tsimpidi et al., 2010, Donahue et al., 2011 and **Paper I** and **II**). In ADCHEM the user can choose whether to use semi-empirically two-product model parameterizations for individual SOA precursors, or the newly developed 2D-VBS method (Jimenez et al., 2009, Donahue et al., 2011).

In the 2D-VBS the organic compounds are divided into different volatility classes and into different oxygen to carbon ratio (O:C-ratio) classes, as a second dimension. The primary advantage of the 2D-VBS compared with the two-product model parameterizations is that it can (although, in a very simplified manner) describe the gradual oxidation of organic compounds in the atmosphere. One large disadvantage is however that the model parameters (e.g. the oxidation reaction rates, and how the volatility of the compounds changes upon oxidation) are poorly known and still need to be tuned based on experimental data (Jimenez et al., 2009 and **Paper I**).

Paper I describes the semi-empirical two-product model parameterizations and 2D-VBS method, how they are implemented in ADCHEM, and finally how they can be used to simulate non-equilibrium SOA formation in the urban plume from Malmö.

If used as equilibrium partitioning models, the semi-empirical two-product model parameterizations and the VBS method require relatively little computational resources, and do not rely on detailed gas- and particle-phase chemistry models to calculate the SOA formation and gradual ageing in the atmosphere. This is probably one of the main reasons why they are used frequently.

As a complement to these simplified descriptions of SOA formation, explicit process based models which combine the state of the art within gas phase chemistry (e.g. Jenkin et al., 2003, Valorso, et. al. 2011), mass transfer limited gas-particle partitioning (e.g. Shiraiwa et al., 2012) and particle phase chemistry (e.g. Ervens and Volkamer, 2010, Pfrang et al., 2011 and Zuend and Seinfeld, 2012) are also needed. This is the main motivation why we developed the ADCHAM model (section 9 and **Paper III**).

4.2 Organic particle phase reactions

SOA formation is most often considered as an equilibrium process driven by the oxidation of organic compounds in the gas-phase (e.g. Pankow, 1994 and Donahue et al. 2011). However, during the last decade reactions in the particle phase (heterogeneous reactions) have also been postulated to be important for the SOA properties and formation. The most important are:

1) oligomerization (polymerization) (e.g. Kalberer et al., 2004),
2) oxidation of organic compounds with e.g. O_3, OH, NO_3 and NO_2 in the particle phase (e.g. Knopf et al., 2005),
3) reactions between organic and inorganic compounds and formation of organic salts (e.g. Na et al., 2007) or organosulphates (e.g. Liggio and Li, 2006), and
4) interactions between inorganic ions, water and organic compounds, which may cause liquid-liquid phase separations or evaporation of organic compounds (salting-out) (e.g. Bertram et al., 2011).

In **paper III** the potential influence from these processes on the SOA properties and formation are studied. Process 1-3 have in common that they in general give less volatile and more viscous SOA. If no particle phase separation occurs, they also decrease the particle mole fractions of the condensable organic compounds which are formed in the gas phase, and hence also their saturation concentrations (eq. 2). Because of these reactive uptake mechanisms, SOA can be formed from compounds which otherwise would be too volatile to go into the particle phase. This may explain why particles around 2 nm in diameter can grow despite the large curvature effect (section 3.4 and e.g. Barsanti et al., 2009).

4.3 Phase state of the organic aerosol particles

Several experiments on laboratory produced pure SOA particles and SOA dominated particles formed in the atmosphere have shown that these particles are composed of solid or semi-solid viscous amorphous materials (like tar or wax) (e.g. Virtanen et al., 2010). For these particles the mixing within the particle phase is kinetically limited. Hence, the gas to particle partitioning cannot be well represented by an equilibrium process (Pöschl, 2011), which the models that build on the traditional partitioning theory assumes (Pankow, 1994). Grieshop et al. (2007) and Vaden et al. (2011) have illustrated that the evaporation of SOA particles formed from α-pinene ozonolysis is order of magnitudes slower than expected from equilibrium partitioning.

In **Paper III** we use the ADCHAM model to study the effects of: (1) mass transfer limited mixing within the particle phase, (2) formation and decomposition of low volatile oligomers and (3) adsorption of low volatile organic compounds at the particle surfaces, on the formation and evaporation rates of SOA particles.

5 Cloud microphysics

In this section an updated version of the adiabatic cloud parcel model, which was used in **Paper II** to estimate the anthropogenic influence on low level clouds, is described. The model calculates the relative humidity, temperature, total liquid water content (LWC), particle number and cloud droplet number size distributions, as a function of the altitude of an air parcel with a pre-specified updraft velocity. For this it takes into account the adiabatic expansion and the latent heat release upon condensation (see e.g. Jacobson, 2005). Equation 2 is used to derive the water saturation concentration at each particle or droplet surface. The activity coefficients for water and the inorganic and organic compounds dissolved in the particle water phase is calculated with the AIOMFAC model (Zuend et al., 2011).

In order to be able to calculate a more realistic cloud droplet distribution, the model was recently extended with an algorithm that takes into account different coagulation mechanisms between particles and cloud droplets (section 3.1). Additionally, the model now also considers the condensation and dissolution of inorganic and organic compounds onto the formed cloud droplets, and the formation of sulphate from the reaction between dissolved SO_2 and H_2O_2 (hydrogen peroxide).

However, the current model version does not take into account entrainment of air from outside the cloud and turbulent mixing within the cloud, which also are important in real convective clouds (see Pruppacher and Klett, 1997 and Cotton et al., 2011). In the future the model is primarily intended to be used as a module coupled to the ADCHEM model. This will enable a more realistic representation of the cloud particle processing. A similar approach has previously been used by Tunved et al. (2010) to simulate in cloud processing with the Chemical and Aerosol Lagrangian Model (CALM).

Figure 10 gives an example of the modelled RH, temperature and LWC as a function of the altitude of a rising air parcel, with an updraft velocity of 1 m/s. During the dry adiabatic expansion the temperature in the sub-saturated air parcel decreases with 9.8 K/km. The cooling of the air parcel increases the RH until it reaches a maximum super-saturation of about 100.25 %, 600 m a.s.l (figure 10 a). At this altitude, particles above a certain minimum particle size (about 100 nm in diameter) are activated and form cloud droplets. Thereby the water uptake from the gas phase increases substantially (figure 10 c), which causes the RH to slowly decrease and prevents even smaller particles from activating. Once the cloud has been formed, a large amount of latent heat is released upon condensation, and the lapse rate (temperature decrease per km) changes to about -5 K/km (figure 10 b).

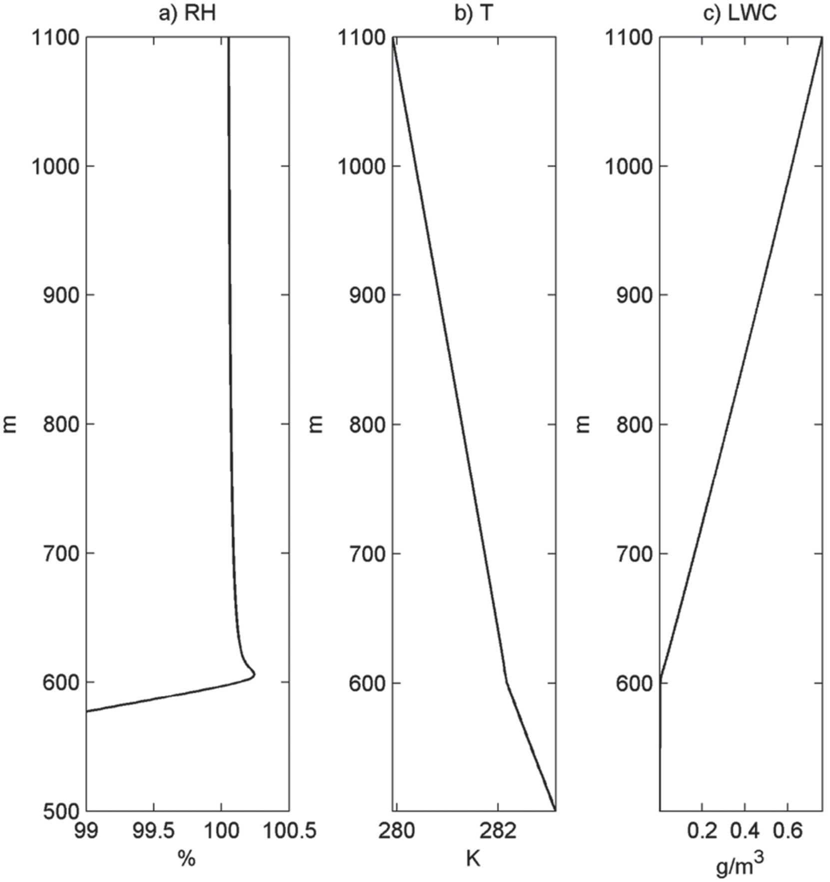

Figure 10. One example of modelled relative humidity **(a)**, temperature **(b)** and liquid water content (LWC) **(c),** as a function of the altitude of a rising air parcel with an updraft velocity of 1 m/s.

6 Optical particle properties and their influence on the radiation balance

To be able to compare and evaluate the measured particle number size distributions and the scattering and absorption coefficients measured with the Nephelometer and soot photometer at Vavihill (see section 2.2 and figure 5), a Mie-theory model for spherical particles with homogeneous composition was developed according to the theory given in e.g. Van de Hulst (1957) and Pilinis (1989). This relatively simple model assumes that the material within each particle is homogeneously mixed, and that the optical properties of the particles can be described by their diameter and an effective refractive index. The Mie-theory model calculates the scattering and absorption efficiencies (Q_a and Q_s) of the measured particle sizes. These single particle properties describe how efficiently the particles scatter or absorb the incident light, relative to their cross sectional area (A_{cross}). The scattering and absorption coefficients (σ_s and σ_a) are given by the product between the particle cross sectional area and the scattering and absorption efficiency, respectively (eq. 6).

$$\sigma_s = A_{cross}Q_s, \qquad \sigma_a = A_{cross}Q_a \tag{6}$$

Several theories exist on how to calculate the effective refractive index. Often it is calculated with a simple volume fraction additive method (see e.g. Ebert et al., 2004). For coated soot particles it is more realistic to use the Maxwell-Garnett mixing rule (Maxwell-Garnett, 1904), where the soot particles are treated as inclusions embedded in a host matrix of coating material (Kahnert et al., 2012).

6.1 Modelling of optical properties of soot particles in the atmosphere

Several global model simulations have estimated that soot or black carbon gives the largest positive radiative forcing (warming) after CO_2 (Jacobson, 2001 and Ramanathan and Carmichael, 2008). Fresh soot particles emitted e.g. by diesel engines are not spherical but consist of fluffy agglomerates composed of many small coagulated primary particles. As the soot particles age in the atmosphere, they are coated with secondary aerosol and water. This eventually leads to a transformation of the fluffy agglomerates into nearly spherical, more compact soot cores (e.g. Zhang et al., 2008). These solid soot cores are encapsulated and not dissolved in the secondary aerosol coating material. Hence, in reality the soot is not homogeneously mixed with the rest of the particle material.

The global warming effect of the soot particles may depend strongly on whether they predominantly are externally or internally mixed with the other aerosol particles in the atmosphere (figure 11). Traditionally, global climate models have treated the soot particles as externally mixed. However, Jacobson, 2001 showed that this may underestimate the global climate warming of soot with a factor of 2.

When the soot particles age in the atmosphere, coagulation and secondary aerosol formation transform the aerosol particles from completely externally mixed to gradually more internally mixed. However, this transformation is poorly known and will depend on the properties of the fresh soot agglomerates and the properties of the coating materials. It will be challenging to treat this gradual transformation and influence on the optical particle properties in global climate models.

Kahnert et al. (2012) modelled the optical properties of soot (light absorbing carbon) agglomerates coated with sulphate with a numerical exact solution of the Maxwell's equations, and compared the results with simplified treatments of the particle properties which are being used in global climate models (figure 11).

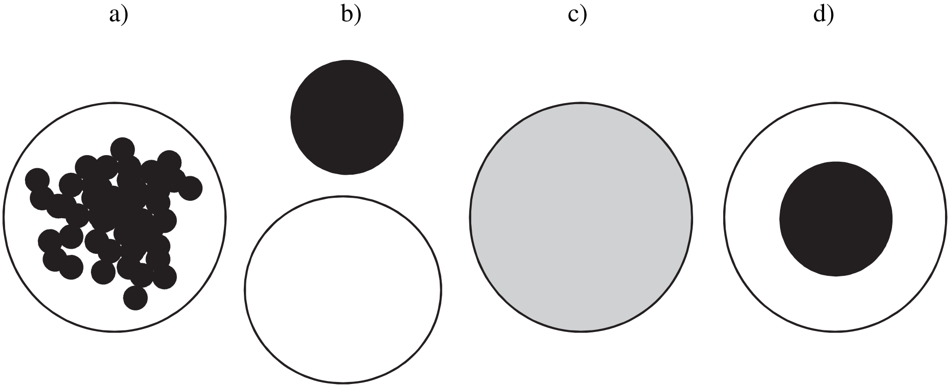

Figure 11. Schematic figures of: **(a)** realistic representation of a soot agglomerate coated with secondary aerosol material, **(b)** externally mixed primary soot and secondary aerosol representation in climate models, **(c)** homogeneously internally mixed soot and secondary aerosol and **(d)** core-shell representation of soot particles coated with secondary aerosol.

As expected, the worst agreement between the simple methods and the numerical exact method was found when the secondary aerosol (sulphate) and soot was completely externally mixed (figure 11b). More surprisingly, the more complex core-shell particle method (figure 11d) in general produced less accurate results than the homogeneous internal mixture method (figure 11c), even though the modelled soot particles were relatively compact with a fractal dimension of 2.6 (3 for spherical particles). At this fractal dimension, which is at the upper end of the range of values that have been observed in the atmosphere (Colbeck et al., 1990 and Nyeki and Colbeck, 1995), the core-shell method significantly underestimates the absorption. The reason for this is that the electromagnetic field cannot penetrate deeply into a massive soot sphere. Hence, the mass inside the compact soot cores is not contributing to the absorption of the incident light. For the same reason, the homogeneous internal mixture method instead overestimates the absorption efficiency slightly and underestimates the scattering efficiency (Kahnert et al., 2012).

Figure 12a shows the modelled Q_a and Q_s for spherical soot particles with or without non absorbing secondary aerosol (SA) coating. The particles were illuminated with visible light with a wavelength of 533 nm. Q_a and Q_s are given as a function of the diameter of the hypothetically spherical soot core. The coated particles were treated as homogeneously internally mixed. The refractive index was calculated with the Maxwell-Garnett mixing rule. The soot particles with coating have a SA to soot volume ratio of 7:1. Hence, the diameters of these particles are twice as large as the diameters of the soot cores. The scattering efficiency is at a maximum when the particle diameter is approximately equal to the wavelength of the incident light.

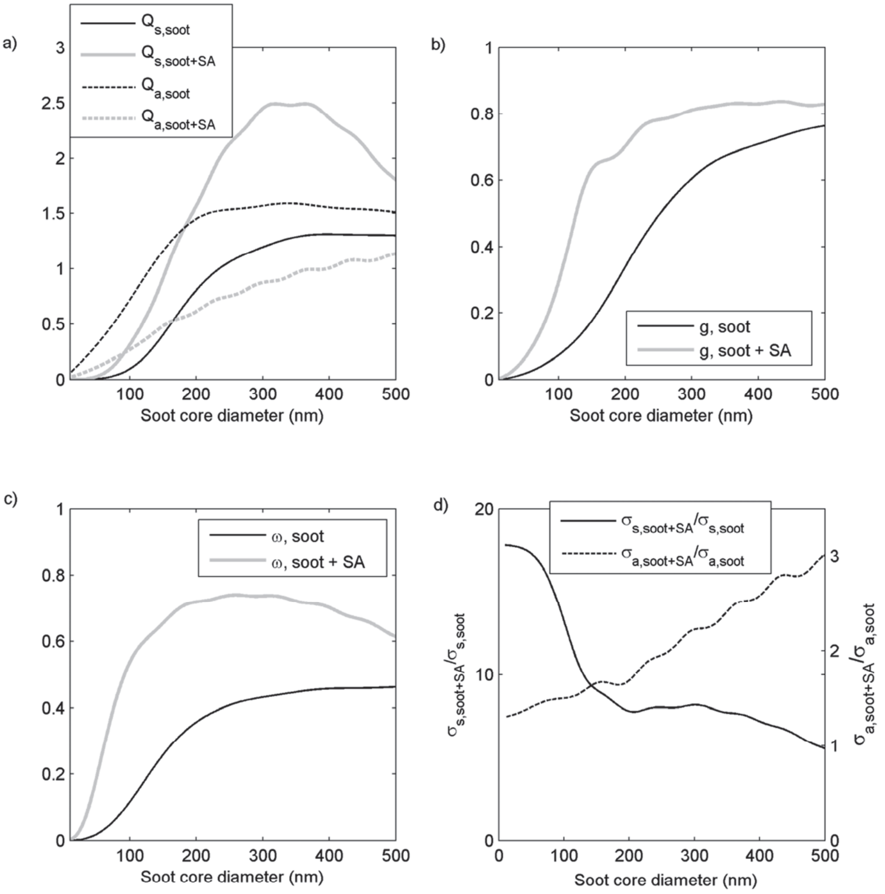

Figure 12. Modelled optical single particle properties of spherical soot particles, with or without secondary aerosol (SA) coating (7:1 SA to soot volume ratio). The refractive index of the soot was set to 1.76-0.63i and the refractive index for SA to 1.43, which with the Maxwell-Garnett mixing rule give an estimated refractive index of 1.4788-0.0723i for the coated soot particles. The wavelength of the incident light was 533.2 nm. Figure **(a)** shows the scattering and absorption coefficients, **(b)** the asymmetry parameters, **(c)** single scattering albedo and **(d)** the ratio between the scattering and absorption coefficients of the coated and uncoated soot particles, as a function of the soot core diameter.

The Mie-theory code is also used in the radiative transfer scheme which is implemented in the ADCHEM model (**Paper I**). There it is used to calculate the asymmetry parameters (g) and single scattering albedos (ω) of the modelled particles and cloud droplets. The asymmetry parameter approximates the phase function of the light which is scattered by the particles. If g is equal to 1, all light is scattered forward, while if g is equal to -1 all light is scattered backward. Particles larger than 0.5 μm in diameter mainly scatter in the forward direction, while particles smaller than approximately 0.05 μm and molecules have symmetric phase functions and emit light with equal intensity in the forward and backward directions (g=0) (so-called Rayleigh scattering) (figure 12b). The single scattering albedo is the ratio between the scattering efficiencies and the extinction efficiency (scattering + absorption).

Fresh soot particles, which usually have a volume equivalent diameter smaller than 100 nm, nearly exclusively absorb the incident light ($\omega<0.2$) (figure 12c). When these particles take up secondary aerosol material the scattering efficiency increases and the absorption efficiency decreases (figure 12a). However, both the scattering and absorption coefficient increases when the particles age. Figure 12d shows the ratio between the pure and coated spherical soot particles scattering and absorption coefficients. As expected the non-absorbing SOA coating has the largest influence on the scattering coefficients. However, also the absorption coefficients increase substantially, especially if the soot core is relatively large. The coating material can be viewed as a lens which scatters the light toward the soot core. In reality this effect will at least partly be cancelled out by the collapse of the initially fluffy agglomerates into more compact spheres. This may explain why recent field measurements only showed a small enhancement of the absorption coefficient because of SA coating of the soot particles (Cappa et al., 2012). The treatment of the fresh soot particles as compact spheres might underestimate their shortwave climate forcing with 50 % (Kahnert, 2010).

6.2 Radiative transfer in a vertically inhomogeneous atmosphere

In order to be able to model the gas phase chemistry of the atmosphere it is crucial that the photolysis rates of different gas phase components can be determined accurately. This is the main reason why the ADCHEM model (**Paper I**) is equipped with a radiative transfer model which describes the intensity of direct (from the sun) and diffuse (scattered light) in the upward and downward direction at different altitudes of the troposphere.

The model uses a two-stream approximation scheme developed by Toon et al. (1989). This scheme can be used to calculate the radiative transfer in a vertically inhomogeneous atmosphere with clouds and aerosols. Two-stream schemes are widely used in weather and climate models. They describe the radiative fluxes with one upward and one downward flux component for the diffuse light. This is of course a simplification. In reality the scattered light will be directed in all possible direction. There are also more sophisticated radiative transfer schemes which use four-stream approximations (e.g. Zhang et al., 2010).

In order to approximate the forward and backward scattered energy with only two components, effective asymmetry parameters are used. These parameters, which are the weighted sum of the asymmetry parameters for gases (Rayleigh scattering), aerosol particles and cloud droplets, are derived with a Mie-theory model (section 6). Additionally the radiative transfer scheme use the effective single scattering albedos and optical depths of gases, aerosol particles and cloud droplets in order to calculate the spectral irradiance at different altitudes of the atmosphere (see **Appendix G in Paper I**). The optical depth at different altitudes of the atmosphere describes how much of the incoming solar radiation that is scattered or absorbed in the air column through which the light is traveling.

Figure 13 shows an example of the modelled direct and net shortwave radiation through a clean marine stratocumulus type cloud with properties derived with the adiabatic cloud parcel model described in section 5. The albedo of the ocean surface below the cloud was set to 0.1. The results are from a simulation with a solar zenith angle corresponding to 22nd of June at 3 pm, and 60°N. At the top of the cloud the solar irradiance is 870 W/m^2. However, although the cloud is relatively thin with a vertical extent of approximately 250 m (figure 13a), the direct light is completely scattered and absorbed by the clouds droplets within less than 100 m from the cloud top (figure 13c). Because of the relatively large size of the cloud droplets, the effective asymmetry parameter within the cloud is 0.87 (figure 13b). Thus, most of the scattered light is directed in the forward direction of the incident light. However, since most of the diffuse light is scattered several times within the clouds, about 400 W/m^2 is still directed upward and back to space at the cloud top (figure 13c). 430 W/m^2 of the diffuse short wave radiation transmit through the cloud and reach the surface of the earth (figure 13d).

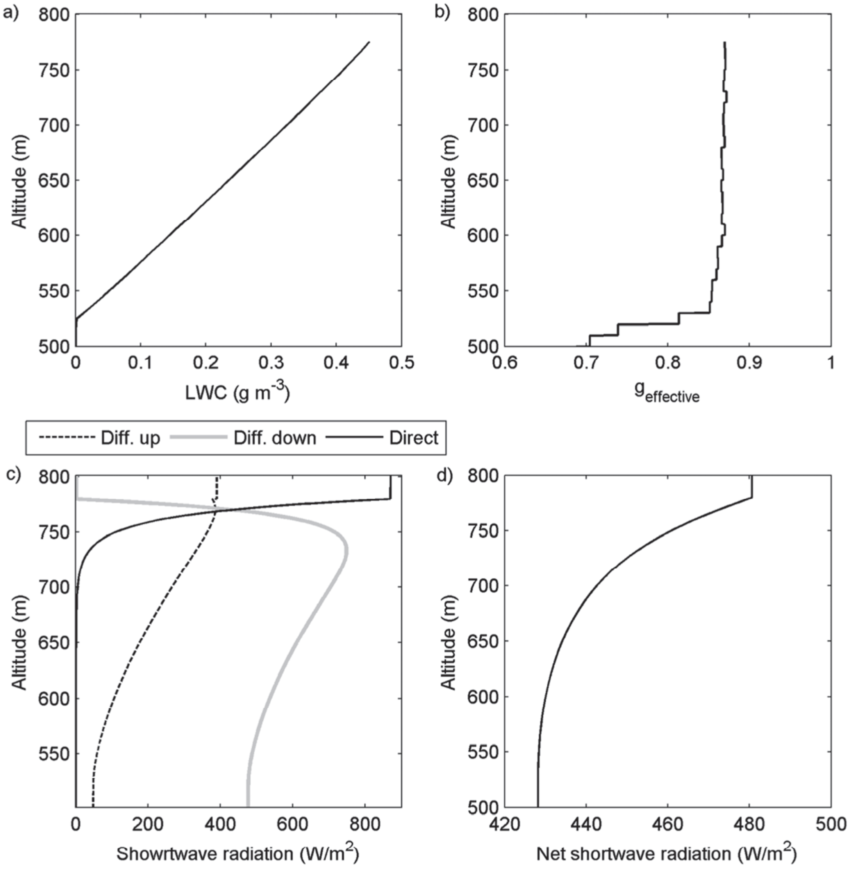

Figure 13. Modelled **(a)** liquid water content (LWC), **(b)** effective asymmetry parameter, **(c)** direct and diffuse downward and upward shortwave radiation and **(d)** net shortwave radiation at different altitudes inside a modelled cloud of clean marine stratocumulus type.

7 Gas phase chemistry

In the troposphere there are thousands of different gas phase compounds of which the majority is organic compounds. The gas phase chemistry of the troposphere is to a large extent controlled by the hydroxyl radical (OH). OH is a very reactive species involved in thousands of different reactions. Many compounds in the atmosphere react in similar ways, for instance alkenes are generally more reactive than alkanes because of their double bounds, and aromatic compounds are generally oxidized efficiently by OH but not by O_3 (Jenkin et al., 2003). By taking such general rules into account, gas phase chemistry models can be simplified. In the gas phase chemistry model used in ADCHEM (**Paper I**) the kinetic code was adapted from Pirjola and Kulmala (1998), originally from EMEP. This code includes *o*-xylene as the only aromatic compound. In ADCHEM the aromatic compounds benzene and toluene were also included. In total the kinetic code in ADCHEM comprises 63 compounds and 119 reactions.

Figure 14 gives an example of the simulated OH radical concentration with ADCHEM. The OH concentration is given for two autumn days, the first sunny and the second day with thin clouds at the top of the boundary layer. Typically the OH concentration reaches a few million molecules per cubic centimetre during a sunny summer day, but just a few hundred or thousand molecules per cubic centimetre during the night.

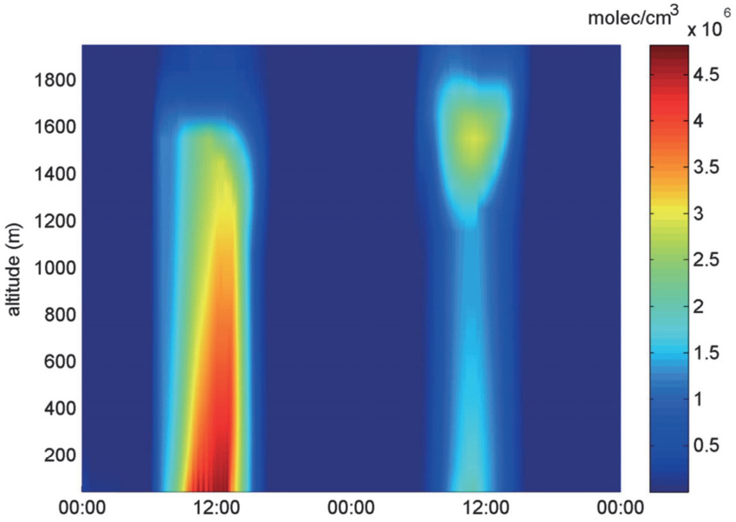

Figure 14. Simulated OH concentrations at different altitudes along a trajectory to and from the Vavihill field station, during the 6th and the 7th of October, 2008.

Although simplified gas phase chemistry codes (as the one which was used in ADCHEM) may be able to predict realistic concentration of e.g. O_3, NO and NO_2, they cannot be used to describe the complex chemistry during the oxidation of SOA precursors. Hence, for the SOA formation these models rely on simplifying semi-empirical parameterizations of the SOA formation and oxidation in the atmosphere (section 4.1).

In the ADCHAM model a more detailed gas phase chemistry model was implemented, which uses the gas phase kinetic code Master Chemical Mechanism v3.2 (MCMv3.2) (Jenkin et al., 2003, **Paper III**). This code is widely used for detailed studies of laboratory chamber experiments (e.g. Bloss et al., 2005a-b and Metzger et al., 2008). In total MCMv3.2 comprises 5710 compounds and 16940 reactions. However, often only a small fraction of them are used for simulations of single precursor experiments.

Despite the complexity of MCMv3.2 much of the gas phase chemistry during the oxidation of common secondary organic aerosol precursors is poorly known. Often the reaction pathways and rates are only qualified guesses. In **Paper III** MCMv3.2 was used to study the oxidation of *m*-xylene, which is a light aromatic compounds found in gasoline car exhausts (Schauer et al., 2002 and **Paper IV**). For these simulations MCMv3.2 overestimated the ozone concentration with nearly a factor of two, and underestimated the OH concentration. This is consistent with the results from Bloss et al. (2005a-b), which showed that MCMv3.2 generally overestimates the ozone concentrations and underestimates the OH concentrations during light aromatic compound oxidation experiments.

In **Paper III** we also tested whether the complexity of the gas phase chemistry of MCMv3.2 is sufficient to be able to model the SOA formation from α-pinene and *m*-xylene, without introducing simplifying tuned semi-empirical two-product or 2D-VBS parameterizations. For these compounds the model can almost reproduce the measured SOA formation, at least for the relatively high precursor concentrations used in the experiments. However, other uncertainties in: (1) the calculated pure-liquid saturation vapour pressures of the condensable organic compounds, (2) the influence of particle phase reactions and (3) the chamber wall effects, make it impossible to draw any precise conclusions concerning the accuracy of the gas-phase kinetics relevant for the SOA formation in the atmosphere.

8 ADCHEM

Figure 15 shows the model structure of ADCHEM. ADCHEM can be divided into three main models:

1) an aerosol dynamics and particle phase chemistry model,
2) a gas phase chemistry model, and
3) a radiative transfer model.

These models are combined with a Lagrangian model which solves the atmospheric diffusion equation (eq. 7) in the vertical (z) and horizontal (y) direction perpendicular to any air mass trajectory (**Paper I**).

$$\frac{dc}{dt} = \frac{\partial}{\partial z}\left(K_z \frac{\partial c}{\partial z}\right) + \frac{\partial}{\partial y}\left(K_y \frac{\partial c}{\partial y}\right) \tag{7}$$

K_z and K_y in equation 7 are the eddy diffusivities (turbulent diffusivities) in the vertical and horizontal directions and c is the concentration of any arbitrary species.

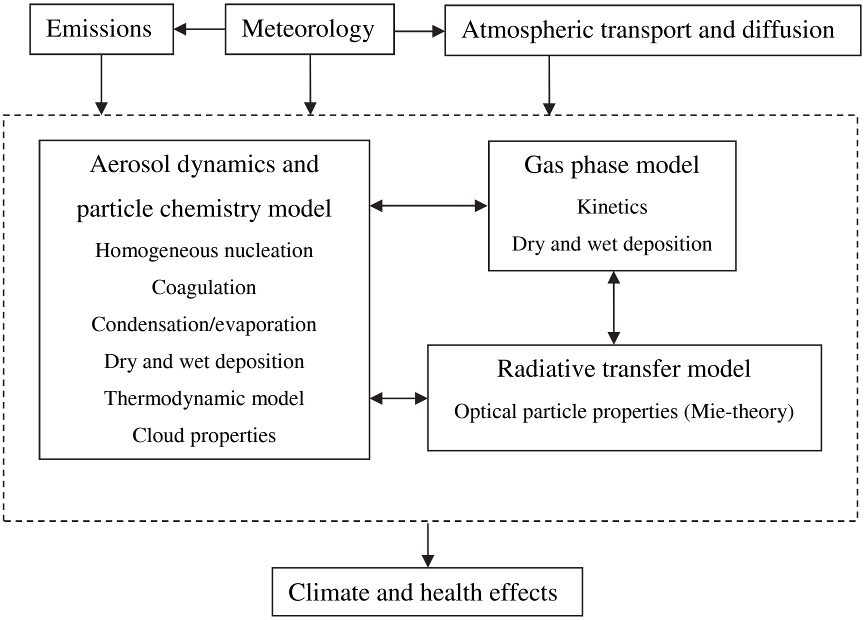

Figure 15. Schematic picture illustrating the model structure of ADCHEM.

8.1 ADCHEM version 2

A model will never be complete. Hence, the ADCHEM model is still developing. Since the description of the first version (**Paper I**) following processes (modules) have been included:

1) an adiabatic cloud parcel model, used to calculate more realistic clouds properties and aerosol cloud processing along the air mass trajectories (section 5 and 10.3),
2) the activity coefficient model AIOMFAC,
3) a more detailed gas phase chemistry code, based on the MCMv3.2 chemistry,
4) an updated gas-particle partitioning module which explicitly treats the condensation and evaporation of condensable organic compounds formed from the detailed gas phase chemistry model, and
5) algorithms for oligomerization and oxidation of organic compounds in the particle phase.

The model updates nr. 2-5 are also included in the ADCHAM model. In **Paper III** these modules (processes) are described and tested.

9 ADCHAM

Figure 16 shows a schematic picture over the model structure of the ADCHAM model. The ADCHAM model is based on the aerosol dynamics model. ADCHAM also includes a detailed particle phase chemistry model which can simulate acid catalysed oligomerization and non-ideal mixing and interactions between organic and inorganic compounds.

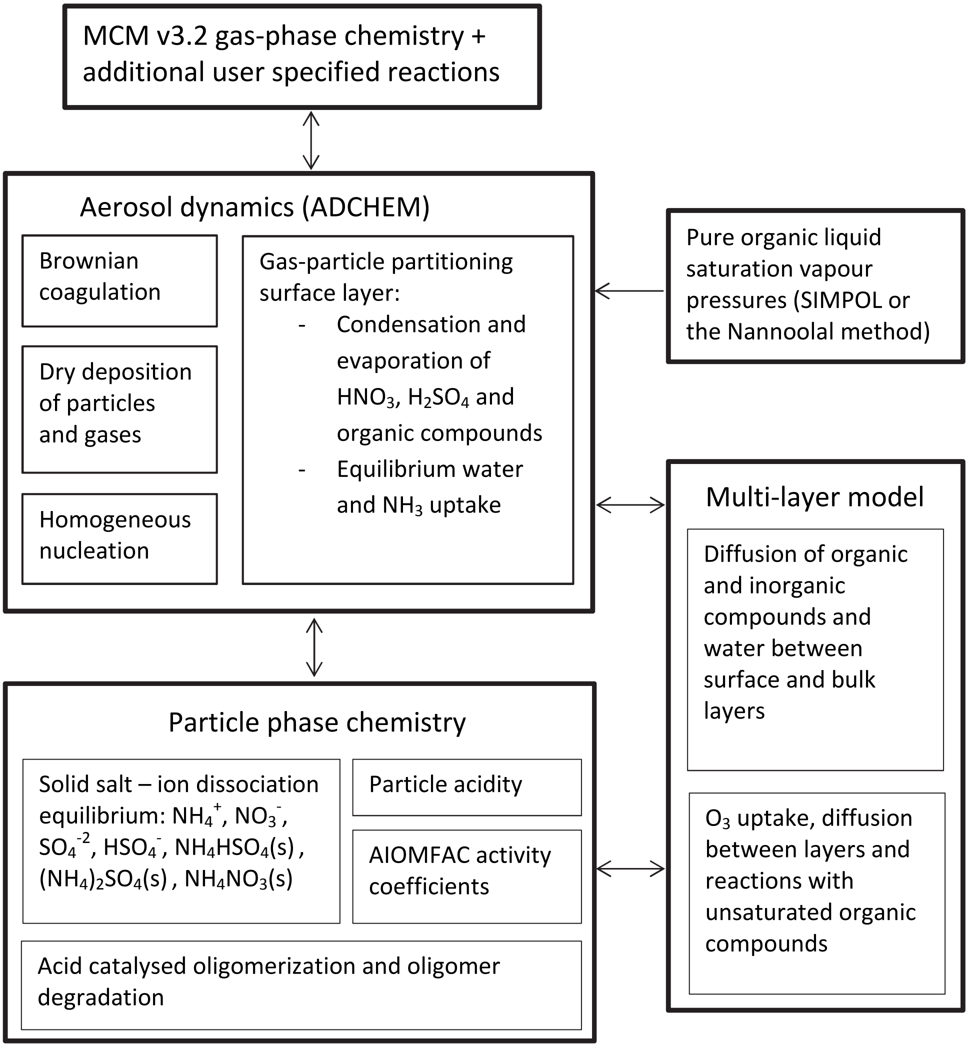

Figure 16. Schematic picture illustrating the model structure of ADCHAM (the figure is from **Paper III**).

Because recent observations of the phase state of SOA particles indicate that they are amorphous and very viscous, the SOA particles will be poorly mixed, and the gas-particle partitioning cannot be well represented by equilibrium partitioning theory (section 4.3). Therefore, ADCHAM includes a kinetic multilayer model which treats the mass transfer limited diffusion of compounds between the particle surface, and between different model layers within the particle bulk. In **Paper III** ADCHAM is used to model the observed mass transfer limited evaporation of SOA particles formed from oxidation of α-pinene.

The gas phase chemistry is modelled with MCMv3.2. With this detailed gas phase chemistry code ADCHAM can model the SOA formation without introducing simplifying representations of the oxidation in the gas phase such as 2D-VBS (**Paper I**). The pure liquid saturation vapour pressures of the formed organic oxidation products can be estimated with different functional group contribution methods (e.g. SIMPOL (Pankow and Asher, 2008) or Nannoolal et al., 2008). The saturation concentrations (pressures) are then derived with the pure-liquid saturation vapour pressures, chemical composition in the particle surface layer and the activity coefficients (eq. 2).

10 Examples of model applications

This chapter presents a few examples of possible applications of ADCHEM and the adiabatic cloud parcel model which now is included in ADCHEMv2. Readers interested in different model applications with the ADCHAM model are referred to **Paper III**.

10.1 Urban plume simulations

So far the ADCHEM model has primarily been used for studies on the ageing of the urban plumes from Malmö (**Paper II**). These urban plume studies illustrate that the primary soot particle emissions within urban areas have a substantial influence on the particle number size distribution. However, this contribution decreases quite rapidly downwind the source regions because of coagulation, dry deposition and vertical mixing (figure 17b). For the urban plume from Malmö, the modelled anthropogenic secondary aerosol contribution dominates over the primary particle mass emission already 2 to 3 hours downwind the city. This is mainly because the ammonia emissions from agriculture and the NO emissions from the road traffic in Malmö substantially amplify the aerosol particle ammonium nitrate (NH_4NO_3) formation (see figure 17a and **Paper II**). If the urban plume air mass is in contact with clouds, the ammonium nitrate coating on the initially hydrophobic primary particles increases the cloud droplet number concentration and thereby the radiative forcing (**Paper II**).

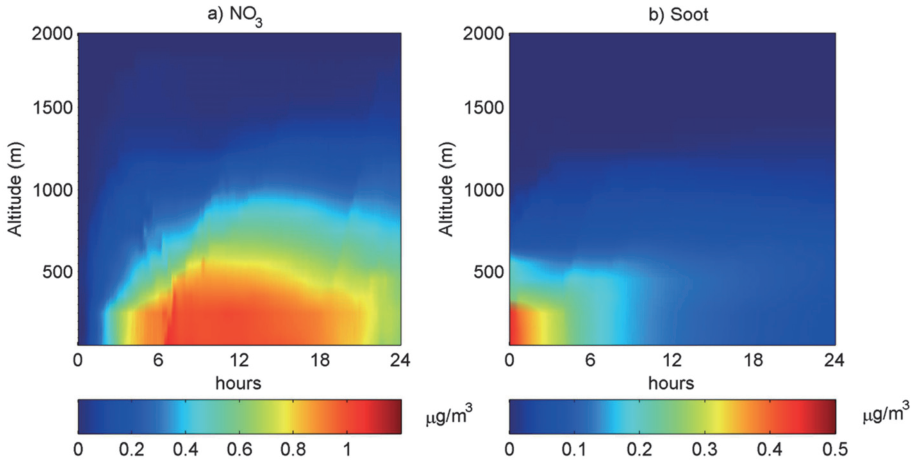

Figure 17. Modelled average mass contribution from the emissions in Malmö, in the centre of the urban plume downwind the city, for (**a**) nitrate and (**b**) soot.

Figure 18 shows the modelled relative contributions of the Malmö emissions to: (1) the particle number deposited dose, (2) surface area deposited dose and (3) mass deposited dose, in the respiratory tract. The results were constructed using the modelled particle properties from ADCHEM together with the ICRP model, which calculates the deposition pattern in the airways (section 1.4). In order to simulate a realistic deposited dose, the hygroscopic growth of the particles within the humid airways (RH≈99.5 %) was considered (see the more detailed description by Löndahl, 2009).

Figure 18 illustrates that in Malmö more than 50 % of the deposited particles in the respiratory system (of a normal healthy person during light exercise) are caused by the local emissions. A large fraction of them are soot particles from road traffic. Downwind Malmö the primary particle contribution decreases substantially. However, at the same time the total deposited mass contribution increases from only 2 % to 7 % 24 hours downwind Malmö. This increase is attributed to the secondary aerosol formation downwind Malmö. The contribution to the surface area dose (which has been suggested as a relevant dose metric for particle-related adverse health effects (section 1.4)), is almost constant within 24 hours downwind Malmö. More than 18 hours downwind Malmö the modelled anthropogenic number dose contribution increases again. This increase is attributed an amplified homogeneous nucleation rate and growth rate within the urban plume.

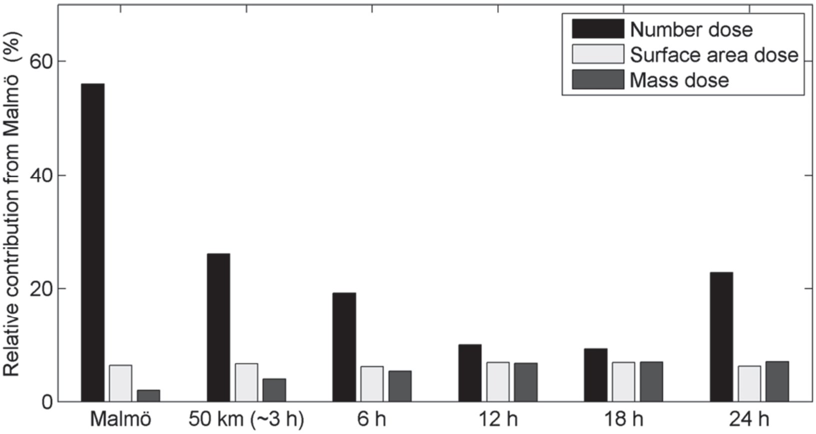

Figure 18. Modelled relative contribution to the respiratory tract deposited particle number, surface area and mass ($PM_{2.5}$) dose from the emissions in Malmö, at different distances (time) downwind the city. The figure shows the averaged values over the whole horizontal model domain (20 km wide) perpendicular to the air mass trajectory.

10.2 Studies of regional new particle formation events

Although ADCHEM was primarily developed for urban plume studies, it can also be used to simulate aerosol properties at clean background conditions. One such application is to study observed new particle formation events and compare the modelled particle properties with the measurements. Figure 19 gives an example of such a comparison, for 10 days between the 1st and 10th of October, 2008. The model results in figure 19 are constructed from 72 different trajectory simulations, each starting 7 days upwind the Vavihill field station and arriving with 3 hours intervals at the station (figure 20).

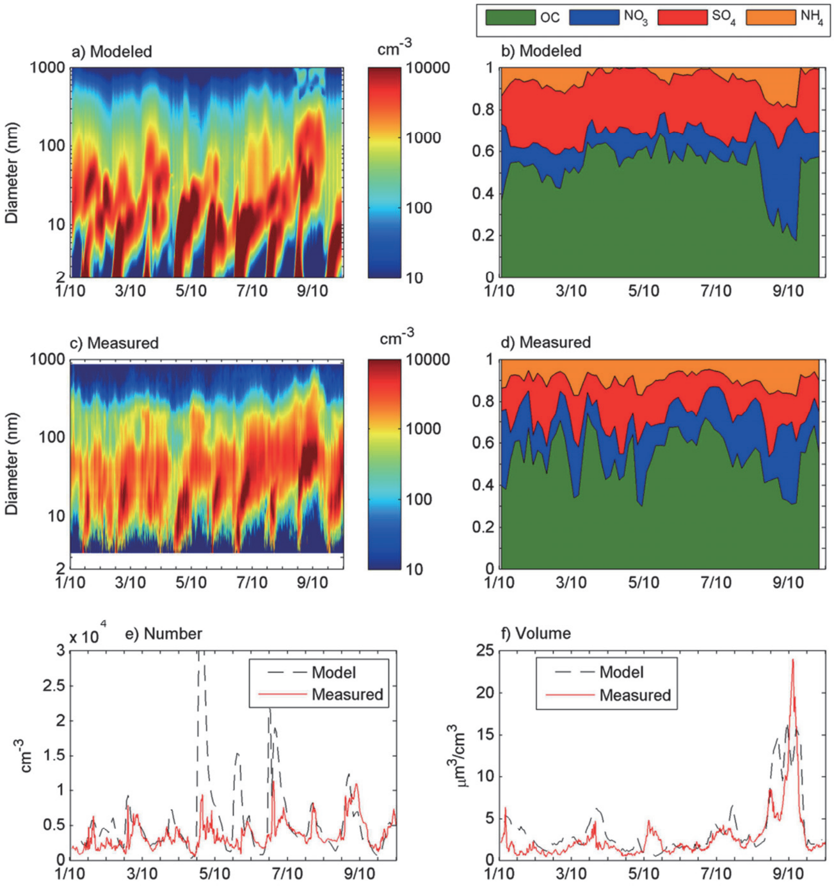

Figure 19. Modelled and measured particle number size distributions **(a)** and **(c),** particle chemical composition (PM1 mass fractions) **(b)** and **(d),** particle number concentration above 3 nm in diameter **(e),** and the volume concentration for particles smaller than 1 μm in diameter **(f)**. The results are from the 1st to 10th of October, 2008 at Vavihill field station. The particle chemical composition was measured with ToF-AMS and the physical particle properties with DMPS.

During most of the time the air mass trajectories originated over the North Atlantic Ocean, Greenland or Canada. These air masses were relatively clean. However, during a period between the 8th and 9th of October, 2008 the air mass trajectories travelled over France, Benelux and Germany before they arrived at Vavihill. During this period the modelled and measured particle mass is about 3 times higher than during the rest of the period (figure 19f).

The homogeneous nucleation was simulated using kinetic nucleation theory (McMurry and Friedlander, 1979) (eq. 4). The formed nucleation clusters were assuming to have an initial diameter of 1.5 nm. The correlation coefficient (K) was set to $3.2\cdot10^{-14}$ $s^{-1}cm^{3}$, which is the median value derived from measurements in Germany (Paasonen et al., 2009).

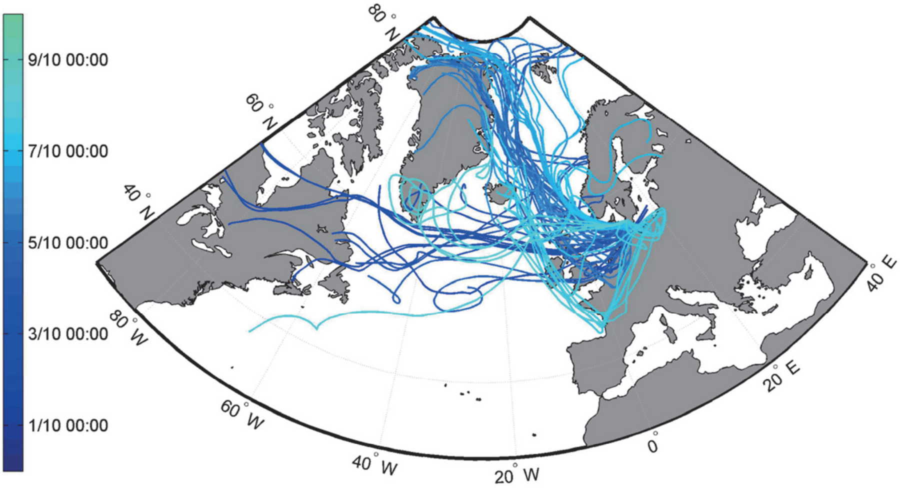

Figure 20. Air mass trajectories starting 7 days before they arrive at the Vavihill field station. The colour coding shows which day during the 10 day period between the 1st and 10th of October, 2008 that the different air mass trajectories arrive at Vavihill.

10.3 Aerosol cloud processing

It has been estimated that only about 10 % of the clouds in the atmosphere form precipitation (Rodhe, 1992). Hence, many aerosol particles are processed several times inside clouds, before they are lost by wet deposition. The ADCHEM model is used to model the aerosol properties along air mass trajectories for more than one week and over large regions of the earth (section 10.2). Along most of these air mass trajectories the aerosol particles will encounter clouds. Hence, in order to be able to model realistic aerosol particle properties within the boundary layer, in cloud processing of aerosol particles often needs to be considered. In the future this will be done with the adiabatic cloud parcel model described in section 5. In this section the adiabatic cloud parcel model is used to illustrate how the aerosol particle properties can be altered when they are processed inside a cumulus cloud.

Figure 21 shows a schematic figure of typical air parcel movements in a shallow cumulus cloud (ch 7, in Cotton et al., 2011). The adiabatic cloud parcel model was started at 500 m a.s.l. at a RH of 95 %. The air parcel rises to 1500 m a.s.l., with an updraft velocity of 1 m/s. After this the air parcel descends back to the original altitude with a downdraft velocity of 1 m/s. This air parcel route is intended to represent a cumulus cloud formation cycle which aerosol particles within the boundary layer may encounter. The path of the air parcel through the cumulus cloud is illustrated with the solid thick black lines in figure 21. Some air parcels will be cycled several times within the cloud, and will also partly be mixed with the new air parcels which enter from below the cloud.

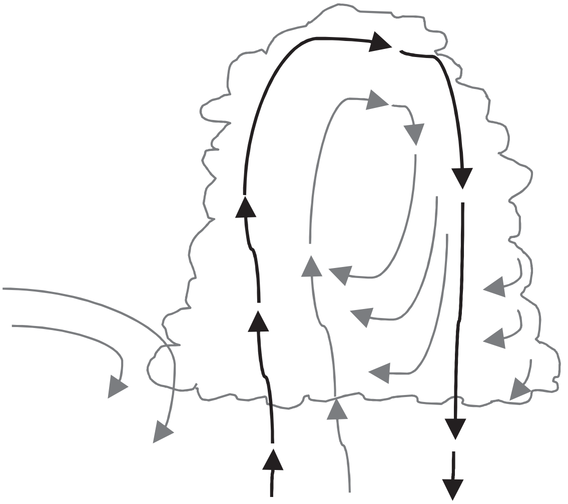

Figure 21. Picture which illustrates the circulation within a shallow cumulus cloud. The black lines represent the air parcel movement simulated in this section (adopted from Cotton et al., 2011).

At the start of the simulations the particles inside the air parcel are composed of an aged internally mixed background aerosol (600 cm^{-3}, 3.1 µg m^{-3}), which in the submicron size range is dominated by organic compounds (55 %), nitrate (14 %), sulphate (12 %) and ammonia (8 %). The particles with a diameter larger than 1 µm are mainly composed of solid mineral dust (40 %), chloride (20 %), sodium (14 %) and organic compounds (11 %). Additionally, freshly emitted submicron primary particles (1100 cm^{-3} and 0.23 µg m^{-3}) of which 81 % is soot, 17 % is OA and 1 % is sulphate are also included.

Initially the freshly emitted primary particles (which are intended to represent road traffic emissions within a city) are either treated as a separate size distribution of externally mixed particles, or directly internally mixed with the background aerosol (as was assumed in **Paper II**). For the more realistic simulation where the freshly emitted primary particles are externally mixed, coagulation inside the cloud gradually transforms these particles into more internally mixed with the background aerosol.

Figure 22 shows the modelled RH (a), particle mass concentrations (b) and gas phase concentrations (c), during the updraft and downdraft of the modelled air parcel. Already before the cloud droplets are activated, they start to take up substantial amounts of HNO_3(g), NH_3(g) and HCl(g). 10 m above the cloud base these gases are almost completely dissolved in the cloud droplets. In the downdraft the formed nitrate, ammonium and chloride stay inside the droplets until the air parcel leaves the cloud. Below the cloud HNO_3 and HCl evaporate, while the ammonium stays in the particles and neutralizes the sulphate rich acidic content.

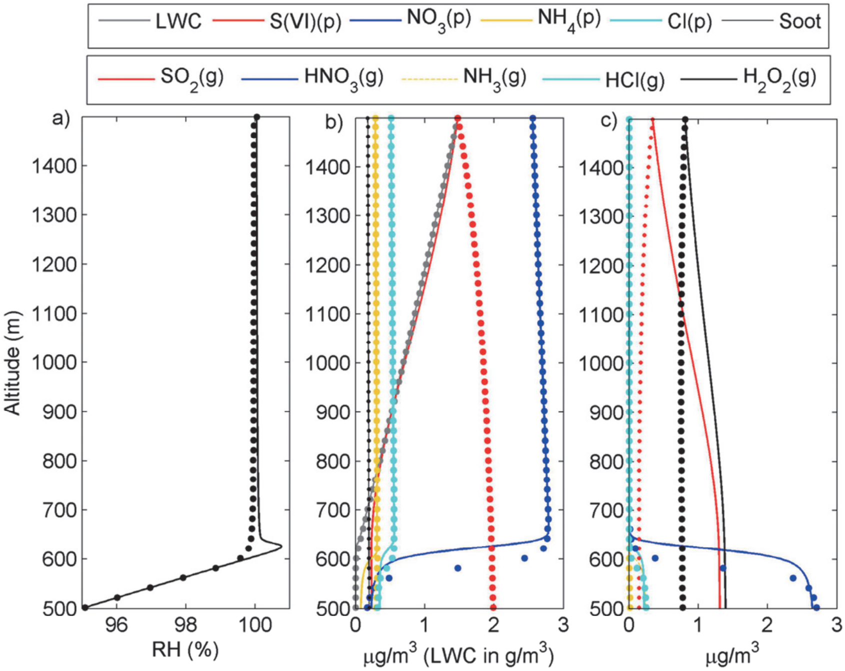

Figure 22. Modelled RH **(a)**, chemical composition in the cloud droplets (particle phase (p)) **(b)**, and gas phase (g) **(c)**, at different altitudes within an adiabatically rising and descending air parcel. The concentrations in the updraft are given by the solid lines while the concentrations in the downdraft are given by dots.

The increasing sulphate concentration is caused by the rapid liquid phase reaction between SO_2 and H_2O_2. The sulphate content is increasing during the whole time which the aerosol particles stay inside the cloud. After the cloud processing only 10 % of the initial SO_2(g) mass concentration of 1.3 μg m^{-3} remains. Because sulphuric acid is a very low volatile compound, the sulphate remains in the particle phase after the cloud droplets have evaporated.

Figure 23 shows the modelled dry particle number size distributions before and after cloud processing for simulations with:

1) initially externally mixed freshly emitted primary particles and aged background particles,
2) simplified treatment of the freshly emitted primary particles as internally mixed with the aged background aerosol,
3) no freshly emitted primary particles, and
4) no uptake of HNO_3, HCl, NH_3, SO_2 or H_2O_2 by the particles and cloud droplets.

The simulated particle number size distributions after the cloud processing show two distinct particle size modes in all simulations except nr 4. The first mode comprises the particles that were not activated as cloud droplets, while the second mode incudes those particles that were activated inside the cloud.

When considering the external mixture of aged hygroscopic background particles and fresh hydrophobic soot particles, only the largest soot particles ($D_p > 110$ nm) are able to activates and form cloud droplets. By number less than 2 % of the fresh soot particles are activated. Hence, they have a relatively small influence on the number of cloud droplets. When assuming completely internally mixed aerosol particles, the separation between the two modes is more distinct in figure 23 and a larger number fraction of the soot particles are able to activate (10 %). This illustrates that models that assume instant mixing between the background particles and freshly emitted primary soot particles overestimate the anthropogenic influence on the cloud properties within the urban area (**Paper II**).

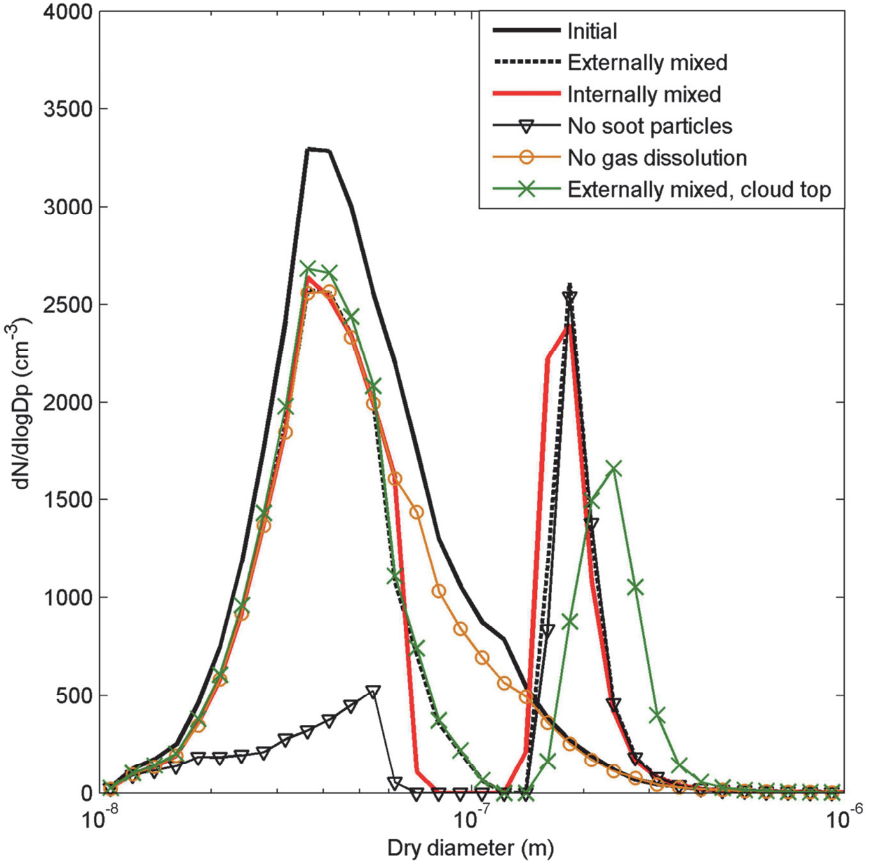

Figure 23. Modelled dry particle number size distributions before and after cloud processing, with 1) externally mixed fresh primary soot particles, 2) completely internally mixed particles, 3) no primary soot particles and 4) same as 1 but without uptake of HNO_3, HCl, NH_3, SO_2 or H_2O_2 in the cloud droplets.

Figure 24 shows the modelled dry particle mass distributions of soot, sulphate and nitrate before and after the aerosol particles have been processed within the cloud. The results are from the simulation with initially externally mixed soot particles. The activated soot particles acquire a sulphate to soot mass coating of between 10 and 100, depending on the initial soot core size. This is in sharp contrast to the non-activated soot particles which after the cloud processing still contain only about 1 mass % sulphate.

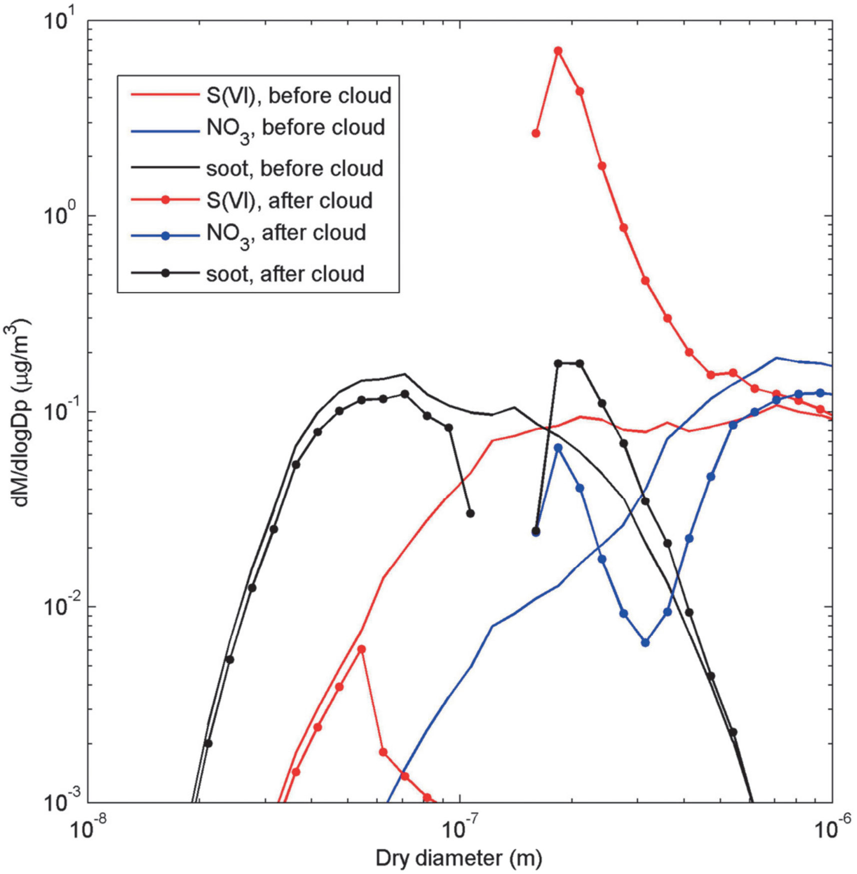

Figure 24. Modelled dry particle mass distributions of soot, sulphate and ammonium before (solid lines) and after (solid lines with dots) cloud processing.

11 Summary and conclusions

In this thesis two models for aerosol dynamics, gas and particle phase chemistry were developed and evaluated. These models were used to study processes that alter the particle properties relevant for climate and health.

The first model, which is called ADCHEM (trajectory model for Aerosol Dynamics, gas and particle phase CHEMistry and radiative transfer), was primarily designed for simulations of aerosol ageing within urban plumes (**Paper I** and **II**). The results from the urban plume studies give valuable knowledge about transformation of the urban gas and particle emissions from the urban background scale (1x1 km) to the grid scale treated by global CTMs and climate models (100x100 km) (**Paper II**).

Recently, ADCHEM was also equipped with an adiabatic cloud parcel model which will be used to study the influence of clouds on the modelled aerosol particle composition (section 10.3).

The second model, which is called ADCHAM (Aerosol Dynamics, gas- and particle-phase chemistry kinetic multi-layer model for CHAMber studies), is primarily intended to be used for detailed process modelling during controlled laboratory chamber experiments (**Paper III** and **IV**). With this model it is possible to study potentially influential but poorly known processes for SOA properties, formation and evaporation (specifically oligomerization, organic salt formation, salting-out effects, oxidation of organic compounds in the particle phase and mass transfer limitations in the particle phase).

Among others, the simulations show that small amount of low-volatile and long lived oligomers, which accumulate in the particle surface layers upon evaporation, can explain the observed slow evaporation of SOA particles (**Paper III**). ADCHAM can be used as a valuable tool for analysing experimental data (**Paper III**), and when planning, designing and selecting which experiments that are needed in order to be able to answer specific research questions (**Paper IV**).

12 Present and future model applications

In the future ADCHAM is planned to be used to study various chamber experiments, with the overall aim to implement the knowledge from detailed laboratory experiments into process based atmospheric models like ADCHEM. As a next up-scaling step, ADCHEM can be used to improve the representation of sub-grid scale processes in regional and global chemistry transport and climate models (figure 25).

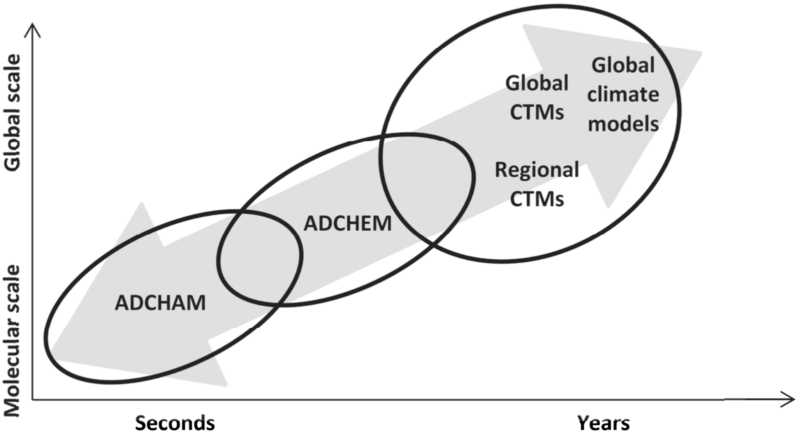

Figure 25. Picture illustrating the different temporal and spatial scales of the models developed and used in this article and how they relate to the scales covered by global CTMs and climate models.

Below a few concrete examples are given of important research questions which ADCHEM and ADCHAM are (or is planned) to be used to answer.

Today much research is being made on secondary organic aerosol formation. However, few studies deal with the secondary ammonium nitrate formation in the atmosphere. In **paper II** it was shown that the secondary aerosol formed downwind Malmö is mainly composed of ammonium nitrate. One important research question is how these emissions influence the optical and hygroscopic properties of the primary soot particles downwind urban regions.

With more detailed gas phase kinetics (MCMv3.2), process based SOA formation (ADCHAM), in cloud processing (section 5 and 10.3), separation of aged internally and fresh externally mixed primary particles (section 10.3), and semi-empirical representations of the gradual collapse of soot agglomerates when coated with inorganic or organic compounds, ADCHEM can be used to increase the knowledge concerning the full climate impact (indirect and direct effects) of anthropogenic primary soot particle emissions.

As illustrated in section 10.2, ADCHEM is also well suited for studies of regional new particle formation events. Currently ADCHEM is used together with a new version of the MALTE model (Boy et al, 2006), MCMv3.2 and the Generator for Explicit Chemistry and Kinetics of Organics in the Atmosphere (GECKO-A) (Valorso et al., 2011), to study the biogenic SOA formation during new particle formation events in the atmosphere. The models are employed along air mass trajectories between three measurement stations (Abisko (68º35'N, 19º05'E), Pallas (67º58'N, 24º07'E) and Värriö (67º46'N, 29º35'E)) in Swedish and Finnish Lapland. Specifically, we want to examine how these models (which together comprise much of the state of the art knowledge within biogenic organic gas phase chemistry and SOA formation) are able to represent the observed SOA mass formation and new particle formation growth rates.

In order to be able to model more realistic emissions of different biogenic SOA precursors, dry deposition losses of particles and gases, and the influence of ozone stress and light conditions on the plant VOC emissions, ADCHEM should in the future also be extended with an in-canopy model (see e.g. Bryan et al., 2012,).

ADCHAM is currently used to simulate the secondary aerosol formation and gas phase chemistry during the gasoline car experiments in **Paper IV**. ADCHAM will also be used to simulate the evaporation of these particles within a thermo-denuder setup. Important questions to be addressed with these simulations are:

1) How large fraction of the formed SOA can be explained by known SOA precursors (in this case mainly light aromatic compounds)?
2) How well can ADCHAM simulate the observed chemical particle phase composition (e.g. O:C-ratios, organonitrates and ammonium nitrate) and the hygroscopic particle properties?
3) How does the gas phase chemistry differs between single light aromatic precursor experiments and the complex organic mixture in gasoline exhausts? And does this in turn influence the SOA properties and formation?
4) How volatile is the formed SOA, and do these experiments support the recent experimental findings that SOA particles are in an amorphous and viscous phase state?

Acknowledgments

First of all I would like to thank my main supervisor professor Erik Swietlicki who always has encouraged me and given me the freedom to follow my own ideas. Erik has many projects going on at the same time, but he always seems to be relaxed and often have time for discussion and good advice. I would also especially like to thank my co-supervisor Dr. Birgitta Svenningsson for hear friendly support and good advice, Joakim Pagels for involving me in the research projects on gasoline car exhausts and diesel soot, his positive feedback and trust in my model constructions. In the projects coordinated by Joakim I have also had the pleasure of working with Erik Nordin, Axel Eriksson and Jonatan Carlsson.

A special thanks also to Michael Boy who invited me to come and work with him and his PhD and master students Ditte Mogensen, Luxi Zhou and Anton Russanen, from whom I have received valuable support during the model development. Of the other people who also have been involved in the model development or implementations I would like to thank: Andy Massling, Mathias Ketzell and Fenjuan Wang, for their interest in using the ADCHEM model in the Copenhagen region, Susanna Gustafsson for help with the implementation of the emission factor in southern Sweden, Kari Lehtinen and Markku Kulmala for valuable help and support during the development of the ADCHEM model, Guy Schurgers and Almut Arneth for providing me with biogenic VOC emissions over Europe, David Simpson for proofreading the ADCHEM papers and valuable comments on the SOA partitioning theory and methods, and Emilie Hermansson for continuing the development and implementation of the model in future research projects.

During the long term measurements and intensive field campaigns in the Brazilian rainforest and at the Vavihill field stations in southern Sweden I have been working with many people. Here, I would like to thank Erik Fors, Jakob Löndahl and Adam Kristensson for introducing me to the field of aerosol measurements and for technical support during the many days at the Vavihill station, and Moa Sporre, Göran Frank and Cerina Wittbom for nice company. In Brazil I had the pleasure of meeting and working with many talented researchers. I would especially like to thank Sachin Gunther, Ulrich Pöschl, Paulo Artaxo, Luciana Rizzo and Fernando Morais.

I would also like to thank everyone at the nuclear physics department (especially Britt-Marie Kallerhed, Anneli Nilsson Ahlm and Per Kristiansson for help with administrative questions), and all the nice people at IKDC who I meet during the coffee and lunch breaks.

Finally I would like to thank my friends and family, and in particular my wife Maria, and my children Edith and Noel, for every day reminding me that there is more in life than just aerosols. Ni betyder allt för mig. Tack för att ni finns!

References

Albrecht, B. A.: Aerosols, Cloud Microphysics, and Fractional Cloudiness, Science, 245, 1227-1230, 1989.

Alm, L.: Aerosol Exchange between Forests and the Atmosphere – Fluxes over a Tropical and a Boreal Forest, ISBN 978-91-7447-051-2, Doctoral dissertation at Stockholm University, Stockholm, Sweden, 2010.

Andreae, M. O.: Aerosol before pollution, Science, 315, 50-51, 2007.

Barsanti, K. C., McMurry, P. H., and Smith, J. N.: The potential contribution of organic salts to new particle growth, Atmos. Chem. Phys., 9, 2949-2957, doi:10.5194/acp-9-2949-2009, 2009.

Bertram, A. K., Martin, S. T., Hanna, S. J., Smith, M. L., Bodsworth, A., Chen, Q., Kuwata, M., Liu, A., You, Y., and Zorn, S. R.: Predicting the relative humidities of liquid-liquid phase separation, efflorescence, and deliquescence of mixed particles of ammonium sulfate, organic material, and water using the organic-to-sulfate mass ratio of the particle and the oxygen-to-carbon elemental ratio of the organic component, Atmos. Chem. Phys., 11, 10995-11006, doi:10.5194/acp-11-10995-2011, 2011.

Bloss, C., Wagner, V., Bonzanini, A., Jenkin, M. E., Wirtz, K., Martin-Reviejo, M., and Pilling, M. J.: Evaluation of detailed aromatic mechanisms (MCMv3 and MCMv3.1) against environmental chamber data, Atmos. Chem. Phys., 5, 623-639, 2005a.

Bloss, C., Wagner, V., Jenkin, M. E., Volkamer, R., Bloss, W. J., Lee, J. D., Heard, D. E., Wirtz, K., Martin-Reviejo, M., Rea, G., Wenger, J. C., and Pilling, M. J.: Development of a detailed chemical mechanism (MCMv3.1) for the atmospheric oxidation of aromatic hydrocarbons, Atmos. Chem. Phys., 5, 641-664, doi:10.5194/acp-5-641-2005, 2005b.

Bond, T. C., Doherty, S. J., Fahey, D. W., Forster, P. Berntsen, M., T., DeAngelo, B. J., Flanner, M. G., Ghan, S., Kärcher, B., Koch, D., Kinne, S., Kondo, Y., Quinn, P. K., Sarofim, M. C., Schultz, M. G., Schulz, M., Venkataraman, C., Zhang, H., Zhang, S., Bellouin, N., Guttikunda, S. K., Hopke, P. K., Jacobson, M. Z., Kaiser, J. W., Klimont, Z., Lohmann, U., Schwarz, J. P., Shindell, D., Storelvmo, T., Warren, S. G., Zender, C. S.: Bounding the role of black carbon in the climate system: A scientific assessment, doi: 10.1002/jgrd.50171, 2013.

Boy, M., Hellmuth, O., Korhonen, H., Nilsson, E. D., ReVelle, D., Turnipseed, A., Arnold, F., and Kulmala, M.: MALTE – model to predict new aerosol formation in the lower troposphere, Atmos. Chem. Phys., 6, 4499-4517, doi:10.5194/acp-6-4499-2006, 2006.

Bryan, A. M., Bertman, S. B., Carroll, M. A., Dusanter, S., Edwards, G. D., Forkel, R., Griffith, S., Guenther, A. B., Hansen, R. F., Helmig, D., Jobson, B. T., Keutsch, F. N., Lefer, B. L., Pressley, S. N., Shepson, P. B., Stevens, P. S., and Steiner, A. L.: In-canopy gas-phase chemistry during CABINEX 2009: sensitivity of a 1-D canopy model to vertical mixing and isoprene chemistry, Atmos. Chem. Phys., 12, 8829-8849, doi:10.5194/acp-12-8829-2012, 2012.

Cappa C. D, Onasch, T. B, Massoli, P, Worsnop, D. R., Bates, T. S, Cross, E. S., Davidovits, P., Hakala, J., Hayden, K. L., Jobson, B. T., Kolesar, K. R., Lack, D. A., Lerner, B. M., Li, S-M., Mellon, D., Nuaaman, I., Olfert, J. S., Petäjä, T., Quinn, P. K., Song, C., Subramanian, R., Williams, E. J., and Zaveri, R. A.: Radiative Absorption Enhancements Due to the Mixing State of Atmospheric Black Carbon, Science, 337, 1078-1081, 2012.

Choi, M. Y., and Chan, K. C.: The effects of Organic Species on the Hygroscopic Behaviors of Inorganic Aerosols, Environ. Sci. Technol, 36, 2422-2428, 2002.

Colbeck, I., Appleby, L., Hardman, E. J., and Harrison, R. M.: The optical properties and morphology of cloud-processed carbonaceous smoke, J. Aerosol Sci. 21, 527–538, 1990.

Cotton, W. R, Bryan, G. H., and Van den Heever, S. C., Storm and Cloud Dynamics 2nd ed., ISBN: 978-0-12-0885428, USA, 2011.

DeCarlo, P. F., Kimmel, J. R., Trimborn, A., Northway, M. J., Jayne, J. T., Aiken, A. C., Gonin, M., Fuhrer, K., Horvath, T., Docherty, K. S., Worsnop, D. R., and Jimenez, J. L.: Field-deployable, high-resolution, time-of-flight aerosol mass spectrometer, Anal. Chem., 78, 8281–8289, 2007.

Dockery, D. W, Pope, C. A., Xu, X. P., Spengler, J. D., Ware, J. H., Fay, M. E., Ferris, B. G., Speizer, F. E.: An Association Between Air-Pollution and Mortality in 6 United-States Cities, New England Journal of Medicine, 329, 1753-1759, 1993.

Donahue, N. M., Robinson, A. L., Stanier, C. O., Pandis, S. N.: Coupled partitioning, dilution, and chemical aging of semivolatile organics. Environmental Science and Technology, 40, 2635–2643, 2006.

Donahue, N. M., Epstein, S. A., Pandis, S. N., and Robinson, A. L.: A two-dimensional volatility basis set: 1. organic-aerosol mixing thermodynamics, Atmos. Chem. Phys., 11, 3303-3318, doi:10.5194/acp-11-3303-2011, 2011.

Ebert, M., Weinbruch, S., Hoffman, P. and Ortner, H. M.: The chemical composition and complex refractive index of rural and urban influenced aerosols determined by individual particle analysis. Atmospheric Environment, 38, 6531-6545, 2004.

Ervens, B. and Volkamer, R.: Glyoxal processing by aerosol multiphase chemistry: towards a kinetic modeling framework of secondary organic aerosol formation in aqueous particles, Atmos. Chem. Phys., 10, 8219-8244, doi:10.5194/acp-10-8219-2010, 2010.

Forsberg, B., Hansson, H. C., Johansson, C., Areskough, H., Persson, K, Jarvholm, B.: Comparative health impact assessment of local and regional particulate air pollutions in Scandinavia, Ambio, 34, 11-19, 2005.

Fuchs, N. A., Sutugin, A. G.: In Topics in Current Aerosol Research, Pergamon Press, 1971.

Grieshop, A. P., Donahue, N. M., and Robinson, A. L.: Is the gas-particle partitioning in alpha-pinene secondary organic aerosol reversible?, Geophys. Res. Lett., 34, L14810, doi:10.1029/2007GL029987, 2007.

Griffin, R. J., Cocker III, D. R., Flagan, R. C., and Seinfeld, J. H.: Organic aerosol formation from the oxidation of biogenic hydrocarbons, J. Geophys. Res., 104, 3555–3567, 1999.

Gunthe S. S., King S. M., Rose D., Chen Q., Roldin P., Farmer D. K., Jimenez J. L., Artaxo P., Andreae M. O., Martin S. T. and Pöschl U.: Cloud condensation nuclei in pristine tropical rainforest air of Amazonia: size-resolved measurements and modeling of atmospheric aerosol composition and CCN activity. Atmos. Chem. Phys., 9, 7551-7575, 2009.

Guyon, P., Frank, G., Welling, M., Chand, D., Artaxo, P., Rizzo, L., Nishioka, G., Kolle, O., Fritsch, H., Silva-Dias, M. A., Gatti, L. V., Cordova, A. M. and Andreae, M. O.: Airborne measurements of trace gas and aerosol particle emissions from biomass burning in Amazonia, Atmos. Chem. Phys., 5, 2989-3002, 2005.

Hazeleger, W., Wang, X., Severijns, C., Stefãnescu, S., Bintanja, R., Sterl, A., Wyser, K., Semmler, T., Yang, S., van den Hurk, B., van Noije, T., van den Linden, E., and van den Wiel, K.: EC-Earth V2.2: description and validation of the new seamless earth system prediction model, Clim. Dyn., 39, 2611-2629, 2012.

Heintzenberg, J., Leck, C., Birmili, W., Wehner, B., Tjernström, M. and Wiedensohler, A.: Aerosol number-size distributions during clear and fog periods in the summer high Arctic: 1991, 1996 and 2001. Tellus B, 58, 41-50, 2006.

Hildebrandt, L., Donahue, N. M. and Pandis, S. N.: High formation of secondary organic aerosol from the photo-oxidation of toluene. Atmos. Chem. Phys. 9, 2973-2986, 2009.

Hoffmann, T., Odum, J. R., Bowman, F., Collins, D., Klockow, D., Flagan, R. C., and Seinfeld, J. H.: Formation of organic aerosols from the oxidation of biogenic hydrocarbons, J. Atmos. Chem., 26, 189–222, 1997.

ICRP Publication 66: Human Respiratory Tract Model for Radiological Protection, 66. International Commission on Radiological Protection, 1995.

IPCC (Intergovernmental Panel on Climate Change). Climate Change 2007 – The Physical Science Basis. Solomon, S., Qin, D. and Manning, M. 1-989.: New York, Cambridge University Press. IPCC Reports. Ref Type: Report, 2007.

Jacobson, M. Z.: Strong radiative heating due to the mixing state of black carbon in atmospheric aerosols, Science, 409, 695-697, 2001.

Jenkin, M. E., Saunders, S. M., Wagner, V. and Pilling, M. J.: Protocol for the development of the Master Chemical Mechanism, MCM v3 (Part B): tropospheric degradation of aromatic volatile organic compounds. Atmos. Chem. Phys., 3, 181-193, 2003.

Jimenez J. L., Canagaratna M. R., Donahue N. M., Prevot A. S. H., Zhang Q., Kroll J. H., DeCarlo P. F., Allan J. D., Coe H., Ng N. L., Aiken A. C., Docherty K. S., Ulbrich I. M., Grieshop A. P., Robinson A. L., Duplissy J., Smith J. D., Wilson K. R., Lanz V. A., Hueglin C., Sun Y. L., Tian J., Laaksonen A., Raatikainen T., Rautiainen J., Vaattovaara P., Ehn M., Kulmala M., Tomlinson J. M., Collins D. R., Cubison M. J., Dunlea E. J., Huffman J. A., Onasch T. B., Alfarra M. R., Williams P. I., Bower K., Kondo Y., Schneider J., Drewnick F., Borrmann S., Weimer S., Demerjian K., Salcedo D., Cottrell L., Griffin R., Takami A., Miyoshi T., Hatakeyama S., Shimono A., Sun J. Y, Zhang Y. M., Dzepina K., Kimmel J. R., Sueper D., Jayne J. T., Herndon S. C., Trimborn A. M., Williams L. R., Wood E. C., Middlebrook A. M., Kolb C. E., Baltensperger U., Worsnop D. R., Evolution of Organic Aerosols in the Atmosphere. Science 326, 1525-1529, 2009.

Kahnert, M.: Modelling the optical and radiative properties of freshly emitted light absorbing carbon within an atmospheric chemical transport model, Atmos. Chem. Phys. 10, 1403–1416, 2010.

Kahnert, M., Nousiainen, T., Lindqvist, H., and Ebert, M.: Optical properties o flight absorbing carbon aggregates mixed with sulfate: assessment of different model geometries for climate forcing calculations, Optics Express, 20, 10042-10058, 2012.

Kalberer, M., Paulsen, D., Sax, M., Steinbacher, M., Dommen, J., Prévôt, A. S. H., Fisseha, R., Weingartner, E., Frankevich, V., Zenobi, R., and Baltensperger, U.: Identification of polymers as major components of atmospheric organic aerosols, Science, 303, 1659–1662, 2004.

Kirkby, J., Curtius, J., Almeida, J., Dunne, E., Duplissy, J., Ehrhart, S., Franchin, A., Gagne, S., Ickes, L., Küerten, A., Kupc, A., Metzger, A., Riccobono, F., Rondo, L., Schobesberger, S., Tsagkogeorgas, G., Wimmer, D., Amorim, A., Bianchi, F., Breitenlechner, M., David, A., Dommen, J., Downard, A., Ehn, M., Flagan, R. C., Haider, S., Hansel, A., Hauser, D., Jud,W., Junninen, H., Kreissl, F., Kvashin, A., Laaksonen, A., Lehtipalo, K., Lima, J., Lovejoy, E. R., Makhmutov, V., Mathot, S., Mikkilä, J., Minginette, P., Mogo, S., Nieminen, T., Onnela, A., Pereira, P., Petäjä, T., Schnitzhofer, R., Seinfeld, J. H., Sipilä, M., Stozhkov, Y., Stratmann, F., Tome, A., Vanhanen, J., Viisanen, Y., Vrtala, A., Wagner, P. E., Walther, H., Weingartner, E., Wex, H., Winkler, P. M., Carslaw, K. S., Worsnop, D. R., Baltensperger, U., and Kulmala, M.: Role of sulphuric acid, ammonia and galactic cosmic rays in atmospheric aerosol nucleation, Nature, 476, 429–433, 2011.

Knopf, D. A., Anthony, L. M., and Bertram, A. K.: Reactive uptake of O3 by multicomponent and multiphase mixtures containing oleic acid, J. Phys. Chem. A, 109, 5579–5589, 2005.

Kulmala, M., Vehkamäki, H., Petäjä, T., Dal Maso, M., Lauri, A., Kerminen, V.-M., Birmili, W. and McMurry, P. H.: Formation and growth of ultrafine atmospheric particles: a review of observations. Aerosol Science 35, 143-176, 2004.

Kulmala, M., Lehtinen, K. E. J., and Laaksonen, A.: Cluster activation theory as an explanation of the linear dependence between formation rate of 3nm particles and sulphuric acid concentration, Atmos. Chem. Phys., 6, 787-793, doi:10.5194/acp-6-787-2006, 2006.

Kulmala, M., Asmi, A., Lappalainen, H. K., Carslow, K. S., Pöschl, U., Baltensberger, U., Hov, Ø, Brenquier, J.-L., Pandis, S. N., Facchini, M. C., Hansson, H.-C., Wiedensohler, A. and O'dowd, C. D.: Introduction: European Integrated Project on Aerosol Cloud Climate and Air Quality interaction (EUCAARI) – integrating aerosol research from nano to global scales. Atmos. Chem. Phys., 9, 2825-2841, 2009.

Kulmala, M., Asmi, A., Lappalainen, H. K., Baltensperger, U.,Brenguier, J.-L., Facchini, M. C., Hansson, H.-C., Hov, Ø., O'Dowd, C. D., Poschl, U., Wiedensohler, A., Boers, R., Boucher, O., de Leeuw, G., Denier van der Gon, H. A. C., Feichter, J., Krejci, R., Laj, P., Lihavainen, H., Lohmann, U., McFiggans, G., Mentel, T., Pilinis, C., Riipinen, I., Schulz, M., Stohl, A., Swietlicki, E., Vignati, E., Alves, C., Amann, M., Ammann, M., Arabas, S., Artaxo, P., Baars, H., Beddows, D. C. S., Bergstrom, R., Beukes, J. P., Bilde, M., Burkhart, J. F., ¨ Canonaco, F., Clegg, S. L., Coe, H., Crumeyrolle, S., D'Anna, B., Decesari, S., Gilardoni, S., Fischer, M., Fjaeraa, A. M., Fountoukis, C., George, C., Gomes, L., Halloran, P., Hamburger, T., Harrison, R. M., Herrmann, H., Hoffmann, T., Hoose, C., Hu, M., Hyvarinen, A., H ¨ orrak, U., Iinuma, Y., Iversen, T., Josipovic, M., Kanakidou, M., Kiendler-Scharr, A., Kirkevag, A., Kiss, G., Klimont, Z., Kolmonen, P., Komppula, M., Kristjansson, J.-E., Laakso, L., Laaksonen, A., Labonnote, L., Lanz, V. A., Lehtinen, K. E. J., Rizzo, L. V., Makkonen, R., Manninen, H. E., McMeeking, G., Merikanto, J., Minikin, A., Mirme, S., Morgan, W. T., Nemitz, E., O'Donnell, D., Panwar, T. S., Pawlowska, H., Petzold, A., Pienaar, J. J., Pio, C., Plass-Duelmer, C., Prev´ ot, A. S. H., Pryor, S., Reddington, C. L., Roberts, G., Rosenfeld, D., Schwarz, J., Seland, Ø., Sellegri, K., Shen, X. J., Shiraiwa, M., Siebert, H., Sierau, B., Simpson, D., Sun, J. Y., Topping, D., Tunved, P., Vaattovaara, P., Vakkari, V., Veefkind, J. P., Visschedijk, A., Vuollekoski, H., Vuolo, R., Wehner, B., Wildt, J., Woodward, S., Worsnop, D. R., van Zadelhoff, G.-J., Zardini, A. A., Zhang, K., van Zyl, P. G., Kerminen, V.-M., S Carslaw, K., and Pandis, S. N.: General overview: European Integrated project on Aerosol Cloud Climate and Air Quality interactions (EUCAARI) – integrating aerosol research from nano to global scales, Atmos. Chem. Phys., 11, 13061–13143, doi:10.5194/acp-11-13061-2011, 2011.

Kulmala, M., Kontkanen, J., Junninen, H., Lehtipalo, K., Manninen, H. E., Nieminen, T., Petäjä, T., Sipilä, M., Schobesberger, S., Rantala, P., Franchin, A., Jokinen, T., Järvinen, E., Äijälä, M., Kangasluoma, J., Hakala, J., Aalto, P. P., Paasonen, P., Mikkilä, J., Vanhanen, J., Aalto, J., Hakola, H., Makkonen, U., Ruuskanen, T., Mauldin III, R. L., Duplissy, J., Vehkamäki, H., Bäck, J., Kortelainen, A., Riipinen, I., Kurtén, T., Johnston, M. V., Smith, J. N., Ehn, M., Mentel, T. F., Lehtinen, K. E. J., Laaksonen, A., Kerminen, V.-M., and Worsnop, D. R.: Direct Observations of Atmospheric Aerosol Nucleation, Science, 339, 943-946, 2013.

Laakso, L., Grönholm, T., Rannik, Ü., Kosmale, M., Fiedler, V., Vehkamäki, H. and Kulmala, M. Ultrafine particle scavening coefficients calculated from 6 years field measurements.: Atmospheric Environment, 37, 3605-3613, 2003

Lane, T. E., Donahue, N. M. and Pandis, N.: Simulating secondary organic aerosol formation using the volatility basis-set apporach in a chemical transport model. Atmospheric Environment, 42, 7439-7451, 2008.

Liggio, J. and Li, S.-M.: Organosulfate formation during the uptake of pinonaldehyde in acidic sulfate aerosols, Geophys. Res. Lett., 33, L13808, doi:10.1029/2006GL026079, 2006.

Löndahl, J.: Experimental Determination of the Deposition of Aerosol Particles in the Human Respiratory Tract, ISBN 978-91-628-7702-6, Doctoral dissertation at Lund University, Dep. of Nuclear Physics, Lund, Sweden, 2009.

Makkonen, R., Asmi, A., Korhonen, H., Kokkola, H., Järvenoja, S., Räisänen, P., Lehtinen, K. E. J., Laaksonen, A., Kerminen, V.-M., Järvinen, H., Lohmann, U., Feichter, J., and Kulmala, M.: Sensitivity of aerosol concentrations and cloud properties to nucleation and secondary organic distribution in ECHAM5-HAM global circulation model, Atmos. Chem. Phys., 9, 1747-1766, 2009.

Martin, S. T, Andreae, M. O., Artaxo, P., Baumgardner, D., Chen, Q, Goldstein, A. H., Guenther, A., Heald, C. L., Mayol-Bracero, O. L., McMurry, P. H., Pauliquevis, T., Pöschl, U., Prather, K. A., Robert, G. C., Saleska, S. R., Dias, M. A. S., Spracklen, D. V., Swietlicki, E. and Trebs, I.: Source and properties of Amazonian aerosol particles. Review of Geophysics, 48, RG2002, 2010.

Martinsson, B. G., Brenninkmeijer, C. A. M., Carn, S. A., Hermann, M., Heue, K.-P., van Velthoven, P. F. J. and Zahn, A.: Influence of the 2008 Kasatochi volcanic eruption on sulfurous and carbonaceous aerosol constituents in the lower stratosphere. Geophysical Research Letters, 36, L12813, doi:10.1029/2009GL038735, 2009.

Maxwell-Garnett, J. C.: Colours in metal glasses and in metallic films, Philos. Trans. R. Soc. Ser. A 203, 385–420, 1904.

McMurry, P. H. and Friedlander, S. K.: New particle formation in the presence of an aerosol. Atmospheric Environment, 13, 1635-1651, 1979.

McMurry, P. H. and Rader, D. J.: Aerosol wall losses in electrically charged chambers. Aerosol Sci. Technol., 4, 249-268, 1985.

Metzger, A., Dommen, J., Gaeggeler, K., Duplissy, J., Pr´ev^ot, A. S. H., Kleffmann, J., Elshorbany, Y., Wisthaler, A., and Baltensperger, U.: Evaluation of 1,3,5 trimethylbenzene degradation in the detailed tropospheric chemistry mechanism, MCMv3.1, using environmental chamber data, Atmos. Chem. Phys., 8, 6453–6468, 2008.

Na, K., Song, C., Switzer, C., and Cocker, D.: Effect of Ammonia on Secondary Organic Aerosol Formation from α-Pinene Ozonolysis in Dry and Humid Conditions. Environ. Sci. Technol., 41, 6096-6102, 2007.

Nannoolal, J., Rarey, J., Ramjugernath, D.: Estimation of pure component properties Part 3. Estimation of the vapor pressure of non-electrolyte organic compounds via group contributions and group interactions, Fuild Phase Equilibria, 269, 117-133, 2008.

Nel, A.: Air pollution-related illness: Effects of particles, Science, 308, 804-806, 2005.

Ng, N. L., Kroll, J. H., Chan, A. W. H., Chhabra, P. S., Flagan, R. C., and Seinfeld, J. H.: Secondary organic aerosol formation from *m*-xylene, toluene, and benzene, Atmos. Chem. Phys., 7, 3909–3922, 2007.

Ng, N. L., Kwan, A. J., Surratt, J. D., Chan, A. W. H., Chhabra, P. S., Sorooshian, A., Pye, H. O. T., Crounse, J. D., Wennberg, P. O., Flagan, R. C., and Seinfeld, J. H.: Secondary organic aerosol (SOA) formation from reaction of isoprene with nitrate radicals (NO3), Atmos. Chem. Phys., 8, 4117–4140, 2008.

Nyeki, S., and Colbeck, I.: Fractal dimension analysis of single, in-situ, restructured carbonaceous aggregates, Aerosol Sci. Technol., 23, 109–120, 1995.

Nygaard, U. C., Samuelsen, M., Aase, A., Lovik, and M.: The capacity of particles to increase allergic sensitization is predicted by particle number and surface area, not by particle mass. Toxicological Sciences, 82, 515-524, 2004.

Mönkkönen, P., Koponen, I. K., Lehtinen, K. E. J., Hämeri, K., Uma, R. and Kulmala, M.: Measurements in a highly polluted Asian mega city: observations of aerosol number size distribution, modal parameters and nucleation events. Atmos. Chem. Phys., 5, 57-66, 2005.

Odum, J. R., Hoffmann, T., Bowman, F., Collins, D., Flagan, R. C. and Seinfeld, J. H.: Gas/Particle Partitioning and Secondary Organic Aerosol Yields. Environ. Sci. Technol., 30, 2580-2585, 1996.

Paasonen, P., Sihto, S.-L., Nieminen, T., Vuollekoski, H., Riipinen, I., Plass-Dülmer, C., Berresheim, H., Birmili, W. and Kulmala, M.: Connection between new particle formation and sulphuric acid at Hohenpeissenberg (Germany) including the influence of organic compounds, Boreal Environmental Research, 14, 616-629, 2009.

Pankow, J. F.: An absorption-model of the gas aerosol partitioning involved in the formation of secondary organic aerosol, Atmos. Environ., 28, 189–193, 1994.

Pankow, J. F. & Asher, W. E.: SIMPOL.1: a simple group contribution method for predicting vapor pressures and enthalpies of vaporization of multifunctional organic compounds, Atmos. Chem. Phys., 8, 2773–2796, 2008.

Pathak, R. K., Presto, A. A., Lane, T. E., Stanier, C. O., Donahue, N. M., and Pandis, S. N.: Ozonolysis of α-pinene: parameterization of secondary organic aerosol mass fraction, Atmos. Chem. Phys., 7, 3811-3821, doi:10.5194/acp-7-3811-2007, 2007.

Pfrang, C., Shiraiwa, M., and Pöschl, U.: Chemical ageing and transformation of diffusivity in semi-solid multi-component organic aerosol particles, Atmos. Chem. Phys., 11, 7343-7354, doi:10.5194/acp-11-7343-2011, 2011.

Pierce, J. R., Engelhart, G. J., Hildebrandt, L., Weitkamp, E. A., Pathak, R. K., Donahue, N. M., Robinson, A. L., Adams, P. J., and Pandis, S. N.: Constraining Particle Evolution from Wall Losses, Coagulation, and Condensation-Evaporation in Smog-Chamber Experiments: Optimal

Estimation Based on Size Distribution Measurements, Aerosol Sci. and Technol., 42:12, 1001-1015, 2008.

Pilinis C.: Numerical Simulation of Visibility Degradation Due to Particulate Matter: Model Development and Evaluation, Journal of Geophysical Research, 94, 9937-9946, 1989.

Pirjola, L. and Kulmala, M.: Modelling the formation of H2SO4-H2O particles in rural, urban and marine conditions, Atmos. Res., 46, 321–347, 1998.

Pope, C. A., Thun, M. J, Namboodiri, M. M., Dockerty, D. W., Evans, J. S., Speizer, F. E., Heath, C. W.: Particulate Air-Pollution As A Predictor of Mortality in A Prospective-Study of Us Adults, American Journal of Respiratory and Critical Care Medicine, 151, 669-674, 1995

Pruppacher, H. R., and Klett, J. D.: Microphysics of Clouds and Precipitation 2nd ed, ISBN: 0-7923-4211-9, USA, 1997.

Pöschl U., Martin S. T., Sinha B., Chen Q., Gunthe S. S., Huffman J. A., Borrmann S., Farmer D. K., Garland R. M., Helas G., Jimenez J. L., King S. M., Manzi A., Mikhailov E., Pauliquevis T., Petters M. D., Prenni A. J., Roldin P., Rose D., Schneider J., Su H., Zorn S. R., Artaxo P. and Andreae M. O.: Rainforest aerosols as biogenic nuclei of clouds and precipitation in the Amazon, Science, 329, 1513-1516, 2010.

Pöschl, U.: Gas–particle interactions of tropospheric aerosols: Kinetic and thermodynamic perspectives of multiphase chemical reactions, amorphous organic substances, and the activation of cloud condensation nuclei, Atmos. Res. 101, 562–573, 2011.

Ramanathan, V., Crutzen, P. J., Kiehl, J. T. and Rosenfeld, D.: Aerosol, Climate, and the Hydrological Cycle. Science, 294, 2119-2124, 2001.

Ramanathan, V., and Carmichael, G.: Global and regional climate changes due to black carbon, Nat. Geosci. 1, 221–227, 2008.

Rissler, J., Swietlicki, E., Zhou, J., Roberts, G., Andreae, M. O., Gatti, L. V. and Artaxo, P.: Physical properties of the sub-micrometer aerosol over the Amazon rain forest during the wet-to-dry season transition – comparison of modeled and measured CCN concentrations. Atmos. Chem. Phys., 4, 2119-2143, 2004.

Rizzo, L. V., Artaxo, P., Müller, T., Wiedensohler, A., Paixão, M., Cirino, G. G., Arana, A., Swietlicki, E., Roldin, P., Fors, E. O., Wiedemann, K. T., Leal, L. S. M., and Kulmala, M.: Long term measurements of aerosol optical properties at a primary forest site in Amazonia, Atmos. Chem. Phys., 13, 2391-2413, 2013.

Rodhe, H.: Time Scales Characterizing the Processing of Water and Cloud Condensation Nuclei by Clouds. Report CM-80, ISSN: 0280-445X, Stockholm University, Sweden, 1992.

Schauer, J. J., Kleeman, M. J., Cass, G. R. and Simoneit, B. R. T. (2002). Measurement of emissions from air pollution sources. 5. C-1-C-32 organic compounds from gasoline-powered motor vehicles. Environ Sci Technol 36(6): 1169-1180.

Schmid, O., Möller, W., Semmler-Behnke, M., Ferron, G. A., Karg, E., Lipka, J., Schulz, H., Kreyling W. G., and Stoeger, T.: Dosimetry and toxicology of inhaled untrafine particles, Biomarker, 14, 67-73, 2009.

Shiraiwa, M., Pfrang, C., Koop, T., and Pöschl, U.: Kinetic multi-layer model of gas-particle interactions in aerosols and clouds (KM-GAP): linking condensation, evaporation and chemical reactions of organics, oxidants and water, Atmos. Chem. Phys., 12, 2777–2794, 2012.

Shrivastava, M. K., Lane, T. E., Donahue, N. M., Pandis, S. N. and Robinson, A. L.: Effects of gas particle partitioning and aging of primary emissions on urban and regional organic aerosol concentrations. Journal of Geophysical Research, 113, D18301, doi:10.1029/2007JD009735, 2008.

Simpson, D., Fagerli, H., Jonson, J. E., Tsyro, S., Wind, P. and Tuovinen, J.-P.: Transboundary Acidification, Eutrophication and Groud Level Ozone in Europe, Part I, Unified EMEP Model Description. EMEP Status Report 2003. ISSN 0806-4520, 2003

Slinn, W. G. N.: Predictions for particle deposition to vegetation canopies, Atmos. Environ., 16, 1785–1794, 1982.

Stone, R. S., Herber, A. Vitale, V., Mazzola, M., Lupi, A., Schnell, R. C., Dutton, E. G., Liu, P. S. K., Li, S. M., Dethloff, K., Lampert, A., Ritter, C., Stock, M., Neuber, R. and Maturilli, M.: A three-dimensional characterization of Arctic aerosols from airborne Sun photometer observations: PAM-ARCMIP, April 2009. Journal of Geophysical Research, 115, D13203, doi:10.1029/2009JD013605, 2010

Toon, O. B., McKay, C. P., Ackerman, T. P. and Santhanam, K.: Rapid Calculation of Radiative Heating Rates and Photodissociation Rates in Inhomogeneous Multiple Scattering Atmospheres. Journal of Geophysical Research, 94, 16287-16301, 1989.

Tran, C. L., Buchanan, D., Cullen, R. T., Searl, A., Jones, A. D., and Donaldson, K.: Inhalation of poorly soluble particles. II. Influence of particle surface area on inflammation and clearance. Inhalation Toxicology, 12, 1113-1126, 2000.

Tsimpidi, A. P., Karydis, V. A., Zavala, M., Lei, W., Molina, L., Ulbrich, I. M., Jimenez, J. L. and Pandis, S. N.: Evaluation of the volatility basis-set approach for the simulation of organic aerosol formation in the Mexico City metropolitan area. Atmos. Chem. Phys., 10, 525–546, 2010.

Tunved, P., Partridge, D. G., and Korhonen, H.: New trajectory driven aerosol and chemical process model Chemical and Aerosol Lagrangian Model (CALM), Atmos. Chem. Phys., 10, 10161-10185, 2010.

Twomey, S., Pollution and Planetary Albedo, Atmospheric Environment, 8, 1251-1256, 1974.

Vaden, T. D., Imreb, D., Beráneka, J., Shrivastavaa, M., and Zelenyuka, A.: Evaporation kinetics and phase of laboratory and ambient secondary organic aerosol, Proc. Natl. Acad. Sci., 108, 2190-2195, 2011.

Valorso, R., Aumont, B., Camredon, M., Raventos-Duran, T., Mouchel-Vallon, C., Ng, N. L., Seinfeld, J. H., Lee-Taylor, J., and Madronich, S.: Explicit modeling of SOA formation from α-pinene photooxidation: sensitivity to vapor pressure estimation. Atmos. Chem. Phys., 11, 6895–6910, 2011.

Van de Hulst, H. C.: Light Scattering by Small Particles. John Wiley and Sons, New York, 1957.

Virtanen, A., Joutsensaari, J., Koop, T., Yli-Pirilä, P., Leskinen, J., Mäkelä, J. M., Holopainen, J. K., Pöschl, U., Kulmala, M., Worsnop, D. R. and Laaksonen, A.: An amorphous solid state of biogenic secondary organic aerosol particles, Nature, 467, 824-827, 2010.

Wiedensohler, A., Birmili, W., Nowak, A., Sonntag, A., Weinhold, K., Merkel, M., Wehner, B., Tuch, T., Pfeifer, S., Fiebig, M., Fjäraa, A. M., Asmi, E., Sellegri, K., Depuy, R., Venzac, H., Villani, P., Laj, P., Aalto, P., Ogren, J. A., Swietlicki, E., Williams, P., Roldin, P., Quincey, P., Hüglin, C., Fierz-Schmidhauser, R., Gysel, M., Weingartner, E., Riccobono, F., Santos, S., Grüning, C., Faloon, K., Beddows, D., Harrison, R., Monahan, C., Jennings, S. G., O'Dowd, C. D., Marinoni, A., Horn, H.-G., Keck, L., Jiang, J., Scheckman, J., McMurry, P. H., Deng, Z., Zhao, C. S., Moerman, M., Henzing, B., de Leeuw, G., Löschau, G., and Bastian, S.: Mobility particle size spectrometers: harmonization of technical standards and data structure to facilitate high quality long-term observations of atmospheric particle number size distributions, Atmos. Meas. Tech., 5, 657-685, 2012.

World Health Organization, The world health report 2002, Reducing the risks, promoting healthy life. Geneva: World Health Organisation, 2002.

Zhang, H., Zhang, F., Fu, Q., Shen, Z., and Lu, P.: Two- and four-stream combination approximations for computation of diffuse actinic fluxes. J. Atmos. Sci., 67, 3238–3252, 2010.

Zhang, L., Gong, S., Padro, J., and Barrie, L.: A size-segregated particle dry deposition scheme for an atmospheric aerosol module, Atmos. Environ., 35, 549–560, 2001.

Zhang, R., Khalizov, A. F., Pagels, J., Zhang, D., Xue, H., McMurry, P. H.: Variability in morphology, hygroscopicity, and optical properties of soot aerosols during atmospheric processing, Proc. Natl. Acad. Sci., 105, 10291-10296, 2008.

Zuend, A., Marcolli C., Booth , A. M., Lienhard, D. M., Soonsin, V., Krieger, U. K., Topping, D. O., McFiggans G., Peter, T., and Seinfeld, J. H.: New and extended parameterization of the thermodynamic model AIOMFAC: calculation of activity coefficients for organic-inorganic mixtures containing carboxyl, hydroxyl, carbonyl, ether, ester, alkenyl, alkyl, and aromatic functional groups., Atmos. Chem. Phys., 11, 9155–9206, 2011.

Zuend, A. and Seinfeld, J. H.: Modeling the gas-particle partitioning of secondary organic aerosol: the importance of liquid-liquid phase separation, Atmos. Chem. Phys., 12, 3857-3882, doi:10.5194/acp-12-3857-2012, 2012.

Paper I

Atmos. Chem. Phys., 11, 5867–5896, 2011
www.atmos-chem-phys.net/11/5867/2011/
doi:10.5194/acp-11-5867-2011

Atmospheric
Chemistry
and Physics

Development and evaluation of the aerosol dynamics and gas phase chemistry model ADCHEM

P. Roldin[1], E. Swietlicki[1], G. Schurgers[2], A. Arneth[2,3], K. E. J. Lehtinen[4,5], M. Boy[6], and M. Kulmala[6]

[1]Division of Nuclear Physics, Lund University, 221 00, Lund, Sweden
[2]Department of Earth and Ecosystem Sciences, Lund University, Sweden
[3]Institute of Meteorology and Climate Research/Atmospheric Environmental Research, Karlsruhe Institute of Technology, Germany
[4]Department of Physics and Mathematics, University of Eastern Finland, Kuopio, Finland
[5]Finnish Meteorological Institute, Kuopio Unit, Kuopio, Finland
[6]Atmospheric Sciences Division, Department of Physics, University of Helsinki, Finland

Received: 14 July 2010 – Published in Atmos. Chem. Phys. Discuss.: 10 August 2010
Revised: 16 May 2011 – Accepted: 30 May 2011 – Published: 22 June 2011

Abstract. The aim of this work was to develop a model suited for detailed studies of aerosol dynamics, gas and particle phase chemistry within urban plumes, from local scale ($1 \times 1\,\mathrm{km}^2$) to regional scale. This article describes and evaluates the trajectory model for Aerosol Dynamics, gas and particle phase CHEMistry and radiative transfer (ADCHEM). The model treats both vertical and horizontal dispersion perpendicular to an air mass trajectory (2-space dimensions). The Lagrangian approach enables a more detailed representation of the aerosol dynamics, gas and particle phase chemistry and a finer spatial and temporal resolution compared to that of available regional 3D-CTMs. These features make it among others well suited for urban plume studies. The aerosol dynamics model includes Brownian coagulation, dry deposition, wet deposition, in-cloud processing, condensation, evaporation, primary particle emissions and homogeneous nucleation. The organic mass partitioning was either modeled with a 2-dimensional volatility basis set (2D-VBS) or with the traditional two-product model approach. In ADCHEM these models consider the diffusion limited and particle size dependent condensation and evaporation of 110 and 40 different organic compounds respectively. The gas phase chemistry model calculates the gas phase concentrations of 61 different species, using 130 different chemical reactions. Daily isoprene and monoterpene emissions from European forests were simulated separately with the vegetation model LPJ-GUESS, and included as input to ADCHEM. ADCHEM was used to simulate the ageing of the urban plumes from the city of Malmö in southern Sweden (280 000 inhabitants). Several sensitivity tests were performed concerning the number of size bins, size structure method, aerosol dynamic processes, vertical and horizontal mixing, coupled or uncoupled condensation and the secondary organic aerosol formation. The simulations show that the full-stationary size structure gives accurate results with little numerical diffusion when more than 50 size bins are used between 1.5 and 2500 nm, while the moving-center method is preferable when only a few size bins are selected. The particle number size distribution in the center of the urban plume from Malmö was mainly affected by dry deposition, coagulation and vertical dilution. The modeled PM2.5 mass was dominated by organic material, nitrate, sulfate and ammonium. If the condensation of HNO_3 and NH_3 was treated as a coupled process (pH independent) the model gave lower nitrate PM2.5 mass than if considering uncoupled condensation. Although the time of ageing from that SOA precursors are emitted until condensable products are formed is substantially different with the 2D-VBS and two product model, the models gave similar total organic mass concentrations.

1 Introduction and background

Since the chemical and physical properties of aerosol particles determine both their climate and health effects, it is important to understand the aerosol dynamic processes that affect these quantities. Particle emissions within a city may

---

Correspondence to: P. Roldin
(pontus.roldin@nuclear.lu.se)

Published by Copernicus Publications on behalf of the European Geosciences Union.

have a significant effect on the population health and climate several tens or hundreds of kilometers downwind of the urban center, although limited quantitative information is available in the literature (Hodzic et al., 2006; Doran et al., 2007; Nolte et al., 2008; Hodzic et al., 2009; Tsimpidi et al., 2010; Wang et al., 2010). The chemical composition of the ambient aerosols is affected by primary particle emissions, condensation, evaporation and coagulation between particles with different composition. The particle number size distribution is altered by emissions, condensation, evaporation, coagulation, dry and wet deposition, formation of new particles by homogeneous nucleation and in-cloud processing.

Since 2007 the trajectory model for Aerosol Dynamics, gas and particle phase CHEMistry and radiative transfer (ADCHEM) has continuously been developed and used at Lund University. In this work ADCHEM was used to model the particle and gas phase properties in the urban plume from the city of Malmö in southern Sweden (13°00′ E, 55°36′ N, 280 000 inhabitants). This article mainly describes the model development and evaluation, while Paper II (Roldin et al., 2011) describes the average particle and gas phase properties within the urban plume from Malmö, and their influence on the radiation balance and cloud properties.

ADCHEM includes both vertical and horizontal dispersion perpendicular to an air mass trajectory (2-space dimensions), which is not treated in Lagrangian box-models (0-space dimensions). The Lagrangian approach allows a more detailed representation of the aerosol dynamics, particle and gas phase chemistry and a finer spatial and temporal resolution than available in regional three-dimensional chemical transport models (3D-CTMs). These features make it well suited both for studies of urban plumes as well as long distance transported air masses (e.g. studies of regional new particle formation events). The disadvantage with Lagrangian models is that they follow one air mass trajectory, and do not account for different wind speed or wind directions at different altitudes. Hence, these models have limitations in some meteorological conditions, and if the emissions within a source region (e.g. a city) show rapid and large temporal variability (see discussion in Sect. 2.1).

Aerosol models can be divided into equilibrium models and dynamic models. The equilibrium models assume equilibrium between the gas and particle phase while dynamic models treat the mass transport between gas and particle phase. Due to computational limitations the detailed aerosol inorganic chemistry models are primarily equilibrium models, e.g. AIM (Wexler and Clegg, 2002), while aerosol dynamics models usually use a more simplified particle chemistry, e.g. UHMA (Korhonen et al., 2004b), or no particle chemistry, e.g. AEROFOR (Pirjola, 1999) and MONO32 (Pirjola et al., 2003).

Once introducing particle chemistry into the aerosol dynamics model it should preferably be coupled to a detailed gas phase chemistry model. One such early study was performed by Pirjola and Kulmala (1998), which modeled binary H_2SO_4–H_2O nucleation in urban and rural environments, using a box model. Fitzgerald et al. (1998) developed the MARBLES model, which is a one dimensional (1-D) Lagrangian aerosol dynamics model developed to simulate multicomponent (sulfuric acid, sea salt and crustal material) aerosol composition in the marine boundary layer. However, this model did not include a detailed gas phase chemistry model.

Boy et al. (2006) were among the first to include a detailed aerosol dynamics model (UHMA) together with a detailed gas phase chemistry model and a meteorological model in 1-D (vertical). This model named MALTE is primarily designed to model new particle formation in the lower troposphere. ADCHEM developed in this work has many similarities with MALTE concerning the aerosol dynamics, gas phase chemistry and dispersion in the vertical direction. In ADCHEM a second horizontal space dimension was introduced to enable the simulation of horizontal inhomogeneous emissions in urban plumes. However, ADCHEM does not include any meteorological model, and therefore relies on meteorological input data along the trajectory. ADCHEM also incorporates a detailed radiative transfer model which treats scattering and absorption from gases, particles and clouds (Toon et al., 1989). The gas phase model included in ADCHEM is developed from the kinetic code incorporated in the model developed by Pirjola and Kulmala (1998).

Recently aerosol dynamics models which treat condensation and evaporation of semi-volatile inorganic gases like ammonia (NH_3), nitric acid (HNO_3) and hydrochloric acid (HCl) have been developed (e.g. Zhang and Wexler, 2008). These models can treat the acid and base mass transfer either as separate processes or simplified as a coupled process. The large advantage of coupling the condensation and evaporation of acid and base (e.g. HNO_3 and NH_3) is that the condensation and evaporation becomes pH independent, and allows the model to take longer time steps when solving the condensation/evaporation process. The disadvantage with the coupled condensation/evaporation process is that it is only valid if the aerosol is near acid neutrality (Zaveri et al., 2008 and Zhang and Wexler, 2008).

To be able to take long time steps (minutes), without causing oscillatory solutions when solving the condensation/evaporation of acid and base as separate processes, Jacobson (2005a) developed the prediction of non-equilibrium growth (PNG) scheme. With this method the condensation (dissolution) and evaporation of HNO_3, HCl and H_2SO_4 is solved first, depending on the pH calculated from the previous time step, and then the NH_3 dissolution is treated as an equilibrium process. With this method the dissolution of NH_3 is linked to the condensation/evaporation of the acids but also depends on the pH in the aerosol liquid phase. Therefore this method is also valid when the aerosol is not near acid neutralized. In ADCHEM, the condensation and evaporation of HNO_3, HCl and NH_3 can either be treated as coupled or uncoupled processes, and the dissolution of NH_3

can either be modeled as a dynamic or equilibrium process. ADCHEM also considers in-cloud processing of aerosol particles, including sulfate (S(VI)) formation from dissolved SO_2 and H_2O_2. The dissolution of SO_2 and H_2O_2 are treated as equilibrium processes.

The main objective of this work was to develop a model which can be used for detailed simulations of ageing processes within urban plumes, from local scale ($1 \times 1\,km^2$) to regional scale. One application of this comprehensive model which is addressed in this work is to study which processes that are most important for accurate representation of aerosol dynamics and particle chemical composition in urban plumes. These results are useful when developing more simplified aerosol dynamics, gas and particle phase chemistry modules or parameterizations for 3D-CTMs or global climate models.

2 Model description

ADCHEM can be divided into three sub-models:

1. an aerosol dynamics and particle chemistry model,
2. a chemical gas phase model,
3. a radiative transfer model.

The aerosol dynamics model in ADCHEM is a sectional model which discretizes the particle number size distribution into finite size bins. The particles are assumed to be internally mixed which means that particles of the same size within the same grid cell have the same composition. The model includes Brownian coagulation, dry deposition, wet deposition, in-cloud processing, condensation, evaporation, primary particle emissions, homogeneous nucleation and dispersion in the vertical (1-D model) and horizontal direction (2-D model) perpendicular to the air mass trajectory. The model treats both organic and inorganic particle phase chemistry with sulfate, nitrate, ammonium, sodium, chloride, non water soluble minerals (metal oxides/hydroxides), soot, Primary Organic Aerosol (POA), Anthropogenic and Biogenic Secondary Organic Aerosol (ASOA and BSOA), and dissolution of sulfur dioxide and hydrogen peroxide into the particles and cloud droplets. In ADCHEM SOA can either be formed by condensation of oxidation products of specific VOCs (e.g. α-pinene, β-pinene, Δ3-carene, D-limonene, isoprene, benzene, toluene and xylene), using the traditional two-product model (Odum et al., 1996) or using the newly developed volatility basis set (VBS) approach (Donahue et al., 2006), which divides all organic compounds into volatility classes without identifying individual compounds. The aerosol dynamics and particle phase chemistry model is coupled to the gas phase chemistry model through condensation, evaporation and homogeneous nucleation.

The gas phase chemistry model calculates the gas phase concentrations of 61 different species, using 130 different chemical reactions. Daily isoprene and monoterpene emissions from European forests were simulated separately with the vegetation model LPJ-GUESS (Smith et al., 2001 and Sitch et al., 2003), in which processbased algorithms of terpenoid emissions were included (Arneth et al., 2007, Schurgers et al., 2009a). The emissions from natural vegetation were corrected for anthropogenic land cover following Ramankutty et al. (2008), in a way similar to that in Arneth et al. (2008).

The actinic flux used to calculate the photochemical reaction rates, is derived with the radiative transfer model. This model uses a quadrature two-stream approximation scheme, where the radiative fluxes are approximated with one upward and one downward flux component. The model can be used to calculate the radiative transfer in a vertically inhomogeneous atmosphere with clouds and aerosol particles (Toon et al., 1989).

Figure 1 illustrates the model structure in ADCHEM. The model starts by calculating the turbulent diffusivity in the vertical and horizontal direction using meteorological and land use category input data. After this the model starts integrating over time using operator splitting for each individual process (module). Each individual process (module) displayed in Fig. 1 is described in detail below.

To our knowledge there are no other models available like ADCHEM which combine schemes of detailed aerosol dynamics, gas phase chemistry, inorganic particle phase chemistry, dynamic and particle size dependent SOA formation, cloud processing and radiative transfer in two space dimensions in a Lagrangian model with high spatial and temporal resolution (~1 km, ~1 min).

Since ADCHEM is a Lagrangian model it relies on separate results from an air mass trajectory model. In this work the air mass trajectory for the studied case was modeled with the Hybrid Single Particle Lagrangian Integrated Trajectory (HYSPLIT) model (Draxler and Rolph, 2011), which was run with meteorological data from the Global Data Assimilation System (GDAS) from National Weather Service's National Centers for Environmental Prediction (NCEP), with a horizontal resolution of 1° × 1 ° and a temporal resolution of 3 h.

Stohl et al. (2001) conducted a model comparison between three different air mass trajectory models and concluded that although the average horizontal position deviations was largest close to the surface, it was not larger than 10 % for 48 h backward trajectory simulations. However, the accuracy of the trajectory model does not just depend on the model structure but also the meteorological input data. Hence, since the HYSPLIT model relies on relatively coarse large scale meteorology data, the wind direction of the modeled trajectory was validated with wind direction measurements in Malmö, at 24 m a.g.l. For the selected case study the modeled and measured wind direction at this altitude agree within five degrees.

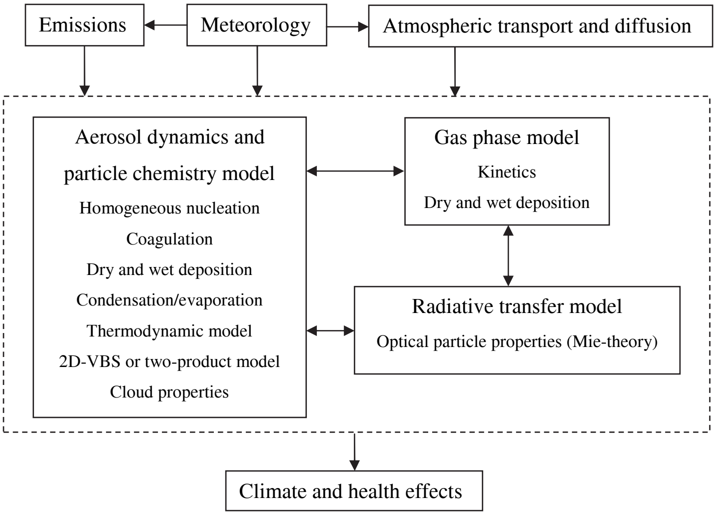

Fig. 1. Schematic picture illustrating the model structure of ADCHEM.

2.1 Atmospheric diffusion

For the simulations performed in this study a model domain of 20 vertical grid cells and 20 horizontal grid cells was used. The vertical and horizontal grid resolution was 100 m and 1000 m respectively. The 2-D model solves the atmospheric diffusion equation (Eq. 1) in the vertical and horizontal direction perpendicular to the air mass trajectory.

$$\frac{dc}{dt}=\frac{\partial}{\partial z}\left(K_z\frac{\partial c}{\partial z}\right)+\frac{\partial}{\partial y}\left(K_y\frac{\partial c}{\partial y}\right) \tag{1}$$

Dry deposition and emissions of primary particles in the surface layer are treated separately, and are not included in the boundary conditions for the atmospheric diffusion equation in order to reduce computing time. Instead of solving the 2-D atmospheric diffusion equation for each particle size bin, for 8 inorganic and up to 110 organic aerosol compounds, and each gas phase species (61 compounds), the model solves the atmospheric diffusion equation once for each grid cell. This is possible because the transport of compounds by turbulent diffusivity in contrast to e.g. molecular diffusion is independent of the properties of the individual species. For the 20 × 20 grid, the diffusion equation has to be solved 400 times in each time step. Equation (1) is solved 400 times by introducing an inert species with initial concentration equal to 1, in one new single grid cell at the time. In all other grid cells the concentration is set to zero. After one time step a new concentration matrix of the inert species is received, which describes the mixing of the air between the grid cell with initial concentration equal to 1 and the surrounding grid cells. If the time step used is short enough the atmospheric diffusion equation does not have to be solved for the whole grid, but rather for the grid cells closest to the grid cell with an initial concentration equal to 1. This way the simulation time can be decreased drastically.

K_z and K_y in Eq. (1) are the eddy diffusivities (turbulent diffusivities) in the vertical and horizontal direction respectively and c is the concentration of any arbitrary species. The eddy diffusivities are calculated for stable, neutral and unstable atmospheric conditions using the representations from Businger and Arya (1974), Myrup and Ranzieri (1976) and Tirabassi and Rizza (1997) (Appendix A). The three turbulence regimens are defined by the dimensionless parameter (h/L), where h is the mixing height and L is the Monin-Obukov length, which describes the relationship between the buoyant and wind shear produced turbulent kinetic energy. For stable conditions the turbulence in the boundary layer is mainly produced by wind shear while for unstable conditions the turbulence is mainly induced by buoyant convection. Hence, for stable and neutral conditions the eddy diffusivity is represented by expressions which depend on the friction velocity while for unstable conditions the friction velocity is replaced with the convective velocity (see Appendix A).

The numerical solution of the atmospheric diffusion equation is described in Appendix B. As upper boundary condition the concentration gradient $\partial c/\partial z$ was set to $10^{-3}\,\mathrm{cm}^{-3}\,\mathrm{m}^{-1}$ to account for the generally decreasing gas and particle concentrations above the model domain (2000 m a.g.l.). This is a rough assumption which could not be verified with measurements. However, because of the vertical stability above the boundary layer it had negligible influence on the concentrations within the boundary layer. As horizontal boundary conditions the concentration gradient $\partial c/\partial y$ was set to zero.

ADCHEM does not consider advection in the horizontal direction perpendicular to an air mass trajectory or that the wind speed may change in the vertical direction. This is the largest disadvantage with the model compared to Eulerian 3D-models. Hence, ADCHEM cannot be used to accurately simulate urban plumes when the wind direction changes significantly in the vertical direction within the boundary layer. The model results are also distorted if the wind speed changes in the vertical direction, but this is mainly a problem if the emissions within the city changes significantly and rapidly. Wind shear changes the wind direction and the wind speed in the vertical direction, while the vertical diffusion prevents these distortions (Tirabassi and Rizza, 1997). Hence, it is during stable conditions (strong wind shear and slow vertical diffusion) that ADCHEM may be less appropriate for urban plume simulations. At long distances downwind of the starting point there will always be some divergence between the air mass trajectories at different altitudes which limits the spatial coverage of Lagrangian models. Hence, the model accuracy for urban plume studies generally deteriorates with the distance downwind of the source region. ADCHEM is therefore mainly useful when studying the first few hours up to possibly one day of ageing downwind of a city. When studying large scale regional air mass transport without the influence from large point sources (e.g. cities) the Lagrangian model approach can however be useful on larger spatial scales (several days) (see e.g. Tunved et al., 2010).

Figure S1 in the Supplement illustrates how different HYSPLIT air mass trajectories which start over Malmö at different altitudes but at the same time, are separated from each other due to different wind speed and wind direction at different altitudes. At Vavihill the trajectories which start at 50 and 300 m a.g.l. over Malmö are separated approximately 5 km in the horizontal direction, due to wind shear in the stable stratified boundary layer. The trajectory which starts 500 m a.g.l. over Malmö (above the boundary layer) passes approximately 10 km to the east of Vavihill.

2.2 Aerosol dynamics

Each aerosol dynamic process is included as a separate process in the model, using operator splitting. As default the model solves all aerosol dynamic processes with a time interval of 60 s.

2.2.1 Size distribution structures

In ADCHEM the changes in the size distributions upon condensation/evaporation or coagulation are solved with the full-stationary, full-moving or moving-center structures which all have different advantages and disadvantages. All these methods are mass and number conserving, which was tested before the methods were implemented in ADCHEM. For a detailed description of the methods see Sect. 13 in Jacobson (2005b).

If using the full-stationary structure when calculating how the particle number size distribution changes in diameter space, the so called splitting procedure has to be used. With this procedure it is assumed that only a fraction of the particles in one size bin will grow to the next size bin, while the rest of the particles will not grow at all (Korhonen, 2004b). This leads to numerical diffusion which makes the particle number size distribution wider and the peak concentration lower (Jacobson, 2005b and Korhonen, 2004b). The reason for this is that splitting makes some particles grow more than in the reality, while others will not grow at all. The numerical diffusion can be decreased by increasing the number of size bins (Korhonen, 2004b).

With the full-moving structure the particles are allowed to grow to their exact size and instead of splitting them back onto a fixed diameter grid the diameter grid moves with the particles. While eliminating the numerical diffusion this causes problems if air mixes between adjacent grid cells and if considering new particle formation. Therefore the full-moving structure will not be used in this study.

The moving-center method is a combination of the full-stationary structure and the full-moving structure. The particles are allowed to grow to their exact size as long as they are not crossing the fixed diameter bin limits. If the particles in a size bin cross the lower or upper diameter limit they are all moved to the adjacent diameter bin and their volume is averaged with the particles in the new bin, which then get a new diameter. Since all the particles in one size bin move to a new bin in the same time step the numerical diffusion is minimized when using the moving-center structure. Therefore this method is preferable when the size distribution is represented by only a few size bins.

2.2.2 Condensation and evaporation

ADCHEM considers the condensation and evaporation of sulfuric acid, ammonia, nitric acid, hydrochloric acid and oxidation products of different organic compounds. Figure 2 illustrates the structure of the condensation/evaporation algorithm used in ADCHEM. The condensation and evaporation is solved by first calculating the single particle molar condensation growth rate of each compound, for each size bin separately (Eq. 2). If considering uncoupled condensation of acids and ammonia the analytic prediction of condensation (APC) scheme and predictor of non-equilibrium growth (PNG) scheme developed and described in detail by Jacobson (1997, 2005a) are used, while if treating the condensation of acids and ammonia as a coupled process the method first proposed by Wexler and Seinfeld (1990) and later applied by e.g. Zhang and Wexler (2008) is used. The coupled condensation growth rate of NH_3 and HX (mol s^{-1}) is given by Eq. (3), where X denotes either Cl or NO_3. The total NH_3 condensation growth rate (I_{NH_3}) is then given by the sum of the HCl, HNO_3 and 2 times the S(VI) condensation growth rates ($I_{NH_3} = 2I_{S(VI)} + I_{HNO_3} + I_{HCl}$). Both methods are mass and number conserving when combined with either the full-stationary, full-moving or moving-center structure. The APC scheme is used for condensation/evaporation of organic compounds, sulfuric acid and for HCl and HNO_3 if they form solid salts with ammonium, while for dissolution of HCl and HNO_3into the particle water phase, the PNG scheme is used instead (Jacobson, 2005a). In this scheme dissolution of ammonia is treated as an equilibrium process solved after the diffusion limited condensation/evaporation of HNO_3, HCl and H_2SO_4. Treating the dissolution of NH_3 as an equilibrium process enables the model to take long time steps (minutes) when solving the condensation/evaporation process (Jacobson, 2005a). This method can easily be modified to treat the ammonia dissolution as a dynamic process. However, this requires that the time step is decreased drastically to prevent oscillatory solutions.

$$\begin{aligned} &I_i = 2D_i D_\mathrm{p} f_i(\mathrm{Kn}_i, \alpha_i)(C_{i\infty} - C_{is}) \\ &f_i(\mathrm{Kn}_i, \alpha_i) = \frac{0.75\alpha_i(1-\mathrm{Kn}_i)}{\mathrm{Kn}_i^2 + \mathrm{Kn}_i + 0.283\mathrm{Kn}_i\alpha_i + 0.75\alpha_i} \end{aligned} \tag{2}$$

$$\begin{aligned} &I_\mathrm{HX} = \frac{\pi D_\mathrm{p}\overline{DC}}{f_{\mathrm{NH_3}}}\left(1 - \sqrt{1 - \frac{4f_{\mathrm{NH_3}}^2\left(C_{\mathrm{NH_3},\infty}C_{\mathrm{HX},\infty} - C_{\mathrm{NH_3},s}C_{\mathrm{HX},s}\right)}{\overline{C}^2}}\right) \\ &\overline{D} = \sqrt{D_{\mathrm{NH_3}}D_\mathrm{HX}} \\ &\overline{C} = (D_{\mathrm{NH_3}}C_{\mathrm{NH_3}} + D_\mathrm{HX}C_{\mathrm{NH_3}})\big/\overline{D} \end{aligned} \tag{3}$$

In Eqs. (2) and (3) I_i $i$to the molar growth rates, f_i is the Fuchs-Sutugin correction factor in the transition region, $C_{i,\infty}$ is the gas phase concentration of species i (moles m^{-3} air) far from the particle surface, $C_{i,s}$ is the saturation gas phase concentration at the particle surface, D_p is the particle diameter, Kn_i is the non-dimensional Knudsen number and α_i is the mass accommodation coefficient. The mass accommodation coefficients for HNO_3, NH_3, H_2SO_4, HCl, SO_2, H_2O_2 and all condensable organic compounds were set to 0.2, 0.1, 1.0, 0.2, 0.11, 0.23 and 0.1, respectively. For the inorganic compounds these numbers are within the range of values tabulated in Sander et al. (2006) over liquid water at temperatures between 260 and 300 K. As a sensitivity test one simulation was also performed with unity mass accommodation coefficients. Usually it is assumed that the saturation vapor pressure of sulfuric acid is zero (Korhonen, 2004a and Pirjola and Kulmala, 1998). The saturation vapor concentrations of ammonia, nitric acid and hydrochloride acid and the equilibrium concentration of sulfuric acid and hydrogen peroxide are calculated using a thermodynamic model described in Sect. 2.2.8. For the organic compounds the saturation vapor concentrations ($C_{i,s}$) are derived with the 2D-VBS method or the two-product model (see Sect. 2.4), while the actual gas phase concentrations ($C_{i,\infty}$) are saved and updated continuously as separate variables.

The VBS approach (Donahue et al., 2006) and the two-product model (Odum et al., 1996), are based on the partitioning theory from Pankow (1994), which describes the equilibrium gas and particle phase partitioning of organic vapors (see Sect. 2.4). When the VBS model is applied, ADCHEM considers the kinetic (diffusion limited) condensation/evaporation of 110 different organic compounds, while when the two-product model is used the number of condensable organic compounds is 40. Both methods take into account the Kelvin effect and give a particle size dependent partitioning of the different condensable organic compounds, with larger fraction of low volatile compounds found on the smaller particle sizes and a larger fraction of more volatile compounds found on the larger particle sizes. This kinetic and particle size dependent condensation/evaporation requires that ADCHEM keeps track of all the different organic compounds in each particle size bin, which is computationally expensive, especially for the coagulation algorithm.

2.2.3 Coagulation

Coagulation has no direct influence on the total particle mass but is important for the total number concentration, the particle number size distribution and the chemical composition distribution, especially for conditions with high number concentrations of nucleation mode particles and a large accumulation mode which the nucleation mode particles can coagulate onto. In cities such conditions can be found in street canyons near the vehicle emissions. Here coagulation is usually the most important aerosol dynamic process (Jacobson and Seinfeld, 2004). The model used in this article treats primary particle emissions occurring on a spatial resolution of 1 × 1 km^2 and not on the street canyon spatial scale (1–100 m). To account for the initial ageing of the primary particle emissions real-world emission size distributions were used, which take into account the first minutes of ageing from street-canyon to urban background (see Sect. 2.2.5). This decreases the influence of coagulation on the modeled particle number size distribution, but still coagulation needs to be considered for the transformation of the particle number size distribution on longer time scales (hours). The solution of the Brownian coagulation equations is given in Appendix C. Independently if using the full-stationary or moving-center structure, splitting needs to be used to fit the particles back onto the diameter grid.

2.2.4 Dry and wet deposition of particles

The dry deposition of particles is treated as a separate process after the atmospheric diffusion equation has been solved. The dry deposition velocities over land are calculated using a resistance model based on the model by Slinn (1982) (modified by Zhang et al., 2001), while over the ocean the model

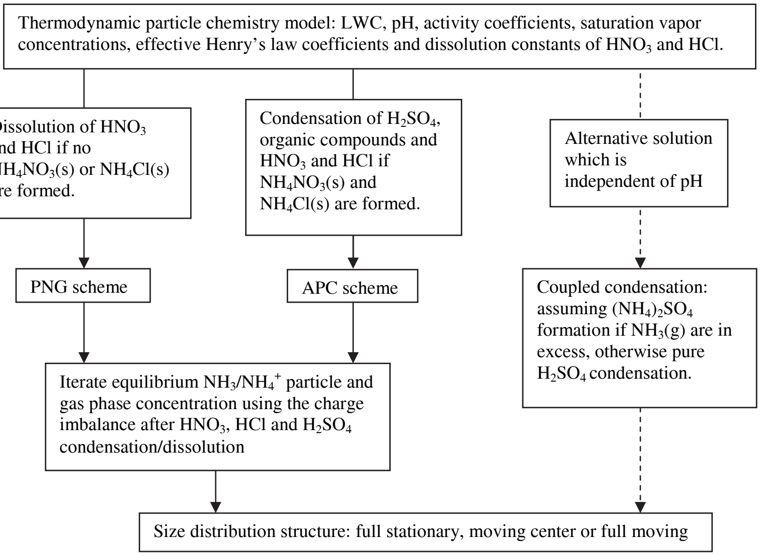

Fig. 2. Schematic picture illustrating the condensation module used in ADCHEM.

by Slinn and Slinn (1980) is used. The particle transport is governed by three resistances in series, the surface layer resistance (r_a), the quasi-laminar layer resistance (r_b) and the surface resistance or canopy resistance (r_c). The dry deposition velocity for large particles also depends on the settling velocity (v_s). If particle losses due to impaction, interception and diffusion are considered to take place in the quasi-laminar layer, the surface resistance can be neglected (Seinfeld and Pandis, 2006). The dry deposition velocity representation is given in Appendix D.

The wet deposition rates (s^{-1}) of different particle sizes are calculated according to the parameterization by Laakso et al. (2003), derived from 6 yr of measurements at Hyytiälä field station in southern Finland. The only input to the wet deposition parameterization apart from the particle diameter is the rainfall intensity in mm h^{-1}. Wet deposition removal of particles is considered for all grid cells below the estimated cloud base and the rainfall intensity was assumed to be constant in the horizontal direction perpendicular to the air mass trajectory. Hence, if the estimated cloud base is above the model domain (more than 2 km a.g.l.) the wet deposition rate is constant within the whole model domain.

2.2.5 Primary particle emissions

Equivalent to the dry deposition the primary particle emissions in the surface layer are treated as a separate process after the atmospheric diffusion equation has been solved. Primary particle emissions included in the model are:

1. marine aerosol emissions,
2. non-industrial combustion,
3. road traffic emissions,
4. ship emissions.

The marine aerosol particle emissions are calculated using the emission parameterization from Mårtensson et al. (2003). The marine particle chemical composition is assumed to be composed of sodium chloride (NaCl) and POA, with NaCl dominating in the coarse mode and organic material dominating in the nucleation and Aitken mode, according to the size resolved chemical analysis of marine aerosol particles at Mace Head during the biological active period (spring, summer and autumn) (O'Dowd et al., 2004).

Size resolved anthropogenic primary particle emissions from non industrial combustion and ship traffic are estimated from PM2.5 mass emissions, by applying an assumed effective particle density of 1000 kg m^{-3} and source specific emission size distributions. The primary particle emissions from road traffic were estimated from NO_x emissions, using a NO_x to particle number conversion factor of 3×10^{14} g^{-1} estimated from data in Kristensson et al. (2004). Table S1 in the Supplement gives the lognormal size distribution parameters used for the road, ship and non industrial combustion emissions. The road emission size distribution was adopted from Kristensson et al. (2004). This particle number size distribution is dominated by a nucleation mode around 20 nm in diameter, which comprises approximately 90 % of the particle number concentration and an accumulation mode around 80 nm in diameter. This type of particle number size distribution is typical for diesel fueled vehicle emissions (Kittelson et al., 2002) which are likely to be the dominating source to the submicron road particle emissions. The nucleation mode particles from diesel engines mainly consist of organic compounds from lubrication oils while the accumulation mode is dominated by non-volatile soot agglomerates coated with organic material (Kittelson et al., 2002). Hence, in this work it was estimated that the nucleation mode particles emitted from road traffic were composed purely of organic material while the emitted accumulation mode particles were composed of soot agglomerates coated with 15 mass percent organic material (POA). The ship emission size distribution was measured by Petzold et al. (2008) and the chemical composition by Moldanová et al. (2009). The non-industrial combustion emissions were assumed to originate entirely from small scale wood combustion. The characteristic particle number size distribution for small scale wood burning emissions was taken from Kristensson (2005) and the chemical composition from Schauer et al. (2001). The emitted anthropogenic primary particle mass not composed of POA or soot was assumed to be composed of water insoluble minerals (metal oxides/hydroxides).

For Denmark and southern Sweden the anthropogenic PM2.5 and NO_x emissions along the trajectories are from Danish National Environmental Research Institute (NERI) and Environmental Dept., City of Malmö (Gustafsson, 2001) respectively (see Sect. 2.3.2). For the rest of Europe the emissions were taken from the European Monitoring and Evaluation Program (EMEP) emission database, for year 2006 (Vestreng et al., 2006). The spatial resolution of the emission data was $50 \times 50\,\mathrm{km}^2$ for the EMEP emissions, $17 \times 17\,\mathrm{km}^2$ for the Danish non-road emissions and $1 \times 1\,\mathrm{km}^2$ for all emissions in southern Sweden and the Danish road emissions.

2.2.6 Aerosol cloud interaction

Clouds are included if the modeled solar irradiance at the surface is larger than the solar irradiance predicted by the HYSPLIT model (Draxler and Rolph, 2011). The altitude of the clouds is determined from the vertical relative humidity profiles along the trajectories, assuming that clouds are present if the $\mathrm{RH} > 98\,\%$. If this relative humidity is not reached within the lower 2000 m of the atmosphere (aerosol dynamics model domain), but the difference between the solar irradiance in ADCHEM (without clouds) and the solar irradiance from the HYSPLIT model still imply that clouds need to be present, the clouds are included above the aerosol dynamics model domain without contact with the modeled aerosol particles. For the case studied in this work the rainfall originated from clouds more than 2000 m a.g.l.

Ideally the cloud droplets number size distribution should be modeled with a dynamic cloud model, which takes into account the meteorological conditions and aerosol properties. However, this would become computationally expensive and the uncertainties concerning the meteorological conditions (e.g. updraft velocity) would make the results uncertain anyhow. For cumulus clouds the cloud droplet diameter typically increases from 7–9 µm at the cloud base to 13–14 µm at the top of the cloud, while for stratus clouds the cloud droplet properties are more uniform within the whole cloud, with usually a narrow droplet distribution which can be approximated with a lognormal or gamma distribution (Rogers and Yau, 1989). Hence, in this work the cloud droplet number size distribution was estimated to be lognormal distributed with a mode diameter of 10 µm and a standard deviation of 1.2 for all conditions. The number of cloud droplets is determined by minimizing the difference between the modeled solar irradiance at the surface, and the solar irradiance from the HYSPLIT model e.g. if the modeled solar irradiance from ADCHEM is larger than given by the HYSPLIT model, the cloud droplet number concentration is increased in ADCHEM until the solar irradiance at the surface is equal with the value given by the HYSPLIT model.

2.2.7 Homogeneous nucleation

For all simulations homogeneous nucleation was included, using the kinetic nucleation theory (Eq. 4) (McMurry and Friedlander, 1979 and Kulmala et al., 2006). Stable nucleation clusters with a particle diameter of 1.5 nm ($N_{1.5\,\mathrm{nm}}$) were assumed to be formed, using a correlation coefficient (K) of $3.2 \times 10^{-14}\,\mathrm{s}^{-1}\,\mathrm{cm}^3$. This value is the median value from measurements at Hohenpeissenberg in Germany (Paasonen et al., 2009).

$$J_{1.5\,\mathrm{nm}} = \frac{dN_{1.5\,\mathrm{nm}}}{dt} = K\,[\mathrm{H_2SO_4}]^2 \qquad (4)$$

2.2.8 Inorganic particle phase chemistry and particle water content

The aerosol dynamics and particle phase chemistry model includes a thermodynamic model. The main purpose of the model is to calculate the saturation vapor pressures (concentrations) of hydrochloride acid, nitric acid and ammonia, and equilibrium concentrations of sulfur dioxide and hydrogen peroxide in the particle or cloud droplet water. In the model it is assumed that the inorganic aerosol particle phase is a pure aqueous solution, even if the relative humidity (RH) in the atmosphere is low. However, if the product of the saturation vapor pressure of ammonia and nitric acid and/or ammonia and hydrochloride acid is lower above a solid ammonium nitrate and/or solid ammonium chloride salt surface than above the aqueous solution, the saturation vapor pressures for ammonia, nitric acid and hydrochloride acid above the solid salt surface are used instead of the saturation vapor pressures above the liquid surface. This method has previously been used by e.g. Zhang and Wexler (2008).

From the modeled particle mole concentrations of ammonium, chloride, sodium, nitrate and sulfate an approximated particle salt composition is estimated for each particle size bin according to the explicit scheme in Appendix E.

Molalities of single salts (m_i^0), for NH_4NO_3, HNO_3, $(NH_4)_2SO_4$, NH_4HSO_4, H_2SO_4, $NaHSO_4$, $(Na)_2SO_4$, NaCl and HCl are calculated according to the parameterizations from Table B.10 in Jacobson (2005b). These parameterizations are high order polynomials as functions of the water activity (a_w). The water mass content (W) in the inorganic particle fraction in each particle size bin is derived using the Zdanovskii-Stokes-Robinson (ZSR) model (Stokes and Robinson, 1966).

The inorganic and organic growth factor (Gf_i and Gf_o) are given by Eqs. (5) and (6), respectively. $V_{\mathrm{p,salt}}$ is the dry particle volume of water soluble inorganic salts and ρ_{water} is the density of water. Using Eq. (6), the organic growth factor is 1.2 when the water activity is equal to 0.9.

$$\mathrm{Gf}_i = \left(\frac{V_{\mathrm{p,salt}} + W/\rho_{\mathrm{water}}}{W/\rho_{\mathrm{water}}} \right)^{1/3} \tag{5}$$

$$\mathrm{Gf}_o = \left(1 + 0.081 \frac{a_w}{(1-a_w)} \right)^{1/3} \tag{6}$$

Once the water content has been calculated the molalities of all ions can be determined. The mean binary solute activity coefficients of each salt in the particle water phase are calculated with the parameters in Table B.9 in Jacobson (2005b). From these binary activity coefficients the mean mixed solute activity coefficients are derived using Bromley's method (Bromley, 1973). The next step is to determine the hydrogen ion concentration in the particle water phase from the ion balance (Eq. 7).

$$\begin{aligned} &[\mathrm{H}^+] + [\mathrm{NH}_4^+] + [\mathrm{Na}^+] = [\mathrm{NO}_3^-] + 2[\mathrm{SO}_4^{-2}] \\ &+ [\mathrm{HSO}_4^-] + [\mathrm{Cl}^-] + [\mathrm{OH}^-] + [\mathrm{HCO}_3^-] + 2[\mathrm{CO}_3^{-2}] \end{aligned} \tag{7}$$

The concentrations in Eq. (7) can be replaced with known equilibrium coefficients, activity coefficients, the partial pressure of CO_2 (390 ppmv), the N(-III) concentration ([NH_3(aq)]+[NH_4^+]), [S(VI)], [N(V)] ([HNO_3(aq)]+ [NO_3^-]) and [Cl(I)] ([HCl(aq)]+ [Cl^-]). The final expression then becomes a 7th order polynomial with [H^+] as the only unknown. The hydrogen ion concentration is given by the maximum real root of this polynomial.

Finally the saturation vapor pressures of ammonia, nitric acid and hydrochloride acid and the equilibrium concentrations of sulfuric acid, and hydrogen peroxide can be determined using the derived hydrogen ion concentration and the mean mixed solute activity coefficients. The saturation vapor pressures (concentrations) are used when solving the condensation/evaporation equation (Eq. 2). The growth rate due to sulfate production, from the reaction between sulfur dioxide and hydrogen peroxide in the particle water phase, is calculated using Eq. (8) (Seinfeld and Pandis, 2006).

$$\frac{d[\mathrm{S(VI)}]}{dt} = \frac{W k_{\mathrm{S(IV)}} [\mathrm{H_2O_2}] \gamma_{\mathrm{H_2O_2}} [\mathrm{HSO_3^-}] \gamma_{\mathrm{HSO_3^-}} [\mathrm{H^+}] \gamma_{\mathrm{H^+}}}{(1 + K_{\mathrm{S(IV)}} [\mathrm{H^+}] \gamma_{\mathrm{H^+}})} \quad (\mathrm{moles\,s^{-1}}) \tag{8}$$

$k_{\mathrm{S(IV)}}$ is the irreversible reaction rate coefficient for the reaction between S(IV) and H_2O_2 in the particle water phase, $K_{\mathrm{S(IV)}}$ is the equilibrium coefficient of S(IV) dissolution and γ_i is the activity coefficient for compound i.

2.3 Gas phase model

The chemical kinetic code included in the gas phase model is solved with MATLABs® ode15s solver for stiff ordinary differential equations. This solver uses an adaptive time step length according to the specified error tolerance. Most of the reactions are taken from the kinetic code used in the model by Pirjola and Kulmala (1998) (originally from EMEP). Some new reactions, mainly concerning the oxidation of benzene, toluene and xylene are also included in the kinetic code. The reaction rates were updated for those of the reactions where new rates were found in the literature (Sander et al., 2006; Seinfeld and Pandis, 2006 and Atkinson et al., 2004). Pirjola and Kulmala (1998) included reactions involving dimethylsulfide (DMS) from the ocean in their model. These reactions were however not considered in the chemical kinetic code used in this work. All natural emission of DMS from the oceans was instead assumed to be sulfur dioxide following Simpson et al. (2003).

The photochemical reactions depend on the spectral actinic flux (photons $\mathrm{cm^{-2}\,s^{-1}\,nm^{-1}}$). The actinic flux is the flux of photons from all directions into a volume of air (Seinfeld and Pandis, 2006). The actinic flux (F_a) is calculated using the radiative transfer model described in Sect. 2.5. The photolysis rates are directly proportional to the actinic flux incident on a volume of air (Cotte et al., 1997). The wavelength (λ) dependent absorption cross sections (σ) and quantum yields (Q) for the different gases undergoing photochemical reactions were found in Sander et al. (2006). Equation (9) below gives the photochemical reaction rates for species A.

$$j_A = \sum_i \sigma_A(\lambda_i, T) Q(\lambda_i, T) F_a(\lambda_i) \Delta\lambda_i \tag{9}$$

2.3.1 Dry deposition and wet deposition of gases

As for the particles the dry deposition velocity of gases depends on an aerodynamic resistance (r_a) and a quasi-laminar resistance (r_b) in series. For gases the surface resistance (r_c), is also needed. The surface resistance depends on the surface structure as well as the reactivity of the gas (Wesely, 1989 and Seinfeld and Pandis, 2006). The model for dry deposition velocity of gases is described in Appendix F.

The below cloud scavenging of SO_2, HNO_3, NH_3, H_2O_2 and HCHO are described by the parameterization used in Simpson et al. (2003). For all other gases the below cloud scavenging was assumed to be an insignificant loss mechanism.

2.3.2 Gas phase emissions

The gas phase chemistry model takes into account emissions of Biogenic volatile organic compounds (BVOCs) and anthropogenic VOC (AVOC) emissions, CO, NO_x, sulfur dioxide and ammonia. The emission data of anthropogenic organic hydrocarbons are not given for each individual species but rather as total Non-Methane Volatile Organic Carbon (NMVOC) emissions. Source specific emissions of non-aromatic hydrocarbons were estimated from the NMVOC emissions, using Table 4.3 in Simpson et al. (2003). The total anthropogenic aromatic hydrocarbon emissions (by Simpson et al. (2003) considered as $O-$xylene emissions) were divided into toluene, xylene and benzene emissions according to the global emissions estimated by Henze et al. (2008). For road traffic emissions 36.7 % of the NMVOC are emitted as aromatic hydrocarbons, while for most of the 9 other emission sources specified in Simpson et al. (2003), the aromatic NMVOC fraction is much smaller. According to Calvert et al. (2002) aromatic hydrocarbons contributes to (∼20–30 %) of the total VOC concentration in urban environments.

The anthropogenic gas phase emissions were adopted from EMEPs emission database for the year 2006 (Vestreng et al., 2006), except for Denmark and southern Sweden where the emissions are from Danish National Environmental Research Institute (NERI) and Environmental Dept., City of Malmö (Gustafsson, 2001) respectively. The EMEP emissions have a spatial resolution of $50 \times 50\,\text{km}^2$, the Swedish emissions have a resolution of $1 \times 1\,\text{km}^2$ and the Danish emissions have a resolution of $1 \times 1\,\text{km}^2$ for road emissions and $17 \times 17\,\text{km}^2$ for all other emission sectors. All emissions were divided into the EMEP emission sectors S1 to S11 as well as ship emissions and natural sulfur dioxide emissions. The yearly emissions were multiplied with country specific diurnal, weekly and monthly emission variation factors based on EMEP's data. The monthly variations in the natural emissions of sulfur dioxide from DMS oxidation were considered using the monthly emission variations from Tarrasón et al. (1995).

The BVOC species considered are isoprene, α-pinene, β-pinene, Δ3-carene and D-limonene based on LPJ-GUESS' ability to assign species-specific emission capacities (e.g., Schurgers et al., 2009b and Arneth et al., 2008), and the monoterpene speciation in Steinbrecher et al. (2009). These species are oxidized by OH, O_3 and NO_3. The products from these reactions are generally less volatile than the initial compounds. Some of them are therefore able to condense after one or several oxidation steps. BVOCs have a relatively short lifetime (minutes to hours) during the daytime in the troposphere (Atkinson and Arey, 2003). Due to the short lifetime of these compounds the concentrations can be considerably higher close to the ground (at the source) than at the top of the boundary layer. Both for the particle and gas phase chemistry it is important to capture the vertical concentration gradient of BVOCs. The emissions of BVOCs from the ground depend strongly on the biomass density and the vegetation species composition, but also on the canopy temperature and for some compounds and vegetation species the photosynthetic active radiation (PAR) (Guenther, 1997).

The emission of BVOCs from different species can either be described as:

1. Volatilization of stored compounds (depend only on temperature when considering short timescales).
2. VOC emissions directly reflecting VOC production (typically varying with temperature and light).

An example of the second case is the light-dependent production of isoprene in the chloroplast. Most monoterpene emissions, particularly those from conifers, are due to volatilization of stored compound (Guenther, 1997), although in recent years light-dependent emissions of non-stored monoterpenes have been found to take place in many broadleaf trees, and may also occur at least from some monoterpene chemical species in conifer (for discussion see Schurgers et al. (2009a) and references therein).

The emissions of stored and synthesized monoterpenes and isoprene were modeled using the vegetation model LPJ-GUESS in combination with isoprene and monoterpene-production linked to their chloroplastic production following Niinemets et al. (1999, 2002). Monoterpene storage and emissions from storage are described in Schurgers et al. (2009a). Short-term variations of modeled emissions display the typically observed light and temperature dependence (Arneth et al., 2007). The model's shortest time step is one day and diurnal course of emissions were calculated from the daily totals following well-established empirical functions for temperature and light-dependencies by Guenther (1997). LPJ-GUESS was applied with 17 tree species and 3 generic shrub and herb types as functional types (Schurgers et al., 2009b). Each of these was associated with an isoprene and monoterpene production potential for standard environmental conditions, implemented as a fractional contribution of photosynthetic electron-transport rate for BVOC production (Niinemets et al., 1999; Arneth et al., 2007). The simulation of tree-species rather than plant functional types allows realistic values of these production capacities to be assigned (Schurgers et al., 2009b). After a 300-year spin-up, the simulation was run for the period 1981–2006 with monthly averaged climate data for Europe from Haylock et al. (2008). For the periods 28 April to 15 October 2005 and 16 May to

28 October 2006 the monthly data were replaced by daily observations to capture the day-to-day variability in emissions. Daily emissions with a spatial resolution of $15' \times 15'$ ($\sim 25 \times 25\,\text{km}^2$) were provided for isoprene and 17 different monoterpene species, the speciation of the monoterpenes was done following Steinbrecher et al. (2009). These emissions from natural vegetation were corrected for the presence of land use with land cover data from Ramankutty et al. (2008).

Since the kinetic code in ADCHEM only includes α-pinene, β-pinene, Δ3-carene and D-limonene, the emissions of all other monoterpenes were distributed among the monoterpenes included in the kinetic code, depending on their emission rates.

2.4 Organic mass partitioning

The secondary organic aerosol formation in ADCHEM can either be modeled with the traditional two-product model approach (Odum et al., 1996), or the recently proposed VBS approach (Donahue et al., 2006 and Robinson et al., 2007). One advantage with the two-product model used in ADCHEM is that it models the SOA formation from source specific organic compounds (e.g. oxidation products of monoterpenes, isoprene, benzene, toluene and xylene) in a computationally inexpensive way.

The VBS scheme lumps all organic species into different bins according to their volatility (given by their saturation concentration (C^*), at 298 K) (Robinson et al., 2007). This method thereby generally loses the information of the chemical reactions which the individual organic compounds are involved in, but is designed to be able to predict realistic SOA formation rates found in the atmosphere using a model with relatively low complexity and only a few model parameters.

Recently, Jimenez et al. (2009) developed a 2D-VBS method which apart from classifying the organic compounds according to their volatility also includes a second dimension, oxygen to carbon ratio (O:C-ratio). This 2D-VBS method is implemented in ADCHEM, with slightly different assumptions which are described in Sects. 2.4.2 and 2.4.3.

Both the 2D-VBS model and the two-product model used in ADCHEM treat the SOA formation as a dynamic process that evolves over time, considering the oxidation agent and SOA precursor concentrations, the time of ageing (exposure time) and meteorological conditions (temperature).

One important difference between the two methods, which influences the dynamic SOA formation, is that the VBS model takes into account the fact that SOA formation generally involves several oxidation steps, while the two-product model simply assumes that it is the initial oxidation step which determines the properties of the final products. Therefore the two-product model used in ADCHEM cannot take into account the fact that more volatile compounds generally need longer time (several oxidation steps) of ageing before they are incorporated into the aerosol particle phase than less volatile compounds.

2.4.1 SOA formation with the two-product model

According to the two-product model developed by Odum et al. (1996) the organic mass partitioning between gas and particle phase can be parameterized as a function of the organic aerosol mass (M_o), using two surrogate compounds with different mass based stoichiometric yields (α_i).

Equation 10 gives the mass fraction (F_i) of the oxidation product $i$which at equilibrium (without curvature effects) will partition into the particle phase. In combination with the Kelvin equation Eq. (10) is used to derive the particle size dependent saturation concentrations which are used in the condensation and evaporation algorithm (See Sect. 2.2.2). $K_{om,i}$ is the partitioning coefficient of product i. Values of α_i and $K_{om,i}$ from Griffin et al. (1999), Svendby et al. (2008), Henze and Seinfeld (2006) and Ng et al. (2007) are given in Table S2 in the Supplement, for all organic oxidation products forming secondary organic aerosol in the model. $K_{om,1}$ and $K_{om,2}$ describes the volatility of the two surrogate oxidation products which represent all the reaction products.

$$F_i = \frac{M_o K_{om,i}}{1 + K_{om,i} M_o} \tag{10}$$

In total the two-product model in ADCHEM considers 40 different surrogate compounds, including 35 compounds for the monoterpene, isoprene, benzene, toluene and xylene oxidation products, two compounds for the non-oxidized intermediate volatile organic carbons (IVOCs) (see Sect. 2.4.4), two compounds for the non-oxidized POA and one non-volatile compound for the IVOC and POA oxidation products (see Table S2). The partitioning coefficients and mass based stoichiometric yields of the two POA compounds were chosen in a way that the volatility should be comparable with what is used in the 2D-VBS (see Sect. 2.4.4).

Benzene, toluene and xylene first react with OH followed by a reaction either with NO, forming products with a low and temperature dependent SOA-yield, or with HO_2, which gives low-volatile products that have a high and temperature independent SOA-yield (at least for $M_o > 10\,\mu\text{g m}^{-3}$). The oxidation products from the HO_2-pathway which form SOA are represented by completely non-volatile surrogate oxidation products (Ng et al., 2007).

At high NO_x/HO_2 ratios, which generally are the case in urban environments, most of the oxidation products react with NO, while at remote regions the HO_2-pathway dominates. Therefore, oxidation of BTX in urban environments generally gives relatively low SOA formation, while moving further away from the source the SOA formation can be considerably higher. Here it is mainly benzene, which is the least reactive of the three compounds, that is left to form SOA (Henze et al., 2008). In ADCHEM both the high- and low-NO_x reaction pathways are considered simultaneously. The fraction reacting through the low-NO$_x$ pathway is given by Eq. (11). The reaction rate for the low-NO$_x$ pathway is given by $k_{RO_2+HO_2} = 1.4 \times 10^{-12}\exp(700/T)\,cm^3$ molecule^{-1} s^{-1} and the reaction rate for the high-NO$_x$ pathway by $k_{RO_2+NO} = 2.6 \times 10^{-12}\exp(350/T)\,cm^3$ molecule^{-1} s^{-1} (the Master Chemical Mechanism v 3.1 (http://www.chem.leeds.ac.uk/Atmospheric/MCM/mcmproj.html)).

$$f_{\mathrm{low-NO_x}} = \frac{k_{RO_2+HO_2}[HO_2]}{k_{RO_2+NO}[NO]+k_{RO_2+HO_2}[HO_2]} \tag{11}$$

The values of the heat of vaporization (ΔH), which gives the temperature dependence of the partitioning coefficients for the two-product model oxidation products from α-pinene, β-pinene, xylene and toluene, were obtained from Svendby et al. (2008). The temperature dependent partitioning coefficients are given by the Clausius Clapeyron relation (Eq. 10) from e.g. Sheehan and Bowman (2001). The heat of vaporization of the compounds formed from oxidation of benzene through the NO-pathway was assumed to be the same as for toluene.

$$K_{om}(T) = K_{om,\mathrm{ref}}\frac{T}{T_{\mathrm{ref}}}\exp\left[\frac{\Delta \mathrm{H}}{R}\left(\frac{1}{T}-\frac{1}{T_{\mathrm{ref}}}\right)\right] \tag{12}$$

2.4.2 SOA formation with the 2D-VBS model

The 2D-VBS scheme used in ADCHEM classifies the organic compounds into 10 discrete volatility bins, separated by powers of 10 in C*, ranging from 10^{-2} to 10^{7}µg m^{-3} and 11 discrete O:C-ratios, separated by 0.1, from 0 to 1 (in total 110 (11 × 10) bins). The mass fraction (F_i) in the particle phase in each volatility bin i is given by Eq. (11) (Donahue et al., 2006) if the Kelvin effect is neglected. Together with the Kelvin equation Eq. (11) is used to derive the particle size dependent saturation concentrations which are used in the condensation and evaporation algorithm (See Sect. 2.2.2).

$$F_i = (1+C_i^*/M_o)^{-1} \tag{13}$$

For compounds with C* equal to 1 µg m^{-3}, Eq. (11) indicates that 50 % of these compounds will be found in the particle phase and 50 % in the gas phase, if the total particle organic mass content (M_o) is equal to 1 µg m^{-3}.

The temperature dependence of C* is given by Eq. (10) if K_{om} is replaced with C*. The heat of vaporization is calculated with a recently proposed expression (Eq. 12) which states that the heat of vaporization can be estimated as a function of the saturation concentration (Epstein et al., 2010). C^*_{300} in Eq. (12) is the saturation concentration at 300 K.

$$\Delta H = -11\cdot\log_{10}C^*_{300}+129 \quad \mathrm{kJ\,mol^{-1}} \tag{14}$$

In the 2D-VBS model used in ADCHEM the traditional SOA precursors (BTX, monterpenes and isoprene) are first allowed to react according to their species specific reaction rates, and then all oxidation products are incorporated into the 2D-VBS. The volatility and O:C-ratio distribution of these first oxidation step reaction products were calculated with the functionalization and fragmentation algorithms used in the 2D-VBS model (see Sect. 2.4.3). The saturation concentrations and O:C-ratios of these primary oxidation products range between 10^7 and 10^1µg m^{-3} and 0 and 0.4, respectively.

Jimenez et al. (2009) assumed that all organic compounds formed after the first oxidation step, react with the OH radical with a gas phase rate constant (k_{OH}) of 3×10^{-11} cm^3 molecules^{-1} s^{-1}, and stated that the heterogeneous oxidation rate of organic compounds in the particle phase is at least 10 times slower. After one or a few oxidation reactions in the atmosphere the oxidation products lose their original signature and become increasingly similar in structure independent of the original molecular structure (Jimenez et al., 2009). Therefore, for all gas phase compounds in the 2D-VBS, the same k_{OH} equal with 3×10^{-11} cm^3 molecules^{-1} s^{-1} as proposed by Jimenez et al. (2009) was also used in ADCHEM. All gas phase compounds in each 2D-VBS bin were also assumed to be oxidized by O$_3$ and NO$_3$ with $k_{O3} = 10^{-17}$ cm^3 molecules^{-1} s^{-1} and $k_{NO3} = 10^{-14}$ cm^3 molecules^{-1} s^{-1} respectively, which are the approximate reaction rates for alkenes (Atkinson, 1997). The heterogeneous reactions were assumed to be insignificant compared to the gas phase reactions, and were therefore neglected.

2.4.3 Functionalization and fragmentation of organic oxidation products

Functionalization is the process by which oxidation reactions create new products with the same carbon number but higher O:C-ratio, while fragmentation creates products with lower carbon number and higher O:C-ratio. In the 2D-VBS model used in ADCHEM the functionalization algorithm was adapted from Jimenez et al. (2009). This algorithm assumes that all functionalization reactions are independent of the properties of the organic reactant. The formed products take-up one to three oxygen atoms, where on molar basis 29 % take-up one oxygen atom, 49 % two oxygen atoms and 22 % three oxygen atoms. Since these oxygen atoms can attach differently to the carbon chain of the original molecule, there are also separate probability functions for the change in volatility (change of C* (ΔC*)) of the products which take-up one, two or three oxygen atoms, varying from -10^1 to -10^7µg m^{-3} (see Table 1). The change in O:C-ratio upon functionalization depends on the number of carbon atoms of the original molecule.

In the 2D-VBS the number of carbon atoms of the surrogate compounds varies between 29 for the bin (C* = 10^{-2}µg m^{-3}, O:C-ratio=0) down to 2.3 for the bin (C* = 10^7µg m^{-3}, O:C-ratio=1). In the 2D-VBS an increase

Table 1. Probability functions for the change in C* when one to three oxygen atoms (O) are added to the organic compounds in the 2D-VBS.

ΔC^* ($\mu g\,m^{-3}$)	-10^1	-10^2	-10^3	-10^4	-10^5	-10^6	-10^7
+1 O	0.30	0.50	0.20				
+2 O		0.19	0.38	0.32	0.11		
+3 O			0.095	0.20	0.41	0.20	0.095

in C* by 10 without changing the O:C-ratio is achieved by removing two carbon atoms from a compound, while an addition of one oxygen molecule decreases the saturation concentration 3.75 times more than if hypothetically one carbon atom is added. These values are in fair agreement with the values given in Pankow and Asher (2008), which estimate that two extra carbon atoms increases the vapor pressure by almost 10 and depending on whether the oxygen atoms form hydroxyl-, aldehyde-, ketone or carboxylic acid- groups the vapor pressure decreases with 2–5 times more than if just adding one carbon atom.

In the 2D-VBS used in ADCHEM all oxidation reactions first follow the functionalization kernel and then a fraction (f) of the formed oxidation products will fragmentize. Equivalent to Jimenez et al. (2009) it is assumed that the molecules that fragmentize have equal probability to split at any of the carbon bonds. Hence, for C11 molecules which fragmentize there will in average be 10 % of all C1 to C10 molecules, on a molar basis. Each of the 2D-VBS bins on the right side of the original molecule (higher C*) bin will therefore receive the same number of molecules, but different masses. Jimenez et al. (2009) assumed that part of the formed fragments have unchanged O:C-ratio while others increase their O:C-ratio. However, in the 2D-VBS used in ADCHEM it was simply assumed that the fragments from the oxidation products (formed from the functionalization reactions) always have the same O:C-ratio as the non-fragmentized molecule. Since the fragments first take up oxygen atoms before they fragmentize, they still always have larger O:C-ratio than the original molecule (before reaction).

One large uncertainty with the VBS model approach is how to estimate the fraction (f) of the oxidation reactions which cause the organic molecules to fragmentize and which fraction that functionalizes. Jimenez et al. (2009) proposed that the fraction of reactions that cause fragmentation at low-NO_x conditions can be given as a function of the O:C-ratio according to Eq. (13). This equation is also used in the 2D-VBS model in ADCHEM, both for low- and high-NO_x conditions.

$$f = \left(\frac{O}{C}\right)^{1/6} \tag{15}$$

The different SOA-yields for benzene, toluene and xylene at low- and high-NO_x conditions are assumed to be caused by the first oxidation reactions, which are considered before the compounds enter the 2D-VBS. To account for the different yields, the benzene, toluene and xylene molecules reacting through the high-NO_x pathway are always assumed to be fragmentized when they are oxidized, while those reacting through the low-NO_x pathway are always functionalized. The monoterpenes and isoprene always follows the low-NO_x pathway, independent of the NO and HO_2 concentrations.

Figure S1 in the Supplement compares the modeled yields with the two-product model parameterization of the measured BTX yields from Ng et al. (2007). For typical atmospheric particle organic mass concentrations (1–10 $\mu g\,m^{-3}$) the BTX yields modeled with the 2D-VBS is about 4–11 % for high-NO_x conditions, while 15–35 % for low-NO_x conditions, at 300 K. This can be compared with the two-product model SOA yields of 5–15 % for benzene, 2–8 % for toluene and 1–4 % for xylene at high-NO_x conditions and 37 % for benzene, 36 % for toluene and 30 % for xylene at low-NO_x conditions.

2.4.4 POA volatility and IVOC emissions

Another key uncertainty with the modeled organic aerosol formation in urban environments is the volatility of the organic emissions traditionally considered to be POA (Shrivastava et al., 2008 and Tsimpidi et al., 2010). Shrivastava et al. (2008) used the 3D-CTM model PMCAMx to model the organic aerosol in the US by either treating these traditional POA emissions as non-volatile ($C^* = 0$) or as semi-volatile (C* between 10^{-2} and $10^4\,\mu g\,m^{-3}$). Their results illustrate that condensation of oxidized organic compounds formed from compounds which first evaporate after dilution and then are oxidized in the atmosphere, has the potential to significantly increase the summertime organic aerosol (OA) in urban environments in the USA. In this work the traditional POA emissions were treated either as non-volatile compounds ($C^* = 0\,\mu g\,m^{-3}$) or as semi-volatile. These semi-volatile POA (SVPOA) mass emissions were divided into different C* channels according to the work by Robinson et al. (2007), Shrivastava et al. (2008) and Tsimpidi et al. (2010). Analogous with Robinson et al. (2007), Shrivastava et al. (2008) and Tsimpidi et al. (2010) the intermediate volatile organic carbon (IVOC) emissions (C* between 10^4 and $10^6\,\mu g\,m^{-3}$), were assumed to be proportional and 1.5 times larger than the POA emissions (see Table S3 in the Supplement).

Recently performed chamber measurements on wood smoke and diesel car POA emissions indicate that the POA may evaporate slowly before reaching an equilibrium with the gas phase (at least 1 h) (Grieshop et al., 2009). The spatial and temporal resolution used in ADCHEM enables the treatment of this mass transfer limited evaporation. Therefore all POA emissions in ADCHEM are initially placed in the particle phase, although they at equilibrium to a large fraction will be found in the gas phase. This enables ADCHEM to study the diffusion-limited evaporation of the SVPOA downwind of the source region, followed by the oxidation of the SVPOA in the gas phase and finally the re-condensation of the oxidized SVPOA several hours after the initial emissions.

2.5 Radiative transfer model

The radiative transfer model is mainly used to calculate the photolysis rate coefficients for the gas phase chemistry model and to estimate the presence of clouds. The radiative transfer model uses the quadrature two-stream approximation scheme, where the radiative fluxes are described with an upward and downward flux component. The phase function and the angular integral of the intensity field are approximated using the asymmetry parameter (g) and single scattering albedo (w_0). The model can be used to calculate the radiative transfer in a vertically inhomogeneous atmosphere with clouds and aerosols (Toon et al., 1989). The asymmetry parameter and single scattering albedo for aerosol particles and cloud droplets are calculated using a Mie-theory model. The radiative transfer model is described more in detail in Appendix G.

3 Methods for urban plume studies

In this section the methods used when modeling the properties of the aerosol particles inside the urban plume from Malmö are described briefly. For a more detailed description of these methods, see Roldin et al. (2011). The model is applied here for one case study, to test the model performance and to illustrate the spatial and temporal variability of the aerosol properties within the urban plume from Malmö.

3.1 Measurements

Particle and/or gas concentrations measured at three different stations in Sweden were either used to validate the model performance or as input to the model. The first station is an urban background station positioned in Malmö (55°36′ N, 13°00′ E, 30 m a.s.l.), the second station is the EMEP background station at Vavihill (56°01′ N, 13° 09′ E, 172 m a.s.l.), about 50 km north from Malmö, and the third station is the EMEP background station at Aspvreten (17° 23′ N, 58°48′ E, 20 m a.s.l.), about 450 km north-east from Malmö. Descriptions of the measurement stations at Vavihill and Aspvreten can be found in Kristensson et al. (2008) and Tunved et al. (2004), respectively.

The selected case study in this article is from the 21 June 2006. Figure 3 displays the selected air mass trajectory for this case. The trajectory was derived with the HYSPLIT model (Draxler and Rolph, 2011). It arrives at 100 m a.g.l. in Malmö, at 6 a.m. and passes over Vavihill background station around 9 a.m. The trajectory starts over England, 48 h upwind of Malmö and end 24 h downwind of Malmö close to Stockholm. Locations A, B and C in Fig. 3 are Malmö, Vavihill and Aspvreten respectively. The trajectory does not pass over Aspvreten, but about 50 km east from the station. Therefore it is unlikely that the urban emissions in Malmö influenced Aspvreten this time of the day. Still the measured ozone level at Aspvreten was used to check if the magnitude of the modeled ozone concentration was reasonable, with the assumption that the background ozone level is relatively uniform over large regional areas.

The particle number size distributions in Malmö and Vavihill were measured with a Scanning Mobility Particle Sizer (SMPS) and a Twin Differential Mobility Particle Sizer (TDMPS). The SMPS system in Malmö measured the urban background particle number size distribution from 10 to 660 nm at a roof top station about 20 m a.g.l., at the town hall in the north-west part downtown Malmö. During southerly air masses this station detects most of the particle emissions from Malmö. A description of the SMPS system in Malmö can be found in Roldin et al. (2011).

The TDMPS system at Vavihill field station measures the rural background particle number size distribution from 3 to 900 nm every 10 min. A detailed description of the TDMPS at Vavihill can be found in Kristensson et al. (2008).

Measured concentrations of NO, NO_2, O_3 and SO_2 at the urban background station in Malmö and O_3 at Vavihill were compared with the modeled gas phase concentrations along the trajectory (for more information about the gas phase measurements see Roldin et al., 2011).

Apart from measured particle and gas concentrations, wind direction measurements from a meteorological mast in Malmö were used to verify that the urban plume from Malmö was directed toward Vavihill. The wind direction was measured at 24 m a.g.l.

3.2 Model input

Vertical temperature and relative humidity profiles, wind speed at two altitudes within the surface layer, rainfall intensity, mixing height and emissions of isoprene, monoterpenes, anthropogenic NMVOCs, NO_x, SO_2, CO, NH_3 and PM2.5 were included along the trajectories.

The meteorological data from the Global Data Assimilation System (GDAS) were downloaded from NOAA Air Resource Laboratory Real-time Environmental Application and Display sYstem (READY) (Rolph, 2011). The rainfall intensity and mixing height data along the trajectory have a spatial

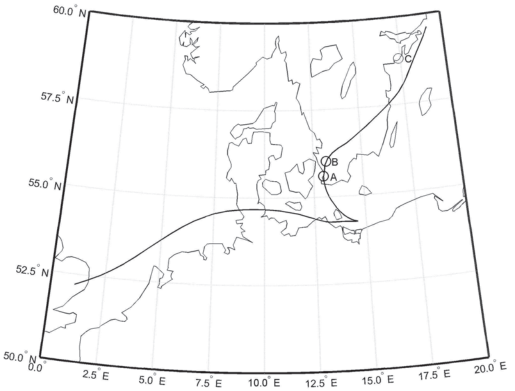

Fig. 3. Map with the air mass trajectory from the HYSPLIT model which was used when the urban plume from Malmö was modeled. The trajectory starts over England 48 h upwind of Malmö. It arrives in Malmö 100 m a.g.l. on the 21 June 2006, at 6 a.m. Downwind of Malmö **(A)** the trajectory moves northward over Sweden. About 3 h downwind of Malmö the trajectory reach Vavihill **(B)** and 18 h downwind of Malmö it passes near the background station Aspvreten **(C)**.

resolution of 1 h and for every three hours, vertical temperature, wind speed and relative humidity profiles were received. The vertical temperature and relative humidity data were linearly interpolated to the fixed vertical grid and the temporal resolution, which were used for the simulations. Figure S2 in the Supplement shows the vertical temperature and relative humidity profiles over Malmö and at 6 and 24 h downwind of Malmö. The meteorological conditions were assumed to be uniform in the horizontal direction perpendicular to the air mass trajectory. The kinematic heat flux is estimated from the horizontal wind speed gradient and potential temperature gradient within the surface layer. The kinematic heat flux is used to calculate the Monin-Obukov length which is applied when deriving the vertical and horizontal eddy diffusivity profiles and the dry deposition velocity.

The initial particle number size distributions in ADCHEM were estimated from the measured background particle number size distribution at Vavihill, according to the method described in Roldin et al. (2011). Initially (48 h upwind of Malmö) the PM2.5 mass fractions of each compound were estimated to be: 0.35 organic material, 0.03 soot, 0.26 sulfate, 0.07 nitrate, 0.12 ammonium and 0.17 minerals (metal oxides/hydroxides) below 1000 m a.g.l. and then changing linearly to the top of the model domain (2000 m a.g.l.), to 0.23 organic material, 0.02 soot, 0.36 sulfate, 0.11 nitrate, 0.17 ammonium and 0.11 minerals. These values are in reasonable agreement with the measured chemical composition at several European sites (Jimenez et al., 2009). The sodium and chloride concentrations were initially set to zero. Because the model is only initiated 48 h upwind of Malmö, these initial particle properties may influence the particle composition within the urban plume from Malmö, especially for the particles larger than $\sim 1\,\mu$m, which have a long lifetime and relatively small sources.

3.3 Spin-up time upwind of Malmö

The total run time of the simulations was 3 days, starting 2 days upwind of Malmö and continuing 1 day downwind of Malmö. The first two days were used to initialize the particle and gas phase chemistry. During these days the particle number size distribution was kept fixed, while everything else were allowed to change. Once the trajectory reached the southern border of Malmö, the estimated local road emission contribution from the particle number size distribution measurements in Malmö, were included according to the method described in Roldin et al. (2011). With this method the modeled particle number size distribution at the measurement station in Malmö become comparable with the measured particle number size distribution at that time. Downwind of the urban background station in Malmö, the particle number size distribution was allowed to change due to the aerosol dynamic processes, and vertical and horizontal mixing.

4 Results and discussion

Results from 23 separate model simulations will be compared and discussed. The simulations were designed to study the influence of: (1) the number of size bins, (2) the size structure methods, (3) aerosol dynamic processes, (4) coupled or uncoupled condensation, (5) the VBS or traditional two-product model for secondary aerosol formation, (6) POA as semi-volatile (SVPOA) or non-volatile, (7) intermediate volatile organic carbon (IVOC) emissions with C^* between 10^4–10^6 μg m^{-3}, (8) the SOA formation from BVOC emissions, (9) the SOA formation from BTX emissions, (10) the influence from all anthropogenic gas phase emissions from Malmö and (11) horizontal and vertical mixing. The model runs are listed below. If not otherwise specified the full-stationary structure with 100 size bins between 1.5 and 2500 nm in diameter was used, the condensation/evaporation was solved as an uncoupled process, both vertical and horizontal mixing was considered, the 2D-VBS method was used for the partitioning of organic compounds between gas and particle phase, POA was assumed to be semi-volatile and IVOC emissions were considered.

1. All processes included (base case)
2. Full-stationary structure with 50 size bins
3. Full-stationary structure with 25 size bins
4. Moving-center structure with 25 size bins
5. Moving-center structure with 10 size bins

6. Combination of full-stationary and moving-center structure with 25 size bins
7. Coupled condensation
8. Two-product model
9. No aerosol dynamic processes
10. No dry deposition
11. No coagulation
12. No condensation
13. No wet deposition
14. No homogeneous nucleation
15. Doubled mixing height.
16. Doubled horizontal turbulent diffusivity
17. 1D model (without horizontal mixing)
18. Non-volatile POA (NVPOA)
19. No IVOC emissions in and downwind of Malmö
20. No BVOC emissions in and downwind of Malmö
21. No anthropogenic gas phase emissions over Malmö (no NO_x, SO_2, NMVOCs and IVOCs emissions)
22. No BTX emissions in and downwind of Malmö
23. Unity mass accommodation coefficients

4.1 Physical particle properties

In Fig. 4a–b the modeled particle number size distributions at Vavihill (3 h downwind of Malmö) and 24 h downwind of Malmö, for different number of size bins and size structure methods, are compared. Given is also the measured particle number size distribution at Vavihill, at the time of arrival of the air mass trajectory. The results are from the center of the urban plume at the surface. At Vavihill (Fig. 4a) all simulations are in good agreement with each other and the measured particle number size distribution. This illustrates that for short time scales (a few hours) the model results are fairly insensitive of the number of size bins and which size structure method that is used, especially if the condensation or evaporation rates are small. 24 h downwind of Malmö (Fig. 4b) the difference between the simulations becomes more evident. This is especially the case for the moving-center method and the full-stationary method when using 25 size bins. For the full-stationary method with 25 size bins, the numerical diffusion significantly broadens the size distribution (see Sect. 2.2.1). With the moving-center method errors can appear when particles from the lower size bins are averaged with the particles in higher size bins, which causes some bins to get too low concentrations (zero concentration) while bordering size bins get too high concentrations. In Fig. 4b this can be seen around 600 nm in diameter. For the moving-center method this problem is solved by decreasing the number of size bins, while for the full-stationary method the accuracy increases with the number of size bins. Figure 4a–b also shows the result from one simulation with 25 size bins, where the moving-center method was used except once every 360th time step (6 h) when the full-stationary method was used. This combination of the two methods gave much smaller numerical diffusion than the full-stationary method and still eliminated the problems seen with the moving-center method.

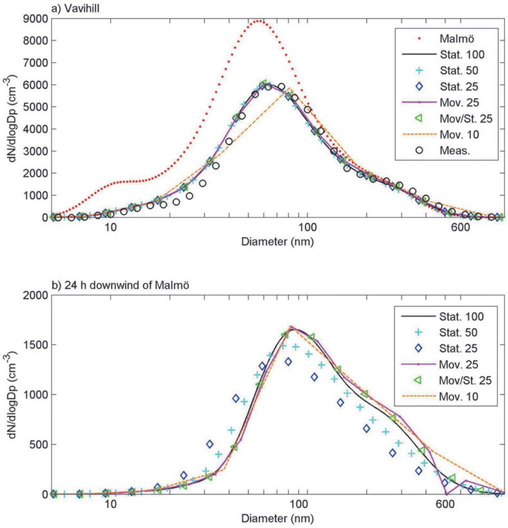

Fig. 4. Modeled particle number size distributions in the center of the urban plume at Vavihill **(a)** and 24 h downwind of Malmö **(b)**, using different size structure methods. The results are from the simulations with the full-stationary structure using 100, 50 or 25 size bins, moving-center structure with 25 or 10 size bins and a combination of the moving-center method and full-stationary method using 25 size bins (Mov/St). Panel **(a)** also displays the modeled (fitted) particle number size distribution at the measurement station in Malmö and the measured particle number size distribution at Vavihill.

Figure 5a–b compares the modeled particle number size distributions with or without different aerosol dynamic processes at Vavihill and 24 h downwind of Malmö. The result without wet deposition is only given at 24 h downwind of Malmö since no rainfall affected the size distribution between Malmö and Vavihill. About 2 h downwind of Vavihill a light rainfall (~0.5 mm h^{-1}) started and continued for a few hours, which affect the size distribution 24 h downwind of Malmö. The rainfall intensity was assumed to be constant within the whole model domain.

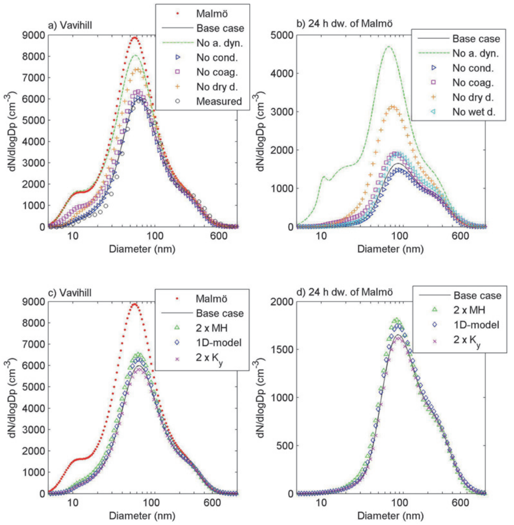

Fig. 5. Modeled particle number size distributions in the center of the urban plume at Vavihill (**a** and **c**) and 24 h downwind of Malmö (b and d), without different aerosol dynamic processes (**a** and **b**) and changed vertical or horizontal mixing (**c** and **d**). Panels **(a)** and **(b)** give the results from the simulations with all aerosol dynamic processes included (base case), no aerosol dynamic processes, no condensation, no coagulation, no dry deposition and no wet deposition (only in **b**)). Panels **(c)** and **(d)** display the results from the base case simulation, doubled mixing height (MH), no horizontal mixing (1D-model) and doubled horizontal mixing (2 × K_y). In **(a)** the modeled (fitted) particle number size distribution at the measurement station in Malmö and the measured particle number size distribution at Vavihill is also illustrated.

The aerosol dynamic processes with largest influence on the particle number concentration both at Vavihill and 24 h downwind of Malmö was dry deposition. The reason for this is mainly the relatively few nucleation mode particles. Condensation and evaporation had little influence on the results at Vavihill but larger influence on the size distribution 24 h downwind of Malmö. Using unity mass accommodation coefficients for all condensable compounds instead of the values given in Sect. 2.2.2 had negligible impact on the modeled particle number size distribution and chemical composition (not shown). The primary particle emissions between Malmö and Vavihill had a marginal impact on the size distribution below 30 nm which can be seen when comparing the initial particle number size distribution and the results without aerosol dynamic processes.

When not considering aerosol dynamic processes the size distribution was almost preserved between Malmö and Vavihill. This illustrates that on short time scales, vertical and horizontal mixing had little influence on the model results in the center of the urban plume. For the vertical mixing, this is mainly due to the low and constant boundary layer height at 300 m between Malmö and Vavihill. An increasing mixing height effectively dilutes the boundary layer. This explains why the number concentration is significantly lower 24 h downwind of Malmö than in the city, even without any aerosol dynamic processes.

The homogeneous nucleation downwind of Malmö had a marginal impact on the modeled particle number size distribution above 5 nm in diameter, within 24 h downwind of Malmö (not shown). The main reason for this was probably not the formation rate ($J_{1.5\,\mathrm{nm}}$) which reached a maximum of about 1 s^{-1} within the boundary layer during the afternoon. Instead the limiting factors were likely the diameter growth rate of the smallest particles and the relatively large coagulation sink. The growth rate of the smallest particles is determined by the concentrations of low-volatile compounds (e.g. H_2SO_4 and some organic compounds). Unfortunately the amount and origin of the low-volatile organic compounds which can contribute to the initial growth of these particles are not well known. Therefore it is not possible to dismiss the possibility that the model significantly underestimated the growth rate of the particles below 5 nm in diameter.

Figure 5c–d illustrate the modeled particle number size distributions at Vavihill and 24 h downwind of Malmö from the simulations with doubled mixing height (MH), no horizontal mixing (1-D model) and doubled horizontal eddy diffusivity (2 × K_y). When doubling the mixing height the particle number concentration became slightly higher. This is mainly due to the decreasing influence of dry deposition. It is important to mention that the initial particle number size distribution in Malmö within the whole boundary layer was assumed to be the same for both mixing heights.

Figure 6 shows the modeled particle number concentration (PN) within the whole 2-dimentional model domain (2 km × 20 km) at different distances (times) downwind of Malmö. At Vavihill (Fig. 6a) the concentration difference between the background and the urban plume is still distinct both in the vertical and horizontal direction. The explanation to this is that the atmospheric stability prevented large horizontal dispersion and the mixing height in the model was fixed at 300 m a.g.l. between Malmö and Vavihill, which prevented significant vertical dilution. Downwind of Vavihill (between 10 a.m. and 12 a.m.) the mixing height in the model rose to 1000 m which effectively diluted the boundary layer. During the evening (4 p.m. until 9 p.m.) the mixing height decreased to 300 m and a stable residual layer was created. The residual layer can be distinguished 12 h downwind of Malmö as a horizontal streak with higher particle number concentrations between 700 and 1000 m a.g.l. (Fig. 6b). This concentration difference was even more pronounced 24 h downwind of Malmö (Fig. 6c). The increasing concentration difference between the boundary layer and the residual layer was caused by the dry deposition losses in the well mixed boundary layer. 24 h downwind of Malmö, when

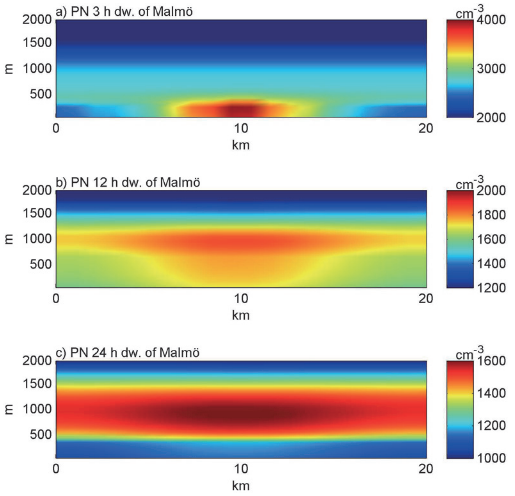

Fig. 6. Modeled total particle number concentration (PN) **(a)** 3 h downwind of Malmö, **(b)** 12 h downwind of Malmö and **(c)** 24 h downwind of Malmö, in the whole model domain (20 km in the horizontal and 2 km in the vertical direction) perpendicular to the air mass trajectory. Vavihill (VVHL) is position in the center of the horizontal model domain 3 h downwind of Malmö.

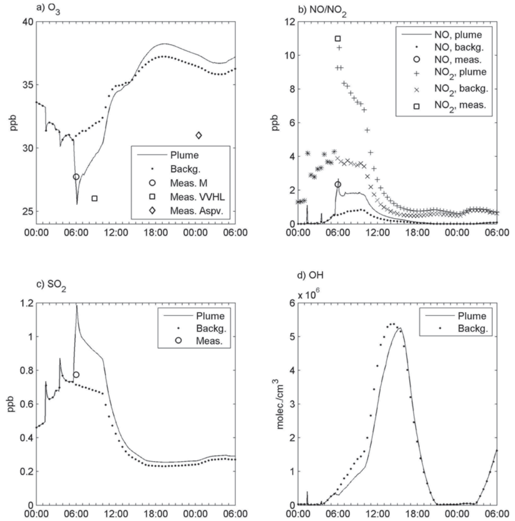

Fig. 7. Modeled concentrations of **(a)** O_3, **(b)** NO and NO_2, **(c)** SO_2 and **(d)** OH at the surface, from 6 h upwind of Malmö (00:00) to 24 h downwind of Malmö (06:00), in the center of the urban plume and outside the urban plume. Given are also the measured O_3 concentrations in Malmö, at Vavihill and at Aspvreten, and the measured NO, NO_2 and SO_2 concentrations in Malmö.

parts of the residual layer had been separated from the surface for up to 12 h, the concentration gradient between the boundary layer (0–300 m) and residual layer (300–1000 m) was much larger than the concentration gradient between the center of the urban plume and the horizontal boundaries (Fig. 6c).

4.2 Chemical gas and particle phase properties

All the measured gases (NO, NO_2, O_3 and SO_2) were well captured by the model in Malmö, when considering the anthropogenic gas phase emissions in the city (Fig. 7). Unfortunately O_3 was the only gas phase compound that was measured with high time resolution at Vavihill and Aspvreten. The modeled O_3 concentration agrees very well with the measured concentrations at Malmö. At Vavihill and Aspvreten the model seems to overestimate the O_3 concentration with 10–20 %.

The modeled PM2.5 mass of ammonium, nitrate, sulfate, organic material and soot, from one hours upwind of Malmö until 24 h downwind of Malmö are given in Fig. 8a. At Malmö there was a significant increase in the soot mass and to a smaller extent the organic mass because of the primary particle emissions in the city. This primary particle mass increase is constrained by the measurements at the urban background station in Malmö (see Sect. 3.3). The soot particle mass emitted in Malmö was primarily lost by dry deposition between Malmö (6 a.m.) and 10 a.m. After this the mixing height rose steeply, which effectively diluted the boundary layer (see e.g. Fig. 10e).

A large fraction of the organic particle mass consists of semi-volatile compounds which can be transported to or from the particle phase when the temperature or concentrations changes (see Fig. 12). Still, the modeled organic PM2.5 mass shows no visible correlation with the semi-volatile ammonium nitrate content. The reason for this is that it was the relative humidity and not the temperature fluctuations which mainly were responsible for the large changes in the PM2.5 ammonium nitrate content. In the model all organic compounds were assumed to be water insoluble and therefore the organic particle mass was not directly affected by the relative humidity. When considering coupled condensation, the particle nitrate content was smaller while the ammonium content was about the same as for the uncoupled condensation simulations. The reason for this is that the particles were not fully neutralized with the uncoupled condensation simulations (between 50 and 20 % of the sulfate was in the form of bisulfate (HSO_4^-) and the rest SO_4^{-2}, with least neutralized particles 24 h downwind of Malmö).

Figure 8b–c illustrates the modeled mass size distributions of the major particle compounds. Noticeable is that the nitrate content is shifted toward larger particle sizes when using uncoupled condensation while the organic mass is mainly

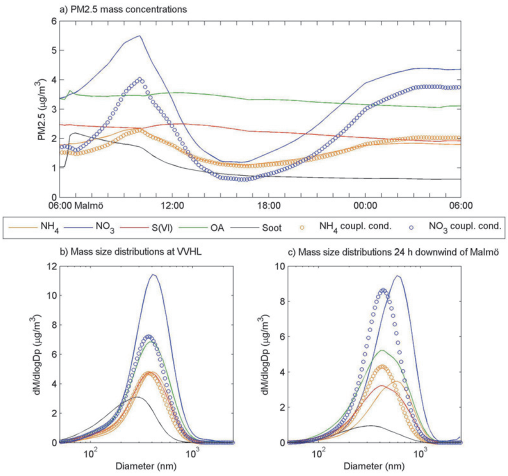

Fig. 8. **(a)** Modeled PM2.5 ammonium, nitrate, sulfate, organic aerosol (OA) and soot masses from 1 h upwind of Malmö (05:00) until 24 h downwind of Malmö. For ammonium and nitrate results are shown both from the uncoupled and coupled condensation simulations. Panels **(b)** and **(c)** gives the modeled particle mass size distributions of the different compounds at Vavihill and 24 h downwind of Malmö.

found on smaller particles. This is especially pronounced 24 h downwind of Malmö. Similar separation of particulate nitrate and organic material on different particle sizes are commonly observed with aerosol mass spectrometer (AMS) at Vavihill (Roldin et al., 2011). The reasons for this will be discussed below.

Figure 9 gives the size resolved mass fractions of ammonium, nitrate, sulfate, sodium, soot and organic material and the pH, in each size bin, from the base case simulation. Ammonium and nitrate were well correlated above 100 nm in diameter and cycle between the accumulation mode and the gas phase, mainly driven by the relative humidity fluctuations. Downwind of Malmö the sulfate was mainly found in the Aitken and accumulation mode while the organic material dominated in the nucleation and Aitken mode, comprising between 50 and 90 % of the total mass below 50 nm in diameter, except in and near Malmö where the Aitken mode particles mainly were composed of soot. The pH of the aerosol particle water content varied with the size of the particles, from about 1 in the nucleation mode to 2.5 in the coarse mode. These pH-values can be compared with the pH of fully neutralized water of 5.6 (at 380 ppmv CO_2). The main reason why the pH increases with the particle size is that the condensation growth rate of sulfuric acid is independent of the pH and the relative molar condensation growth rate is proportional to the Fuchs-Sutugin-corrected aerosol surface area (approximately proportional to the particle diameter) and not to the particle volume. Since the diameter to volume ratio increases with decreasing particle size, the sulfate concentration in the particle water phase decreases with increasing particle diameter. The lower hydrogen ion concentration in the larger particles explains why the nitrate was shifter toward larger particles when using uncoupled condensation but not when using coupled condensation (no pH dependence).

Figure 10 gives the modeled vertical PM2.5 mass profiles of different chemical compounds, in the center of the model domain, 6 h upwind of Malmö until 24 h downwind of Malmö. The mixing height is also illustrated. As a complement to Fig. 10, Fig. S4 in the Supplement shows the gas phase concentrations of ammonia, nitric acid, sulfuric acid and NO_x in the vertical direction. The PM2.5 nitrate and ammonium masses have a maximum 4 to 6 h downwind of Malmö in the whole boundary layer, caused by the high relative humidity at that time (∼90 %). In contrast, the gas phase ammonia and nitric acid show a different pattern with maximum concentrations upwind of Malmö. The PM2.5 sulfate content was larger above the boundary layer over Malmö than in the boundary layer. The organic PM2.5 mass was highest near the ground and up to about 1200 m which was approximately the maximum altitude of the boundary layer upwind and downwind of Malmö. The soot mass increased quickly over Malmö within the boundary layer but was effectively diluted when the mixing height rose steeply around 10 a.m. As expected the NO_x concentration (Fig. S4d) is well correlated with the soot particle mass. The reason for this is that both compounds mainly originate from the diesel fueled vehicle emissions in Malmö.

4.2.1 Organic particle content

Figure 11 displays the PM2.5 organic mass difference between the base case simulation and the following case studies: (1) without anthropogenic gas phase emissions in Malmö, (2) without BTX emissions in and downwind of Malmö, (3) without IVOC emissions in and downwind of Malmö, (4) no BVOC emissions in and downwind of Malmö, (5) Non-volatile POA (NVPOA) instead of SVPOA and (6) the two-product model instead of the 2D-VBS.

As a result of the lower OH concentration and higher NO concentration induced by the anthropogenic gas phase emissions in Malmö (see Fig. 7), the modeled organic PM2.5 mass becomes larger without anthropogenic gas phase emissions in Malmö for the first 10 h downwind of Malmö. However, more than 10 h downwind of the city the organic PM2.5 mass becomes slightly higher for the base case.

As expected the simulations without BTX, IVOC or BVOC emissions, all give lower organic mass than the base case simulation. One major difference between the BTX and the IVOCs is that the IVOCs generally only need to be oxidized one or two steps, while BTX need at least two oxidation steps, before they are low-volatile enough to form

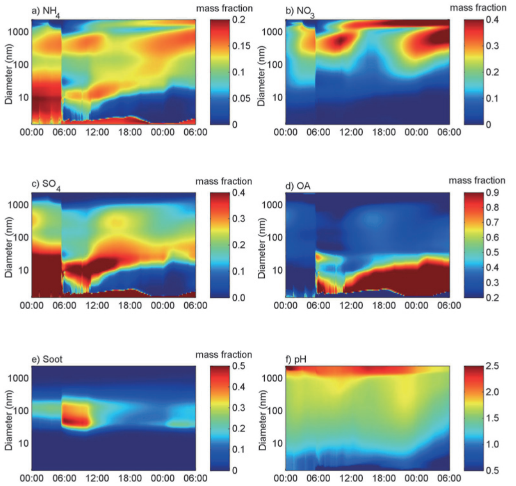

Fig. 9. Modeled size resolved particle mass fractions and pH in each size bin, starting 6 h upwind of Malmö (00:00) and ending 24 h downwind of Malmö, **(a)** for ammonium, **(b)** nitrate, **(c)** sulfate, **(d)** organic aerosol, **(e)** soot and **(f)** pH.

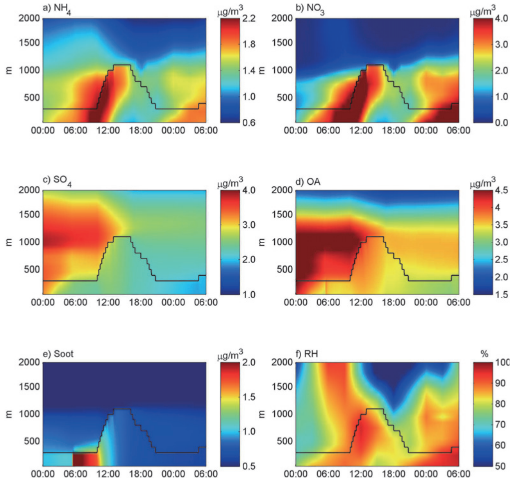

Fig. 10. Modeled PM2.5 masses of ammonium **(a)**, nitrate **(b)**, sulfate **(c)**, organic aerosol **(d)**, soot **(e)** and the relative humidity **(f)**, from 6 h upwind of Malmö (00:00) until 24 h downwind of Malmö, in the vertical direction (0–2000 m a.g.l.), in the center of the urban plume. The mixing height along the trajectory is also displayed.

SOA. Therefore the IVOC emissions from Malmö mainly increased the organic mass within 6 h downwind of the city (during the morning) while the BTX oxidation products (dominated by xylene oxidation products) mainly formed ASOA between 6 and 12 h downwind of the city (during the afternoon). During the evening and night (15–22 h downwind of the city) the OH concentration was very low (Fig. 7d) and therefore little ASOA was formed during this time period. 24 h downwind of Malmö the IVOC and BTX emissions from Malmö contributed to approximately 0.1 $\mu g\,m^{-3}$ of the modeled organic PM2.5 mass, 24 h downwind of the city. This can be compared with the biogenic SOA formation from the BVOC emissions from the Swedish forest of 0.35 $\mu g\,m^{-3}$, 24 h downwind of Malmö.

Although the uncertainties are large, especially for the IVOC emissions, and the daily variability in the BVOC emissions can be considerable, these results indicate that during the summer months the ASOA formation more than a few hours downwind of Malmö is small compared to the BSOA which is formed from the Swedish forest emissions.

The uncertainties concerning the modeled organic aerosol mass is not just related to the SOA formation but also the magnitude of the POA emissions and the volatility of these emissions. If treating the POA emissions in and downwind of Malmö as non-volatile instead of semi-volatile, the POA mass becomes larger at and near the emission source (see Fig. 11). If the POA is considered to be semi-volatile, part of it will evaporate from the particle phase, within a time scale of approximately one hour after the emissions. The compounds are then oxidized in the atmosphere and form less volatile oxidized organic compounds which can condensate on the available particle surfaces. For the 2D-VBS model simulations, most of these compounds returned to the particle phase between 4 to 7 h downwind of Malmö, and more than 7 h downwind of the city, the organic PM2.5 mass from the base case simulation even exceeded the simulation with NVPOA (see Fig. 11). There are at least two reasons why the organic mass becomes larger with SVPOA instead of NVPOA. One reason is that the dry and wet deposition losses of organic gas phase compounds are insignificant compared to the dry and wet deposition losses of particles. Hence, the evaporated POA found in the gas phase will not be deposited before it re-condensates. A second reason is that the molar mass of the organic compounds increases when they are oxidized in the atmosphere.

Apart from the uncertainties related to the magnitude of the POA and SOA precursor emissions and their volatility, the model results also depend on the structure of the organic partitioning model (see Sect. 2.4). In Fig. 11 the difference in organic PM2.5 mass between the two-product model and 2D-VBS model base case simulation is displayed. The overall difference is relatively small and within the range of variability related to the POA volatility, and BVOC and anthropogenic VOC emissions. However, the dynamics of the organic mass formation downwind of Malmö is substantially different. Within 4 h downwind of the city the difference in the organic PM2.5 mass between the base case and the

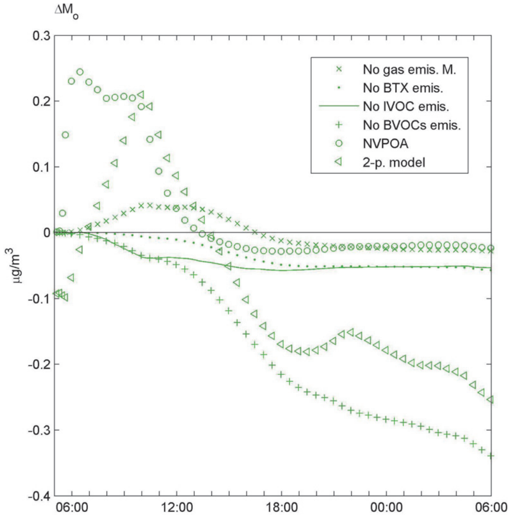

Fig. 11. Modeled organic PM2.5 mass difference (ΔM_o) between the base case and the following case studies: (1) without any anthropogenic gas phase emissions in Malmö, (2) no BTX emissions in and downwind of Malmö, (3) no IVOC emissions in and downwind of Malmö, (4) no BVOC emissions downwind of Malmö, (5) with NVPOA in and downwind of Malmö and (6) the two-product model simulation.

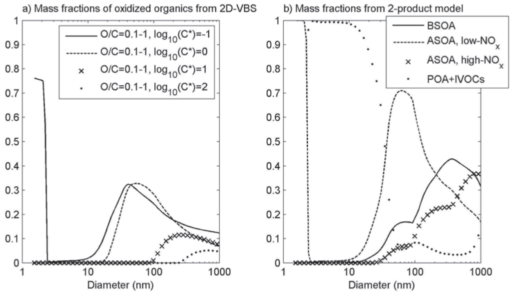

Fig. 12. **(a)** Size resolved organic mass fractions of oxidized compounds (O:C-ratio between 0.1 and 1) with different saturation concentrations (C*). The results are from the base case simulation with the 2D-VBS model, 24 h downwind of Malmö. **(b)** Size resolved mass fractions of BSOA, ASOA from BTX oxidation through the low- and high-NO_x pathway, and POA and IVOC oxidation products. The results in **(b)** are from the two-product model simulation, 24 h downwind of Malmö.

two-product model simulations changes from $-0.1\,\mu g\,m^{-3}$ to $0.2\,\mu g\,m^{-3}$. The main reason for this is the faster recondensation of the evaporated POA and condensation of the IVOCs oxidation products with the two-product model compared to the 2D-VBS model (base case).

Both with the 2D-VBS model and the two-product model ADCHEM considers the diffusion limited condensation and evaporation of organic compounds with a wide range of volatilities. Because of the Kelvin effect more volatile compounds are shifted toward larger particle sizes than less volatile compounds. The least volatile compounds ($C^* < 10^{-1}\mu g\,m^{-3}$) which condense onto the Fuchs-Sutugin-corrected aerosol surface area size distribution evaporate slowly, while more volatile compounds ($C^* > 10^1\,\mu g\,m^{-3}$) quickly condensate and evaporate from the particle surfaces until equilibrium between the gas phase and all particle sizes is reached.

In Fig. 12a the size resolved organic mass fractions of oxidized compounds (O:C-ratio between 0.1 and 1) with different volatility (C*) are displayed. The model results are from the base case model run with the 2D-VBS model, 24 h downwind of Malmö. The oxidized organic compounds originate from gas phase compounds or from POA which has evaporated. As a consequence of the Kelvin effect, the oxidized organic compounds are distributed differently depending on their volatility. For instance the compounds with C* equal to 10 are not found on particles smaller than 100 nm in diameter while compounds with C* equal to 0.1 are even found on the nucleation mode particles below 2 nm in diameter.

Figure 12b gives the size resolved organic mass fractions of BSOA, ASOA from BTX oxidation products formed through the high- or low-NO_x pathway, and POA and IVOCs oxidation products, modeled with the two-product model. In the two-product model the BTX oxidation products formed through the low-NO_x pathway are assumed to be non-volatile ($C^* = 0$). Hence, these organic compounds are not affected by the Kelvin effect and can condensate even on the smallest particle sizes. The POA dominated over the SOA in the size range between 3 and 30 nm but contributed to less than 10 % of the organic mass content between 50 and 1000 nm in diameter. The BSOA and ASOA compounds formed from the BTX oxidation through the high-NO_x pathway have variable volatility but none of these compounds is completely non-volatile. The BSOA is mainly found on particles larger than 100 nm in diameter but a smaller fraction of less volatile compounds is also found on the particles between 10 and 100 nm in diameter. The ASOA formed from the BTX oxidation through the high-NO_x pathway is separated into three distinct volatility classes. The least volatile of these compounds are found on particle sizes down to 30 nm in diameter, an intermediate volatile class of compounds is found on particles larger than 100 nm in diameter and the most volatile compounds are mainly distributed onto particles larger than 300 nm in diameter.

5 Summary and conclusions

In this work a trajectory model for Aerosol Dynamics, gas phase CHEMistry and radiative transfer calculations (ADCHEM) was developed and evaluated. The model considers both vertical and horizontal dispersion perpendicular to an air mass trajectory. The Lagrangian approach makes the model computationally faster than available regional 3D-CTMs. This enables a more detailed representation of the aerosol dynamics, gas and particle phase chemistry with size resolved partitioning of 110 different organic compounds and a fine spatial and temporal resolution. These features make it well suited for modeling of ageing processes relevant for climate and population health, from local to regional scales. Possible ADCHEM applications are:

- Studies of particle size dependent condensation and evaporation of semi-volatile gas phase species (e.g. HNO_3, NH_3, HCl and oxidation products of VOCs).
- Modeling the urban influence on the oxidizing capacity of the atmosphere (e.g. ozone, OH, HO_2, NO_3, NO concentrations affecting the ASOA and BSOA formation).
- Transformation of real-world size-resolved primary particle emissions to a grid scale treated by regional and global 3D-CTMs, accounting for sub-grid scale processes.
- Studies of new particle formation and growth within urban plumes or large scale regional nucleation events.
- Estimating the urban influence on cloud condensation nuclei (CCN) properties (indirect effect).
- Studies of the urban emissions influence on the aerosol optical properties and radiative balance (direct effect).
- Population exposure and respiratory dose studies.

When using more than 50 size bins between 1.5 and 2500 nm the full-stationary method gave relatively little numerical diffusion, while when using only 10 size bins the moving-center method which almost eliminates numerical diffusion was a better choice. When using 25 size bins neither of these two methods was ideal, but a combination of the two methods gave good representation of the particle number size distribution.

The dry deposition together with the vertical dilution when the mixing height increases were the processes with largest influence on the particle number size distribution and number concentration downwind of Malmö. Hence, together these processes effectively decrease the horizontal and vertical particle number concentration gradient between urban plume and the background. During the night when a residual layer is formed the dry deposition causes a significantly lower particle number concentration within the boundary layer compared to the residual layer.

When using uncoupled condensation, significantly more particle phase nitrate was formed than if assuming coupled condensation. The particle nitrate is also shifted towards larger particle sizes with uncoupled condensation compared to coupled condensation. These differences occur since the aerosol particles were not fully neutralized and the pH increases with the particle size. This illustrates that coupled condensation should not be used if the aerosol particles are not fully neutralized.

For the considered case study the air mass trajectory spent much time over the ocean upwind of Malmö (see Fig. 3). Here there are no or very small emissions of ammonia but relatively large emissions of SO_2 from ship traffic. This can explain why the aerosol particles were not fully neutralized. If the air mass instead would have been traveling over large agricultural areas in Europe the aerosol would likely have been more neutralized and the agreement between the uncoupled and coupled condensation simulations would have been better.

The 2D-VBS model and the two-product model in ADCHEM consider the diffusion limited condensation and evaporation of 110 and 40 organic compounds respectively, with a wide range of volatilities. This gives a realistic particle size dependent and dynamic organic mass partitioning which cannot be treated by available equilibrium models. The dynamic and size resolved organic mass partitioning is especially important during the ageing of SVPOA, which starts with diffusion limited evaporation, followed by oxidation reactions in the gas phase and then finally the re-condensation of the formed oxidized organic compounds. Unfortunately, it is computationally expensive to keep track of all organic compounds in each size bin and each grid cell, and hence this dynamic and size resolved partitioning of organic compounds can probably not be used in available regional 3D-CTMs.

Lane et al. (2008) compared the modeled organic aerosol from the PMCAMx 3D-CTM using the two-product model or VBS approach and concluded that the model framework (e.g. two-product model or VBS) is less important than the parameters used in the model (e.g. saturation concentrations and yields). The good agreement of the total organic particle mass found between 2D-VBS and the two-product model simulations in this study support this finding. However, since the two-product model used in ADCHEM assumes that it is the first oxidation reaction that is rate limiting and determines the properties of the final products, the dynamics of the organic mass formation downwind of Malmö cannot be as precisely represented as with the 2D-VBS model. The largest advantage with the two-product model compared to the 2D-VBS model is that the simplified oxidation mechanism makes it computationally feasible to keep track of the origin to the formed OA (e.g. if it is BSOA, ASOA or POA). Hence, the two-product model and the 2D-VBS models used in ADCHEM are good complement to each other, and the choice of model should be made according to the type of application.

For more information about the Malmö emissions influence on climate relevant particle properties within the urban plume, the reader is referred to Roldin et al. (2011), where ADCHEM is applied to 26 trajectories for the period April 2005 to October 2006.

Appendix A

Atmospheric diffusion

The kinematic heat flux (F_{H}) is used in the model when calculating the eddy diffusivity coefficients and the dry deposition velocities. The kinematic heat flux in the surface layer can be approximated with Eq. (A1) (Stull Appendix H, 2000).

$$F_{\mathrm{H}} = -K_{\mathrm{H}} \cdot \frac{\Delta\theta}{\Delta z}, \quad K_{\mathrm{H}} = \kappa^2 \cdot z^2 \cdot \left|\frac{\Delta v}{\Delta z}\right| \tag{A1}$$

v is the horizontal wind speed, κ is the von Kármán constant, K_{H} is the heat eddy viscosity, z is the altitude and θ is the potential temperature.

The eddy diffusivity in the vertical direction in the boundary layer is calculated using Eqs. (A2), (A3) and (A4) for stable, near neutral and unstable conditions, respectively. Equation (A2) is adopted from Businger and Arya, 1974, Eq. (A3) from Myrup and Ranzieri, 1976 and Eq. (A4) from Tirabassi and Rizza, 1997. Above the boundary layer the eddy diffusivity is approximated using Eq. (A2).

$$K_z = \frac{\kappa u_* z}{0.74 + 4.7(z/L)} \exp\left(\frac{-8fz}{u_*}\right) \qquad \frac{h}{L} > 10 \tag{A2}$$

$$K_z = \begin{cases} \kappa u_* z & \frac{z}{h} < 0.1 \\ \kappa u_* z(1.1 - \frac{z}{h}) & 0.1 \le \frac{z}{h} \le 1 \end{cases} \qquad -10 \le \frac{h}{L} \le 10 \tag{A3}$$

$$K_z = \kappa w_* z\left(1 - \frac{z}{h}\right) \qquad \frac{h}{L} < -10 \tag{A4}$$

h is the mixing height, u_* is the friction velocity, f is the Coriolis parameter, L is the Monin-Obukhov length and w_* is the convective scaling velocity.

The horizontal eddy diffusivity is estimated using Eq. (A5), if the flux Richardson number is negative (unstable atmosphere) (Seinfeld and Pandis, 2006). If the atmosphere is stable the horizontal diffusivity is set as two times the largest vertical eddy diffusivity (Tirabassi and Rizza, 1997).

$$K_y = 0.1 w_* h \tag{A5}$$

Appendix B

Numerical solution to the atmospheric diffusion equation

The atmospheric diffusion equation (Eq. 1) is discretized using the second order five-point formula (Eq. B1).

$$\begin{aligned} &\text{For} \quad \text{k=1,....N}, \quad \text{n=1,....N} \\ &\frac{\Delta c}{\Delta t}_{k,n} = \frac{1}{\Delta z^2}\left(K_{z,k-\frac{1}{2}} c_{k-1,n} + K_{z,k+\frac{1}{2},n} c_{k+1,n}\right) \\ &+ \frac{1}{\Delta y^2}\left(K_{y,n-\frac{1}{2}} c_{k,n-1} + K_{y,n+\frac{1}{2}} c_{k,n+1}\right) \\ &- \frac{1}{\Delta z^2}\left(K_{z,k-\frac{1}{2}} + K_{z,k+\frac{1}{2}}\right) c_{k,n} - \frac{1}{\Delta y^2}\left(K_{y,n-\frac{1}{2}} + K_{y,n+\frac{1}{2}}\right) + h_{k,n} \end{aligned} \tag{B1}$$

N is the number of grid cells in the vertical and horizontal direction. $h_{k,n}$ is the rest terms containing the boundary values. If dry deposition and emissions are included directly in the atmospheric diffusion equation these terms will enter here.

As horizontal boundary conditions the concentration gradient $\partial c/\partial y$ was set to zero. If the ground-level emission rate (E) and dry deposition are included in the boundary conditions at the ground they are described by Eq. (B2). The boundary conditions at the top of the vertical model domain are given by Eq. (B3).

$$v_d c - K_z \frac{\partial c}{\partial z} = E \tag{B2}$$

$$\frac{\partial c}{\partial z} = 10^{-3}\,\mathrm{cm}^{-3}\mathrm{m}^{-1} \tag{B3}$$

v_d and E is the dry deposition velocity and emission of particles or gases.

Equation (B1) can be written in matrix form with one matrix for each space dimension ($\mathbf{T}_z$ and $\mathbf{T}_y$) (Eq. B4).

$$\frac{\Delta c}{\Delta t} = \left(\frac{1}{\Delta z^2}\mathbf{T}_z + \frac{1}{\Delta y^2}\mathbf{T}_y\right)c + h_{z,y} \tag{B4}$$

For each time step that the model takes, Eq. (B4) is solved using the second order implicit trapezoidal rule (Crank-Nicolson method). The procedure is described by Iserles (2004). Equation (B5) is the final expression used to solve the atmospheric diffusion equation in 2-space dimensions.

$$\begin{aligned} c^{j+1} &= \left[1 - \frac{1}{2}\frac{\Delta t}{\Delta z^2}\mathbf{T}_z\right]^{-1}\left[1 + \frac{1}{2}\frac{\Delta t}{\Delta z^2}\mathbf{T}_z\right]\left[1 - \frac{1}{2}\frac{\Delta t}{\Delta y^2}\mathbf{T}_y\right]^{-1} \\ &\cdot \left[1 + \frac{1}{2}\frac{\Delta t}{\Delta y^2}\mathbf{T}_y\right] \cdot \left(c^j + \frac{1}{2}\Delta t \cdot h^j_{z,y}\right) + \frac{1}{2}\Delta t \cdot h^{j+1}_{z,y} \end{aligned} \tag{B5}$$

Appendix C

Brownian coagulation

The coagulation coefficient between two particles of same or different diameters is given by Eq. (C1). β is the Fuchs correction factor, given by Eq. (C2) (Seinfeld and Pandis, 2006).

$$K_{ij} = 2\pi\beta_{ij}\left(D_{\mathrm{p}i} D_i + D_{\mathrm{p}i} D_j + D_{\mathrm{p}j} D_i + D_{\mathrm{p}j} D_j\right) \tag{C1}$$

$$\beta_{ij}=\left[\frac{D_{\mathrm{p}i}+D_{\mathrm{p}j}}{D_{p1}+D_{\mathrm{p}i}+2(\delta_i^2+\delta_j^2)^{1/2}}+\frac{8\alpha(D_i+D_j)}{(\bar{c}_i^2+\bar{c}_j^2)^{1/2}(D_{\mathrm{p}i}+D_{\mathrm{p}j})}\right]^{-1}$$

$$\bar{c}_i=\left(\frac{8kT}{\pi m_i}\right)^{1/2}, \tag{C2}$$

$$\delta_i=\frac{1}{3D_{\mathrm{p}i}l_i}\left[(D_{\mathrm{p}i}+l_i)^3-(D_{\mathrm{p}i}^2+l_i^2)^{3/2}\right]-D_{\mathrm{p}i},l_i=\frac{8D_i}{\pi\bar{c}_i}$$

α is the collision efficiency which can be assumed to be 1 for all particle sizes (Clement et al., 1996), m_i is the singe particle mass in size bin $i,\bar{c}_i$ is the mean particle velocity and l_i is the mean free path.

Equation (C1) is used to calculate a matrix containing all possible coagulation rates between two particles with different or equal diameters for the finite diameter size bins considered.

The splitting parameters used to divide the formed single particle volumes into the fixed size bins, are calculated with Eq. (C3).

$$y_{1,i,j}=\frac{(V_{\mathrm{p},i+1}-V_{\mathrm{p,coag},i,j})}{(V_{\mathrm{p}i+1}-V_{\mathrm{p}i})},\quad V_{\mathrm{p,coag},i,j}=V_{\mathrm{p},i}+V_{\mathrm{p},j}$$
$$y_{2,i,j}=1-y_{1,i,j} \tag{C3}$$

$y_{1,i}$ is the fraction of the single particle volume of the formed particle ($V_{\mathrm{p,coag},i,j}$) which will fall into the smaller size bin i and $y_{2,i}$ is the fraction of particle volume which will fall into the larger size bin $i+1$.

The coagulation sink and source are described by Eqs. (C4) and (C5). Combining the coagulation sources and sinks gives the final equations used to calculate new particle size distributions, in each grid cell (Eq. C6).

$$\mathrm{Coag}_{\mathrm{sink},i,j}=K_{ij}c_i\cdot c_j \tag{C4}$$

$$\mathrm{Coag}_{\mathrm{source},i,j}=a_{i,j}K_{ij}c_i\cdot c_j,\ \text{if}$$
$$i=j,\ a_{i,j}=0.5,\ \text{else}\ a_{i,j}=1 \tag{C5}$$

$$c_i=c_i+\sum_j^N\big(y_{1,i,j}\cdot\mathrm{Coag}_{\mathrm{source},i,j}+y_{2,i-1,j}\cdot$$
$$\mathrm{Coag}_{\mathrm{source},i-1,j}-\mathrm{Coag}_{\mathrm{sin}k,i,j}\big)\cdot\Delta t \tag{C6}$$

The volume change of different species (k) in the aerosol particle phase due to coagulation between particles in size bin i and j is derived with Eq. (C7).

$$\begin{aligned}\frac{dV_{i,j,k}}{dt}&=y_{1i,j}\cdot\mathrm{Coag}_{\mathrm{source},i,j}\cdot x_{\mathrm{coag}i,k}\cdot V_{\mathrm{p,coag},i}\\&+y_{2i-1,j}\cdot\mathrm{Coag}_{\mathrm{source},i-1,j}\cdot x_{\mathrm{coag}i-1,k}\cdot V_{\mathrm{p,coag},i-1}\\&-\mathrm{Coag}_{\mathrm{sink},i,j}\cdot V_{\mathrm{p},i}\cdot x_{i,k}\end{aligned} \tag{C7}$$

$x_{i,k}$ is the volume fraction of species k in size bin i and $x_{\mathrm{coag},i,k}$ is the volume fraction of species k in the formed particle.

Equation (C8) gives the volume of species k in each size bin.

$$V_{i,k}=V_{\mathrm{p},i}\cdot x_{i,k}+\sum_j^N\frac{dV_{i,j,k}}{dt}\cdot\Delta t \tag{C8}$$

Appendix D

Dry deposition velocities of particles

Equation (D1) gives the dry deposition loss rate (v_d) of particles. r_a is the surface layer resistance, r_b the quasi-laminar layer resistance and v_s is the settling velocity.

$$v_d=\frac{1}{r_a+r_b+r_ar_bv_s}+v_s \tag{D1}$$

The settling velocity is given by Eq. (D2).

$$v_s=\frac{\rho_pD_{\mathrm{p}}^2gC_c}{18\mu} \tag{D2}$$

ρ_p is the particle density, μ is the dynamic viscosity, C_c is the Cunningham slip correction factor and g is the acceleration of gravity

The surface layer resistance can be expressed by Eqs. (D3) and (D4) for stable and unstable atmosphere, respectively (Seinfeld and Pandis, 2006).

$$r_a=\frac{1}{\kappa u_*}(\ln(\frac{z}{z_0})+4.7(Rf_s-Rf_0) \tag{D3}$$

$$r_a=\frac{1}{\kappa u_*}(\ln(\frac{z}{z_0})+\ln(\frac{(\eta_0^2+1)(\eta_0+1)^2}{(\eta_s^2+1)(\eta_s+1)^2})+2(\tan^{-1}\eta_s-\tan^{-1}\eta_0))$$
$$\eta_0=(1-15Rf_0)^{1/4},\ \eta_s=(1-15Rf_s)^{1/4},\ Rf_0=\frac{z_0}{L},\ Rf_s=\frac{z_s}{L} \tag{D4}$$
$$\kappa=0.4\ \text{(von Karman constant)}$$

z_0 is the roughness length and u_* is the friction velocity. The surface layer height (z_s) can be approximated as one tenth of the total mixing height (Seibert et al., 1997). Rf_0 is the non-dimensional flux Richardson number at the roughness length scale height (z_0) and Rf_s is the flux Richardson number at the surface layer height. If Rf is larger than zero, the atmosphere is stable and Eq. (D3) is used, and if Rf is smaller than zero, the atmosphere is unstable and Eq. (D4) is used instead.

The quasi-laminar resistance is calculated with Eq. (D5) over land (Zhang et al., 2001, Seinfeld and Pandis, 2006) and with Eq. (D6) over ocean (Slinn and Slinn, 1980).

$$r_b=\frac{1}{3u_*R_1(Sc^{-\gamma}+(St/(\alpha+St))^2+0.5(D_{\mathrm{p}}/A)^2)}$$
$$R_1=\exp\big(-St^{1/2}\big) \tag{D5}$$

$$r_b=\frac{\kappa\cdot\nu}{u_*^2}\frac{1}{(Sc^{-1/2}+10^{-3/St})} \tag{D6}$$

R_1 is the fraction of particles that stick to the surface upon contact. A, α and γ are surface specific parameters given by Zhang et al. (2001) for 12 different land use categories. St is the Stokes number and Sc is the Schmidt number.

Table E. Explicit scheme used to estimate the particle salt molar composition.

Salt	if $n_{S(VI)} >$ $n_{NH_4} + n_{Na}$	if $n_{S(VI)} <$ $n_{NH_4} + n_{Na}$ & $n_{S(VI)} + n_{NO_3}$ $> n_{NH_4} + n_{Na}$	if $n_{S(VI)} + n_{NO_3}$ $\le n_{NH_4} + n_{Na}$ & $2n_{S(VI)} + n_{NO_3}$ $> n_{NH_4} + n_{Na}$	if $2n_{S(VI)} + n_{NO_3}$ $\le n_{NH_4} + n_{Na}$
$(Na)_2SO_4$	0	0	$n_{Na} - n_{Cl}$	$n_{Na} - n_{Cl}$
$NaHSO_4$	$n_{Na} - n_{Cl}$	$n_{Na} - n_{Cl}$	0	0
NaCl	n_{Cl}	n_{Cl}	n_{Cl}	n_{Cl}
$(NH_4)_2SO_4$	0	0	$n_{NH_4} + n_{Na} - n_{NO_3}$ $- n_{S(VI)} - n_{(Na)_2SO_4}$	$n_{S(VI)} - n_{(Na)_2SO_4}$
NH_4HSO_4	n_{NH_4}	$n_{S(VI)} - n_{NaHSO_4}$	$n_{S(VI)} - n_{(NH_4)_2SO_4}$	0
H_2SO_4	$n_{S(VI)} - n_{NH_4}$ $- n_{NaHSO_4}$	0	0	0
NH_4NO_3	0	$n_{NH_4} - n_{NH_4HSO_4}$	n_{NO_3}	n_{NO_3}
HNO_3	n_{NO_3}	$n_{NO_3} - n_{NH_4NO_3}$	0	0
NH_3	0	0	0	$n_{NH_4} - n_{NO_3}$ $- 2n_{(NH_4)_2SO_4}$

Appendix E

Inorganic particle salt composition

Table E displays the explicit scheme which is used to estimate the particle salt molar composition.

Appendix F

Dry deposition velocity for gases

The dry deposition velocities for the different gases are given by Eq. (F1) (Seinfeld and Pandis, 2006).

$$v_d = \frac{1}{r_a + r_b + r_c} \tag{F1}$$

The dry deposition can be a significant loss term for acid species like HNO_3 and H_2SO_4 which has a very large effective Henry's law constant. The effective Henry's law constants used for the different species in the chemical gas phase model are taken from Table 19.4 in Seinfeld and Pandis (2006) which is valid for a pH of about 6.5. For most of the species no effective Henry's law constant were found, then the Henry's law constants given by Table 5.4 in Sander et al. (2006) were used instead. For many of the hydrocarbon species no Henry's law constants were found at all. It was then assumed that their solubility in water is practically zero.

The aerodynamic resistance is a function of the stability of the atmosphere but is independent of whether it is gases or particles that are deposited. The aerodynamic resistances for gases as well as for particles are therefore given by Eqs. (D3) and (D4).

The quasi-laminar resistance for gases over land is described by Eq. (F2) (Seinfeld and Pandis, 2006). Equation (F3) gives the quasi-laminar resistance over ocean (Hicks and Liss, 1976).

$$r_b = \frac{5Sc_i^{2/3}}{u*} \tag{F2}$$

$$r_b = \frac{1}{\kappa u^*} \ln\left(\frac{z_0 \kappa u^*}{D}\right) \tag{F3}$$

The canopy resistance depends on the structure of the ground. For vegetated land surfaces the resistance is divided into foliar resistance and ground resistance. Canopy resistance is the sum of the foliar resistance and the ground resistance in parallel (Seinfeld and Pandis, 2006).

The foliar resistance is divided into resistance to uptake at the surface of the leaves and at the plant stomata. The stomata resistance (r_{st}) can be further divided into the stomata pore resistance (r_p) and the mesophyll resistance (r_m) which is the resistance to dissolution in the leaf interior (Seinfeld and Pandis, 2006). The stomata resistance is usually very important for the dry deposition of gases. Since stomata are only open during the day it will lead to a diurnal pattern in the dry deposition velocity, with considerably higher values during the day than during the night (Pirjola and Kulmala, 1998 and Seinfeld and Pandis, 2006).

The complete surface resistance for species i is given by Eq. (F4) (Seinfeld and Pandis, 2006 originaly from Wesely, 1989). Apart from the stomata resistance the surface resistance also depends on the outer surface resistance in the upper canopy (r_{lu}), transfer resistance by buoyant convection (r_{dc}), the resistance to uptake by leaves, twigs and other surfaces (r_{cl}) and the resistance at the ground including transfer resistance due to canopy height (r_{ac}) and resistance in the soil (r_{gs}).

$$r_c^i = \left(\frac{1}{r_{st}^i} + \frac{1}{r_{lu}^i} + \frac{1}{r_{dc}^i + r_{cl}^i} + \frac{1}{r_{ac}^i + r_{gs}^i} \right)^{-1} \tag{F4}$$

Appendix G

Radiative transfer model

The radiative transfer equation for solar irradiance can be written as in Eq. (G1) (Jacobson, 2005).

$$\mu \frac{dI_{\lambda,\mu,\phi}}{d\tau_\lambda} = I_{\lambda,\mu,\phi} - J_{\lambda,\mu,\phi}^{\text{diffuse}} - J_{\lambda,\mu,\phi}^{\text{direct}} \tag{G1}$$

The diffuse component is given by Eq. (G2) and the direct component by Eq. (G3).

$$J_{\lambda,\mu,\phi}^{\text{diffuse}} = \sum_k \left(\frac{\sigma_{s,k,\lambda}}{\sigma_\lambda} \frac{1}{4\pi} \int_0^{2\pi} \int_{-1}^{1} I_{\lambda,\mu',\phi'} P_{s,k,\lambda,\mu,\mu',\phi,\phi',d\mu',d\phi'} \right) \tag{G2}$$

$$J_{\lambda,\mu,\phi}^{\text{direct}} = \frac{1}{4\pi} E_{s,\lambda}^{-\tau_\lambda/\mu_s} \sum_k \left(\frac{\sigma_{s,k,\lambda}}{\sigma_\lambda} P_{s,k,\lambda,\mu,-\mu_s,\phi,\phi_s} \right) \tag{G3}$$

λ is the wavelength of light, I_λ is the the spectral radiance, E_s is the solar irradiance, τ_λ is the optical depth, $\emptyset_s$ is the solar zenith angle, σ is the extinction coefficient, σ_s is the scattering coefficient, $\mu_s = \cos(\emptyset_s)$ and Φ_s gives the direction of the solar radiation, μ and Φ gives the orientation of the beam of interest, μ' and Φ' gives the direction of the diffuse radiation and P_s is the scattering phase function, which gives the angular distribution of the scattered energy.

Approximating the integral in Eq. (G2) with quadrature two-stream equations gives Eq. (G4) (Jacobson, 2005).

$$\frac{1}{4\pi} \int_0^{2\pi} \int_{-1}^{1} I_{\lambda,\mu',\phi'} P_{s,k,\lambda,\mu,\mu',\phi,\phi',d\mu',d\phi'} \approx \begin{cases} \frac{1+g_{a,k,\lambda}}{2} I\uparrow + \frac{1-g_{a,k,\lambda}}{2} I\downarrow & \text{upward} \\ \frac{1+g_{a,k,\lambda}}{2} I\downarrow + \frac{1-g_{a,k,\lambda}}{2} I\uparrow & \text{downward} \end{cases} \tag{G4}$$

$I\uparrow$ is the upward radiance and $I\downarrow$ is the downward radiance.

Combining Eqs. (G2) and (G4) gives Eq. (G5).

$$J_{\lambda,\mu,\phi}^{\text{diffuse}} \approx \begin{cases} \omega_{s,\lambda} \frac{1+g_{a,\lambda}}{2} I\uparrow + \omega_{s,\lambda} \frac{1-g_{a,\lambda}}{2} I\downarrow & \text{upward} \\ \omega_{s,\lambda} \frac{1+g_{a,\lambda}}{2} I\downarrow + \omega_{s,\lambda} \frac{1-g_{a,\lambda}}{2} I\uparrow & \text{downward} \end{cases} \tag{G5}$$

$\omega_{s,\lambda} = \frac{\sigma_{s,\lambda}}{\sigma_\lambda}$, is the single scattering albedo and $g_{a,\lambda}$ is the effective asymmetry parameter, calculated from the asymmetry parameters for gases ($g_{a,g,\lambda}$), particles ($g_{a,p,\lambda}$) and cloud drops ($g_{a,c,\lambda}$) (Eq. G6).

$$g_{a,\lambda} = \frac{\sigma_{s,a,\lambda} g_{a,p,\lambda} + \sigma_{s,c,\lambda} g_{a,c,\lambda}}{\sigma_{s,g,\lambda} + \sigma_{s,p,\lambda} + \sigma_{s,c,\lambda}} \tag{G6}$$

If using the quadrature approximation (Eq. G4), Eq. (G1) can be written as:

$$\begin{cases} \mu_1 \frac{dI\uparrow}{d\tau} = I\uparrow - \omega_s \frac{1+g_a}{2} I\uparrow - \omega_s \frac{1-g_a}{2} I\downarrow - \frac{\omega_s}{4\pi}(1 - 3g_a\mu_1\mu_s) E_s e^{-\tau/\mu_s} \\ -\mu_1 \frac{dI\downarrow}{d\tau} = I\downarrow - \omega_s \frac{1+g_a}{2} I\downarrow - \omega_s \frac{1-g_a}{2} I\uparrow - \frac{\omega_s}{4\pi}(1 + 3g_a\mu_1\mu_s) E_s e^{-\tau/\mu_s} \end{cases} \tag{G7}$$

μ_1 is equal to $1/\sqrt{3}$ when using the quadrature approximation. The spectral radiation terms in Eq. (G7) can be replaced with the spectral irradiance using the conversion:

$$E\uparrow = 2\pi\mu_1 I\uparrow, \quad E\downarrow = 2\pi\mu_1 I\downarrow \tag{G8}$$

This gives Eq. (G9) (Jacobson, 2005):

$$\begin{cases} \frac{dE\uparrow}{d\tau} = \gamma_1 E\uparrow - \gamma_2 E\downarrow - \gamma_3 \omega_s E_s e^{-\tau/\mu_s} \\ \frac{dE\downarrow}{d\tau} = -\gamma_1 E\downarrow + \gamma_2 E\uparrow + (1-\gamma_3)\omega_s E_s e^{-\tau/\mu_s} \end{cases} \tag{G9}$$

Where

$$\gamma_1 = \frac{1-\omega_s(1+g_a)/2}{\mu_1}, \quad \gamma_2 = \frac{\omega_s(1-g_a)}{2\mu_1}, \quad \gamma_3 = \frac{1-3g_a\mu_1\mu_s}{2}$$

Equation (G9) is discretized and solved according to the numerically stable scheme developed by Toon et al. (1989).

Combining the direct and the diffuse spectral radiance gives the net spectral radiation:

$$I_{\text{net}}(\tau_n) = I\uparrow(\tau_n) - I\downarrow(\tau_n) - I_{dir}(\tau_n) \tag{G10}$$

Multiplying the net spectral radiance with 4π gives the spectral actinic flux in W m^{-2} nm^{-1}.

Tabel 4.2 in Seinfeld and Pandis (2006) originally from Fröhlich and London (1986) gives the solar spectral irradiance at the top of the atmosphere (E_{top}), normalized to a solar constant (S) of 1367 W m^{-2}. Since this spectral irradiance is independent of the composition of the atmosphere, it can be used together with a radiative transfer model to predict the actinic flux at different altitudes in the atmosphere.

The solar zenith angle (Φ_z) is calculated with Eq. (G11) (Stull, 2000).

$$\begin{aligned} &\sin(\phi_z) = \sin(\psi)\sin(\delta_s) - \cos(\psi)\cos(\delta_s)\cos\left[\frac{360 t_{UTC}}{t_d} - \lambda_e\right] \\ &\delta_s = 23.45\cos\left[\frac{360(d-173)}{365}\right] \end{aligned} \tag{G11}$$

δ_s is the solar declination angle, ψ is the latitude and λ_e is the longitude.

Supplementary material related to this article is available online at: http://www.atmos-chem-phys.net/11/5867/2011/acp-11-5867-2011-supplement.pdf.

Acknowledgements. This work has been supported by the European Commission 6th Framework program projects: EUCAARI, contract no 036833-2 (EUCAARI) and EUSAAR, contract no 026140 (EUSAAR). We also gratefully acknowledge the support by the Swedish Research Council through project no 2007-4619, the Strategic Research Program MERGE: Modeling the Regional and Global Earth System and the Lund University center for studies of Carbon cycle and Climate Interactions, LUCCI. The Swedish Research Council also funded the purchase of the HR-ToF-AMS instrument through Research Equipment Grant no 2006-5940. The DMPS measurements at Vavihill were supported by the Swedish Environmental Protection Agency within the Swedish Environmental Monitoring Program. The support by the Swedish Research Council for Environment, Agricultural Sciences and Spatial Planning (Formas) through project no 2009-615 is also gratefully acknowledged.

The authors would also like to thank Henrik Nilsson and Susanna Gustafsson at Environmental Dept., City of Malmö for the gas and meteorological measurements in Malmö and the gas and PM emission data for southern Sweden, Emilie Stroh at the Dept. of Epidemiology and environmental medicine at Lund University for help with the implementation of the southern Sweden emission data, Matthias Ketzel and Fenjuan Wang from Danish National Environmental Research Institute for help with the Danish anthropogenic gas and particle emissions and David Simpson from the Norwegian Meteorological Institute, Oslo, and Dept. Earth and Space Science, Chalmers, Gothenburg for help with the SOA partitioning theory.

Edited by: A. Wiedensohler

References

Arneth, A., Niinemets, Ü., Pressley, S., Bäck, J., Hari, P., Karl, T., Noe, S., Prentice, I. C., Sera, D., Hickler, T., Wolf, A., and Smith, B.: Process-based estimates of terrestrial ecosystem isoprene emissions: incorporating the effects of a direct CO_2-isoprene interaction, Atmos. Chem. Phys., 7, 31–53, doi:10.5194/acp-7-31-2007, 2007.

Arneth, A., Schurgers, G, Hickler, T, and Miller, P. A.: Effects of species composition, land surface cover, CO_2 concentration and climate on isoprene emissions from European forests, Plant Biology, 10, 150–162, doi:110.1055/s-2007-965247, 2008.

Atkinson, R.: Gas-phase tropospheric chemistry of volatile organic compounds 1. Alkanes and alkenes, J. Phys. Chem. Ref. Data, 26, 215–290, 1997.

Atkinson, R. and Arey, J.: Gas-phase tropospheric chemistry of biogenic volatile organic compounds: a review, Atmos. Environ., 37, 197–219, 2003.

Atkinson, R., Baulch, D. L., Cox, R. A., Crowley, J. N., Hampson, R. F., Hynes, R. G., Jenkin, M. E., Rossi, M. J., and Troe, J.: Evaluated kinetic and photochemical data for atmospheric chemistry: Volume I-gas phase reactions of O_x, HO_x, NO_x and SO_x species, Atmos. Chem. Phys., 4, 1461–1738, doi:10.5194/acp-4-1461-2004, 2004.

Boy, M., Hellmuth, O., Korhonen, H., Nilsson, E. D., ReVelle, D., Turnipseed, A., Arnold, F., and Kulmala, M.: MALTE – model to predict new aerosol formation in the lower troposphere, Atmos. Chem. Phys., 6, 4499–4517, doi:10.5194/acp-6-4499-2006, 2006.

Bromley, L. A.: Thermodynamic properties of strong electrolytes in aqueous solutions, AIChE J., 19, 313–320, 1973.

Businger, J. A. and Arya, S. P. S.: Height of the mixed layer in the stably stratified planetary boundary layer, Adv. Geophys., 18A, 73–92, 1974.

Calvert, J. G., Atkinson, R., Becker, K. H., Kamens, R. M., Seinfeld, J. H., Wallington, T. J., and Yarwood, G.: The Mechanisms of Atmospheric Oxidation of Aromatic Hydrocarbons, Oxford University Press, New York, 556 pp., 2002.

Clement, F. C., Kulmala, M., and Vesala, T.: Theoretical consideration on sticking probabilities, J. Aerosol Sci., 27(6), 869–882, 1996.

Cotte, H., Devaux, C., and Carlier, P.: Transformation of Irradiance Measurements into Spectral Actinic Flux for Photolysis Rates Determination, J. Atmos. Chem., 26, 1–28, 1997.

Donahue, N. M., Robinson, A. L., Stanier, C. O., and Pandis, S. N.: Coupled partitioning, dilution, and chemical aging of semivolatile organics, Environ. Sci. Technol., 40, 2635–2643, 2006.

Doran, J. C., Barnard, J. C., Arnott, W. P., Cary, R., Coulter, R., Fast, J. D., Kassianov, E. I., Kleinman, L., Laulainen, N. S., Martin, T., Paredes-Miranda, G., Pekour, M. S., Shaw, W. J., Smith, D. F., Springston, S. R., and Yu, X.-Y.: The T1-T2 study: evolution of aerosol properties downwind of Mexico City, Atmos. Chem. Phys., 7, 1585–1598, doi:10.5194/acp-7-1585-2007, 2007.

Draxler, R. R. and Rolph, G. D.: HYSPLIT (Hybrid Single-Particle Lagrangian Integrated Trajectory) Model access via NOAA ARL READY Wedsite (http://ready.arl.noaa.gov/HYSPLIT.php), NOAA Air Resources Laboratory, Silver Spring, MD, 8:26 AM, Tuesday, March 01, 2011.

Epstein, S., Riipinen, I., and Donahue, N. M.: A Semiempirical Correlation between Enthalpy of Vaporization and Saturation Concentration for Organic Aerosol, Environ. Sci. Technol., 44, 743–748, 2010.

Fitzgerald, J. W., Hoppel, W. A., and Gelbard, G.: A one-dimensional sectional model to simulate multicomponent aerosol dynamics in the marine boundary layer 1. Model description, J. Geophys. Res., 103, 16085–16102, 1998.

Fröhlich, C. and London, J. (Eds.): Revised Instruction Manual on Radiation Instruments and Measurements, World Climate Research Program (WCRP) Publication Series 7, World Meteorological Organization/TD No. 149, Geneva, 1986.

Grieshop, A. P., Miracolo, M. A., Donahue, N. M., and Robinson, A. L.: Constraning the Volatility Distribution and Gas-Particle Partitioning of Combustion Aerosols Using Isothermal Dilution and Thermodenuder Measurements, Environ. Sci. Technol., 43, 4750–4756, 2009.

Griffin, R. J., Cocker III, D. R., Flagan, R. C., and Seinfeld, J. H.: Organic aerosol formation from the oxidation of biogenic hydrocarbons, J. Geophys. Res., 107(D3), 3555–3567, 1999.

Guenther, A.: Seasonal and Spatial Variations in Natural Volatile Organic Compound Emissions, Ecol. Appl., 7, 34–45, 1997.

Gustafsson, S.: Uppbyggnad och validering av emissionsdatabas avseende luftföroreningar för Skåne med basår, Licentiat Dissertation at National Environmental Research Institute, Lund University, nr 9, 2001.

Haylock, M., Hofstra, N., Klein Tank, A., Klok, E., Jones, P., and New, M. A.: European daily high-resolution gridded data set of surface temperature and precipitation for 1950–2006, J. Geophys. Res., 113, D20119, doi:10.1029/2008JD010201, 2008.

Henze, D. K. and Seinfeld, J. H.: Global secondary organic aerosol from isoprene oxidation, Geophys. Res. Lett., 33, L09812, doi:10.1029/2006GL025976, 2006.

Henze, D. K., Seinfeld, J. H., Ng, N. L., Kroll, J. H., Fu, T.-M., Jacob, D. J., and Heald, C. L.: Global modeling of secondary organic aerosol formation from aromatic hydrocarbons: high- vs. low-yield pathways, Atmos. Chem. Phys., 8, 2405–2420, doi:10.5194/acp-8-2405-2008, 2008.

Hicks, B. B. and Liss, P. S.: Transfer of SO_2 and other reactive gases across the air-sea interface, Tellus, 28, 348–354, 1976.

Hodzic, A., Vautard, R., Chazette, P., Menut, L., and Bessagnet, B.: Aerosol chemical and optical properties over the Paris area within ESQUIF project, Atmos. Chem. Phys., 6, 3257–3280, doi:10.5194/acp-6-3257-2006, 2006.

Hodzic, A., Jimenez, J. L., Madronich, S., Aiken, A. C., Bessagnet, B., Curci, G., Fast, J., Lamarque, J.-F., Onasch, T. B., Roux, G., Schauer, J. J., Stone, E. A., and Ulbrich, I. M.: Modeling organic aerosols during MILAGRO: importance of biogenic secondary organic aerosols, Atmos. Chem. Phys., 9, 6949–6981, doi:10.5194/acp-9-6949-2009, 2009.

Iserles, A.: A First Course in the Numerical Analysis of Differential Equations, Cambridge University Press, Cambridge, United Kingdom and New York, NY, USA, ISBN: 0 521 55376 8, 2004.

Jacobson, M. Z.: Numerical techniques to solve condensational and dissolutional growth equations when growth is coupled to reversible aqueous reactions, Aerosol Sci. Technol., 27, 491–498, 1997.

Jacobson, M. Z. and Seinfeld, J. H.: Evolution of nanoparticle size and mixing state near the point of emission, Atmos. Environ., 38, 1839–1850, 2004.

Jacobson, M. Z.: A Solution to the Problem of Nonequilibrium Acid/Base Gas-Particle Transfer at Long Time Step, Aerosol Sci. Technol., 39, 92–103, 2005a.

Jacobson, M. Z.: Fundamentals of Atmospheric Modelling (2^{nd}edition), Cambridge University Press, Cambridge, United Kingdom and New York, NY, USA, ISBN: 0 521 54865 9, 2005b.

Jimenez, J. L., Canagaratna, M. R., Donahue, N. M., Prevot, A. S. H., Zhang, Q., Kroll, J. H., DeCarlo, P. F., Allan, J. D., Coe, H., Ng, N. L., Aiken, A. C., Docherty, K. S., Ulbrich, I. M., Grieshop, A. P., Robinson, A. L., Duplissy, J., Smith, J. D., Wilson, K. R., Lanz, V. A., Hueglin, C., Sun, Y. L., Tian, J., Laaksonen, A., Raatikainen, T., Rautiainen, J., Vaattovaara, P., Ehn, M., Kulmala, M., Tomlinson, J. M., Collins, D. R., Cubison, M. J., Dunlea, E. J., Huffman, J. A., Onasch, T. B., Alfarra, M. R., Williams, P. I., Bower, K., Kondo, Y., Schneider, J., Drewnick, F., Borrmann, S., Weimer, S., Demerjian, K., Salcedo, D., Cottrell, L., Griffin, R., Takami, A., Miyoshi, T., Hatakeyama, S., Shimono, A., Sun, J. Y, Zhang, Y. M., Dzepina, K., Kimmel, J. R., Sueper, D., Jayne, J. T., Herndon, S. C., Trimborn, A. M., Williams, L. R., Wood, E. C., Middlebrook, A. M., Kolb, C. E., Baltensperger, U., and Worsnop, D. R.: Evolution of Organic Aerosols in the Atmosphere, Science, 326, 1525–1529, 2009.

Kittelson, D. B., Watts, W., and Johnson, J.: Diesel aerosol sampling methodology, CRC E-43 Final Report, University of Minnesota, 2002.

Korhonen, H.: Model studies on the size distribution dynamics of atmospheric aerosols, Report series in aerosol science, No 65, Finnish association for aerosol research, ISBN: 952-5027-46-5, 2004a.

Korhonen, H., Lehtinen, K. E. J., and Kulmala, M.: Multicomponent aerosol dynamics model UHMA: model development and validation, Atmos. Chem. Phys., 4, 757–771, doi:10.5194/acp-4-757-2004, 2004b.

Kristensson, A., Johansson, C., Westerholm, R., Swietlicki, E., Gidhagen, L., Widequist, U., and Vesely, V.: Real-world traffic emission factors of gases and particles measured in a road tunnel in Stockholm, Sweden, Atmos. Environ., 38, 657–673, 2004.

Kristensson, A.: Aerosol Particle Sources Affecting the Swedish Air Quality at Urban and Rural Level, Doctoral Dissertation at Department of Physics, Lund University, ISBN: 91-628-6573-0, 2005.

Kristensson, A., Dal Maso, M., Swietlicki, E., Hussein, T., Zhou, J., Kerminen, V.-M., and Kulmala, M.: Characterization of new particle formation events at a background site in Southern Sweden: relation to air mass history, Tellus, 60B, 330–344, 2008.

Kulmala, M., Lehtinen, K. E. J., and Laaksonen, A.: Cluster activation theory as an explanation of the linear dependence between formation rate of 3 nm particles and sulphuric acid concentration, Atmos. Chem. Phys., 6, 787–793, doi:10.5194/acp-6-787-2006, 2006.

Laakso, L., Grönholm, T., Rannik, Ü., Kosmale, M., Fiedler, V., Vehkamäki, H., and Kulmala, M.: Ultrafine particle scavening coefficients calculated from 6 years field measurements, Atmos. Environ., 37, 3605–3613, 2003.

Lane, T. E., Donahue, N. M., and Pandis, S. N.: Simulating secondary organic aerosol formation using the volatility basis-set apporach in a chemical transport model, Atmos. Environ., 42, 7439–7451, 2008.

Moldanová, J., Fridell, E., Popovicheva, O., Demirdjian, B., Tishkova, V., Faccinetto, A., and Focsa, C.: Characterisation of particulate matter and gaseous emissions from a large ship diesel engine, Atmos. Environ., 43, 2632–2641, 2009.

Myrup, L. O. and Ranzieri, A. J.: A Consistent Scheme for Estimating Diffusivities to Be Used in Air Quality Models, Report CA-DOT-TL-7169-3-76-32, California Department of Transportation, Sacramento, 1976.

McMurry, P. H. and Friedlander, S. K.: New particle formation in the presence of an aerosol, Atmos. Environ., 13, 1635–1651, 1979.

Mårtensson, E. M., Nilsson, E. D, de Leeuw, G., Cohen, L. H., and Hansson, H.-C.: Laboratory simulations and parameterization of the primary marine aerosol production, J. Geophys. Res., 108(D9), 4297, doi:10.1029/2002JD002263, 2003.

Ng, N. L., Kroll, J. H., Chan, A. W. H., Chhabra, P. S., Flagan, R. C., and Seinfeld, J. H.: Secondary organic aerosol formation from m-xylene, toluene, and benzene, Atmos. Chem. Phys., 7, 3909–3922, doi:10.5194/acp-7-3909-2007, 2007.

Niinemets, Ü., Tenhunen, J. D., Harley, P. C., and Steinbrecher, R.: A model of isoprene emissions based on energetic requirements for isoprene synthesis and leaf photosynthetic properties for *Liquidambar* and *Quercus*, Plant Cell and Environ., 22, 1319–1335, 1999.

Niinemets, U., Seufert, G., Steinbrecher, R., and Tenhunen, J.: A model coupling foliar monoterpene emissions to leaf photosynthetic characteristics in Mediterranean evergreen Quercus species, New Phytol., 153, 257–275, 2002.

Nolte, C. G., Bhave, P. V., Arnold, J. R., Dennis, R. L., Zhang, K. M., and Wexler, A. S.: Modeling urban and regional aerosols-Application of the CMAQ-UCD Aerosol Model to Tampa, a coastal urban site, Atmos. Environ., 42, 3179–3191, 2008.

O'Dowd, C. D., Facchini, M. C., Cavalli, F., Ceburnis, D., Mircea, M., Decesari, S., Fuzzi, S., Yoon, J. Y., and Putaud, J.-P.: Biogenically driven organic contribution to marine aerosol, Nature, 431, 676–680, 2004.

Odum, J. R., Hoffmann, T., Bowman, F., Collins, D., Flagan, R. C., and Seinfeld, J. H.: Gas/Particle Partitioning and Secondary Organic Aerosol Yields, Environ. Sci. Technol., 30, 2580–2585, 1996.

Pankow, J. F.: An absorption model of the gas/aerosol partitioning involved in the formation of secondary organic aerosol, Atmos. Environ., 28, 189–193, 1994.

Pankow, J. F. and Asher, W. E.: SIMPOL.1: a simple group contribution method for predicting vapor pressures and enthalpies of vaporization of multifunctional organic compounds, Atmos. Chem. Phys., 8, 2773–2796, doi:10.5194/acp-8-2773-2008, 2008.

Paasonen, P., Sihto, S.-L., Nieminen, T., Vuollekoski, H., Riipinen, I., Plass-Dülmer, C., Berresheim, H., Birmili, W., and Kulmala, M.: Connection between new particle formation and sulphuric acid at Hohenpeissenberg (Germany) including the influence of organic compounds, Boreal Environmental Research, 14, 616–629, 2009.

Petzold, A., Hasselbach, J., Lauer, P., Baumann, R., Franke, K., Gurk, C., Schlager, H., and Weingartner, E.: Experimental studies on particle emissions from cruising ship, their characteristic properties, transformation and atmospheric lifetime in the marine boundary layer, Atmos. Chem. Phys., 8, 2387–2403, doi:10.5194/acp-8-2387-2008, 2008.

Pirjola, L.: Effects of the increased UV radiation and biogenic VOC emissions on ultrafine sulphate aerosol formation, J. Aerosol Sci., 30, 355–367, 1999.

Pirjola, L. and Kulmala, M.: Modelling the formation of H_2SO_4-H_2O particles in rural, urban and marine conditions, Atmos. Res., 46, 321–347, 1998.

Pirjola, L., Tsyro, S., Tarrason, L., and Kulmala, M.: A monodisperse aerosol dynamic module, a promising candidate for use in long-range transport models: Box model tests, J. Geophys. Res., 108(D9), 4258, doi:10.1029/2002JD002867, 2003.

Ramankutty, N., Evan, A. T., Monfreda, C., and Foley, J. A.: Farming the planet: 1. Geographic distribution of global agricultural lands in the year 2000, Global Biogeochem. Cy., 22, GB1003, doi:10.1029/2007GB002952, 2008.

Robinson, A. L., Donahue, N. M., Shrivastava, M. K., Weitkamp, E. A., Sage, A. M., Grieshop, A. P., Lane, T. E., Pierce, J. R., and Pandis, S. N.: Rethinking organic aerosols: Semivolatile emissions and photochemical aging, Science, 315, 1259–1262, 2007.

Rogers, R. R. and Yau, M. K.: A Short Course in Cloud Physics 3^{rd} Edition, Pergamon Press, Oxford, Great Britain ISBN: 0-08-034864-5, 1989.

Roldin, P., Swietlicki, E., Massling, A., Kristensson, A., Löndahl, J., Eriksson, A., Pagels, J., and Gustafsson, S.: Aerosol ageing in an urban plume – implication for climate, Atmos. Chem. Phys., 11, doi:10.5194/acp-11-5897-2011, 5897–5915, 2011.

Rolph, G. D.: Real-time Environmental Applications and Display sYstem (READY) Website (http://ready.arl.noaa.gov/index.php), NOAA Air Resources Laboratory, Silver Spring, MD, 8:26 AM, Tuesday, March 01, 2011.

Sander, S. P., Friedl, R. R., Golden, D. M., Kurylo, M. J., Moortgat, G. K., Keller-Rudek, H., Wine, P. H., Ravishankara, A. R., Kolb, C. E., Molina, M. J., Finlayson-Pitts, B. J., Huie R. E., and Orkin, V. L.: Chemical Kinetics and Photochemical Data for Use in Atmospheric Studies, Evaluation Number 15, NASA, 2006.

Seibert, P., Beyrich, F., Gryning, S.-E., Joffre, S., Rasmussen, A., and Tercier, P.: Mixing Height Determination for Dispersion Modelling, COST Action 710, Preprocessing of Meteorological Data for Dispersion Modelling, Report of Working Group 2, 1997.

Schauer, J. J., Kleeman, M. J., Cass, G. R., and Simoneit, B. R. T.: Measurement of Emissions from Air Pollution Sources 3. C-C Organic Compounds from Fireplace Combustion of Wood, Envir. Sci. Tech., 35, 1716–1728, 2001.

Schurgers, G., Arneth, A., Holzinger, R., and Goldstein, A. H.: Process-based modelling of biogenic monoterpene emissions combining production and release from storage, Atmos. Chem. Phys., 9, 3409–3423, doi:10.5194/acp-9-3409-2009, 2009a.

Schurgers, G., Hickler, T., Miller, P. A., and Arneth, A.: European emissions of isoprene and monoterpenes from the Last Glacial Maximum to present, Biogeosciences, 6, 2779–2797, doi:10.5194/bg-6-2779-2009, 2009b.

Seinfeld, J. H. and Pandis, S. N.: Atmospheric Chemistry and Physics: From Air Pollution to Climate Change, (2nd edition), Wiley, New Jersey, ISBN: 0-471-72018-6, 2006.

Sheehan, P. E. and Bowman, F. M.: Estimated Effects of Temperature on Secondary Organic Aerosol concentrations, Environ. Sci. Technol., 35, 2129–2135, 2001.

Shrivastava, M. K., Lane, T. E., Donahue, N. M., Pandis, S. N., and Robinson, A. L.: Effects of gas particle partitioning and aging of primary emissions on urban and regional organic aerosol concentrations, J. Geophys. Res., 113, D18301, doi:10.1029/2007JD009735, 2008.

Simpson, D., Fagerli, H., Jonson, J. E., Tsyro, S., Wind, P., and Tuovinen, J.-P.: Transboundary Acidification, Eutrophication and Groud Level Ozone in Europe, Part I, Unified EMEP Model Description, EMEP Status Report 2003, ISSN 0806-4520, 2003.

Sitch, S., Smith, B., Prentice, I., Arneth, A., Bondeau, A., Cramer, W., Kaplan, J., Levis, S., Lucht, W., Sykes, M., Thonicke, K., and Venevsky, S.: Evaluation of ecosystem dynamics, plant geography and terrestrial carbon cycling in the LPJ Dynamic Global Vegetation Model Global Change Biology, 9, 161–185, 2003.

Slinn, S. A. and Slinn, W. G. N.: Predictions for particle deposition on natural waters, Atmos. Environ., 14, 1013–1016, 1980.

Slinn, W. G. N.: Predictions for particle deposition to vegetation canopies, Atmos. Environ., 16, 1785–1794, 1982.

Smith, B., Prentice, I. C., and Sykes, M. T.: Representation of vegetation dynamics in the modeling of terrestrial ecosystems: comparing two contrasting approaches within European climate space, Global Ecol. Biogeogr., 10, 621–637, 2001.

Steinbrecher, R., Smiatek, G., Köble, R., Seufert, G., Theloke, J., Hauff, K., Ciccioli, P., Vautard, R., and Curci, G.: Intra- and inter-annual variability of VOC emissions from natural and semi-natural vegetation in Europe and neighbouring countries, Atmos. Environ., 43, 1380–1391, 2009.

Stokes, R. H. and Robinson, R. A.: Interactions in Aqueous Nonelectrolyte Solutions. I. Solute-Solvent Equilibrium, J. Phys. Chem., 70, 2126–2131, 1966.

Stohl, A., Haimberger, L, Scheele, M. P., and Wernli, H.: An intercomparison of results from three trajectory models, Meteorol. Appl., 8, 127–135, doi:10.1017/S1350482701002018, 2001.

Stull, R. B.: Meteorology for Scientists and Engineers, (2^{nd} edition), ISBN: 0-534-37214-7, 2000.

Svendby, T. M., Lazaridis, M., and Tørseth, K.: Temperature dependent secondary organic aerosol formation from terpenes and aromatics, J. Atmos. Chem., 59, 25–46, 2008.

Tarrasón, L., Turner, S., and Fløisand, I.: Estimation of seasonal dimethyl sulphide fluxes over the North Atlantic Ocean and their contribution to European pollution levels, J. Geophys. Res., 100, 11623–11639, 1995.

Tirabassi, T. and Rizza, U.: Boundary Layer Parameterization for a Non-Gaussian Puff Model, J. Appl. Meteorol., 36, 1031–1037, 1997.

Toon, O. B., McKay, C. P., Ackerman, T. P., and Santhanam, K.: Rapid Calculation of Radiative Heating Rates and Photodissociation Rates in Inhomogeneous Multiple Scattering Atmospheres, J. Geophys. Res., 94, 16287–16301, 1989.

Tsimpidi, A. P., Karydis, V. A., Zavala, M., Lei, W., Molina, L., Ulbrich, I. M., Jimenez, J. L., and Pandis, S. N.: Evaluation of the volatility basis-set approach for the simulation of organic aerosol formation in the Mexico City metropolitan area, Atmos. Chem. Phys., 10, 525–546, doi:10.5194/acp-10-525-2010, 2010.

Tunved, P., Ström, J., and Hansson, H.-C.: An investigation of processes controlling the evolution of the boundary layer aerosol size distribution properties at the Swedish background station Aspvreten, Atmos. Chem. Phys., 4, 2581–2592, doi:10.5194/acp-4-2581-2004, 2004.

Tunved, P., Partridge, D. G., and Korhonen, H.: New trajectory-driven aerosol and chemical process model Chemical and Aerosol Lagrangian Model (CALM), Atmos. Chem. Phys., 10, 10161–10185, doi:10.5194/acp-10-10161-2010, 2010.

Vestreng, V., Rigler, E., Adams, M., Kindbom, K., Pacyna, J. M., van der Gon, D., Reis, H. S., and Traynikov, O.: Inventory review 2006, Emission data reported to LRTAP and NEC Directive, Stage 1, 2 and 3 review and Evaluation of Inventories of HM and POPs, EMEP/MSC-W Technical Report 1/2006 ISSN 1504-6179, available from http://www.emep.int/, 2006.

Wang, F., Roldin, P., Massling, A., Kristensson, A., Swietlicki, E., Fang, D., and Ketzel, M.: Aerosol dynamics in the Copenhagen urban plume during regional transport, Atmos. Chem. Phys. Discuss., 10, 8553–8594, doi:10.5194/acpd-10-8553-2010, 2010.

Wesely, M. L.: Parameterization of surface resistance to gaseous dry deposition in regional-scale, numerical models, Atmos. Environ., 23, 1293–1304, 1989.

Wexler, A. S. and Clegg, S. L.: Atmospheric aerosol models for systems including the ions H^+, NH_4^+, Na^+, SO_4^{2-}, NO_3^-, Cl^-, Br^-, and H_2O, J. Geophys. Res., 107(D14), 4207, doi:10.1029/2001JD000451, 2002.

Wexler, A. S. and Seinfeld, J. H.: The distribution of ammonium salts among a size and composition dispersed aerosol, Atmos. Environ., 24, 1231–1246, 1990.

Zaveri, R. A., Easter, R. C., Fast, J. D., and Peters, L. K.: Model for Simulating Aerosol Interactions and Chemistry (MOSAIC), J. Geophys. Res., 113, D13204, doi:10.1029/2007JD008782, 2008.

Zhang, L., Gong, S., Padro, J., and Barrie, L.: A size-segregated particle dry deposition scheme for an atmospheric aerosol module, Atmos. Environ., 35, 549–560, 2001.

Zhang, K. M. and Wexler, A. S.: Modeling urban and regional aerosols-Development of the UCD Aerosol Module and implementation in CMAQ model, Atmos. Environ., 42, 3166–3178, 2008.

Paper II

Atmos. Chem. Phys., 11, 5897–5915, 2011
www.atmos-chem-phys.net/11/5897/2011/
doi:10.5194/acp-11-5897-2011

Atmospheric
Chemistry
and Physics

Aerosol ageing in an urban plume – implication for climate

P. Roldin[1], **E. Swietlicki**[1], **A. Massling**[1,*], **A. Kristensson**[1], **J. Löndahl**[1], **A. Eriksson**[1,2], **J. Pagels**[2], **and S. Gustafsson**[3]

[1]Division of Nuclear Physics, Lund University, 221 00, Lund, Sweden
[2]Division of Ergonomics and Aerosol Technology, Lund University, Sweden
[3]Environmental Department, City of Malmö, Sweden
[*]now at: National Environmental Research Institute, Dept. of Atmospheric Environment, Aarhus University, Denmark

Received: 14 July 2010 – Published in Atmos. Chem. Phys. Discuss.: 10 August 2010
Revised: 20 January 2011 – Accepted: 14 February 2011 – Published: 22 June 2011

Abstract. The climate effects downwind of an urban area resulting from gaseous and particulate emissions within the city are as yet inadequately quantified. The aim of this work was to estimate these effects for Malmö city in southern Sweden (population 280 000). The chemical and physical particle properties were simulated with a model for Aerosol Dynamics, gas phase CHEMistry and radiative transfer calculations (ADCHEM) following the trajectory movement from upwind of Malmö, through the urban background environment and finally tens and hundreds of kilometers downwind of Malmö. The model results were evaluated using measurements of the particle number size distribution and chemical composition. The total particle number concentration 50 km (~ 3 h) downwind, in the center of the Malmö plume, is about 3700 cm^{-3} of which the Malmö contribution is roughly 30%. Condensation of nitric acid, ammonium and to a smaller extent oxidized organic compounds formed from the emissions in Malmö increases the secondary aerosol formation with a maximum of 0.7–0.8 µg m^{-3} 6 to 18 h downwind of Malmö. The secondary mass contribution dominates over the primary soot contribution from Malmö already 3 to 4 h downwind of the emission sources and contributes to an enhanced total surface direct or indirect aerosol shortwave radiative forcing in the center of the urban plume ranging from -0.3 to -3.3 W m^{-2} depending on the distance from Malmö, and the specific cloud properties.

1 Introduction

In recent years several studies have shown that anthropogenic emissions of trace gases and aerosol particles from urban areas are important for particle properties relevant for climate and population health, not only within the source region itself but also several hundred kilometers downwind (e.g. Seinfeld et al., 2004; Gaydos et al., 2007; Hodzic et al., 2009; Tie et al., 2009). Hence, there is an urgent need to accurately incorporate these urban emissions into regional and global three dimensional Chemistry Transport Models (3-D-CTMs) and even global climate models. The urban background stations measure freshly emitted particles in the beginning of the ageing process. Still, the distances from the emission sources are much shorter than the spatial scales used in global and regional CTMs (Pierce et al., 2009). Therefore, it is important to study the chemical and physical transformation of particles from urban background scale (0.1–1 km) to CTM grid scale (10–100 km scale). Several urban plume studies have been carried out within comprehensive but short field campaigns in large cities (>1 million people), e.g. Mexico City (Doran et al., 2007; Hodzic et al., 2009; Tsimpidi et al., 2010), Tampa (Nolte et al., 2008), Paris (Hodzic et al., 2006) and Copenhagen (Wang et al., 2010), while very few, if any, such studies have been carried out in small to midsize cities (<1 million people). Still, about 60% of the urban population of the world live in small to midsize cities (Population Div. of the Dep. of Economic and Social Affairs of the UN Secretariat), and by number they are far more common and well distributed over the globe than those who live in large cities. Even though one small city's emissions alone are of little concern on a global scale, they together cause a large portion of the global anthropogenic particle and gas phase emissions. Therefore it is important to consider these emissions when discussing climate and health effects of particles and gases on any spatial scale and to implement them into regional and global CTMs.

Most previous studies which have approached to model the ageing of urban particle and gas phase emissions downwind of urban areas have used Eulerian 3-D-CTMs with detailed gas and particle phase chemistry, but with relatively coarse spatial horizontal resolution (5×5 km – 36×36 km)

Correspondence to: P. Roldin
(pontus.roldin@nuclear.lu.se)

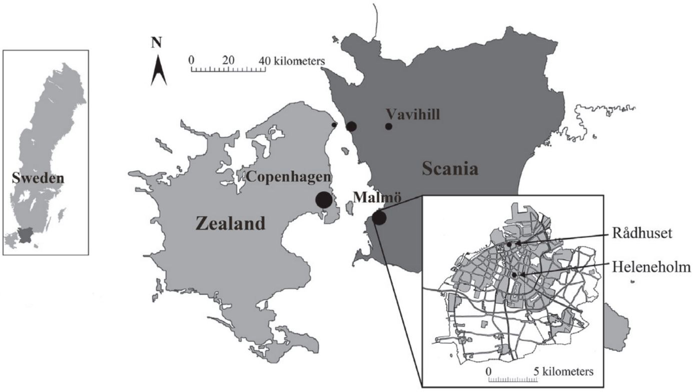

Fig. 1. Geographic map displaying the measurement station in Malmö (Rådhuset), the meteorological mast (Heleneholm) and the Vavihill field station in southern Sweden.

and only very few particle size bins (6–10) (e.g. Hodzic et al., 2006; Gaydos et al., 2007; Nolte et al., 2008; Hodzic et al., 2009). However, when implementing urban background emissions into CTMs, the spatial resolution should preferably be at least $1 \times 1\,\mathrm{km}^2$ and the size resolved chemical and physical properties relevant for climate and health effects are only poorly represented when using only a few size bins.

In this work a trajectory model for Aerosol Dynamics, gas phase CHEMistry and radiative transfer calculations (ADCHEM), developed at Lund University (Roldin et al., 2011), has been used to simulate the aging of the urban plume from the city of Malmö in Southern Sweden (13°00′ E, 55°36′ N, 280 000 people) during the year 2005 and 2006. ADCHEM includes all important aerosol dynamic processes, detailed gas and particle phase chemistry and dispersion in the vertical and horizontal direction, perpendicular to the urban plume. The computational advantage of the Lagrangian compared to the Eulerian approach allows the user to include a large number of size bins (in this study 100 size bins between 1.5 and 2500 nm in diameter) and still to keep a high horizontal and temporal resolution (in this study 1 km and 1 min). Hence, ADCHEM can be used to model the ageing of urban emissions from urban background to regional scales (several hundred kilometers from the source).

This work mainly describes the methods used to estimate the regional influence from the Malmö particle and gas phase emissions, the average results from these urban plume studies and finally gives estimates of different particle properties relevant for climate on the regional scale. For a detailed description and evaluation of ADCHEM the reader is referred to Roldin et al. (2011).

The aim of this study was to estimate the influence of the urban particle and gas phase emissions in Malmö on climate relevant particle properties downwind of the city, e.g. radiative forcing (ΔF). A second aim was to test methods and provide results that could form a basis for up-scaling from urban sub-grid emissions to the regional scale which can be treated by and implemented in regional and global 3-D-CTMs.

2 Methods for urban plume studies

In this section the methods used to characterize the properties of the aerosol particles inside the urban plume from Malmö is described. These methods were applied for 26 urban plume cases and the average and median results are presented in this article.

2.1 Measurements

Particle and gas phase concentration data from two different stations in Sweden were either used as input data in ADCHEM or to evaluate the model results. The stations were an urban background station positioned in Malmö (Rådhuset, 55°36′ N, 13°00′ E, 30 m a.s.l.) and the European Monitoring and Evaluation Program (EMEP) background station Vavihill (56°01′ N, 13°09′ E, 172 m a.s.l.), about 50 km north from Malmö (Fig. 1). A description of the measurement station Vavihill can be found in Kristensson et al. (2008).

The particle number size distributions in Malmö and Vavihill were measured with a Scanning Mobility Particle Sizer (SMPS) and a Twin Differential Mobility Particle Sizer (TDMPS), respectively. The SMPS system in Malmö measured the urban background particle number size distribution at the roof top level of the town hall (Rådhuset) in the north-western part downtown Malmö (Fig. 1). During southerly wind directions the station detected particle concentrations which are representative for the major particle emissions from Malmö.

The SMPS system in Malmö sampled air through a PM_{10} inlet (Patashnik and Rupprecht, 1991). The sampled particles were brought to charge equilibrium using a bipolar charger before size separation in a medium Vienna-type Differential Mobility Analyzer (DMA) (Winklmayr et al., 1991) and were subsequently counted by a Condensation Particle Counter (CPC) (model CPC 3760A) (TSI Inc., Shoreview, MN, USA). This way a full particle number size distribution between 10 and 660 nm in diameter was measured within 3 min. The short sampling time enabled the instrument to capture the rapidly changing particle concentrations at the urban site.

The TDMPS system at the Vavihill field station measured the rural background particle number size distribution from 3 to 900 nm with 10 min time resolution, in a similar way as the SMPS system in Malmö (Kristensson et al., 2008).

As an independent way of testing the accuracy of the ADCHEM model in describing the aerosol chemical composition, data from Time of Flight Aerosol Mass Spectrometry (ToF-AMS) measurements at Vavihill were compared with the average model results. The AMS measurements were not conducted at the time of the modeled period but during two campaigns in October 2008 and March 2009 (Eriksson, 2009). The AMS results (in total 40 h of data) are selected for periods with southerly originated air masses passing over the Malmö region between 1–6 h before they reach Vavihill. According to HYSPLIT model trajectories (Draxler and Rolph, 2011) these air masses have their origin from similar European source regions as the trajectories for the modeled case studies (e.g. Great Britain, Germany, Denmark, Benelux and Poland) (see Fig. 2). Because of the relatively few hours with AMS results for southerly originated air masses and the lack of AMS measurements at the time of the modeled period (April–November, 2005 and 2006), the model results cannot be directly compared with these measurements. The main reason for this is that meteorological conditions show both large diurnal and seasonal variations, which have a large influence on the gas to particle partitioning and formation rate of e.g. nitrate and condensable organic compounds. However, the AMS data still give a representative picture of the relative concentrations of different compounds in different size classes and hence, it is of great value for the evaluation of modeled chemical composition. Measured concentrations of NO, NO_2, O_3 and SO_2 at the urban background station in Malmö and in addition O_3 at Vavihill, from the modeled time periods, were compared with the modeled gas phase concentrations along the trajectory for each urban plume case. All gas concentrations were averaged to 1 h time resolution data when compared with the model results. NO_2 and NO_x were measured with chemiluminescence technique and SO_2 with UV-fluorescence technique. The total NO_x concentration is detected by first oxidizing all NO to NO_2. At both stations O_3 was measured using the principle of UV-absorption.

Apart from measured particle and gas phase concentrations, measurements of the wind direction from a meteorological mast in Malmö (Heleneholm) were used to verify that the urban plume from Malmö was directed towards Vavihill. The wind direction was measured at 24 m a.g.l. The position of the meteorological mast is displayed in Fig. 1.

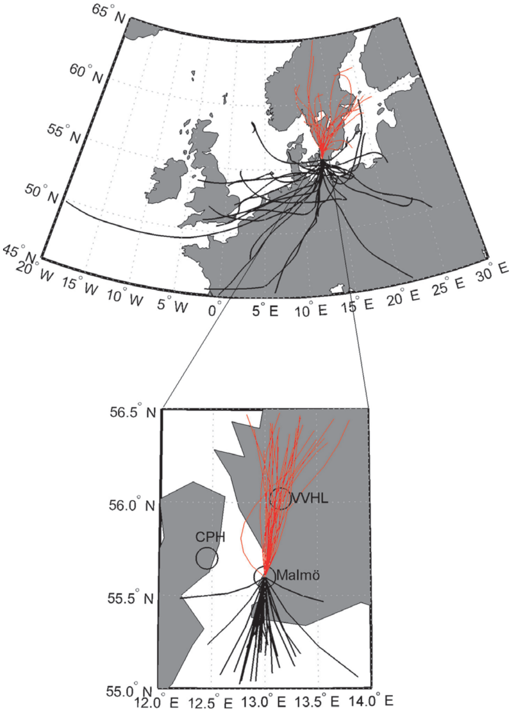

Fig. 2. 24 h forward trajectories (red) and 48 h backward trajectories (black) with starting point in Malmö for all the 26 urban plume cases. Vavihill (VVHL), Malmö and Copenhagen (CPH) are illustrated with circles.

2.2 The ADCHEM model

For more detailed information about all the modules and methods (e.g. condensation/evaporation algorithms, SOA formation models and size structure methods) and their influence on the model results the reader is referred to Roldin et al. (2011).

ADCHEM can be divided into three sub-models:

1. an atmospheric aerosol dynamics and particle chemistry model,
2. a chemical gas phase model,
3. a radiative transfer model.

The aerosol dynamic model is a sectional model which discretizes the particle number size distribution into finite size bins. The particles are assumed to be internally mixed which means that all particles of a certain size have equal composition. The model includes the following processes: condensation, evaporation, dry deposition, Brownian coagulation, wet deposition, in-cloud processing with dissolution of SO_2 and H_2O_2 forming sulfate (S(VI)), primary particle emissions, homogeneous nucleation and dispersion in the vertical (1-D model) and horizontal direction (2-D model) perpendicular to an air mass trajectory. The particle number size distribution changes upon condensation/evaporation and coagulation is either treated with the full-moving, full-stationary or moving-center structure method, which are all mass and number conserving (e.g. Jacobson, 2005b). The full-moving method is only useful for box-model simulations, because it cannot be used when particles are mixed between adjacent grid cells. In Roldin et al. (2011) it was shown that the moving-center structure method can give unrealistic size distributions if more than approximately 25 size bins between 1.5 and 2500 nm in diameter are used, while the full-stationary structure method gives significant numerical diffusion if less than 50 size bins are used. Because high size bin resolution was preferred, the full-stationary method with 100 size bins between 1.5 and 2500 nm in diameter was used for all simulations performed in this work.

The modeled aerosol particles are composed of sulfate, nitrate, ammonium, sodium, chloride, non water soluble minerals (metal oxides/hydroxides), soot, Primary Organic Aerosol (POA), Anthropogenic and Biogenic Secondary Organic Aerosol (ASOA and BSOA). With ADCHEM the SOA formation can either be modeled using the 2-product model approach (Odum et al., 1996), or using the 2-D-VBS method, which apart from saturation concentration (C^*) includes oxygen to carbon ratio (O/C-ratio) as a second dimension (Jimenez et al., 2009).

The condensation and evaporation of H_2SO_4, HNO_3, HCl and NH_3 can either be modeled as uncoupled or coupled processes (e.g. Zhang and Wexler, 2008). One advantage using the approach of coupled condensation is that the mass transfer of acids and bases becomes independent of pH in the particle water phase. The disadvantage is however that this method can only be used if the particles are near acid neutralized (S(VI) in the form of SO_4^{-2}) (Zaveri et al., 2008; Zhang and Wexler, 2008; Roldin et al., 2011). When using the approach of uncoupled condensation the condensation processes of acids and bases are treated as separate processes which depend on the pH in the particle water phase. Therefore this method can also be used when the aerosol particles are not fully acid neutralized. When considering uncoupled condensation ADCHEM uses the prediction of non-equilibrium growth (PNG) scheme developed by Jacobson (2005a). In this scheme the dissolution of ammonia is treated as an equilibrium process after the diffusion limited condensation/evaporation of all inorganic acids. This enables the model to take long time steps (minutes) without causing the modeled pH to start oscillating.

The gas phase model considers 130 different chemical reactions between 61 individual species. The majority of the reactions considered in the kinetic code was described by Pirjola and Kulmala (1998) but is originally from EMEP. Daily isoprene and monoterpene emissions were simulated separately with the vegetation model LPJ-GUESS (Smith et al., 2001; Sitch et al., 2003), in which process-based algorithms of terpenoid emissions were included (Arneth et al., 2007; Schurgers et al., 2009). These natural emissions were corrected for anthropogenic land cover according to Ramankutty et al. (2008).

In the present version of ADCHEM about one third of the non-methane volatile organic carbon (NMVOC) emissions from road traffic are benzene, toluene and xylene (BTX). These light aromatic compounds first react with OH followed by either reaction with NO forming products with low SOA-yields, or with HO_2 resulting in products with generally higher SOA-yields (Ng et al., 2007). In the supplementary material to Roldin et al. (2011) the benzene, toluene and xylene SOA yields from the 2-D-VBS model, for low and high NO_x conditions, are given as function of the total organic particle mass. At high NO_x/HO_2 ratios, which generally are the case in urban environments, most of the oxidation products will react with NO, while at remote regions and in the free troposphere the HO_2-pathway usually dominates. Hence, oxidation of BTX in urban environments generally gives relatively low SOA formation, while moving further away from the source the SOA formation can be considerably higher. Here it is mainly benzene, which is the least reactive of the three compounds, that is left to form SOA (Henze et al., 2008). In ADCHEM both the high and low NO_x reaction pathways are considered simultaneously. The reaction rate for the low-NO_x pathway is given by $k_{RO_2 + HO_2} = 1.4\times10^{-12}\exp(700/T)\,\mathrm{cm^3\,molecule^{-1}\,s^{-1}}$ and the reaction rate for the high-NO_x pathway by $k_{RO_2 + NO} = 2.6\times10^{-12}\exp(350/T)\,\mathrm{cm^3\,molecule^{-1}\,s^{-1}}$ (the Master Chemical Mechanism v 3.1 (http://www.chem.leeds.ac.uk/Atmospheric/MCM/mcmproj.html)).

The radiative transfer model is used to derive the spectral actinic flux which affects the photochemical reaction rates. This model uses a quadrature two-stream approximation scheme, where the radiative fluxes are approximated with one upward and one downward flux component. This scheme was developed and used by Toon et al. (1989) to calculate the radiative transfer in a vertically inhomogeneous atmosphere with clouds and aerosol particles.

In Roldin et al. (2011) it was illustrated that the particles in the urban plume from Malmö are at least not always completely acid neutralized. Hence, for all simulation performed in this work the condensation of acids and bases were treated as uncoupled processes. The SOA formation was modeled with 2-D-VBS for high and low NO_x conditions according to the parameterization in Roldin et al. (2011). The POA was modeled as semi-volatile (with a C^* between 10^{-2} and $10^4\,\mu g\,m^{-3}$) and the intermediate VOC (IVOC) emissions (C^* between 10^4 and $10^6\,\mu g\,m^{-3}$) was assumed to be 1.5 times larger than the anthropogenic POA emissions according to Robinson et al. (2007). The volatility of the POA emissions and the IVOC emissions are uncertain, but these values have been used as best estimates in several previous model studies (e.g. Robinson et al., 2007; Shrivastava et al., 2008; Tsimpidi et al., 2010). For all simulations performed in this work the POA emissions were initially treated as entirely in the particle phase. However, downwind of the emission source most of this organic material evaporates from the particles. In the gas phase this material is oxidized and then again returns to the particle phase as oxidized organic compounds. In Roldin et al. (2011) several sensitivity tests were performed with ADCHEM to study the effect of SVPOA or non-volatile POA and the importance of the IVOC emissions.

The 2-D-VBS model in ADCHEM considers the kinetic (diffusion limited) condensation/evaporation of 110 different organic compounds, separated into 10 different volatility classes with C^* between 10^{-2} and $10^7\,\mu g\,m^{-3}$ and 11 different O:C-ratio levels from 0 to 1. One large assumption with the 2-D-VBS is that the gas phase compounds, independent of their origin, react with OH with the same reaction rate, equal to $3 \times 10^{-11}\,cm^3\,molecule^{-1}$ (Jimenez et al., 2009). The reaction rates for the first oxidation step of all monoterpenes, isoprene, benzene, toluene and xylene, are however species specific and considered before the formed oxidation products enter the VBS. The only compounds which enter directly into the VBS before they have been oxidized are POA species and IVOCs. For each oxidation reaction in the 2-D-VBS, one to three oxygen atoms are added to the oxidized molecule according to a probability distribution function. The formed oxidation product can then either stay intact (functionalize) or fragmentize into several smaller molecules. Depending on the size of the fragments and the number of added oxygen atoms, they can either have lower or higher volatility than the original molecule. However, if the oxidation product is not fragmentized it will always have lower volatility than the original molecule (see Roldin et al., 2011 for details).

The 2-D-VBS model gives a particle size dependent partitioning of the different condensable organic compounds, with larger fraction of low volatile compounds found in the smaller particle sizes and a larger fraction of more volatile compounds found in the larger particle sizes. The kinetic and particle size dependent condensation/evaporation processes require that ADCHEM keeps track of all the different organic compounds in each particle size bin, which is computationally expensive, especially for the coagulation algorithm (for more information see Roldin et al., 2011).

2.3 Model inputs

Meteorological data from the Global Data Assimilation System (GDAS) were downloaded from NOAA Air Resource Laboratory Real-time Environmental Application and Display sYstem (READY) (Rolph, 2011). Along each trajectory, data of solar irradiance, mixing height and rainfall intensity with one hour time resolution was included. For every three hours along the trajectories, vertical temperature and relative humidity profiles were received. The vertical temperature and relative humidity data was linearly interpolated to the fixed vertical grid that was used for the simulations. Linear interpolation of all meteorological data was also carried out to increase the temporal resolution to 1 min, which was the time step used by ADCHEM.

Country specific forest and meadow/pasture area coverage information from Simpson et al. (1999), and emissions of isoprene and monoterpenes from LPJ-GUESS and anthropogenic NMVOCs, NO_x, SO_2, CO, NH_3 and $PM_{2.5}$ emissions were included along the trajectories. For Denmark and southern Sweden (54°48′ N to 56°22′ N) the anthropogenic yearly average emissions along the trajectories were received from the National Environmental Research Institute (NERI) in Denmark and the Environmental Dept., City of Malmö (Gustafsson, 2001) in Sweden, respectively. For Danish road emissions, a spatial resolution of $1 \times 1\,km^2$ was obtained, based on NERI's traffic database with traffic volumes on all road links in Denmark for the year 2005, together with emission factors from the COPERT IV model applied for 2008. For other (non-road) sources in Denmark, an emission inventory with $17 \times 17\,km^2$ spatial resolution was used based on Danish national emission inventories for the year 2007 provided by NERI (http://emission.dmu.dk). For southern Sweden, all anthropogenic emissions had a spatial resolution of $1 \times 1\,km^2$. The southern Swedish emission data base has previously primary been used for epidemiological studies in relation to NO_x and NO_2 exposure (e.g. Chaix et al., 2006; Stroh et al., 2007). For the rest of Europe the emissions within our study were taken from the EMEP emission database for year 2006 (Vestreng et al., 2006). These emissions have a spatial resolution of $50 \times 50\,km^2$. The yearly anthropogenic emissions were multiplied with country specific diurnal, weekly and monthly variation factors based on the EMEP emission database. The forest and meadow/pasture data was used to estimate the surface albedo and roughness length.

The measured particle number size distributions were averaged to 30 min values in Malmö and at Vavihill. They were parameterized by fitting 5 modal lognormal distributions to the data using the automatic lognormal fitting algorithm DO-FIT, version 4.20 (Hussein et al., 2005). Because of the lower detection limit of 10 nm for the SMPS system in Malmö, the actual number concentration of the nucleation mode particles in Malmö is uncertain. The particle number size distributions upwind of Malmö were estimated from the measured background conditions at Vavihill (see Sect. 2.4) and used as initial condition in the model. Limitations and uncertainties with this method are discussed in Sect. 2.7. The contribution from local emissions in Malmö was derived as the difference between the estimated background size distribution and the measured size distribution in Malmö. These particles mainly originate from road traffic within the city. In Sect. 2.5 a description is given of how these local particle emissions were introduced into the model over Malmö.

The initial (48 h upwind of Malmö) $PM_{2.5}$ chemical composition was estimated from the aerosol mass spectrometer (AMS) measurements carried out at several European sites (Jimenez et al., 2009) with approximately 35% organic matter, 26% sulfate, 7% nitrate, 12% ammonium, 3% soot and 17% minerals (metal oxides/hydroxides) below 1000 m a.g.l. and changing linearly to the top of the model domain (2000 m a.g.l.) to 23% organic matter, 36% sulfate, 11% nitrate, 17% ammonium, 2% soot and 11% minerals.

2.4 Background particle properties outside the urban plume

To be able to estimate the contribution of urban emissions to the regional background particle concentration between Malmö and Vavihill, the background without influence of the urban plume has to be approximated. This was achieved by selecting measured particle number size distributions averaged to 30 min values before and after the time of arrival of the urban plume from Malmö, at Vavihill. The background was estimated as the average of these two 30 min averages. This background particle number size distribution was also used to represent the conditions upwind of Malmö (see Sect. 2.7). The detailed criteria for the selection of background distributions are:

1. The trajectories should not move over Malmö or Copenhagen before they reach Vavihill.
2. At the time for the measurement of the estimated background, the air mass trajectory reaching Vavihill should originate from the same source region, 48 h backward in time, as the trajectory influenced by the Malmö plume.
3. The selected background particle number size distribution should have been measured within 6 h before or after the urban plume reached Vavihill.
4. The selected background particle number size distributions before and after the Malmö plume observed at Vavihill should have similar shape and magnitude.
5. The original particle number size distribution at 10 min time resolution should show only low temporal variability within the averaging period.
6. If several particle number size distributions seemed to obey criteria 1 to 5 equally well, the distribution measured nearest in time before or after the Malmö plume reached Vavihill was selected.

2.5 Spin-up time upwind of Malmö

The total run time of each simulation was three days, starting two days before the air mass trajectory reached Malmö and continuing one day downwind of Malmö. The first two days of the simulations were used to initialize (equilibrate) the particle and gas phase chemistry. During this time the particle number size distribution was kept fixed, while all other parameters were allowed to change. After the trajectory reached the urban background station in Malmö, the particle number size distribution was also allowed to change.

When the trajectory arrived at the southern border of Malmö, the estimated size dependent local particle number concentration contribution was included in each grid cell within the boundary layer, according to Eqs. (1) and (2). With these equations the particle emissions are scaled horizontally using the accumulated horizontal (west to east) NO_x-emission profile (E_{NO_x}) from the southern border of Malmö to the measurement station. Equation (1) gives the estimated particle number concentration in each diameter size bin at the time when the trajectory arrived at the measurement station in Malmö, while Eq. (2) gives the estimated particle number concentration in each diameter size bin for each time step (i) between the southern border of Malmö ($i=1$) and the measurement station ($i=N$), at the north western part of the city. Equation (2) takes into account the dynamic and chemical processing of the aerosol number size distribution in each time step between the southern border and the measurement station in the northern part of Malmö. Hence, it is not just a simple linear interpolation of the particle number size distribution between these two points ($i=1$ and $i=N$). Instead it is a linear interpolation for each time step, but of a different kind that includes the effects of dynamic and chemical processing on the particle number size distribution in the previous time step. In other words, for each of the time steps (i), the interpolation is performed between the concentration one time step backwards ($i-1$) from the current time step and the final time step at the measurement station (time step N).

$$c_N^j(D_\mathrm{p}) = c_\mathrm{backg}(D_\mathrm{p}) + \frac{\sum\limits_{k=1}^{N} E_{\mathrm{NO_x}}^{j}}{\sum\limits_{k=1}^{N} E_{\mathrm{NO_x}}^{\mathrm{center}}} c_\mathrm{traffic}(D_\mathrm{p}) \quad (1)$$

$$c_i^j(D_\mathrm{p}) = \left(\frac{N-i}{N} c_{i-1}^j(D_\mathrm{p}) + \frac{i}{N} c_N^j(D_\mathrm{p}) \right) \quad (2)$$

$c(D_\mathrm{p})$ in Eqs. (1) and (2) is the concentration of particles with a diameter equal to D_p. N is the number of time steps which the trajectory travels over Malmö before reaching the measurement station. c_backg (D_p) is the estimated background particle number concentration outside Malmö (initial concentration), j is the horizontal grid cell index (1–20), $E_{\mathrm{NO_x}}^{j}$ is the $\mathrm{NO_x}$ emissions factor from road traffic at the horizontal grid cell index j, $E_{\mathrm{NO_x}}^{\mathrm{center}}$ is the $\mathrm{NO_x}$ emission factor from road traffic in the center of the horizontal model domain ($j = 10$ and 11) and i is the time step index which starts at 1 when the air mass reaches the southern border of Malmö and reaches N, when the trajectory arrives at the measurement station. $c_{\mathrm{traffic}}(D_{\mathrm{p}})$ is the estimated size-dependent local particle number concentration contribution from road traffic in the center of the urban plume, which was derived by taking the difference between the measured particle number size distribution in Malmö and the estimated upwind background particle number size distribution (Sect. 2.4). When using Eq. (1) the particle number size distribution at the center of the urban plume within the boundary layer becomes comparable to the measured particle number size distribution in Malmö at that time. The horizontal (west to east) $\mathrm{NO_x}$ emission profile ($E_{\mathrm{NO_x}}$) for Malmö was derived from the $\mathrm{NO_x}$ emission database from road traffic within Malmö by averaging the horizontal $\mathrm{NO_x}$ emission profiles at the western and eastern side of the trajectory, upwind of the measurement station. The $\mathrm{NO_x}$ emission profile resembles a Gaussian distribution with a maximum in the center of the urban plume ($E_{\mathrm{NO_x}}^{\mathrm{center}}$) and with a full width at half maximum of 7 km. Since the $\mathrm{NO_x}$ emissions from road traffic in Malmö are largest in the center of the horizontal model domain, the particle concentrations derived in the model are highest at the measurement station and drop towards the estimated background concentrations at the horizontal boundaries.

2.6 When does the urban plume from Malmö influence Vavihill?

Wind direction measurements from the meteorological mast in Malmö together with HYSPLIT trajectories were used for a first selection of days with possible influence from Malmö on the background station Vavihill. In total 39 days were identified between April 2005 and October 2006. From these days 232 case studies were selected to cover all periods with possible influence from Malmö on Vavihill. All these cases were then modeled using a simplified 1-D version of ADCHEM, excluding detailed particle and gas phase chemistry and homogeneous nucleation, and assuming a fixed concentration of 10^7 molecules cm^{-3} of a non-volatile condensable compound with a molar mass of 150 g mol^{-1}. The modeled particle number size distributions at Vavihill were compared with the measured particle number size distributions at Vavihill at the time of arrival of the trajectories. For cases with less than 20% difference between the measured and modeled number and surface area concentration, and less than 30% difference in the volume concentration between 10 and 600 nm in diameter, it was considered to be likely that the Malmö emissions influenced Vavihill. In total, 67 out of 232 cases, from 26 out of 39 days fulfilled these criteria. Cases with rainfall between Malmö and Vavihill were not considered. However, for several cases rainfall was occurring both upwind of Malmö and downwind of Vavihill. The 67 cases were then modeled with a complex 1-D version of ADCHEM, which included all processes considered by the model except horizontal dispersion. From these simulations, the case with best agreement between the model and measurements, from each of the 26 days was finally selected. Only one case was selected for each day to ensure that certain conditions were not overrepresented, when deriving the average properties of the urban plume. For all of these 26 cases the modeled and measured number and surface area concentration agreed within 10% and the volume concentration within 20% for particles between 10 and 600 nm in diameter. Table 1 gives the diurnal, weekly and monthly distribution of all 26 case studies. Due to a lack of parallel measurements at Vavihill and Malmö station, no urban plume studies for the period November to March could be carried out.

Table 1. Diurnal, weekly and monthly distribution of all 26 simulated cases. The time is given as local wintertime at the time when the trajectories arrived in Malmö.

Day	Mon.	Tue.	Wed.	Thu.	Fri.	Sat.	Sun.
No. of sim.	6	2	1	6	1	5	5
Month	Apr.	May	Jun.	Jul.	Aug.	Sep.	Oct.
No. of sim.	1	4	8	3	0	3	7
Time	00:00–06:00	06:00–12:00		12:00–18:00		18:00–00:00	
No. of sim.	7	7		7		5	

2.7 The upwind background particle number size distributions

The background contribution to the particle number size distribution in Malmö and upwind of Malmö was approximated with the measured Vavihill background size distribution as described in Sect. 2.4. This relies on the premise that the particle number size distribution for the background is not changing between upwind of Malmö and Vavihill which is a distance of about 50 km. However, the distributions are not identical at these sites in reality due to aerosol dynamic processes. To illustrate this, the modeled background particle number size distribution outside the urban plume at Vavihill can be compared with the estimated upwind of Malmö particle number size distribution (measured Vavihill background particle number size distribution) (see Fig. S1 in the online supplementary material). Figure S1 shows that the particle number size distribution is altered during the air mass transport between upwind of Malmö and Vavihill for the average of the 26 model cases described in Sect. 2.6. On the other hand, the second message from this exercise is that this change is relatively small (about 200 cm^{-3} or 8% lower particle number concentration between 5 and 1000 nm, outside the urban plume at Vavihill compared with upwind of Malmö), and hence can be considered acceptable for the model experiments.

2.8 Estimating the secondary aerosol formation within the urban plume

All 26 selected case studies were modeled with and without anthropogenic gas phase emissions in Malmö. The anthropogenic gases considered were NO_x, SO_2, CO, NMVOCs, and the IVOCs. All other conditions for the simulations except the emissions of these gases in Malmö were identical for the two model setups. The difference between the results with or without anthropogenic gas phase emissions in Malmö were then used to estimate the importance of these emissions for the secondary aerosol formation and to answer the question of how this secondary aerosol formation influences the climate relevant particle properties downwind of the city.

2.9 Climate relevant particle properties downwind of Malmö

Using the modeled average particle properties within the urban plume downwind of Malmö, attempts were made to estimate the shortwave radiative forcing (ΔF) of Malmö emissions on the regional scale, with and without clouds. The radiative forcing due to the gas phase and particle emissions in Malmö was calculated for different distances (or hours) downwind of Malmö.

To be able to estimate the yearly average shortwave radiative forcing from the Malmö emissions, the average particle properties for the 26 case studies were assumed to be representative for the yearly average particle properties in the Malmö urban plume within the boundary layer. From October to March the boundary layer height was assumed to be 300 m during the night reaching a maximum of 500 m during the day, while between April and September it was assumed to be 300 m during the night reaching a maximum of 1200 m during the day. For the investigation of light scattering and absorption of the aerosol particles, the average relative humidity profile from all 26 simulations in Malmö was used, with an average relative humidity of 78% within the lowest 2000 m of the atmosphere. The particle growth factors due to water uptake were calculated with the thermodynamic model used in ADCHEM. Size-resolved refractive indices of the aerosol particles were estimated from the modeled volume fractions of soot, organic matter, minerals (metal oxides/hydroxides), water soluble inorganic salts and water, with refractive indices reported by Schmid et al. (2009), Horvath (1998) and Sokolik and Toon (1999).

The radiative forcing at the surface and at the top of the atmosphere (TOA) caused by the emissions in Malmö was calculated by taking the difference between the modeled irradiance inside and outside the urban plume. The shortwave radiative forcing of the Malmö particle emissions was calculated for each hour of the day (24 h) of each month of the year and then averaged to get the estimated yearly average shortwave radiative forcing in the urban plume from Malmö.

To be able to estimate the radiative forcing during the presence of clouds an adiabatic cloud parcel model was used to derive realistic cloud properties (Jacobson, 2005b). Although they are realistic, these cloud properties are only hypothetical and will not be fully representative of the yearly average cloud cover in the Malmö region. Therefore, the derived shortwave radiative forcing during the presence of clouds should not be considered as the best estimate of the yearly average shortwave radiative forcing from the Malmö emissions. The calculations are instead intended to illustrate that the shortwave radiative forcing of the gas and particle emissions can be substantially different during completely cloudy and non-cloudy days.

The adiabatic cloud parcel model calculates the relative humidity, temperature, total liquid water content (LWC), particle number and cloud droplet number size distributions, as a function of the altitude of an air parcel with a pre-specified updraft velocity, taking into account the adiabatic expansion and the latent heat release upon condensation. Raoult's law and the Kelvin effect are used to derive the water saturation concentration in moles per cubic centimeter of air above each particle or droplet surface, and then the concentration gradient between the gas and particle phase, which drives the mass transfer to or from the particle surfaces, is updated for each time step. For a more detailed description of the model, the reader is referred to Jacobson (2005b).

According to Rogers and Yau (1989) typical updraft velocities for stratus clouds are on the order of a few tens of centimeters per second and for cumulus clouds in the order of meters per second. For the simulations performed in this work the updraft velocity inside the clouds was assumed to be $1.0\,\mathrm{m\,s^{-1}}$. The mass accommodation of the condensing water as well as the thermal accommodation coefficient used to calculate the thermal conductivity of the latent heat release of evaporating water were set equal to one. The number of size bins was set to 200 between 50 nm and 1000 nm in dry particle diameter. The chemical and physical particle properties from ADCHEM were linearly interpolated to fit the diameter size resolution. Only the inorganic salts were allowed to take up water, while the organic fraction was treated together with minerals and soot as an insoluble core. The condensation/evaporation solver used the full moving structure method to account for the changing particle sizes (see e.g. Jacobson, 2005b or Roldin et al., 2011).

In the radiative transfer model 100 m or 500 m thick clouds with properties modeled with the adiabatic cloud parcel model were included at the top of the boundary layer. The absorption of infrared radiation inside the clouds was not considered in the model.

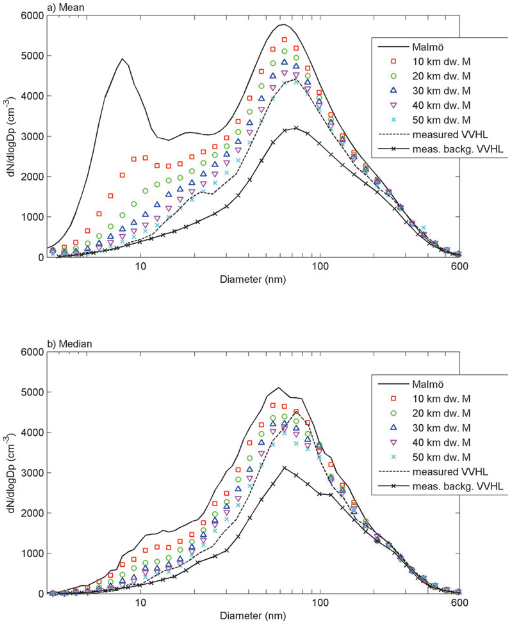

Fig. 3. Modeled average **(a)** and median **(b)** particle number size distributions in the center of the urban plume, 10, 20, 30, 40 and 50 km downwind of Malmö, together with the measured particle number size distributions in Malmö and at Vavihill (50 km downwind of Malmö). The displayed size distributions in Malmö were derived from the SMPS measurements applying the lognormal fitting algorithm from Hussein et al. (2005) for each individual size distribution and then taking the average and median of these size distributions.

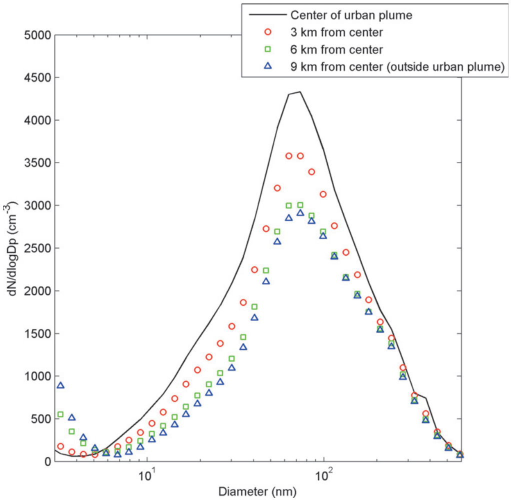

Fig. 4. Modeled average particle number size distributions at different distances (perpendicular to the air mass trajectories) from the center of the urban plume at Vavihill.

3 Results and discussion

The influence of Malmö city emissions on rural background particle concentrations is studied in 26 different cases using HYSPLIT air mass trajectories starting upwind of Malmö, going over Malmö and stretching hundreds of kilometers downwind of Malmö (Fig. 2). Most of the simulated trajectories originate over continental Europe (e.g. Germany, Poland and Benelux) or Great Britain. The trajectories pass over the EMEP background station Vavihill, ca 50 km downwind and north of Malmö. Vavihill is used for the validation of aerosol properties modeled with ADCHEM. Downwind of Vavihill, the majority of trajectories continue northward over Sweden.

3.1 Modeled and measured particle number size distributions in the urban plume of Malmö

Figure 3 illustrates the modeled average (a) and median (b) particle number size distributions in Malmö and at different distances downwind of Malmö in the center of the urban plume. As a comparison the measured average and median particle number size distributions at Vavihill, with or without influence from Malmö are also displayed. The shape of the size distribution 50 km downwind of Malmö from modeling and from measurements at Vavihill is identical in the urban plume and the total number concentration agrees to within 3% and 0.2% for the average and median, respectively. This indicates that the modeled particle number size distributions in the urban plume between Malmö and Vavihill are realistic. The relatively large concentration ($\sim 2000\,\mathrm{cm}^{-3}$) in the nucleation mode for the average particle number size distribution in Malmö is due to two daytime cases when the nucleation mode in Malmö was clearly dominating the total number concentration. These particles have a relatively short lifetime (minutes to hours) because of coagulation and dry deposition processes downwind of Malmö. However, a fraction (∼ 30%) of these particles survives in the atmosphere all the way to Vavihill, where they appear as a mode around 18 nm in diameter. The lognormal parameterizations of the modeled particle number size distributions in Fig. 3a and b, derived with the DO-FIT algorithm, are given in Table S1 and S2 in the online supplementary material.

Figure 4 shows the modeled average particle number size distributions at the time of arrival at Vavihill at different distances from the center of the urban plume (perpendicular to the air mass trajectory). The results illustrate that for a compact and homogeneously populated city like Malmö the urban influence on the particle properties 50 km downwind of the city often decreases steeply from the urban plume center

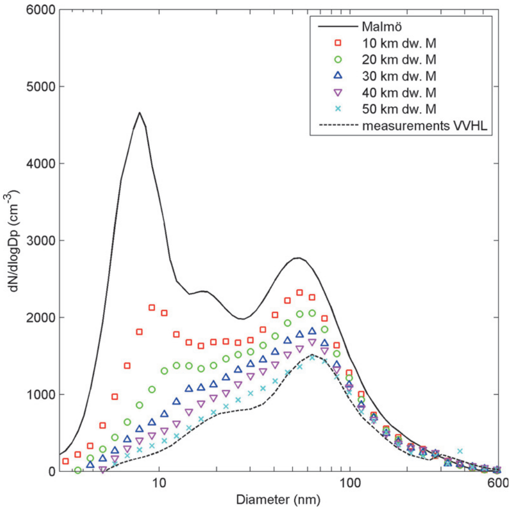

Fig. 5. Estimated average local emission contribution from Malmö, in Malmö, 10, 20, 30, 40 and 50 km downwind of the city. The particle number size distributions were derived by subtracting the modeled background particle number size distribution from the modeled particle number size distributions in the center of the urban plume, at different distances downwind of Malmö. The result from Vavihill was derived by subtracting the measured particle number size distribution at Vavihill when the station was not influenced by the Malmö plume from the measured particle number size distribution at Vavihill when the station was influenced by the Malmö plume.

Table 2. Estimated average and median particle number, surface area and volume concentration (PN_{tot}, PA_{tot}, and PV_{tot} respectively) and its contribution from Malmö (difference between the center of the urban plume and the background) (ΔPN_{urban}, ΔPA_{urban}, and ΔPV_{urban}) for particles between 5 and 1000 nm in diameter in the center of the urban plume, at different distances downwind of Malmö (dw. M.).

Location	$PN_{tot}/\Delta PN_{urban}$ (cm^{-3})	$PA_{tot}/\Delta PA_{urban}$ (µm^2 cm^{-3})	$PV_{tot}/\Delta PV_{urban}$ (µm^3 m^{-3})
Malmö mean	6577/3825	204.1/48.1	8.28/1.49
Malmö median	4459/2049	151.8/30.2	5.53/0.75
10 km dw. M. mean	5313/2587	198.8/43.3	8.25/1.48
10 km dw. M. median	4001/1619	146.7/26.0	5.47/0.74
20 km dw. M. mean	4728/2082	197.6/41.2	8.38/1.46
20 km dw. M. median	3707/1416	146.0/26.6	5.60/0.82
30 km dw. M. mean	4325/1734	197.5/41.2	8.57/1.61
30 km dw. M. median	3486/1235	147.8/29.0	5.86/1.07
40 km dw. M. mean	4029/1520	198.5/43.1	8.82/1.82
40 km dw. M. median	3311/1117	147.7/27.9	6.00/1.11
50 km dw. M. mean	3763/1291	198.3/42.2	9.02/1.90
50 km dw. M. median	3128/960	143.9/23.1	5.86/0.86
VVHL mean	3648/1177*	197.0/40.8*	8.98/1.86*
VVHL median	3135/968*	144.5/23.7*	5.70/0.70*

* Derived from the DMPS measurements at Vavihill.

towards the urban plume boundaries with only marginal influence more than 6 km outside the center of the urban plume.

By subtracting the modeled background particle number size distribution outside the urban plume (9 km from the center of the urban plume) from the modeled distributions inside the plume, the urban emission contribution in the center of the urban plume was estimated at different distances downwind of Malmö (see Fig. 5). As a validation of the model results the urban contribution at Vavihill (50 km downwind of Malmö) was also derived directly from the measured particle number size distributions inside and outside the urban plume. Within Malmö city and close to Malmö the emissions have a large influence on the nucleation and Aitken mode particle concentration. However, most of the nucleation mode particles formed in Malmö are lost by coagulation and dry deposition before the urban plume reaches Vavihill. The soot mode particles mostly originated from traffic, indicated at about 50 nm in Malmö, grew because of condensation to about 65 nm, 50 km downwind of the city. As will be shown in Sect. 3.4 this condensational growth is important for these particles' ability to form cloud droplets.

Table 2 gives the average and median total particle number, surface area and volume concentration (PN_{tot}, PA_{tot} and PV_{tot}) and average and median corresponding urban contribution (ΔPN_{urban}, ΔPA_{urban} and ΔPV_{urban}) for particles between 5 and 1000 nm in diameter at different distances downwind of Malmö. The urban contribution was derived by taking the difference between the concentration in the center of the urban plume and outside the urban plume (background). The total particle number concentration decreases rapidly downwind of Malmö, mainly due to coagulation of the freshly emitted particles onto the long distance transported accumulation mode particles. The estimated Malmö city average contribution to the urban background number concentrations is 58% or 3825 cm^{-3} in absolute terms. At Vavihill, 50 km downwind of Malmö, the average Malmö number concentration contribution is 34% (1291 cm^{-3}) according to the model and 32% (1177 cm^{-3}) according to the DMPS measurements. The modeled volume concentration contribution from the emissions in Malmö increases with 28% between Malmö and 50 km downwind of the city center (from 1.49 to 1.9 µm^3 m^{-3}), mainly attributed to the secondary aerosol formation within the urban plume. The last two rows in Table 2 give the estimated average and median number, surface area and volume concentration contribution at Vavihill, derived from the particle number size distribution measurements. The number concentration contribution derived from the model at Vavihill is 10% higher for the average and less than 1% lower for the median concentration contribution compared to the measurements. For the surface area and volume concentration contribution the model gives 3% and 2% higher average and 3% lower and 23% higher median values compared to the measurements at Vavihill, respectively.

3.2 Uncertainties with the urban emission contribution downwind of Malmö

There are several reasons why the modeled and measured urban concentration contributions are uncertain. Listed are the two reasons which are regarded as the most important.

1. The method used to estimate the urban contribution downwind of Malmö requires that the measured background particle number size distribution at Vavihill is representative for the background conditions outside the urban plume between Malmö and Vavihill. The criteria for the selection of the background distributions were therefore designed to fulfill this requirement (see Sect. 2.4). However, since the background distributions at the time of arrival of the urban plume have to be approximated from the measurements a few hours before and after the urban plume influences Vavihill, some uncertainties with the derived background distributions still remain. Also instrumental errors influence the size distribution. In an intercomparison workshop at the Leibniz Institute for Tropospheric Research in Leipzig, Germany (Wiedensohler, et al., 2010), different SMPS/DMPS systems agreed within ± 10% for a simulated size distribution in the size range from 20 to 200 nm in diameter. In reality, the total concentration spans over several magnitudes, the size range below 20 nm increases the error margin, and the instrument control and maintenance is not as thoroughly supervised as under laboratory conditions. The uncertainty of the choice of the background size distribution and the instrumental uncertainties should add up to a total uncertainty a few percent higher than the ± 10% uncertainty estimated at the workshop. In order not to underestimate the uncertainty, a conservative value of 20% was chosen as the total uncertainty. A 20% error in the estimated average background number concentration outside Malmö would cause an error in the estimated urban contribution within the city of only 13%. However, at Vavihill, where the difference between the background and urban plume number concentration is smaller, the error would become 38%.

2. Another difficulty is the selection of the periods when the urban plume from Malmö affects the background station. In this work, wind direction measurements, HYSPLIT air mass trajectories and aerosol dynamics model simulations were used to find out when the plume from Malmö influenced the background station at Vavihill. On the one hand, these methods are objective in the sense that they do not introduce any bias in terms of individual opinions on how the size distribution downwind of the city "should" look like. On the other hand, these methods are an uncertain way to trace the anthropogenic influence. For better precision, the methods could be complemented with measurements of NO_x or CO at the background station, which could be used as tracers for the urban influence. Unfortunately, these measurements were not available from the station at Vavihill for time periods when this study was carried out.

Other processes with large model uncertainties but with only small to moderate influence of the urban contribution within 50 km downwind of Malmö are:

1. The homogeneous nucleation rate and initial growth rate of the smallest particles.

2. The primary particle emissions downwind of Malmö.

3. The gaseous emissions both upwind and downwind of Malmö and the corresponding SOA formation.

For none of the 26 days which were modeled, significant new particle formation was observed for several consecutive hours at both measurement stations. This indicates that for none of these days large scale regional nucleation events were occurring. Hence, the new particle formation between Malmö and Vavihill was likely also moderate or insignificant for these days, indicated by the good agreement between the model results and the measurements at Vavihill. For 2 out of 26 days large numbers of particles were however observed in the nucleation mode at the measurement station in Malmö. These particles were likely formed from local sources in or near Malmö (e.g. ship traffic). Even though none of the 26 selected days was characterized by large scale nucleation events, homogeneous nucleation can possibly have biased the average results presented in this study. The reason for this is that the simplified model used to make a first selection of possible days with influence from Malmö at Vavihill did not consider homogeneous nucleation and therefore systematically filtered out days with large new particle formation between Malmö and Vavihill.

Although the primary particle emissions downwind of Malmö are uncertain, only marginal effects are expected because of this uncertainty between Malmö and Vavihill. However, the effect might become much larger up to 24 h downwind of Malmö, both for the particle concentrations and chemical composition.

The gaseous emissions both upwind and downwind of Malmö are also uncertain (especially for the IVOCs), which affects the precision of secondary aerosol formation. Finally, most of the reactions involved in the secondary organic aerosol formation are unknown, which gives high uncertainty for this process. Most of these reactions are believed to be too slow to form large amount of SOA between Malmö and Vavihill. However, as for the other processes the uncertainties increase significantly with the distance downwind of Malmö.

Table 3. Measured and modeled average gas phase concentrations in Malmö and at Vavihill for the 26 model cases.

Species and location	Measured average (ppb)	Modeled average (ppb)
O_3 Malmö	25.7	31.5
O_3 Vavihill	32.4	34.3
NO Malmö	2.8	3.5
NO_2 Malmö	11.2	9.5
SO_2 Malmö	1.1	1.1

3.3 Modeled and measured particle and gas phase chemistry

A reasonable agreement between the modeled and the measured gas phase concentrations is important for the modeled particle chemistry. Although the deviation for certain gas phase species is higher than 100% for single case studies, the agreement is better between the average modeled and the measured concentrations as shown in Table 3.

The modeled average ozone concentration in Malmö is about 20% higher than the measured average value, while at Vavihill the model is less than 6% higher than the measurements. Both the measurements and the model give considerably lower ozone levels in Malmö than at Vavihill, with larger differences for the measurements compared to the modeled values.

For NO and NO_2 the modeled concentrations deviate with about 25% and −20% compared to the measured concentrations, respectively. However, the modeled NO_x ($NO + NO_2$) concentration is only 7% lower than the measurements. In the model the molecular NO/NO_x emission ratio was set to 0.9 for all NO_x emission sources. This ratio should probably be lower for better agreement between the modeled and the measured NO and NO_2 concentrations in Malmö. The modeled average SO_2 concentration in the surface layer is identical to the measured concentration.

Figure 6 displays the modeled average $PM_{2.5}$ mass fractions of all chemical compounds considered by the model from 6 h upwind of Malmö until 24 h downwind of Malmö. At Malmö the soot, organic matter and mineral (metal oxides/hydroxides) mass concentrations increase because of the primary particle emissions in the city. According to the model the total organic particle content makes up between 25% and 33% of the total $PM_{2.5}$ mass, with a minimum about 15 h downwind of Malmö. In Malmö 28% of the total organic $PM_{2.5}$ mass is composed of non-oxidized organic material (O:C-ratio equal to zero). This non-oxidized organic material decreases continuously and comprises only 22% of the total organic $PM_{2.5}$ mass 24 h downwind of Malmö. The only sources for these non-oxidized compounds in the 2-D-VBS are low volatile POA emissions which stay in the particle phase upon dilution in the atmosphere. The inorganic salt content is dominated by ammonium nitrate, with a nitrate $PM_{2.5}$ mass fraction varying between a minimum of 24% in Malmö to a maximum of 36% 15 h downwind of Malmö. As expected, the ammonium concentrations show a clear correlation with the nitrate content. According to the model the PM in the urban plume is fully or partly neutralized, with an average of between 1.86 and 1.74 ammonium ions available to neutralize each sulfate ion. The particles were least neutralized 24 h downwind of Malmö.

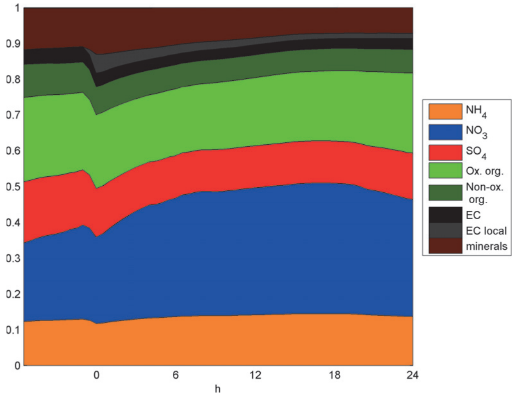

Fig. 6. Modeled average $PM_{2.5}$ mass fractions from 6 h upwind to 24 h downwind of Malmö, at the surface within the urban plume. The organic mass is divided into non-oxidized (O:C-ratio equal to zero) and oxidized material. In the model the only source for the non-oxidized organic material is low volatile POA emissions.

Figure 7 displays PM_1 mass fraction pie charts and mass size distributions of the modeled and measured chemical compounds which can be detected with ToF-AMS. Overall, the modeled PM_1 mass fractions are almost the same as the measured ones. However, the number of ammonium ions per sulfate and nitrate ion is slightly lower for the modeled values compared to the measurements, which illustrates that the AMS detected more neutralized aerosol particles than the model. The shape of the modeled mass size distributions agree with the measurements. ADCHEM is able to reproduce the larger mode diameter for the nitrate and ammonium mass size distributions compared to the organic mass size distribution. However, the measured organic mass size distribution is shifted to even smaller particles compared to the modeled total mass size distribution. Possibly, the measured organic mass size distribution is composed of a larger fraction of low volatile organic compounds than simulated in the model. This would shift the organic content to smaller particle sizes (see Fig. 8b) and discussion below). In future studies we plan to compare the AMS data inside and outside the urban plume in a similar manner to what was done with the SMPS-data.

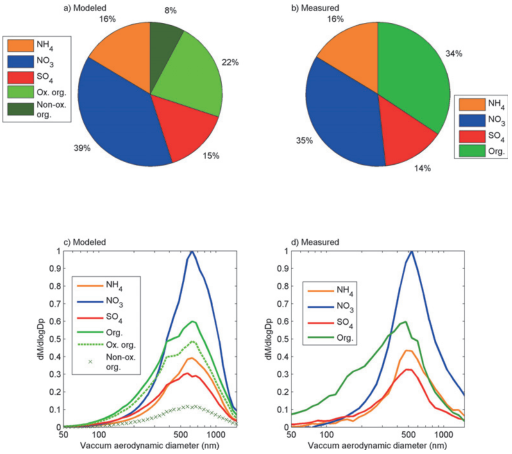

Fig. 7. Modeled (**a** and **c**) and measured (**b** and **d**) PM_1 mass fractions and mass size distributions of the compounds that can be detected with ToF-AMS. The mass size distributions were normalized with the maximum of the nitrate distributions. The chloride content was very low for the modeled and measured values and is therefore not shown. The model data is the average of the 26 model cases during 2005/2006, while the AMS data averages are from the Vavihill October and March campaigns during 2008/2009. The modeled organic mass is divided into total organics (Org.), non-oxidized (O:C-ratio equal to zero) and oxidized material. In the model the only source for the non-oxidized organic material is low volatile POA emissions.

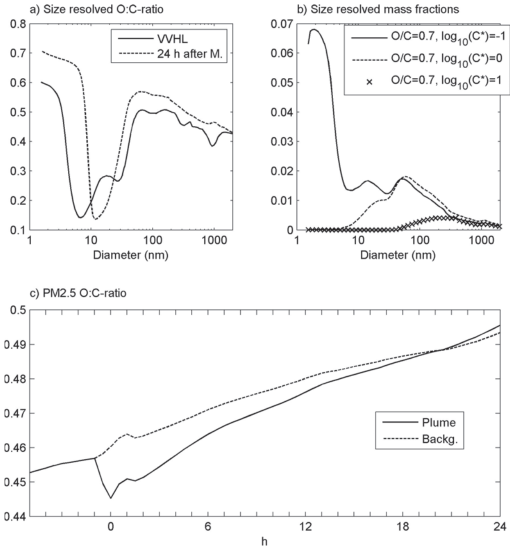

Fig. 8. Modeled organic aerosol particle properties with the 2-D-VBS model in ADCHEM. **(a)** size resolved O:C-ratio at Vavihill and 24 h downwind of Malmö, **(b)** size resolved organic aerosol mass fractions at Vavihill for three 2-D-VBS compounds with different volatility (C^*) but equal O:C-ratio and **(c)** Average $PM_{2.5}$ O:C-ratio inside and outside the urban plume downwind of Malmö.

Figure 8a shows the modeled size resolved O:C-ratio at Vavihill and 24 h downwind of Malmö. The O:C-ratios were derived with the size resolved 2-D-VBS model (see Sect. 2.2 and Roldin et al., 2011). The minimum in the O:C-ratio between 4 and 50 nm in diameter at Vavihill and 10 and 40 nm 24 h downwind of Malmö is attributed to the large influence from non-oxidized primary particle emissions within this size range. The maximum O:C-ratio is found at the smallest particle sizes where the size distribution is mainly affected by homogeneous nucleation. These particles mainly grow by condensation of low volatile organic compounds which generally have high O:C-ratios. Figure 8c gives the average $PM_{2.5}$ O:C-ratio inside and outside the urban plume downwind of Malmö. Because of the primary particle emissions in Malmö the O:C-ratio between Malmö and until 18 h downwind of the city is lower inside than outside the urban plume. Figure 8b gives an example of how condensable organic compounds with different volatility (C^*) are distributed between different particle sizes. The more volatile the compounds are the larger are the particles where these compounds are found. The reason for this is that low-volatile compounds ($C^* < 10^{-1}\,\mu g\,m^{-3}$) condense onto the Fuchs-Sutugin-corrected aerosol surface area size distribution and evaporate very slowly, while more volatile compounds ($C^* > 10^{-1}\,\mu g\,m^{-3}$) quickly condense and evaporate from the particle surfaces, until an equilibrium between the gas phase and all particle sizes is reached. Because of the Kelvin effect more volatile compounds are shifted toward larger particle sizes than less volatile compounds. This also explains why the O:C-ratio (which can be seen as a proxy for the SOA volatility) generally decreases with increasing particle size (Fig. 8a).

The secondary aerosol formation in the surface layer, formed by the anthropogenic gas phase emissions in Malmö, was estimated by taking the difference between the model results with and without anthropogenic gas phase emissions in Malmö (Fig. 9). The total $PM_{2.5}$ secondary mass contribution in the center of the model domain, downwind of Malmö, varies from -0.04 to $0.84\,\mu g\,m^{-3}$, with the maximum between 6 and 18 h downwind of Malmö. This secondary aerosol formation is dominated by condensation of nitric acid, which is neutralized by ammonium. The modeled SOA contribution due to the Malmö emissions is small compared to the ammonium nitrate formation but increases in importance with the distance from Malmö, with a maximum of $0.04\,\mu g\,m^{-3}$ at the end of the model runs 24 h downwind of Malmö. The SOA formation will likely continue to increase in importance beyond the spatial and temporal scales studied

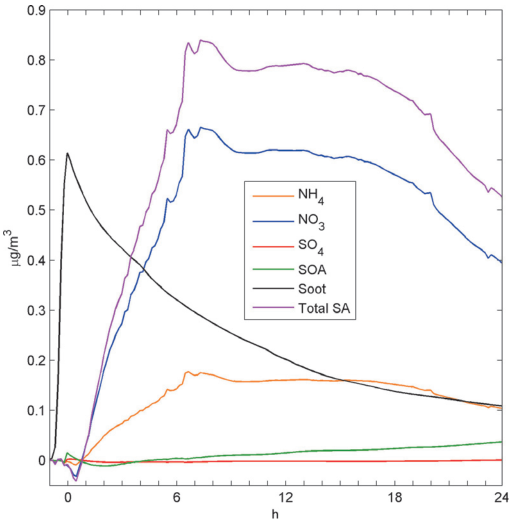

Fig. 9. Modeled average secondary aerosol (SA) formation and primary soot contribution to the $PM_{2.5}$ mass, due to gas and particle phase emissions in Malmö in the surface layer downwind of Malmö. The effective density of the soot particle emissions over Malmö was estimated to be 700 kg m^{-3}. The organic contribution only takes into account the SOA in and downwind of Malmö.

in this work. The small negative secondary aerosol contribution within one hour downwind of Malmö occurs because the oxidizing capacity within the urban plume decreases (e.g. the OH and O_3 concentration decreases) and therefore BVOCs, AVOCs, SO_2 and NO_2 are oxidized more slowly within the urban plume than outside.

Figure 9 also displays the $PM_{2.5}$ soot mass contribution from the primary particle emissions in Malmö. The freshly emitted soot particles which are porous soot agglomerates were assumed to have an effective density of 700 kg m^{-3} when determining the mass emissions. This effective density agrees with measured values for diesel exhaust particles between 100 and 150 nm in diameter (Park et al., 2003). The $PM_{2.5}$ mass contribution from the soot particle emissions in Malmö decreases downwind of Malmö and more than 3 h downwind of the city the secondary aerosol mass formed from the gas phase emissions in Malmö exceeds the $PM_{2.5}$ mass contribution from soot.

3.4 Shortwave radiative forcing of the Malmö emissions

The 3-D-bar charts in Fig. 10 display modeled cloud properties for 100 m thick clouds at different distances (or h) downwind of Malmö for different distances (0–9 km) from the center of the urban plume. The cloud formation was modeled using an adiabatic cloud parcel model described in Sect. 2.9.

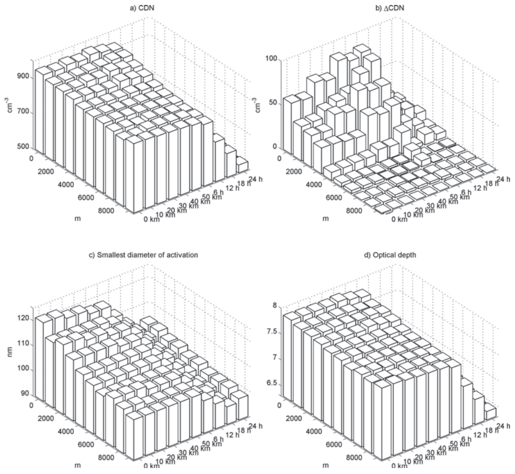

Fig. 10. Modeled cloud properties of a 100 m thick cloud, at different distances from the center of the urban plume (0–10 km) and different distances (or h) downwind of Malmö for **(a)** total Cloud Droplets Number (CDN) concentration, **(b)** number of extra cloud droplets (ΔCDN) due to the gas and particle emissions in Malmö, **(c)** the dry diameter of the smallest particles that are activated and **(d)** cloud optical depth of visible light.

In Fig. 10a the total number of cloud droplets is shown, while Fig. 10b displays the number of droplets formed because of the emissions in Malmö. Initially downtown Malmö the number of cloud droplets formed from the primary particle emissions is 58 cm^{-3} (6%) higher in the center of the urban plume compared to the background, while 6 h downwind of Malmö the number of droplets reaches a maximum of 88 cm^{-3} (9%) higher at the center of the urban plume compared to the background. The increasing influence of the urban emissions on the number of cloud droplets from Malmö until 6 h downwind of Malmö are mainly due to the secondary nitrate formation. More than 6 h downwind of Malmö the modeled cloud droplet contribution due to the emissions in Malmö decreases continuously, reaching 15 cm^{-3} (3%), 24 h downwind of Malmö.

ADCHEM assumes that all particles are internally mixed, while in reality the freshly emitted soot particles in Malmö will be externally mixed in and at short distances downwind of the city. Since these externally mixed soot particles are non-water soluble they will not influence the cloud droplet number (CDN) concentration in Malmö. Therefore the modeled number of cloud droplets formed by the primary particle emissions from Malmö will most likely be overestimated in and near the city. However, more than 30 km downwind of the city the amplified CDN concentration within the urban plume is also caused by the secondary nitrate formation, and the assumption of treating the soot particles as internally mixed particles has less influence on the results.

While the number concentration of cloud droplets is higher inside than outside the urban plume, the total cloud water content is essentially the same. Hence, the geometric mean diameter (GMD) of the cloud droplets decreases with increasing number of droplets. The smallest dry particle activation diameter is also changed because of the urban emissions. In the center of the urban plume in the greater Malmö area the smallest diameter of activation is about 15 nm larger compared to the background (Fig. 10c). This is attributed to the lower water uptake of the freshly emitted primary particles in Malmö compared to the background, but also due to a lower maximum supersaturation in the more polluted clouds. Figure 10d shows the optical depth of the 100 m thick clouds downwind of Malmö. The optical depth is between 6.5 and 8 at all locations which is realistic for continental air. For these optically relatively thin clouds the cloud droplet properties have larger influence on the cloud albedo compared to thick clouds (Twomey, 1977).

The 3-D-bar charts in Fig. 11 show the calculated anthropogenic shortwave radiative forcing due to the Malmö gas and particle phase emissions at the surface without (a) and with (b) 100 m thick clouds being present at different distances (or h) downwind of Malmö and for different distances (0–9 km) from the center of the urban plume. Figure 11c and d display the radiative forcing only caused by the secondary aerosol (SA) formed from the gas phase emissions in Malmö with and without the 100 m thick clouds. Without clouds the shortwave radiative forcing in the center of the urban plume decreases with 30% from Malmö to 6 h downwind of the city (from -3.34 to $-2.31\,\mathrm{W\,m^{-2}}$), while when 100 m thick clouds are present the radiative forcing is instead increasing from $-2.4\,\mathrm{W\,m^{-2}}$ in Malmö to $-2.7\,\mathrm{W\,m^{-2}}$, 6 h downwind of the city. This can be explained by the condensation of nitric acid and ammonia (Figs. 9 and 11d), which increases the number of particles which are activated as cloud droplets (Fig. 10b). However, more than 6 h downwind of Malmö the radiative forcing decreases even when clouds are present. The reason for this is that the number of available cloud condensation nuclei (CCN) decreases due to dry and wet deposition and coagulation. Without clouds the secondary aerosol formation has insignificant influence on the radiative forcing at short distances (~ 20 km) downwind of the city. But between 6 and 24 h downwind of Malmö, when the secondary aerosol contribution from Malmö is largest (Fig. 9), the influence becomes more pronounced and explains between 10 and 20% of the total surface shortwave radiative forcing and 30 to 60% of the TOA (top of the atmosphere) shortwave radiative forcing. In contrast to the primary particle shortwave radiative forcing, which is much larger at the surface, the secondary aerosol radiative forcing is almost identical at the surface and the TOA. The reason for this is that the secondary aerosol only scatters the light while the primary particles, which mainly are composed of soot, absorb much of the solar radiation and heat the atmosphere, but still prevent the solar irradiance from reaching the surface.

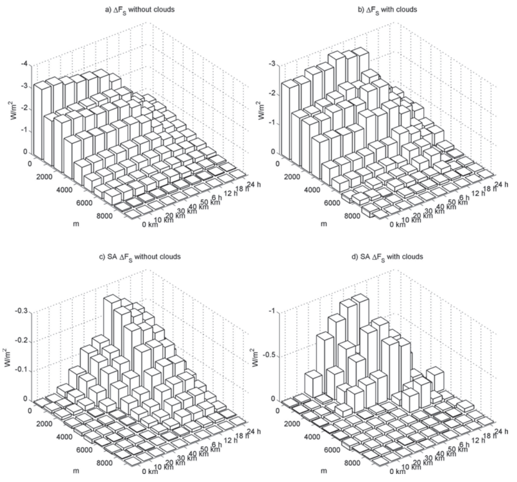

Fig. 11. Modeled anthropogenic shortwave radiative forcing at the surface due to Malmö gas and particle phase emissions at different distances (or h) downwind of Malmö and at different distances from the center of the urban plume for **(a)** conditions without clouds, **(b)** conditions with 100 m thick clouds at low altitude, **(c)** radiative forcing due to secondary aerosol (SA) formation from Malmö gas phase emissions for conditions without clouds and **(d)** same as **(c)** but with 100 m thick clouds. The secondary aerosol radiative forcing was derived by taking the difference between the modeled radiative forcing when the anthropogenic gas phase emissions from Malmö was included in the ADCHEM model and when they were not.

Table 4 displays the average radiative forcing within the 20 km wide horizontal model domain at the surface and at the TOA, at different distances (or h) downwind of Malmö with 100 m thick clouds, 500 m thick clouds or without clouds being present. At the TOA the shortwave radiative forcing is several times smaller than at the surface, especially without clouds present. If 500 m thick clouds are present instead of 100 m thick clouds the modeled shortwave radiative forcing becomes about three times smaller both at the surface and at the TOA. The reason for this is that for these much thicker clouds (optical depth between 60 and 75) the aerosol particle (cloud droplet) properties have less influence on the cloud albedo (Twomey, 1977).

It is important to remember that the average particle properties used for the radiative forcing calculations are derived from cases with southerly air masses, which generally originate from relatively polluted regions in Europe. Therefore the number of cloud droplets at the background will likely be higher compared to air masses originated over e.g. the northern part of Sweden. This condition decreases the estimated climate impact from the emissions in Malmö, especially if the emissions influence the cloud properties.

Table 4. Average radiative forcing within the 20 km wide model domain at the surface (ΔF_S) and at the TOA (ΔF_{TOA}), with or without clouds, at different distances downwind of Malmö.

Position	ΔF_S without clouds ($W m^{-2}$)	ΔF_S with 100 m thick clouds ($W m^{-2}$)	ΔF_S with 500 m thick clouds ($W m^{-2}$)	ΔF_{TOA} without cloud ($W m^{-2}$)	ΔF_{TOA} with 100 m thick clouds ($W m^{-2}$)	ΔF_{TOA} with 500 m thick clouds ($W m^{-2}$)
Malmö	−1.147	−0.762	−0.221	−0.262	−0.289	−0.107
10 km dw. M	−1.113	−0.743	−0.215	−0.237	−0.271	−0.101
20 km dw. M	−1.08	−0.784	−0.245	−0.219	−0.322	−0.129
30 km dw. M	−1.053	−0.851	−0.271	−0.207	−0.397	−0.153
40 km dw. M	−1.047	−0.922	−0.300	−0.204	−0.471	−0.179
50 km dw. M	−1.026	−0.908	−0.297	−0.200	−0.465	−0.178
6 h dw. M.	−0.931	−0.999	−0.337	−0.185	−0.600	−0.222
12 h dw. M.	−0.652	−0.747	−0.314	−0.169	−0.479	−0.225
18 h dw. M.	−0.467	−0.413	−0.159	−0.139	−0.227	−0.105
24 h dw. M.	−0.346	−0.295	−0.102	−0.101	−0.153	−0.062

3.5 Health effects of the ageing urban aerosol

It could be noted that in addition to the effects on the radiation balance, the alteration in chemical and physical properties of the aerosol during its ageing has an impact on human health. For instance there may be a difference in toxicity between the fresh and the aged aerosol because of variations in concentration and ability of the particles to deposit in the human lungs. The fresh aerosol contains a larger proportion of ultrafine particles with a high probability to deposit in the lungs and by number the amount of deposited particles will thus be high compared to that for the aged aerosol. On the other hand the increase in mass and the shift in hygroscopicity of the aged aerosol results in a higher particle deposition in the lungs by mass. This kind of lung deposition estimates can be derived using the results from the ADCHEM model.

4 Summary and conclusions

In this work a coupled aerosol dynamics, gas phase chemistry and radiative transfer model (ADCHEM) has been used first, to test if it can correctly model an ageing urban plume, in this case generated by Malmö, a city with 280 000 inhabitants in Southern Sweden. However, the main objective has been to use ADCHEM to estimate the climate impacts of the ageing plume.

ADCHEM was able to accurately model the ageing of the particle number size distribution for 26 different case studies between an urban background site in Malmö and the rural site Vavihill, 50 km downwind of Malmö. At Vavihill, the model results were validated with particle number size distribution measurements. The differences between average modeled and measured concentrations of O_3, NO, NO_2 and SO_2 in Malmö were smaller than 25%. Hence, the model is able to capture the main features of the gas phase chemistry in the Malmö plume, which is required to be able to accurately predict the secondary aerosol formation.

The modeled inorganic and organic particle composition is comparable with ToF-AMS measurements at Vavihill. This illustrates that ADCHEM can be used to model realistic size-resolved particle chemical composition in urban plumes, and that the model results can further be used to calculate the optical and hygroscopic properties relevant for climate and health effects.

Malmö contributes with about 1200 particles cm^{-3} at Vavihill, where the number concentration is dominated by primary emissions in the nucleation and Aitken mode. While the primary particle number contribution continuously decreases downwind of the emission sources, the contribution to the aerosol particle mass from secondary aerosol formation continues to increase up to several hundred kilometers (∼ 12 h) downwind of Malmö. The secondary aerosol formation is dominated by condensation of nitric acid, formed from the NO_x emissions in Malmö. The maximum secondary aerosol contribution from the gas phase emissions in Malmö of between 0.7 and 0.8 $\mu g\ m^{-3}$ in the urban plume is reached between 6 and 18 h downwind of Malmö.

The secondary aerosol formation downwind of Malmö leads to growth of the freshly emitted primary particles, which results in a more hygroscopic aerosol. This increases its impact on the cloud properties within the urban plume. Hence, the cloud radiative forcing due to the emissions in Malmö is largest about 40–200 km (∼ 2–12 h) downwind of Malmö and not within or very near the city.

Because 60% of the world population lives in cities with less than 1 million people, i.e. of the same size as Malmö, the climate and health impact of these cities need to be addressed. The urban emission contribution downwind of the city center estimated from this study can be used for up-scaling of urban sub-grid emissions to regional scales treated by global and regional chemistry transport models and climate models. The results can further be used to estimate how the particle emissions influence adjacent grid cells of these models. However, since the meteorological conditions, emission sources, and geographical and population extension vary between different cities, more detailed studies of different urban regions around the world are needed to better account for their influence on climate and population health on regional and global scales.

Nevertheless, this study has shown that it is not sufficient to account only for aerosol dynamic processes during the transformation of local scale anthropogenic emissions to larger scales of regional and global models. Gas-phase chemistry and secondary aerosol formation are necessary entities to account for during the prediction of climate and health effects of particles in the ageing urban plumes.

Supplementary material related to this article is available online at: http://www.atmos-chem-phys.net/11/5897/2011/ acp-11-5897-2011-supplement.pdf.

Acknowledgements. This work has been supported by the European Commission 6th Framework program projects: EUCAARI, contract no 036833-2 (EUCAARI) and EUSAAR, contract no 026140 (EUSAAR). We also gratefully acknowledge the support by the Swedish Research Council through project no 2007-4619, the Swedish strategic research area ModElling the Regional and Global Earth system, MERGE and the Lund University center for studies of Carbon cycle and Climate Interactions, LUCCI. The Swedish Research Council also funded the purchase of the HR-ToF-AMS instrument through Research Equipment Grant no 2006-5940. The DMPS measurements at Vavihill were supported by the Swedish Environmental Protection Agency within the Swedish Environmental Monitoring Program. The support by the Swedish Research Council for Environment, Agricultural Sciences and Spatial Planning (Formas) through project no 2009-615 and 2008-1467 is also gratefully acknowledged.

The authors would also like to thank Almut Arneth and Guy Schurgers at Department of Earth and Ecosystem Sciences, Lund University, for providing BVOC emissions over Europe, Harri Kokkola, Joni-Pekka Pietikäinen and Jussi Malila at Kuopio University, for valuable help during the development of the adiabatic cloud parcel model, Henrik Nilsson at Environmental Dept., City of Malmö for the gas and wind direction measurements in Malmö, Tareq Hussein from Helsinki University for help with the lognormal-fitting of the measured and modeled particle number size distributions, Matthias Ketzel and Fenjuan Wang from Danish National Environmental Research Institute for help with the implementation of the Danish anthropogenic gas and particle phase emissions and David Simpson at the Global Environmental Measurement and Modelling Group, Department of Radio and Space Science, Chalmers, Gothenburg for help with the SOA partitioning theory.

Edited by: A. Wiedensohler

References

Arneth, A., Niinemets, Ü, Pressley, S., Bäck, J., Hari, P., Karl, T., Noe, S., Prentice, I. C., Serça, D., Hickler, T., Wolf, A., and Smith, B.: Process-based estimates of terrestrial ecosystem isoprene emissions: incorporating the effects of a direct CO_2-isoprene interaction, Atmos. Chem. Phys., 7, 31–53, doi:10.5194/acp-7-31-2007, 2007.

Chaix, B., Gustafsson, S., Jerrett, M., Kristersson, H., Lithman, T., Boalt, Å., and Merlo, J.: Children's exposure to nitrogen dioxide in Sweden: investigating environmental injustice in an egalitarian country, J. Epidemiol. Comm. H., 60, 234–241, 2006.

Doran, J. C., Barnard, J. C., Arnott, W. P., Cary, R., Coulter, R., Fast, J. D., Kassianov, E. I., Kleinman, L., Laulainen, N. S., Martin, T., Paredes-Miranda, G., Pekour, M. S., Shaw, W. J., Smith, D. F., Springston, S. R., and Yu, X.-Y.: The T1-T2 study: evolution of aerosol properties downwind of Mexico City, Atmos. Chem. Phys., 7, 1585–1598, doi:10.5194/acp-7-1585-2007, 2007.

Draxler, R. R. and Rolph, G. D.: HYSPLIT (Hybrid Single-Particle Lagrangian Integrated Trajectory) Model, available at: http://ready.arl.noaa.gov/HYSPLIT.php, NOAA Air Resources Laboratory, Silver Spring, MD, (last access: 01 March 2011) 2011.

Eriksson, A.: Calibration and First Field Deployment of an Aerosol Mass Spectrometer, M. Sc dissertation at Department of Physics and Department of Design Sciences, Lund University, 2009.

Gaydos, T. M., Pinder, R., Koo, B., Fahey, K. M., Yarwood, G., and Pandis, S. N.: Development and application of a three-dimensional aerosol chemical transport model, PMCAMx, Atmos. Environ., 41, 2594–2611, 2007.

Gustafsson, S.: Uppbyggnad och validering av emissionsdatabas avseende luftföroreningar för Skåne med basår, Licentiat Dissertation at National Environmental Research Institute, Lund University, 9, 2001.

Henze, D. K., Seinfeld, J. H., Ng, N. L., Kroll, J. H., Fu, T.-M., Jacob, D. J., and Heald, C. L.: Global modeling of secondary organic aerosol formation from aromatic hydrocarbons: high- vs. low-yield pathways, Atmos. Chem. Phys., 8, 2405–2420, doi:10.5194/acp-8-2405-2008, 2008.

Hodzic, A., Vautard, R., Chazette, P., Menut, L., and Bessagnet, B.: Aerosol chemical and optical properties over the Paris area within ESQUIF project, Atmos. Chem. Phys., 6, 3257–3280, doi:10.5194/acp-6-3257-2006, 2006.

Hodzic, A., Jimenez, J. L., Madronich, S., Aiken, A. C., Bessagnet, B., Curci, G., Fast, J., Lamarque, J.-F., Onasch, T. B., Roux, G., Schauer, J. J., Stone, E. A., and Ulbrich, I. M.: Modeling organic aerosols during MILAGRO: importance of biogenic secondary organic aerosols, Atmos. Chem. Phys., 9, 6949–6981, doi:10.5194/acp-9-6949-2009, 2009.

Horvath, H.: Influence of atmospheric aerosols upon the global radiation balance, in: Atmospheric Particles IUPAC Series on Analytical and Physical Chemistry of Environmental Systems, edited by: Harrison, R. M. and Van Greiken, R., Wiley, New York, 5, 1998.

Hussein, T., Dal Maso, M., Petaja, T., Koponen, I. K., Paatero, P., Aalto, P. P., Hämeri, K., and Kulmala, M.: Evaluation of an automatic algorith for fitting the particle number size distributions, Boreal Environ. Res., 10, 337–355, 2005.

Jacobson, M. Z.: A Solution to the Problem of Nonequilibrium

Acid/Base Gas-Particle Transfer at Long Time Step, Aerosol Sci. Tech., 39, 92–103, 2005a.

Jacobson, M. Z.: Fundamentals of Atmospheric Modelling, 2nd Edn., Cambridge University Press, Cambridge, United Kingdom and New York, NY, USA, 2005b.

Jimenez, J. L., Canagaratna, M. R., Donahue, N. M., Prevot, A. S. H., Zhang, Q., Kroll, J. H., DeCarlo, P. F., Allan, J. D., Coe, H., Ng, N. L., Aiken, A. C., Docherty, K. S., Ulbrich, I. M., Grieshop, A. P., Robinson, A. L., Duplissy, J., Smith, J. D., Wilson, K. R., Lanz, V. A., Hueglin, C., Sun, Y. L., Tian, J., Laaksonen, A., Raatikainen, T., Rautiainen, J., Vaattovaara, P., Ehn, M., Kulmala, M., Tomlinson, J. M., Collins, D. R., Cubison, M. J., Dunlea, E. J., Huffman, J. A., Onasch, T. B., Alfarra, M. R., Williams, P. I., Bower, K., Kondo, Y., Schneider, J., Drewnick, F., Borrmann, S., Weimer, S., Demerjian, K., Salcedo, D., Cottrell, L., Griffin, R., Takami, A., Miyoshi, T., Hatakeyama, S., Shimono, A., Sun, J. Y, Zhang, Y. M., Dzepina, K., Kimmel, J. R., Sueper, D., Jayne, J. T., Herndon, S. C., Trimborn, A. M., Williams, L. R., Wood, E. C., Middlebrook, A. M., Kolb, C. E., Baltensperger, U., and Worsnop, D. R.: Evolution of Organic Aerosols in the Atmosphere, Science, 326, 1525–1529, 2009.

Kristensson, A., Dal Maso, M., Swietlicki, E., Hussein, T., Zhou, J., Kerminen, V.-M., and Kulmala, M.: Characterization of new particle formation events at a background site in Southern Sweden: relation to air mass history, Tellus, 60B, 330–344, 2008.

Ng, N. L., Kroll, J. H., Chan, A. W. H., Chhabra, P. S., Flagan, R. C., and Seinfeld, J. H.: Secondary organic aerosol formation from *m*-xylene, toluene, and benzene, Atmos. Chem. Phys., 7, 3909–3922, doi:10.5194/acp-7-3909-2007, 2007.

Nolte, C. G., Bhave, P. V., Arnold, J. R., Dennis, R. L., Zhang, K. M., and Wexler, A. S.: Modeling urban and regional aerosols-Application of the CMAQ-UCD Aerosol Model to Tampa, a coastal urban site, Atmos. Environ., 42, 3179–3191, 2008.

Odum, J. R., Hoffmann, T., Bowman, F., Collins, D., Flagan, R. C., and Seinfeld, J. H.: Gas/Particle Partitioning and Secondary Organic Aerosol Yields, Environ. Sci. Technol., 30, 2580–2585, 1996.

Park, K., Cao, F., Kittelson, D. B., and McMurry, P. H.: Relationship between Particle Mass and Mobility for Diesel Exhaust Particles, Environ. Sci. Technol., 37, 577–583, 2003.

Patashnick, H. and Rupprecht, E. G.: Continuous PM_10 measurements using the tapered element oscillating microbalance, J. Air Waste Manage. Ass., 41, 1079–1083, 1991.

Pierce, J. R., Theodoritsi, G., Adams, P. J., and Pandis, S. N.: Parameterization of the effect of sub-grid scale aerosol dynamics on aerosol number emission rates, Aerosol Sci., 40, 385–393, 2009.

Pirjola, L. and Kulmala, M.: Modelling the formation of H_2SO_4-H_2O particles in rural, urban and marine conditions, Atmos. Res., 46, 321–347, 1998.

Population Division of the Department of Economic and Social Affairs of the United Nations Secretariat, World Population Prospects: The 2006 Revision and World Urbanization Prospects: The 2007 Revision, available at: http://esa.un.org/unup (last acess: 01 March 2011), 2007.

Ramankutty, N., Evan, A. T., Monfreda, C., and Foley, J. A.: Farming the planet: 1. Geographic distribution of global agricultural lands in the year 2000, Global Biogeochem. Cy., 22, GB1003, doi:10.1029/2007GB002952, 2008.

Robinson, A. L., Donahue, N. M., Shrivastava, M. K., Weitkamp, E. A., Sage, A. M., Grieshop, A. P., Lane, T. E., Pierce, J. R., and Pandis, S. N.: Rethinking organic aerosols: Semivolatile emissions and photochemical aging, Science, 315, 1259–1262, 2007.

Rogers, R. R. and Yau, M. K.: A Short Course in Cloud Physics, 3rd Edn., Pergamon Press, Oxford, Great Britain, 1989.

Rolph, G. D.: Real-time Environmental Applications and Display sYstem (READY), NOAA Air Resources Laboratory, Silver Spring, MD, available at: http://ready.arl.noaa.gov/, 2011.

Roldin, P., Swietlicki, E., Schurgers, G., Arneth, A., Lehtinen, K. E. J., Boy, M., and Kulmala, M.: Development and evaluation of the aerosol dynamics and gas phase chemistry model ADCHEM, Atmos. Chem. Phys., 11, doi:10.5194/acp-11-5867-2011, 5867–5896, 2011.

Seinfeld, J. H., Carmichael, G. R., Arimoto, R., Conant, W. C., Brechtel, F. J., Bates, T. S., Cahill, T. A., Clarke, A. D., Doherty, S. J., Flatau, P. J., Huebert, B. J., Kim, J., Markowicz, K. M., Quinn, P. K., Russell, L. M., Russell, P. B., Shimizu, A., Shinozuka, Y., Song, C. H., Tang, Y., Uno, I., Vogelmann, A. M., Weber, R. J., Woo, J.-H., and Zhang, X. Y.: ACE-ASIA – Regional Climatic and Atmospheric Chemical Effects of Asian Dust and Pollution, Bull. Am. Meteorol. Soc, 85, 367–380, 2004.

Schmid, O., Chand, D., Karg, E., Guyon, P., Frank, G. P., Swietlicki, E., and Andreae, M. O.: Derivation of the Density and Refractive Index of Organic Matter and Elemental Carbon from Closure between Physical and Chemical Aerosol Properties, Environ. Sci. Technol., 43, 1166–1172, 2009.

Schurgers, G., Arneth, A., Holzinger, R., and Goldstein, A. H.: Process-based modelling of biogenic monoterpene emissions combining production and release from storage, Atmos. Chem. Phys., 9, 3409–3423, doi:10.5194/acp-9-3409-2009, 2009.

Shrivastava, M. K., Lane, T. E., Donahue, N. M., Pandis, S. N., and Robinson, A. L.: Effects of gas particle partitioning and aging of primary emissions on urban and regional organic aerosol concentrations, J. Geophys. Res., 113, D18301, doi:10.1029/2007JD009735, 2008.

Simpson, D., Winiwarter, W., Börjesson, G., Cinderby, S., Ferreiro, A., Guenther, A., Hewitt, N., Janson, R., Khalil, M. A. K., Owen, S., Pierce, T. E., Puxbaum, H., Shearer, M., Skiba, U., Steinbrecher, R., Tarrasón, L., and Öquist, M. G.: Inventorying emissions from nature in Europe, J. Geophys. Res., 104, 8113–8152, 1999.

Sitch, S., Smith, B., Prentice, I., Arneth, A., Bondeau, A., Cramer, W., Kaplan, J., Levis, S., Lucht, W., Sykes, M., Thonicke, K., and Venevsky, S.: Evaluation of ecosystem dynamics, plant geography and terrestrial carbon cycling in the LPJ Dynamic Global Vegetation Model, Glob. Change Biol., 9, 161–185, 2003.

Smith, B., Prentice, I. C., and Sykes, M. T.: Representation of vegetation dynamics in the modeling of terrestrial ecosystems: comparing two contrasting approaches within European climate space, Glob. Ecol. Biogeogr., 10, 621–637, 2001.

Sokolik, I. N. and Toon, O. B.: Incorporation of mineralogical composition into models of radiative properties of mineral aerosol from UV to IR wavelength, J. Geophys. Res., 104, 9423–9444, 1999.

Stroh, E., Harrie, L., and Gustafsson, S.: A study of spatial resolution in pollution exposure modeling, Int. J. Health Geogr., 6(1), 19–19, doi:10.1186/1476-072X-6-19, 2007.

Tie, X., Madronich, S., Li, G., Ying, Z., Weinheimer, A., Apel, E., and Campos, T.: Simulation of Mexico City plumes during the

MIRAGE-Mex field campaign using the WRF-Chem model, Atmos. Chem. Phys., 9, 4621–4638, doi:10.5194/acp-9-4621-2009, 2009.

Toon, O. B., McKay, C. P., Ackerman, T. P., and Santhanam, K.: Rapid Calculation of Radiative Heating Rates and Photodissociation Rates in Inhomogeneous Multiple Scattering Atmospheres, J. Geophys. Res., 94, 16287–16301, 1989.

Tsimpidi, A. P., Karydis, V. A., Zavala, M., Lei, W., Molina, L., Ulbrich, I. M., Jimenez, J. L., and Pandis, S. N.: Evaluation of the volatility basis-set approach for the simulation of organic aerosol formation in the Mexico City metropolitan area, Atmos. Chem. Phys., 10, 525–546, doi:10.5194/acp-10-525-2010, 2010.

Twomey, S.: The Influence of Pollution on the Shortwave Albedo of Clouds, J. Atmos. Sci., 34, 1149–1152, 1977.

Vestreng, V., Rigler, E., Adams, M., Kindbom, K., Pacyna, J. M., van der Gon, D., Reis, H. S., and Traynikov, O.: Inventory review 2006, Emission data reported to LRTAP and NEC Directive, Stage 1, 2 and 3 review and Evaluation of Inventories of HM and POPs, EMEP/MSC-W Technical Report 1/2006, 1504–6179, available at: http://www.emep.int/, 2006.

Wang, F., Roldin, P., Massling, A., Kristensson, A., Swietlicki, E., Fang, D., and Ketzel, M.: Aerosol dynamics in the Copenhagen urban plume during regional transport, Atmos. Chem. Phys. Discuss., 10, 8553–8594, doi:10.5194/acpd-10-8553-2010, 2010.

Wiedensohler, A., Birmili, W., Nowak, A., Sonntag, A., Weinhold, K., Merkel, M., Wehner, B., Tuch, T., Pfeifer, S., Fiebig, M., Fjäraa, A. M., Asmi, E., Sellegri, K., Depuy, R., Venzac, H., Villani, P., Laj, P., Aalto, P., Ogren, J. A., Swietlicki, E., Roldin, P., Williams, P., Quincey, P., Hüglin, C., Fierz-Schmidhauser, R., Gysel, M., Weingartner, E., Riccobono, F., Santos, S., Grüning, C., Faloon, K., Beddows, D., Harrison, R. M., Monahan, C., Jennings, S. G., O'Dowd, C. D., Marinoni, A., Horn, H.-G., Keck, L., Jiang, J., Scheckman, J., McMurry, P. H., Deng, Z., Zhao, C. S., Moerman, M., Henzing, B., and de Leeuw, G.: Particle mobility size spectrometers: harmonization of technical standards and data structure to facilitate high quality long-term observations of atmospheric particle number size distributions, Atmos. Meas. Tech. Discuss., 3, 5521–5587, doi:10.5194/amtd-3-5521-2010, 2010.

Winklmayr, W., Reischl, G. P., Lindner, A. O., and Berner, A.: A new electromobility spectrometer for the measurement of aerosol size distributions in the size range from 1 to 1000 nm, J. Aerosol Sci., 22, 289–296, 1991.

Zaveri, R. A., Easter, R. C., Fast, J. D., and Peters, L. K.: Model for Simulating Aerosol Interactions and Chemistry (MOSAIC), J. Geophys. Res., 113, D13204, doi:10.1029/2007JD008782, 2008.

Zhang, K. M. and Wexler, A. S.: Modeling urban and regional aerosols-Development of the UCD Aerosol Module and implementation in CMAQ model, Atmos. Environ., 42, 3166–3178, 2008.

Paper III

Modelling non-equilibrium secondary organic aerosol formation and evaporation with the aerosol dynamics, gas- and particle-phase chemistry kinetic multi-layer model ADCHAM

P. Roldin[1], A. C. Eriksson[1], E. Z. Nordin[2], E. Hermansson[1], D. Mogensen[3], A. Rusanen[3], M. Boy[3], E. Swietlicki[1], B. Svenningsson[1], J. Pagels[2]

[1]{Division of Nuclear Physics, Lund University, P.O. Box 118 SE-221 00 Lund, Sweden}

[2]{Ergonomics and Aerosol Technology, Lund University, P.O. Box 118 SE-221 00 Lund, Sweden}

[3]{Department of Physics, P.O. Box 48, University of Helsinki, 00014, Finland}

Correspondence to: P. Roldin (pontus.roldin@nuclear.lu.se)

Abstract

We have developed the novel Aerosol Dynamics, gas- and particle- phase chemistry model for laboratory CHAMber studies (ADCHAM). The model combines the detailed gas phase Master Chemical Mechanism version 3.2, an aerosol dynamics and particle phase chemistry module (which considers acid catalysed oligomerization, heterogeneous oxidation reactions in the particle phase and non-ideal interactions between organic compounds, water and inorganic ions) and a kinetic multilayer module for diffusion limited transport of compounds between the gas phase, particle surface and particle bulk phase. In this article we describe and use ADCHAM to study: 1) the mass transfer limited uptake of ammonia (NH_3) and formation of organic salts between ammonium (NH_4^+) and carboxylic acids (RCOOH), 2) the slow and almost particle size independent evaporation of α-pinene secondary organic aerosol (SOA) particles, and 3) the influence of chamber wall effects on the observed SOA formation in smog chambers.

ADCHAM is able to capture the observed α-pinene SOA mass increase in the presence of NH_3(g). Organic salts of ammonium and carboxylic acids predominantly form during the early

stage of SOA formation. These salts contribute substantially to the initial growth of the homogeneously nucleated particles.

The model simulations of evaporating α-pinene SOA particles support the recent experimental findings that these particles have a semi-solid tar like amorphous phase state. ADCHAM is able to reproduce the main features of the observed slow evaporation rates if low-volatility and viscous oligomerized SOA material accumulates in the particle surface layer upon evaporation. The evaporation rate is mainly governed by the reversible decomposition of oligomers back to monomers.

Finally, we demonstrate that the mass transfer limited uptake of condensable organic compounds onto wall deposited particles or directly onto the Teflon chamber walls can have profound influence on the observed SOA formation. During the early stage of the SOA formation the wall deposited particles serve as a SOA sink from the air to the walls. However, at the end of smog chamber experiments the semi-volatile SOA material may start to evaporate from the chamber walls. In order to capture the observed temporal evolution of the SOA formation from our *m*-xylene oxidation experiment ADCHAM need to consider oligomerization and/or heterogeneous oxidation reactions.

With these three model applications, we demonstrate that several poorly quantified processes (mass transport limitations within the particle phase, oligomerization, heterogeneous oxidation and chamber wall effects) can have substantial influence on the SOA formation, lifetime and chemical and physical particle properties. In order to constrain the uncertainties related to these processes, future experiments are needed where as many of the influential variables as possible are varied. ADCHAM can be a valuable model tool in the design and analysis of such experiments.

1 Introduction

Aerosol particles in the atmosphere have substantial impact on the global climate, air quality and public health. Measurements around the world have demonstrated that a large fraction of the submicron aerosol particles are composed of organic compounds (Jimenez et al., 2009). Today many important biogenic and anthropogenic SOA precursors have been identified. However, the scientific knowledge about their SOA formation mechanisms, the SOA composition and properties is still very uncertain (Kroll and Seinfeld, 2008 and Hallquist et al., 2009).

Traditionally, the important SOA formation mechanisms are modelled as pure gas phase oxidation processes followed by equilibrium partitioning between the gas and a liquid organic particle phase (e.g. Pankow, 1994 and Donahue et al., 2011). However, during the last ~10 years other processes occurring in the particle phase have also been identified as important mechanisms for the formation and properties of SOA. These include acid catalysed oligomerization (e.g. Gao et al., 2004, Iinuma et al., 2004, Kalberer et al., 2004, and Tolocka et al., 2004), heterogeneous oxidation reactions (e.g. Knopf et al., 2005, Nash et al., 2006, Rudich et al., 2007, Maksymiuk et al., 2009), organic salt formation (e.g. Na et al., 2007, Smith et al., 2010, Kuwata and Martin, 2012 and Yli-Juuti et al., 2013), organosulphate formation (e.g. Liggio and Li, 2006, Surratt et al., 2007) and salting-out effects (e.g. Smith et al., 2011, Bertram et al., 2011). The term salting-out refers to the process in which interactions with dissolved ions (generally inorganic) drive nonpolar organic compounds out of the mixed phase, either into a different organic-rich (liquid) phase or out to the gas phase (Zuend et al., 2011).

Several independent laboratory experiments have also shown that secondary organic aerosol particles can form a solid or semi-solid amorphous phase (e.g. Virtanen et al., 2010, Kuwata and Martin, 2012), at least for relative humidities (RH) below 60 % (Saukko et al., 2012). Recently, Abramson et al. (2013) studied the evaporation of pyrene coated with SOA formed from α-pinene ozonolysis and estimated a diffusion coefficient of $2.5\text{x}10^{-17}$ cm^2 s^{-1} for pyrene in the fresh SOA. For particles aged for ~24 hours the diffusion rate was ~3 times slower. Using the Stokes–Einstein relation for the binary diffusion coefficients gives a SOA viscosity of ~10^8 Pa s for fresh SOA and ~$3\text{x}10^8$ Pa s for the aged particles. These high viscosity values are typical for tar or pitch like substances (Koop et al., 2011). For a particle with a diameter of 100 nm, this gives a characteristic time of mass-transport (e-folding time of equilibration) of ~28 hours for fresh SOA and ~84 hours for the aged SOA particles (Shiraiwa et al., 2011).

If a viscous phase is formed, the mixing within the particle bulk will be kinetically limited and the gas to particle partitioning cannot be well represented by an equilibrium process (Pöschl, 2011), which the traditional partitioning theory assumes (Pankow, 1994). This may not be evident from pure SOA mass formation experiments where the condensable organic compounds are continuously formed by gas phase oxidation of different precursor compounds (see e.g. Odum et al., 1996, Hoffmann et al., 1997, Griffin et al., 1999, Ng et al., 2007, Pathak et al., 2007). However, in the atmosphere the aerosol is exposed to much more variable concentration, temperature and humidity conditions. Hence, the atmospheric aerosol will never be entirely in equilibrium with the gas phase. Dzepina et al. (2009) showed that their equilibrium partitioning model substantially overestimate the evaporation of SOA in the Mexico City metropolitan area.

In well controlled laboratory experiments Grieshop et al. (2007) and Vaden et al. (2011) have illustrated that the evaporation of SOA particles formed from α-pinene ozonolysis is orders of magnitude slower than expected from equilibrium partitioning. This slow evaporation of SOA can be due to mixing effects, mass transfer limitations, decomposition of weakly bonded oligomers (Grieshop et al., 2007) and adsorption of certain organic compounds at the particle surfaces (Vaden et al., 2011). Vaden et al. (2011) also illustrated that the evaporation of ambient SOA particles are even slower than for the pure α-pinene SOA and better resembles the evaporation of aged α-pinene SOA particles coated with different hydrophobic organic compounds. If the ambient SOA particles studied by Vaden et al. (2011) are representative of typical atmospheric SOA particles, the evaporation due to dilution in the atmosphere (e.g. in urban plumes downwind the source) will be almost negligible. This can increase the lifetime and concentrations of SOA (and e.g. NH_4NO_3) in the atmosphere (Vaden et al., 2011).

A number of model studies have been performed to explore detailed gas phase reaction mechanisms which can be responsible for the SOA formation of known biogenic and anthropogenic SOA precursors (e.g. Bloss et al., 2005a-b, Johnson et al., 2005 and 2006, Li et al., 2007, Hu et al., 2007, Metzger et al., 2008, Rickard et al., 2010, Camredon et al., 2010 and Valorso et al., 2011). However, relatively few attempts have been made to perform detailed process-based modelling on the influence of phase state (Shiraiwa et al., 2010, 2011 and 2012, Pfrang et al., 2011), oligomerization (Vesterinen et al. 2007, Pun and Seigneur, 2007, Li et al., 2007, Hu et al., 2007, Ervens and Volkamer, 2010), heterogeneous oxidation mechanisms (Shiraiwa et al., 2010, 2011 and 2012, Pfrang et al., 2011), organic-inorganic interactions (e.g. salting-out effects, acidity effects) (Zuend et al. 2010, and Zuend and Seinfeld, 2012), organic salt formation (Barsanti et al., 2009), and non-equilibrium gas-particle partitioning and aerosol dynamics (e.g. Korhonen, et al. 2004, Vesterinen et al. 2007, Boy et al., 2006, and Roldin et al., 2011a-b,) on the SOA formation and properties, and to our knowledge no one has previously included all these processes in the same model.

In this article we describe and apply a newly developed aerosol dynamics and gas- and particle-phase chemistry model for chamber studies (ADCHAM). As the name implies the model is primarily aimed to be used as a flexible model tool for evaluation and design of controlled experiments in e.g. smog chambers (e.g. Nordin et al., 2012), thermo-denuders (e.g. Riipinen et al., 2010), evaporation chambers (e.g. Vaden et al., 2011), flow-tube reactors (e.g. Jonsson et al., 2008) or hygroscopicity measurements set-ups (e.g. Svenningsson et al., 2006). However, the overall aim is to gain better understanding of which processes (e.g. gas phase chemistry, particle phase reactions, particle phase state, aerosol water uptake, cloud droplet activation, and aerosol dynamics) are relevant for the aerosol properties and formation in the atmosphere.

In the future we intend to use this knowledge, to develop the ADCHEM model (Roldin et al., 2011a). ADCHEM is a 2D-Lagrangian model for Aerosol Dynamics, gas phase CHEMistry and radiative transfer (ADCHEM) which has been used for urban plume studies (Roldin et al., 2011b). One of the main purposes with ADCHEM is to improve the sub-grid scale aerosol particle representation in large scale chemistry transport models (e.g. Bergström et al., 2012). In the first version of ADCHEM the ageing of the organic compounds in the atmosphere was simulated with a non-equilibrium 2D-VBS approach. The 2D-VBS method treats the oxidation of organic compounds in a simplified way by generalized OH reactions rates, functionalization and fragmentation patterns (Jimenez et al., 2009, Roldin et al., 2011a and Donahue et al., 2011).

In ADCHAM the secondary aerosol formation is instead modelled by combining the Master Chemical Mechanism version 3.2 (MCMv3.2) (Jenkin et al., 1997, Jenkin et al., 2003, Saunders et al., 2003) and an updated version of the aerosol dynamics and particle phase chemistry module from ADCHEM, which now considers acid catalysed oligomerization, oxidation reactions in the particle phase (e.g. secondary ozonide formation) and the diffusion limited transport of compounds between the gas phase, particle surface and particle bulk phase. In this work we test the capability of ADCHAM to simulate, (1) the mass transfer limited uptake of NH_3 and formation of organic salts between ammonium and carboxylic acids (Na et al., 2007 and Kuwata and Martin, 2012), (2) the slow and almost particle size independent evaporation of α-pinene SOA particles (Vaden et al., 2011) and (3) the influence of heterogeneous reactions on the SOA formation and properties.

Regional and global scale chemistry transport models (e.g. the EMEP model (Bergström et al., 2012) rely on semi-empirical parameterizations for the SOA formation (e.g. VBS) derived from smog chamber experiments. This is one of many reasons why it is important to constrain the uncertainties related to specific chamber effects. Hence, as a final application, we illustrate how ADCHAM can be used to study the influence of chamber wall effects on the SOA mass formation, particle number size distribution and gas phase chemistry during a *m*-xylene oxidation experiment from Nordin et al., (2013).

The aims of this article are:
1) To describe a novel model for non-equilibrium partitioning of semi-volatile organic and inorganic compounds between gas and particle phase and chemical reactions in the gas and particle phase.
2) To illustrate the wide applicability of the ADCHAM model.
3) Investigate potentially influential but poorly known processes for SOA formation and volatility, e.g. oligomerization, heterogeneous oxidation, organic salt formation, and diffusion limited transport in the particle surface and bulk.
4) To demonstrate how ADCHAM can be used to constrain the chamber wall effects on the observed SOA formation.

For several of the model applications presented in this article many of the model parameters are unknown (e.g. diffusion coefficients in the particle bulk phase and oligomerization rates). For these conditions we have run the model with different parameter values and studied how sensitive the model results are to different unknown processes (parameters). In those cases, the model results should be considered as sensitivity tests and not as a best estimate of the process or parameters we try to model.

2 Model description

ADCHAM consist of:

1) a detailed gas phase kinetic code (in this work with reactions from MCMv3.2),
2) an aerosol dynamics code (Roldin et al., 2011a) which include Brownian coagulation, homogeneous nucleation, dry deposition to chamber walls and a detailed condensation/evaporation algorithm,
3) a novel particle phase chemistry module which is closely connected to the condensation evaporation algorithm and,
4) a kinetic multi-layer model which treats the diffusion of compounds between the particle surface and several bulk layers, analogous to Shiraiwa et al. (2010).

Figure 1 shows a schematic picture of the ADCHAM model structure. The model explicitly treats the bulk diffusion of all compounds (including O_3 and potentially other oxidation agents) between different particle layers and bulk reactions. For all compounds except O_3 the gas-surface exchange is modelled with a condensation/evaporation equation which considers the gas-surface diffusion limitations and non-unity sticking probability at the surface layer (surface mass accommodation) (Eq. 1). In each particle layer the model considers acid catalysed oligomerization, equilibrium reactions between inorganic and organic salts and their dissolved ions, and oxidation of SOA with O_3.

In ADCHAM the different processes are solved with separate modules using operator splitting. For each main model time step (in this work 10 s) ADCHAM considers homogeneous nucleation, followed by dry deposition of particles (Sect. 2.2.3) and potentially gases, emissions of gases and particles, gas phase chemistry (Sect. 2.1) and coagulation (Sect. 2.2.2). After this ADCHAM handles the condensation and evaporation of all organic and inorganic compounds (Sect. 2.2.1) and the uptake, diffusion and reactions of O_3 in the different particle layers (Sect. 2.4.2). For these processes ADCHAM uses a much shorter internal time step (in this work 1-10 ms). The gas-particle partitioning rely upon updated activity coefficients (Sect. 2.3.1), hydrogen ion concentrations (Sect. 2.3.2), water content, concentrations of inorganic and organic salts (Sect. 2.3.3) and their corresponding anion and cations. Therefore, the gas-particle partitioning is usually the most time demanding process in ADCHAM. Finally the model considers the diffusion of organic and inorganic compounds between all particle layers (Sect. 2.4.1) and acid catalysed oligomerization (Sect. 2.3.4).

2.1 Gas phase chemistry

To be able to implement the detailed MCMv3.2 gas phase chemistry together with user specified reactions and reaction rates (e.g. chamber wall effects) in a computationally efficient way in MATLAB, we constructed a program which automatically creates a system of equations which can be used to calculate the concentrations of the user specified compounds. The only required input to the program is the MCMv3.2 names of the compounds which can be downloaded at http://mcm.leeds.ac.uk/MCM. The output from the program is a set of coupled ordinary equations (one for each compound) and the Jacobian matrix which is used by the ode15s solver in MATLAB. The constructed code can either be used as a standalone code for separate gas phase chemistry simulations, or used as a module in the ADCHEM or ADCHAM model. The ode15s solver in MATLAB is intended to be used for stiff ordinary differential equation systems. The solver uses an adaptive and error tolerance controlled internal time step in order to solve the gas phase chemistry.

In Sect. 3.2 and 3.3 we simulate the SOA formation from ozonolysis of α-pinene in the presence of CO or cyclohexane as OH scavenger. We constructed an equation system consisting of all MCMv3.2 reactions involving inorganic gas phase chemistry and all oxidation products of α-pinene and cyclohexane (in total 668 compounds and 2093 reactions). In Sect. 3.4 we also model the SOA formation oxidation of *m*-xylene with the MCMv3.2 gas phase chemistry (273 compounds and 878 reactions).

2.2 Aerosol dynamics

The aerosol dynamics module in ADCHAM is based on the aerosol dynamics code from the ADCHEM model (Roldin et al., 2011a). A shorter description with focus on the important updates is given below.

2.2.1 Condensation and evaporation

In ADCHAM the gas-particle partitioning depends on the chemical composition in the particle surface layer. Dissolution of ammonia into the particle water and/or organic phase surface layer is treated as an equilibrium process, considered after the diffusion limited condensation/evaporation of HNO_3, H_2SO_4 and organic compounds (Eq. 1) (of which carboxylic acids influence the particle acidity and hence the ammonia dissolution).

$$I_i = 2D_iD_pf_i(Kn_i, \alpha_{s,i})(C_{i,\infty} - C_{i,s}), \qquad f_i(Kn_i, \alpha_{s,i}) = \frac{0.75\alpha_{s,i}(1-Kn_i)}{Kn_i^2+Kn_i+0.283Kn_i\alpha_{s,i}+0.75\alpha_{s,i}} \qquad (1)$$

In Eq. (1) I_i is the contributions of species i to the particle molar growth rates, f_i is the Fuchs-Sutugin correction factor in the transition region, $C_{i,\infty}$ is the gas phase concentration of species i far from the particle surface (mol m^{-3} air), $C_{i,s}$ is the saturation gas phase concentration at the particle surface, D_i is the gas phase diffusion coefficient, D_p is the particle diameter, Kn_i is the non-dimensional Knudsen number and $\alpha_{s,i}$ is the surface mass accommodation coefficient.

In this work we estimate the pure-liquid saturation vapour pressures (p_0) of the MCMv3.2 oxidation products using either the group contribution method SIMPOL (Pankow and Asher, 2008) or the method by Nannoolal et al. (2008) (here referred to as the Nannoolal method). The corresponding equilibrium vapour pressures ($p_{s,i,j}$) for each particle size bin (j) are derived with Raoult's law, using the mole fractions of each organic compound ($x_{i,j}$), the activity coefficients ($\gamma_{i,j}$) calculated with the AIOMFAC thermodynamic model (Zuend et al., 2008 and 2011) (Sect. 2.3.1), and the Kelvin effect ($C_{k_{i,j}}$) (Eq. 2). The surface tension (σ_i) of the organic compounds were assumed to be 0.05 Nm^{-1} following Riipinen et al. (2010).

$$p_{s,i,j} = p_{0,i} \cdot x_{i,j} \cdot \gamma_{i,j} \cdot C_{k_{i,j}}, \quad C_{k_{i,j}} = e^{\left(\frac{4M_i\sigma_i}{RT\rho_pD_{p,j}}\right)} \qquad (2)$$

T is the temperature in Kelvin, R is the universal gas constant (J mol^{-1} K^{-1}), M_i is the molar mass of compound i and ρ_p is the density of the phase which the compound partition to.

The mole fraction for compound i in Eq. (2) is the mole fraction of the organic compound in the surface layer organic phase which compound i partitions into (dissolves). In this article we either treat all SOA (monomers + oligomers + organic salts) as one phase or as two completely separated phases. Hence, if the model treats the oligomers and organic salts as a separate phase, then this material has no influence on the saturation vapour pressures of the monomers (Eq. 2). However, adsorption of low-volatility oligomers at the surface layer still affects the gas-particle partitioning of monomer SOA, by altering the surface mass accommodation (Sect. 2.4.1) and by decreasing the monomer SOA fraction in the surface layer.

In this work the condensation and evaporation mechanism includes all organic compounds with modelled pure-liquid saturation vapour pressures less than 1 Pa. For the α-pinene oxidation experiments which we model in Sect. 3.2 and 3.3 this involves 154 non-radical MCMv3.2 organic compounds, while for the *m*-xylene SOA formation experiment modelled in Sect. 3.4 we consider 112 condensable organic MCMv3.2 compounds.

2.2.2 Coagulation

ADCHAM also includes a Brownian coagulation algorithm (Roldin et al., 2011a). However, it still remains a challenge to combine the coagulation algorithm with the kinetic multilayer model, when the number of particle layers depends on the particle size. In this first version of ADCHAM it is only possible to treat coagulation between particles composed of maximum three layers (e.g. a surface monolayer layer, a bulk layer and a seed aerosol core). When two particles composed of such a layer structure collide the layers are simply assumed to merge together forming a new spherical particle with a surface layer, a bulk layer and a seed aerosol core. Because the surface area of the formed particle is always less than the sum of the surface areas of the two original particles the width of the surface layer increases. Hence, in order to keep the width of the surface layer at approximately the thickness of one monolayer, part of the surface layer material (by default with identical composition as the remaining surface layer) is transferred to the particle bulk.

2.2.3 Dry deposition and chamber wall effects

It is well known that dry deposition losses of particles onto the chamber walls have large influence on many chamber experiments (see e.g. Pierce et al., 2008). A commonly used method (see e.g. Hildebrandt et al., 2009 and Loza et al., 2012) is to scale the formed SOA mass with the measured relative seed aerosol (typically ammonium sulphate) loss rate. With this method it is assumed that the particles deposited on the chamber walls continue to take up SOA as if they were still present in the gas phase. A second method which was also used by Hildebrandt et al. (2009) and Loza et al., (2012) is to assume that once the particles have deposited on the chamber walls the gas-particle partitioning stops. These two correction methods can be considered to be two extremes, where the first method gives an upper bound of the SOA mass formed during the experiments while the second method gives a lower bound of the SOA formed during the experiments (at least if the SOA particles on the chamber walls are not evaporating and the gas phase losses directly to the chamber walls are negligible).

ADCHAM considers the dry deposition of particles onto chamber walls and also keeps track of the particles deposited on the walls. The model also treats the mass transfer limited gas to particle partitioning between the gas phase and the wall deposited particles. Hence, ADCHAM can be used to study the influence of chamber wall effects on the SOA mass formation and help constraining the uncertainties of the formed SOA mass (SOA mass yield).

For non-charged particles, ADCHAM uses the indoor dry deposition loss rate model from Lai and Nazaroff (2000) which accounts for different dry deposition loss rates on upward, downward and vertical facing surfaces. However, if a considerable fraction of the particles are charged (e.g. at Boltzmann charge equilibrium) the effective dry deposition loss rate of particles can be considerably enhanced (Pierce et al., 2008). Hence, in order to be able to model realistic dry deposition loss rates of charged particles, ADCHAM keeps track of the fraction of particles suspended in the air with zero, one, two or three elemental charges in each particle size bin. The first order deposition loss rate (s^{-1}) due to charge (k_{charge}) is calculated with Eq. (3) where v_e is the characteristic average deposition velocity due to electrostatic forces (m/s) (McMurry and Rader, 1985). The dry deposition loss rates depend on the friction velocity and for charged particles also on the mean electrical field strength within the chamber ($\overline{\boldsymbol{E}}$). Unfortunately both of these parameters are usually poorly known and need to be estimated.

McMurry and Rader, (1985) found that $\overline{\boldsymbol{E}}$ was ~45 V cm^{-1} in an almost spherical ~0.25 m^3 Teflon chamber. On the chamber surfaces they measured a negative electrical field of -300±150 V cm^{-1}. They attributed the lower empirically derived electric field within the chamber to the fact that the particles in the bag will be influenced by a net electrical field, which has contributions from all points on the chamber surfaces. Hence, the shape and size of the chamber will also influence the mean electrical field.

$$k_{charge} = \frac{A_{chamber}\, v_e}{V_{chamber}}, \qquad v_e = \frac{neC_c\overline{E}}{3\pi\mu D_p} \tag{3}$$

$A_{chamber}$ is the chamber surface area, $V_{chamber}$ is the chamber volume, n is the number of elemental charges of the particle, e is the elementary charge, C_c is the Cunningham slip correction factor and μ is the dynamic viscosity of air.

The mass transfer limited uptake of gases to and from the chamber walls need to be considered in order to take into account the potential uptake (dissolution) of organic compounds in the SOA particles deposited on the chamber walls (Hildebrandt et al., 2009), as well as directly onto the Teflon chamber surfaces (Matsunaga and Ziemann, 2010). For the condensation uptake or evaporation loss of SOA from the particles deposited on the walls, we assume that the particles deposited on the walls behave as if they were still suspended in (direct contact with) a thin (1 mm) air layer adjacent to the chamber walls. As more particles get deposited on the walls, the SOA concentration on the chamber wall will increase. The condensable organic compounds in the thin air layer next to the chamber walls can dissolve into the organic particle phase on the walls. However, semi-volatile organic compounds may also evaporate from the particles on the walls. The gas-particle partitioning between the wall-deposited particles and the thin air layer next to the chamber walls is modelled with the condensation and evaporation module described in Sect. 2.2.1.

ADCHAM also considers the adsorption and desorption of condensable organic compounds onto the Teflon surface film. This is modelled as a reversible process in accordance with Matsunaga and Ziemann, 2010. The adsorption of gas phase organic compounds onto the chamber walls is represented by a first order loss rate from the near wall gas phase to the walls ($k_{g,w}$). The desorption rate from the Teflon surfaces out to the thin layer next to the chamber walls ($k_{w,g,i}$) depends on the pure-liquid saturation vapour pressures ($p_{0,i}$) of the adsorbed compounds (Eq. 4) (Matsunaga and Ziemann, 2010). Equation 5 and 6 describe the rate of change of the organic compound (X_i) (due to adsorption and desorption) on the chamber walls and in the air layer adjacent to the wall, respectively. [$X_{i,g,w}$] is the concentrations of compound X_i in the thin layer adjacent to the chamber walls. The concentration at the chamber wall ([$X_{i,w}$]) is given as an effective chamber volume concentration (total number of X_i molecules on the walls divided by the total chamber volume ($V_{chamber}$)). V_{wall} is the air volume of the thin (1 mm) layer adjacent to the chamber walls, C_w is an effective wall equivalent mass concentration which the organic compounds can dissolve into, M_w is the average molar mass of the Teflon film, and $\gamma_{w,i}$ is the activity coefficient of compound i in the Teflon film. $k_{g,w}$ and $C_w/(M_w \cdot \gamma_{w,i})$ in Eq. (4) was experimentally determined by (Matsunaga and Ziemann, 2010) for n-alkanes, 1-alkenes, 2-alcoholes and 2-ketones to 9, 20, 50 and 120 µmol m^{-3}, respectively.

$$k_{w,g,i} = \frac{k_{g,w}}{(RT/p_{0,i} \cdot C_w/(M_w \cdot \gamma_{w,i})} \tag{4}$$

$$\frac{d[X_{i,w}]}{dt} = \left(k_{g,w}\left[X_{i,g,w}\right] - k_{w,g,i}\left[X_{i,w}\right]\right)\frac{V_{wall}}{V_{chamber}} \tag{5}$$

$$\frac{d[X_{i,g,w}]}{dt} = -k_{g,w}\left[X_{i,g,w}\right] + k_{w,g,i}\left[X_{i,w}\right] \tag{6}$$

For a compound with p_0=2.5x10^{-2} Pa and $C_w/(M_w \cdot \gamma_{w,i})$=10 µmol m^{-3}, Eq. (4) partitions ~50 % to the gas phase and ~50 % to the chamber walls, at equilibrium and room temperature. At equilibrium, compounds with a vapour pressure <10^{-3} Pa and $C_w/(M_w \cdot \gamma_{w,i})$>10 µmol m^{-3} will almost exclusively be found at the walls, if they are not able to form SOA rapidly enough. Hence, the SOA formation in the smog chamber will depend on: (1) the formation rate of condensable organic compounds, (2) the particle deposition losses, (3) the magnitude of the condensation sink to the particles in the air and onto the chamber walls, and (4) the diffusion limited uptake onto the chamber walls and particles on the walls.

The concentration gradient in the laminar layer adjacent to the chamber walls generally drives condensable gas phase components from the well mixed chamber volume to the chamber walls (thin model layer next to the wall). In this work we model this mass transfer with Fick's first law of diffusion, assuming a linear concentration gradient across the laminar layer next to the chamber wall (see Fig. 2).

The width of the laminar layer was used as a model fitting parameter. The gas phase chemistry and the gas particle mass transfer (condensation) in the well mixed chamber volume and in the thin layer adjacent to the chamber wall were solved using operator splitting with a model time step of 10 ms. The mass transfer between the well mixed chamber volume and the thin layer next to the chamber wall was modelled with a time step of 0.1 ms. The model needs to take short time steps because of the large condensation sink (or evaporation source) of the wall deposited particles and the Teflon surfaces which may rapidly alter the concentrations in the thin air layer next to the chamber walls.

2.2.4 Size distribution structures

Analogous to ADCHEM (Roldin et al., 2011a) ADCHAM include several methods (full-stationary, full-moving and moving-centre) in order to treat the changes in the particle number size distribution upon condensation/evaporation or coagulation. These methods are all mass and number conserving and have different advantages and disadvantages (Korhonen, et al. 2004, Jacobson, 2005 and Roldin et al., 2011a). For all simulations performed in this article, we have used the full-moving method where the diameter grid moves with the particles. Hence, this method has no numerical diffusion problems when particles grow by condensation or evaporate. Homogeneous nucleation is considered by adding new particle size bins when new particles are formed (Sect. 3.2 and 3.3).

2.3 Particle phase chemistry

2.3.1 Activity coefficients and organic-inorganic interactions

The AIOMFAC model is based on the UNIFAC model for organic mixtures but also considers organic-inorganic interaction which allows us to study salt-effects on the SOA formation. AIOMFAC considers interactions between 12 different ions (including NH_4^+, NO_3^-, H^+, SO_4^{-2} and HSO_4^-) and alkyls, hydroxyls, carboxyls, ketones, aldehydes, ethers, esters, alkenyls, aromatic carbon-alcohols and aromatic hydrocarbons (Zuend et al., 2008 and 2011). For other important functional groups i.e. nitrates, nitros, PANs and peroxides no ion-organic functional group interaction parameterizations are available. Hence, for these functional groups we only consider organic-organic functional group interactions. In total the model considers 52 different UNIFAC functional subgroups, with interaction parameters from Hansen et al. (1991), except for alcohols (Marcolli and Peter, 2005) and nitrates, PANs and peroxides for which we use the parameterization from Compernolle et al. (2009). In ADCHAM, the activity coefficients are calculated before the condensation algorithm is used and when updating the hydrogen ion concentration ($[H^+]$) for the acid catalysed oligomerization.

2.3.2 Acidity and dissociation of inorganic compounds in organic rich phases

The hydrogen ion concentration is calculated in the condensation algorithm and when considering acid catalysed oligomerization. Analogous to the procedure in ADCHEM (Roldin et al., 2011a) [H^+] in the particle water or particle water + organics phase is calculated by solving the ion balance equation (Eq. 7). In ADCHAM we have extended the ion balance equation with dissociation products of carboxylic acids ($RCOO^-$). In this work we assume that all carboxylic acids have identical dissociation constants (see Sect. 3.2). Hence, [$RCOO^-$] in Eq. (7) represent the total concentration (mol/kg solvent) of dissociated carboxylic acids.

$$[H^+] + [NH_4^+] + [Na^+] = [NO_3^-] + 2[SO_4^{2-}] + [HSO_4^-] + [Cl^-] + [OH^-] + [HCO_3^-] + 2[CO_3^{2-}] + [RCOO^-] \quad (7)$$

In order to calculate [H^+], all concentrations except the hydrogen ion concentration in Eq. (7) is replaced with known equilibrium coefficients, activity coefficients from AIOMFAC, and the total concentration of dissolved dissociated and non-dissociated compounds, ([RCOOH]+[$RCOO^-$]), ([NH_3(aq)]+[NH_4^+]), ([SO_4^{2-}] +[HSO_4^-]), ([HNO_3]+ [NO_3^-]) and ([HCl(aq)]+ [Cl^-]). In this work the uptake of CO_2 in the particles was treated as an equilibrium process. The HCO_3^- and CO_3^{-2} concentrations depend on the hydrogen ion concentration and the CO_2 partial pressure (390 ppbv). When all unknown ion concentrations have been replaced with the known parameters, Eq. (7) becomes an 8th order polynomial with [H^+] as the only unknown variable. The hydrogen ion concentration is given by the maximum real root of this polynomial.

To treat the CO_2 uptake as an equilibrium process may not be realistic if the particles are very viscous (see Sect. 1). However, the estimated diffusion coefficients of other small “guest” molecules (e.g. O_3, OH and H_2O) in an amorphous glassy organic matrix is in the order of 10^{-10}-10^{-12} cm^2 s^{-1} at room temperature (Koop et al., 2011, Zobrist et al., 2011). This gives corresponding e-folding times of equilibration for submicron particles in the range of seconds.

All experiments which we model in this paper were performed at dry conditions (RH ≤ 5 %). For the α-pinene SOA experiments (Sect. 3.2-3.3), the modelled particle water mass content is only ~0.4 % at a RH of 5 %. For these particles the solvent will therefore mainly be the organic compounds and not water. Hence, in this work the concentrations of the inorganic ions (including H^+) is not given for the aqueous but for the combined organics and water phase. Henry’s law coefficients (K_H) and dissociation rates (K_a) of the inorganic compounds and carboxylic acids, are (if at all) usually only available for aqueous solutions. However, there is often a relationship between the ΔpK_a ($-\log_{10}(K_{a,base}) + \log_{10}(K_{a,acid})$) and the proton transfer between the Brønsted acid and the Brønsted base, in protic ionic liquids (Greaves and Drummond, 2008). Thus, we will use the aqueous dissociation rates and Henry's law coefficients for the organic amorphous SOA and water mixtures, and take into account the non-ideal interactions between the ions, organic solvents and water using AIOMFAC (Sect. 2.3.1).

With these assumptions in mind, the modelled absolute values of [H^+] should be interpreted with caution. However, we believe that the model can give a realistic representation of the relative influence of different types of dissolved compounds on the particle acidity. For instance, carboxylic acids will most likely increase [H^+] also in an organic rich phase, while dissolved ammonia will decrease [H^+]. For all other organic compounds except the carboxylic acids, the dissociation rates were assumed to be equal to that of pure water ($pK_a = 14$). Hence, equivalent to aqueous solutions the acidity will mainly be governed by the carboxylic acids and inorganic compounds.

2.3.3 Inorganic and organic salt formation

In ADCHAM the inorganic salts $(NH_4)_2SO_4$, NH_4HSO_4 and NH_4NO_3 and the organic salts of ammonium and different carboxylic acids (NH_4RCOO) can be considered to form. All these salts contain NH_4^+ and which of these salts that will be formed depend on the solubility constants, the ammonium concentration, the concentration of the different anions and the activity coefficients. Because all these salts contain ammonium the salt which forms first will limit the formation of other salts. In this work, we only simulate experiments performed on pure organic particles or organic particles which take up NH_3(g). Hence, NH_4RCOO(s) was the only (solid) salt which was considered to be formed in the particle organics-water phase. The solid salt concentrations are updated iteratively every time step which the condensation/evaporation algorithm is used.

When updating the NH_4RCOO(s) concentration, ADCHAM starts by estimating the activity coefficients and the hydrogen ion concentration (Eq. 7). After this non-equilibrium NH_4^+ and $RCOO^-$ concentrations ($[NH_4^+]^*$ and $[RCOO^-]^*$) can be derived, and the total concentrations of NH_4 ($[NH_{4,tot}]=[NH_4^+]^*+[NH_4RCOO]_{t-1}$) and RCOO ($[RCOO_{tot}]=[RCOO^-]^*+[NH_4RCOO]_{t-1}$) are estimated. These values are then inserted into the solubility product equation (Eq. 8). Rearranging Eq. (8) gives a second order polynomial where the new NH_4RCOO concentration ($[NH_4RCOO]_t$) is given by the smallest positive real root. Finally the NH_4^+ and $RCOO^-$ concentrations are updated and the iteration starts from the beginning by deriving the hydrogen ion concentration again. The iteration proceeds until the relative change in the NH_4^+, $RCOO^-$ and H^+ concentrations all are less than 10^{-3} between one iteration step.

$$K_{NH_4RCOO} = \gamma_{NH_4}\gamma_{RCOO}[NH_4^+][RCOO^-] = \gamma_{NH_4}\gamma_{RCOO}([NH_4, tot] - [NH_4RCOO])(RCOO_{tot} - [NH_4RCOO]) \quad (8)$$

2.3.4 Acid catalysed oligomerization

Any oligomerization mechanisms in the gas phase, particle phase or on the particle surfaces (including different functional groups, ozonolysis, acid catalysed reactions, and radicals), can easily be implemented in ADCHAM. In this work we consider six different oligomerization mechanisms (R1-R6) which have been listed as possible reaction pathways for oligomer formation in the overview by Hallquist et al. (2009). Currently ADCHAM only considers the reactions between monomers which form dimers and not the possible reactions between dimers and dimers-monomers.

$$hydroperoxides(p) + aldehydes(p) + H^+ \leftrightarrow peroxyhemiacetals(p) \quad \text{(R1a)}$$

$$hydroperoxides(p.s.) + aldehydes(g) + H^+ \leftrightarrow peroxyhemiacetals(p.s.) \quad \text{(R1b)}$$

$$aldehydes(p) + aldehydes(p) + H^+ \leftrightarrow aldol\, reaction\, prod.(p) \quad \text{(R2a)}$$

$$aldehydes(p.s.) + aldehydes(g) + H^+ \leftrightarrow aldol\, reaction\, prod.(p.s.) \quad \text{(R2a)}$$

$$alcoholes(p) + aldehydes(p) + H^+ \leftrightarrow hemiacetals(p) \quad \text{(R3)}$$

$$alcoholes(p) + carboxylic\ acids(p) + H^+ \leftrightarrow esters(p) + H_2O(p) \quad \text{(R4)}$$

$$RO_2\,(g) + RO_2\,(g) \leftrightarrow ROOR - type\, peroxides(g) \quad \text{(R5)}$$

$$carbonyls(p) + carbonyls\ (p) + O_3(p) \leftrightarrow secondaryozonides(p) \quad \text{(R6)}$$

The notation within the brackets denotes weather the compounds are in the gas phase (g), particle phase (p) or particle-surface layer (p.s.) upon reaction. If H^+ is included in the reaction, the formation of oligomer is acid catalysed, which is generally the case in the particle phase (Hallquist et al., 2009). The acid catalysed formation rate of a dimer can generally be considered to be proportional to the hydrogen ion concentration (see e.g. schemes by Tolocka et al., 2004 and Iinuma et al., 2004). ADCHAM explicitly treats the formation and the degradation of dimers back to monomers as separate reactions (R7-R8) and not as an equilibrium process.

$$[\mathrm{monomer}_j] + [\mathrm{monomer}_i] + [\mathrm{H}^+] \rightarrow [\mathrm{dimer}_{ji}] \tag{R7}$$

$$[\mathrm{dimer}_{ji}] \rightarrow [\mathrm{monomer}_j] + [\mathrm{monomer}_i] + [\mathrm{H}^+] \tag{R8}$$

The acid catalysed dimer formation rates in the particle phase (*$F_f(p)$*) or particle surface (*$F_f(p.s.)$*) between monomer *i* and *j* depend on a reaction specific formation rate constant (k_f) and the hydrogen ion concentration (c_{H^+}) (R7 and Eq. 9 and 10). The dimer formation rate in the particle surface layer formed between compound *j* found in the gas phase and compound *i* found at the particle surface is treated as a reactive uptake. The dimer degradation rate in the particle bulk or at the particle surface (F_d(p) and $F_d(p.s.)$) simply depends on the dimer concentration and a dimer specific degradation reaction rate constant (k_d) (Eq. 11 and 12).

$$F_f(p) = k_f(p) \cdot c_{H^+}(p) \cdot c_{m,i}(p) \cdot c_{m,j}(p) \tag{9}$$

$$F_f(p.s.) = k_f(p.s) \cdot c_{H^+}(p.s.) \cdot c_{m,i}(p.s.) \cdot c_{m,j}(g) \tag{10}$$

$$F_d(p) = k_d(p) \cdot c_{d,i}(p) \tag{11}$$

$$F_d(p.s.) = k_d(p.s.) \cdot c_{d,i}(p.s.) \tag{12}$$

The temporal evolution of the dimer and monomer concentrations (c_d and c_m) in the particle bulk layers and surface layer are derived with a kinetic model. This code solves a coupled ordinary differential equation system, consisting of one ordinary differential equation for each SOA monomer (Eq. 13), and one ordinary differential for each dimer (Eq. 14). The equations are given by the sum of all dimer degradation and formation rates for the individual reactions which each compound *i* is involved in.

$$\frac{dc_{m,i}}{dt} = \sum_{k=1}^{Z} F_{di,k} x_{m,i} - \sum_{k=1}^{N} F_{fi,k} \tag{13}$$

$$\frac{dc_{d,i}}{dt} = -\sum_{k=1}^{P} F_{di,k} + \sum_{k=1}^{Q} F_{fi,k} x_{d,i} \tag{14}$$

In order to not end up with an enormous coupled ordinary differential equation system, the different dimers are classified into 7 different categories depending on the type of reaction (R1a-R5). Secondary ozonide formation (R6) is treated by a separate kinetic multilayer module for ozone uptake, diffusion and reactions with SOA (see Sect. 2.4.2). In order to be mass conserving the number of moles of dimer formed is corrected with the molar ratio (x_d) between the molar mass of the product(s) and the sum of the molar masses of the reacting compounds. In ADCHAM all dimers have by default a molar mass of 400 g/mol. When we lump the dimers into different categories the information about their exact chemical composition and origin are lost. This can be a problem when considering the reversible reactions back to monomers. In this work we have assumed that the dimer SOA is converted back to the different monomers with fractions (x_m) corresponding to the (current time step) relative abundance of each monomer SOA compound which is involved in the dimer formation. This is a reasonable assumption if the monomer SOA composition does not change substantially on a time scale longer than the lifetime of the dimer.

The modelled relative amount and composition of oligomer SOA in each particle layer depends on: (1) the monomer SOA composition, (2) the hydrogen ion concentration, (3) the dimer formation rates, (4) the oligomer degradation reaction rates, (5) possible evaporation and condensation of monomers and dimers (vapour pressures), (6) the mixing between different particle layers (diffusion coefficients of monomers and dimers), (7) the ozone uptake at the particle surface, (8) the ozone diffusion rate within the particle bulk phase, (9) the reaction rates of ozone with unsaturated organic compounds in the particle phase, and (10) the time of ageing.

2.4 Kinetic multi-layer model

To be able to model the diffusion limited mass transfer of ozone from the gas-particle interface to the particle core, and the reaction between ozone and the organic compounds in the particle phase, Shiraiwa et al. (2010) developed the kinetic multilayer model KM-SUB which is based on the PRA concept of gas-particle interactions (Pöschl-Rudich-Amman, 2007 and Ammann and Pöschl, 2007). This model divides the particles into a sorption layer, a quasi-static surface layer, near-surface bulk, and multiple bulk layers and considers the gas-surface transport, reversible adsorption, surface layer reactions, surface-bulk transport, bulk diffusion and bulk reactions. Recently, Shiraiwa et al. extended the kinetic multilayer model to also include condensation, evaporation and heat transfer (KM-GAP) (Shiraiwa et al., 2012).

In ADCHAM we do not separate the quasi-static surface layer and near-bulk surface layer into two separate layers, but instead have one monolayer thick surface layer. The uptake of all organic and inorganic compounds except O_3 into the surface layer is modelled as a condensation/evaporation process where we take into account the possibility of non-unity sticking probability (surface mass accommodation) (Sect. 2.2.1). Analogous to KM-SUB and KM-GAP, ADCHAM explicitly treats the bulk diffusion of all compounds between the surface and the different bulk layers using first-order mass transport rate equations.

The kinetic multilayer model in ADCHAM consists of two separate modules. The first module (Sect. 2.4.1) treats the diffusion of all organic and inorganic compounds (except O_3 and potentially other oxidation agents) between the different bulk layers. The second module (Sect. 2.4.2) considers the exchange of O_3 between the gas phase, particle surface and particle bulk and the reactions with organic compounds in the particle phase.

2.4.1 Diffusion of organic and inorganic compounds

The transport velocity of compound X_i between the bulk layers or the surface and first-bulk layer is given by Eq. (15). D_{X_i} is the diffusion coefficient of compound X_i, and δ_k and δ_{k+1} represent the width of the two adjacent layers (k and k+1) which X_i is transported between. Shiraiwa et al., (2010, 2012) use identical layer width for all bulk-layers. Hence, in their expression for the bulk to bulk transport velocity the average travel distance of molecular diffusion between two layers is simply given by the layer width and not the more general $(\delta_{k+1} + \delta_k)/2$.

$$k_{k+1,k,X_i} = k_{k,k+1,X} = \frac{4D_{X_i}}{\pi(\delta_{k+1}+\delta_k)/2} \tag{15}$$

The transport of compound X_i between the particle layers (including the exchange between the surface and first-bulk layer) is modelled with Eq. (16). A_k and V_k represent the area of exchange between layer k-1 and k and the volume of layer k, respectively. $[X_i]_k$ is the volume concentration (volume fraction) of compound X_i in layer k.

$$\frac{d[X_i]_k}{dt} = (k_{k-1,k}[X_i]_{k-1} - k_{k,k-1}[X_i]_k)\frac{A_k}{V_k} + (-k_{k,k+1}[X_i]_k + k_{k+1,k}[X_i]_{k+1})\frac{A_{k+1}}{V_k} \tag{16}$$

In order to keep the volume of each layer intact, the total volume flux from one layer should be identical to the volume flux into that layer. In order to accomplish this we use a volume flux matching approach where the total net volume transport between each A_k is zero. With this method the flux of each compound from the direction with the larger total volume flux is simply corrected down with a factor (x_k) equal to the ratio between the smaller and larger of the two total volume fluxes (Eq. 17). Hence, if one bulk layer consists of completely solid non-diffusing material (e.g. crystalline salt) no material can be moved in or from this layer and the transport across this layer is completely shut down.

$$x_k = \frac{\min(\sum_{i=1}^{N}(k_k[X_i]_k), \sum_{i=1}^{N}(k_{k-1}[X_i]_{k-1}))}{\max(\sum_{i=1}^{N}(k_k[X_i]_k), \sum_{i=1}^{N}(k_{k-1}[X_i]_{k-1}))}, \qquad N\text{=total number of compounds} \qquad (17)$$

The equations describing the concentration change of all compounds in all layers (Eq. 16) comprise a system of N x N_L coupled ordinary differential equations (N_L=number of particle layers) which we solve with the ode15s solver in MATLAB.

Figure 3 shows a schematic picture of the kinetic multilayer module in ADCHAM. In contrast to the kinetic multilayer model by Shiraiwa et al. (2010, 2012) the number of particle layers increases when the particles grow. Hence, particles of different sizes are composed of different number of layers.

Once the depth of the surface layer becomes larger than 1.1 nm, material is moved from this layer to the first bulk-layer, leaving a 1 nm thick surface layer. If the first bulk-layer becomes larger than a certain value (by default 3 nm thick) it is split into a first and second bulk layer with identical compositions, 1 and 2 nm thick, respectively.

By default the material which moves from the surface layer to the first bulk-layer has the same composition as the surface layer. However, it is also possible to treat certain compounds as a separate phase which accumulate in the surface layer (adsorb) and do not move into the particle bulk when the particles grow. These compounds will limit the uptake of other compounds. In ADCHAM this is represented by scaling the surface mass accommodation coefficient of the condensable compound X with the relative surface coverage of the adsorbed species (θ_s) Eq. 18 (Pöschl et al., 2007). In Sect. 3.3 we illustrate that the adsorption of material in the surface layer can be important to consider when modelling partitioning of SOA between the gas and particle phase.

$$\alpha_{s,X} = \alpha_{s,0,X}(1-\theta_s) \qquad (18)$$

Upon evaporation material is lost from the surface layer and if the layer thickness becomes less than 0.99 nm, material is moved from the first bulk layer to the surface layer, to keep the surface layer width intact. If the first bulk layer width becomes less than a certain value (by default 0.8 nm), this layer is merged together with the second bulk layer and together they form a new first bulk layer. The rest of the particle bulk is divided into layers of almost constant width (by default 2 nm thick). The width of these layers may vary somewhat due to chemical reactions (e.g. between O_3 and unsaturated hydrocarbons and mass transfer limited water uptake).

In each particle layer the model considers different oligomerization reactions and the equilibrium reactions between salts and their dissolved ions in the organic + water phase (Sect. 2.3.3 and 2.3.4). The formed oligomers and salts make up a particle volume fraction (f_p) with much lower diffusivity than the rest of the compounds. Hence, oligomerization and solid salt formation increases the viscosity which also limits the diffusion of the liquid compounds according to the obstruction theory (Stroeve, 1975). The treatment of the oligomers as solid non-diffusing compounds which limits diffusion of the liquid compounds were adopted from Pfrang et al. (2011) which used KM-SUB to model degradation of an organic 12-component mixture with ozone.

According to the obstruction theory the diffusivity of compound X_i, D_{Xi}, is a function of the fraction of solid or semi-solid material and the diffusivity, $D_{0,Xi}$, without any solid or semi-solid material (Eq. 19). The diffusivity of organic compounds can vary from ~10^{-5} cm^2 s^{-1} in a liquid to ~ 10^{-20} cm^2 s^{-1} in a solid organic matrix (Shiraiwa et al., 2011).

$$D_{Xi} = D_{0,Xi}(2 - 2f_p)/(2 + f_p) \tag{19}$$

2.4.2 O_3 diffusion and reactions with SOA

The diffusion of O_3 and potentially other oxidation agents between the particle bulk layers is equivalent to the treatment of other compounds (Eq. 15 and 16), except that we do not consider that the dissolved O_3 in the particle phase take up a bulk volume of its own.

The uptake of ozone from the gas phase to the particle surface is treated as a reversible adsorption process (Fig. 3). This approach was adopted from Shiraiwa et al. (2010). The surface accommodation coefficient of O_3 is given by Eq. (20). θ_{s,O_3} is the relative coverage of adsorbed

O_3 on the particle surface. The adsorption of O_3 from the near surface gas phase (gs) to the sorption layer (so) and the desorption from the sorption layer to the near surface-gas phase is given by Eq. (21) and (22), respectively. ω_{O_3} is the mean thermal velocity of O_3 and $\tau_{d,O_3}$is the desorption lifetime of O_3.

The transport velocity of O_3 from the surface layer to the sorption layer is given by Eq. (23). δ_s is the width of the monolayer thick surface layer and $d_{O_3}$is the width of the sorption layer. Hence, $(\delta_s + d_{O_3})/2$ in Eq. (23) represents the average travel distance between the sorption and surface layer. The transport velocity of O_3 from the sorption layer to the surface layer can then be calculated from Eq. (24). K_{H,O_3} is the Henry's law coefficient of O_3.

$$\alpha_{s,O_3} = \alpha_{s,0,O_3}\left(1 - \theta_{s,O_3}\right), \theta_{s,O_3} = \frac{[O_3]_{so} \cdot {d_{O_3}}^2 \pi}{4} \tag{20}$$

$$J_{ads,O_3} = [O_3]_{gs} \cdot \omega_{O_3} \cdot \alpha_{s,O_3}/4 \tag{21}$$

$$J_{des,O_3} = \tau_{d,O_3}^{-1} [O_3]_{so} \tag{22}$$

$$k_{su,so,O_3} \approx \frac{4 D_{O_3}}{\pi(\delta_s + d_{O_3})/2} \tag{23}$$

$$k_{so,su,O_3} = \frac{4 k_{su,so,O_3} K_{H,O_3} \tau_{d,O_3}^{-1}}{\alpha_{s,O_3} \omega_{O_3}} \cdot T \cdot R \tag{24}$$

Equations 25-27 form a differential equation system which describes the rate of change of the ozone concentration in the particle sorption layer, particle surface layer, and particle bulk layers. The chemical oxidation reactions between ozone and the organic compounds (X_i) are represented by the last term in Eq. (26) and Eq. (27), where the summation is over all compounds which react and consume O_3 in the particle phase. The module also calculates the temporal evolution of the organic compounds (X_i) which are consumed by ozone and the organic compounds which are formed from the oxidation reactions (Y_i) (Eq. 28 and 29). The diffusion of these compounds is treated by the kinetic multilayer module described in Sect. 2.4.1.

$$\frac{d[O_3]_{so}}{dt} = J_{ads,O_3} - J_{des,O_3} - k_{so,su,O_3}[O_3]_{so} + k_{su,so,O_3}[O_3]_{su} \tag{25}$$

$$\frac{d[O_3]_{su}}{dt} = (k_{so,su}[O_3]_{so} - k_{su,so}[O_3]_{su})\frac{A_{su}}{V_{su}} + (-k_{su,b1}[O_3]_{su} + k_{b1,su}[O_3]_{b1})\frac{A_{b1}}{V_{su}} - \sum_{i=1}^{N} k_{Ox,i}[X_i]_{su}[O_3]_{su} \tag{26}$$

$$\frac{d[O_3]_{bk}}{dt} = (k_{bk-1,bk}[O_3]_{bk-1} - k_{bk,bk-1}[O_3]_{bk})\frac{A_{bk}}{V_{bk}} + (-k_{bk,bk+1}[O_3]_{bk} + k_{bk+1,bk}[O_3]_{bk+1})\frac{A_{bk+1}}{V_{bk}} - \sum_{i=1}^{N} k_{Ox,i}[X_i]_{bk}[O_3]_{bk} \tag{27}$$

$$\frac{d[X_i]_{bk}}{dt} = -k_{Ox,i}[X_i]_{bk}[O_3]_{bk} \tag{28}$$

$$\frac{d[Y_i]_{bk}}{dt} = k_{Ox,i}[X_i]_{bk}[O_3]_{bk} \tag{29}$$

Table 1 gives the values of different parameters used in the multilayer module for ozone uptake, diffusion and reactions within the particle phase. Most of the values were adopted from Table 1 in Pfrang et al. (2011).

The coupled ordinary differential equation system describing the temporal evolution of O_3 and the concentration of compounds which are consumed or formed from the O_3 oxidation is solved with the ode15s solver in MATLAB.

3 Model applications

In order to test and illustrate the capability of ADCHAM we apply the model to four different types of experiments which has been published by different research groups. In Sect. 3.1 we model the evaporation experiments of liquid dioctyl phthalate (DOP) particles from Vaden et al. (2011). The same experiments have already been modelled by Shiraiwa et al. (2012) with the KM-GAP model. In Sect. 3.2 we model the SOA formation, ammonia uptake, and organic salt (NH_4RCOO) formation in the α-pinene - NH_3 - O_3 experiments by Na et al. (2007). In Sect. 3.3 we use ADCHAM to model the evaporation experiments of α-pinene SOA particles by Vaden et al., (2011). Finally, we apply ADCHAM to a *m*-xylene oxidation experiment from Nordin et al., 2012 (Sect. 3.4). These examples serve to illustrate the wide applicability of ADCHAM.

For the simulations in Sect. 3.2-3.3 we model the condensational growth of particles formed by homogeneous nucleation using the condensation module described in Sect. 2.2.1 using the full moving method (see Sect. 2.2.4). We start with one particle size and add new particle size bins during the early stage of particle formation. The new particles are assumed to be composed of non-volatile SOA material and are introduced into the model at an initial diameter of 5 nm. Hence, in this work we do not treat the initial activation and growth of the formed molecular clusters. The new particle formation rate (J_{5nm}) is assumed to be constant during the experiments. A new size bin is added for the time step when the smallest particle size grows larger than 10 nm in diameter. For the experiments which we simulate in this work the SOA mass (condensation sink) increases rapidly during the early stage of SOA formation. This effectively prevents the newly formed particles from growing and thus generally keeps the number of model particle size bins down to less than 20 (see Fig. S1 in the supplementary material).

3.1 Simulations of DOP particle evaporation

Before modelling complex multicomponent SOA particle formation, growth and evaporation we test ADCHAM on a simpler system: the evaporation experiments of liquid DOP particles from Vaden et al. (2011). The particles were evaporated in a 7 L evaporation chamber with 1 L of activated charcoal at the bottom of the chamber. The particle number concentration was kept low (~150 cm^{-3}) in order to keep the gas phase concentration close to zero. Before the aerosol was introduced into the chamber it was passed through two charcoal denuders in order to remove all DOP in the gas phase (Vaden et al., 2011).

Here we adopt the approach from Shiraiwa et al. (2012) who modelled the gas phase loss to the charcoal denuder using Fick's first law on a laminar layer (Δx) adjacent to the charcoal denuder on the bottom of the chamber. Since the layer thickness is poorly known, we modelled the DOP(g) loss rate using different laminar layer thickness (from 3 cm, which is the approximate half height of the chamber (Shiraiwa et al., 2012) to 0 cm (perfect gas phase loss)). Coagulation and particle wall losses were not considered. In this small chamber the wall losses can be substantial, however particles deposited on the chamber walls not coated with charcoal will likely continue to evaporate and contribute to the gas phase DOP. Neglecting the particle wall losses is equivalent to assume that the particles deposited on the walls behave as if they were still in the gas phase (Sect. 2.2.3).

The assumption of neglecting coagulation for this case can be justified by modelling the Brownian coagulation loss rate of monodisperse aerosol particles with an initial concentration of 150 cm^{-3}. If the particles have a mode diameter of 100 nm or 1000 nm and a geometric standard deviation of 1.2 the number concentration decreases by 1.1 and 0.5 % after 24 hours, respectively.

Vaden et al. (2011) and Shiraiwa et al. (2012) used a binary diffusion coefficient for DOP in air of 0.044 cm^2 s^{-1} from Ray et al. (1988). This value was measured at a pressure of 98 Torr (0.13 atm) which is lower than the vapour pressure used in the experiments from Vaden et al. (2011). If we instead use Eq. 13 in Ray et al. (1988) for the DOP gas mean free path as a function of pressure and temperature we arrive at a binary diffusion coefficient (D_{DOP}) of 5.5x10^{-3} cm^2 s^{-1} at 296 K and 1 atm. This value is 8 times smaller than the value used by Vaden et al. (2011) and Shiraiwa et al. (2012). When using this lower diffusion coefficient together with the Fuchs-Sutugin transition regime correction factor (Fuchs and Sutugin, 1971) in ADCHAM we substantially underestimated the DOP evaporation rates for all particle sizes even with unity surface mass accommodation coefficients. Hence, instead we decided to estimate D_{DOP} with the Chapman-Enskog theory (Chapman and Cowling, 1970) (in accordance with Zhang et al., 1993), or with the more simple Eq. (30) (Jacobson, 2005). With the Chapman-Enskog theory (see e.g. Rader et al., 1987) D_{DOP} become 2.3 x10^{-2} cm^2 s^{-1} while with Eq. 30 D_{DOP} = 1.5x10^{-2} cm^2 s^{-1} at 1 atm and 296 K. With D_{DOP} of 1.5x10^{-2} cm^2 s^{-1} and a laminar layer of 3.0 cm adjacent to the charcoal denuder wall we are able to reproduce the observed evaporation rates using unity mass accommodation, for all particle sizes except the 500 nm particles for which the laminar layer has to be decreased to 0.1 cm in order to not underestimate the evaporation rate (see Fig. 4). When we use a diffusion coefficient of 2.3 x10^{-2} cm^2 s^{-1} the mass accommodation coefficient has to be less than unity (~0.5 for the 296 and 500 nm DOP particles) and (~0.25 for the 697 and 836 nm DOP particles) in order to get the model results in agreement with the measurements.

From these simulations we can conclude that, to be able to constrain the values of the mass accommodation coefficient from evaporation experiments on low-volatility compounds (e.g. DOP), the binary diffusion coefficients and chamber wall effects need to be well constrained.

$$D_i = \frac{5}{16 N_a d_i \rho_{air}} \sqrt{\frac{RTM_{air}}{2\pi}\left(\frac{M_i + M_{air}}{M_i}\right)} \qquad (30)$$

N_a is Avogadro's number, d_i is the collision diameter of compound i (d_{DOP}=0.86 nm), ρ_{air} is the density of air, M_{air} is the molar mass of air and M_i is the molar mass of compound i (M_{DOP}=390.56 g mol^{-1}).

3.2 Modelling of organic salt formation between carboxylic acids and ammonia

Here we model the SOA formation in the α-pinene – NH_3 – O_3 experiments by Na et al. (2007), in a dark indoor 18 m^3 Teflon chamber. In the experiments CO (~200 ppm) was used as OH-scavenger. The chamber was operated at a temperature of 21±1 °C, and dry conditions. For the simulations we use a RH of 5 % and a temperature of 21 °C. Once the α-pinene and NH_3 initial target concentrations were reached, the experiments started by injecting O_3 for approximately 20 minutes, to produce an O_3 concentration of 200 ± 5 ppb. In the model, emissions corresponding to 250 ppb unreacted O_3 were added during the first 20 minutes, in order to simulate the experimental target O_3 concentrations.

In the experiments Na et al. (2007) observed a substantially higher SOA formation when NH_3(g) was present. The authors also performed experiments on *cis*-pinonic acid (a common α-pinene oxidation product), and found a dramatic increase in particle number and volume concentration when NH_3 was added to the system. From these experiments they concluded that most of the observed SOA mass enhancement in the presence of NH_3 could be explained by acid-base reactions which drive the carboxylic acids into the particle phase. Similar organic salt formation in the presence of NH_3 was observed both at dry and humid conditions (RH=50 %).

Several experiments were performed at initial NH_3(g) concentration between 0-400 ppb and an α-pinene concentration of ~220 ppb (see Table 1 in Na et al., 2007). The formed aerosol particle mass increases when more NH_3 is added. However, when the ammonia concentration exceeded 200 ppb no substantial additional mass formation was observed. The reason for this could be that in principle all gas phase carboxylic acids already have formed particle mass at 200 ppb NH_3 (Na et al., 2007).

Recently, Kuwata and Martin (2012) conducted experiments with an Aerosol Mass Spectrometry (AMS) on SOA formed from ozonolysis of α-pinene at low and high relative humidity (RH<5% and RH>94%). In these experiments, the α-pinene SOA particles were formed at dry conditions before they were exposed to varying degree of humidification and ammonia (see Fig. 1 in

Kuwata and Martin, 2012). An ~10 times greater uptake of ammonia was observed at high RH compared to low RH, which was attributed to a more rapid diffusion uptake of ammonia in the less viscous humidified aerosol particles. However, since the gas phase was not removed from the aerosol between the generation and the exposure to ammonia, part of the ammonia uptake could be attributed to reactive uptake of NH_3 and organic acids from the gas phase (Kuwata and Martin, 2012).

In this work we model the organic salt formation between ammonium and carboxylic acids as a process occurring in the particle surface layer and particle bulk and not in the gas phase. The partitioning of carboxylic acids and ammonia between the gas phase and particle surface layer are modelled as separate pH dependent dissolution processes using the condensation/evaporation module (Sect. 2.2.1). The amount of organic acids, ammonia/ammonium and organic salts which exists in the particles depend on the pure-liquid saturation vapour pressures or Henry's law constant (K_H), acid dissociation constants (K_a), activity coefficients, surface tension (Barsanti et al., 2009) and the solubility product of the formed salts (K_s) (R9-R13). The aerosol particle formation will be favoured by low pure-liquid saturation vapour pressures of the carboxylic acids, large solubility (Henry's law coefficient) of NH_3, large difference between the carboxylic acids and NH_4^+ K_a values (Greaves and Drummond, 2008) and low solubility of the formed salts (K_s).

$$\mathrm{RCOOH(g)} \leftrightarrow \mathrm{RCOOH(l)} \tag{R9}$$

$$\mathrm{RCOOH(l)} \leftrightarrow \mathrm{RCOO^-} + \mathrm{H^+}, \quad K_a = \frac{[\mathrm{RCOO^-}][\mathrm{H^+}]\gamma_{\mathrm{H^+}}\gamma_{\mathrm{RCOO^-}}}{[\mathrm{RCOOH}]\gamma_{\mathrm{RCOOH}}} \tag{R10}$$

$$\mathrm{NH_3(g)} \leftrightarrow \mathrm{NH_3(l)}, \quad K_H = \frac{[\mathrm{NH_3}(l)]\gamma_{\mathrm{NH_3}}}{p_{\mathrm{NH_3}}} \tag{R11}$$

$$\mathrm{NH_3(l)} + \mathrm{H^+} \leftrightarrow \mathrm{NH_4^+}, \quad \frac{1}{K_{a,NH_4^+}} = K_{NH_3} = \frac{[\mathrm{NH_4^+}]\gamma_{NH_4^+}}{[\mathrm{NH_3}(l)][\mathrm{H^+}]\gamma_{\mathrm{NH_3}}\gamma_{H^+}} \tag{R12}$$

$$\mathrm{NH_4^+} + \mathrm{RCOO^-} \leftrightarrow \mathrm{NH_4RCOO(s)}, \quad K_s = [\mathrm{NH_4^+}][\mathrm{RCOO^-}]\gamma_{\mathrm{NH_4^+}}\gamma_{\mathrm{RCOO^-}} \tag{R13}$$

Table 2 lists different model parameter values used for the base case simulations in this section. The K_a values are unknown for most carboxylic acids, even in aqueous solutions. However, for two major ozonolysis products (*cis*-pinic acid) and (*cis*-pinonic acid) (Hallquist et al., 2009), the estimated aqueous pK_a values were found in the literature (see e.g. Hyder et al., 2012 and Barsanti et al., 2009). These acids have nearly the same pK_a values (~4.6). Hence, in this work we will assume that all carboxylic acids from α-pinene ozonolysis which partition into the particle organic rich phase have pK_a values equal to 4.6.

Unfortunately we could not find any values of solubility products between carboxylic acids and ammonium in the literature. Hence, we decided to define an effective solubility product (K_s^*) as the product between the ammonium concentration and the total deprotonated carboxylic acid concentration ($[RCOO^-]_{tot}$) (Eq. 31). K_s^* was used as an unknown parameter which we varied in order to find the best agreement between the model and measurements.

$$K_s^* = [\mathrm{NH_4^+}][\mathrm{RCOO^-}]_{\mathrm{tot}} \tag{31}$$

If not otherwise specified, the pure-liquid saturation vapour pressures of the organic compounds were estimated with the SIMPOL method, K_s^* was set to 0.1 mol^2 m^{-6}, and the NH_4RCOO salts were mixed with the other organic compounds (no separate phase). Because the interactions between the NH_4RCOO and other organic compounds and inorganic ions are unknown (see Sect. 2.3.1), NH_4RCOO was not considered to influence the activity coefficients of the other compounds. However, as a second extreme condition we performed simulations where we treated NH_4RCOO and the other organic compounds + inorganics as two completely separate phases (liquid-liquid phase separated or NH_4RCOO as crystalline salts (see Sect. 1)). The diffusion coefficients for monomer SOA and ammonia/ammonium were estimated with the Stoke-Einstein relationship using a viscosity of ~10^8 Pa s (see Sect. 1). Because the viscosity of the SOA is uncertain and depend on the experimental conditions and time of ageing, we also performed simulations with less viscous particles ($D_{0,monomer,SOA}$=10^{-15} cm^2 s^{-1}, $D_{0,ammonium}$=10^{-13} cm^2 s^{-1}).

In Table 3 we have listed the measured and model initial concentrations, concentration change of ozone ($\Delta[O_3] = [O_3]_{max} - [O_3]_{t=6h}$) and α-pinene Δ[α-pin.], and SOA yields. Figure 5 shows the modelled temporal evolution of the α-pinene, O_3, NH_3 and OH concentrations in the gas phase. The O_3 concentration rises during the first 20 minutes while O_3 is continuously applied to the chamber. The OH concentration reaches a maximum of ~10^6 molecules cm^{-3} at the same time as the maximum O_3 concentration. Hence, according to the model the experiments with CO as OH scavenger is not a pure O_3 oxidation experiments, but a fraction of the α-pinene and the oxidation products are also oxidized with OH. Figure S2 in the supplementary material shows the cumulative fraction of reacted α-pinene which was oxidized by O_3 during the evolution of the experiment. In the beginning of the experiment only 86 % of the consumed α-pinene was oxidized by O_3, while at the end of the experiment 92 % of the consumed α-pinene was oxidized by O_3.

In Fig. 6 we compare the modelled and measured SOA yields from experiments conducted with approximately 220 ppb α-pinene, 200 ppb O_3 and varying initial NH_3 concentrations. The model results in Fig. 6a is from the base case simulation set-up (Table 2). Figure 6b shows model results from simulations performed with pure-liquid saturation vapour pressures from Nannoolal et al. (2008). The results in Fig. 6c are from model runs with unity activity coefficients (Raoult's law for ideal solution) and Fig. 6d shows results from simulations with less viscous particles ($D_{0,monomer,SOA}=10^{-15}$ cm^2 s^{-1}, $D_{0,ammonium}=10^{-13}$ cm^2 s^{-1} and $D_{0,NH4RCOO}=0$ cm^2 s^{-1}). For a particle with a diameter of 250 nm these values of the diffusion coefficients give an e-folding time of equilibration of 2.6 minutes for NH_3 and 4.4 hours for SOA monomers.

For the base case simulations the agreement between the modelled and measured SOA mass and SOA yields are surprisingly good, both with and without addition of NH_3. One reason for this is that the organic salt effective solubility product (Eq. 31) was used as a model fitting parameter. However, in order for the model to agree with the measurements the amount of semi-volatile carboxylic acids formed from the α-pinene oxidation still needs to be reasonably well predicted, which seems to be the case. Figure S3 in the supplementary material shows the modelled temporal evolution of the total carboxylic acid concentration (gas + particle phase).

We find the largest difference between the model runs, and between the model and measurements, when we use the pure-liquid saturation vapour pressure method from Nannoolal et al. (2008) instead of SIMPOL (Pankow and Asher, 2008) (Fig. 6b). The model then underestimates the SOA mass with ~200 µg m^{-3} (~30 %), irrespectively of the amount of NH_3 added.

Figure S4 in the supplementary material shows a comparison of the volatility basis set (VBS) parameterization from Pathak et al. (2007) and VBS parameterizations which we have derived from the MCMv3.2 condensable α-pinene oxidation products using either the method from Nannoolal et al. (2008) or SIMPOL. The MCMv3.2 α-pinene oxidation product VBS parameterizations are given both for CO and cyclohexane as OH-scavenger. The VBS parameterizations show large differences both between the vapour pressure methods and the type of OH scavenger used. By comparing the VBS parameterizations we can conclude that SIMPOL gives the largest SOA mass at high α-pinene concentrations (this work). However, at low (atmospherically more realistic) α-pinene concentrations the Nannoolal method will give the least volatile SOA and highest SOA mass.

Barley and McFiggans, 2010 have shown that the uncertainties of the calculated pure-liquid saturation vapour pressures are large, especially for low-volatility compounds with several functional groups. However, because of other large uncertainties, e.g. oligomerization processes and gas phase chemistry mechanisms (see Sect. 1), we cannot predict which of the two liquid saturation vapour pressure methods that give the most realistic vapour pressures. In Sect. 3.3 we illustrate how the estimated volatility of the α-pinene gas phase oxidation products can have substantial effects on the particle evaporation loss rates.

In contrast to the vapour pressures, the modelled activity coefficients have only small influence on the simulated SOA mass formation (compare Fig. 6a and 6c). This is consistent with the conclusions from McFiggans et al. (2010), and Zuend and Seinfeld (2012) for conditions without dissolved inorganic ions and low relative humidity. The mass difference between the model runs ($[OA_{ideal}]$-$[OA_{activity}]$) is small without added NH_3, but increases when the free particle ammonium concentration increases. The reason for this is that the dissolved ammonium ions generally increase the organic molecule activity coefficients (salting-out effect). At atmospheric more realistic relative humidities (>30 %), salt effects which either cause liquid-liquid phase separation or drive the organic compounds out from the particles, may have large effects on the SOA formation (see e.g. Zuend and Seinfeld, 2012).

If we assume that the SOA is less viscous (Fig. 6d), the mass yields are slightly larger (60.7 % compared to 57.5% without NH_3 addition, and 69.1 % compared to 67.0 % when 200 ppb NH_3 is added at the start of the experiments).

Figure S5 in the supplementary material shows the total SOA mass and NH_4RCOO mass for varying initial NH_3 concentration, $K_s^* = 0.01$ or 0.1 mol^2 m^{-6} and semi-solid SOA particles. As expected the NH_4RCOO mass concentration, and the total particle mass increases when K_s^* is lowered. However, for 200 ppb NH_3 the difference becomes negligible since almost all carboxylic acids are anyhow found in the particle phase. The results also reveal a moderate salting-out effect of the ammonium on the SOA (see the decrease in the total particle mass with increasing NH_3 when $K_s^*=0.01$ mol^2 m^{-6}).

In order to test which processes that can explain the observed NH_3 uptake in α-pinene SOA particles, exposed to $NH_3(g)$ after particle formation (Kuwata and Martin, 2012 and Na et al., 2007), we also performed simulations where the SOA particles were allowed to age for 6 hours before they were exposed to 200 ppb $NH_3(g)$. To test the effect of mass transfer limited uptake of NH_3, the particles were either treated as glassy solids (no mixing) or semi-solids ($D_{0,monomer,SOA}=10^{-15}$ cm^2 s^{-1}, $D_{0,ammonium}=10^{-13}$ cm^2 s^{-1}).

In Fig. 7a the temporal evolution of the modelled SOA mass from these simulations are shown. As a comparison, the results from simulations with 200 ppb $NH_3(g)$ added at the start of the experiments are also plotted. After the addition of NH_3, the SOA mass increases rapidly both with and without mass transfer limited diffusion uptake in the particles (semi-sold or solid particles). This indicates that the rapid uptake of $NH_3(g)$, by the particles, mainly is caused by reactive uptake of carboxylic acids(g) and $NH_3(g)$ and not by the diffusion of NH_3/NH_4^+ into the particle bulk. However, the temporal evolution of the formed NH_4RCOO salts and dissociated and non-dissociated carboxylic acids (Fig. 7b), reveal that the mass of NH_4RCOO salts formed in the semi-solid particles are twice as high, and the carboxylic acid mass concentration is substantially lower, than if treating the SOA as solid. This difference is attributed to the mass transfer limited uptake and reaction of NH_3/NH_4^+ with the carboxylic acids found in the semi-solid particle bulk interior.

However, although the NH_4RCOO concentration becomes higher if the particles are semi-solid (less viscous), the total aerosol mass 3 hours after the addition of ammonium is lower than if the particles are solid (compare simulation Nr. 4 and 5 in Fig. 7a). The reason for this is the salting-out effect of NH_4^+ which causes the nonpolar organic compounds to evaporate. For these simulations, the salting-out effect is mainly important if both the NH_3/NH_4^+ and the organic compounds can be transported between the bulk and particle surface layer. In the laboratory experiments (see Fig. 2a in Na et al., 2007) no SOA mass loss could be seen after the NH_4RCOO formation. This experiment continued less than 1 hour after the addition of NH_3, but it at least indicates that the mixing of organic compounds within the particle phase is mass transfer limited, and/or that the NH_4RCOO salts form a separate phase, which limits the salting-out of other SOA compounds from the particles to the gas phase.

Figure 7a also shows the simulated SOA mass formation when we treat the NH_4RCOO salts as a separate phase (e.g. crystalline salt) which other condensable organic compounds cannot dissolve into. When NH_3(g) is added during the start of the experiments the difference between the model runs with and without a separate NH_4RCOO phase is relatively small. However, if the NH_3(g) is added after the solid SOA particles have formed, only a moderate SOA mass increase is accomplished (~9 %). This is in sharp contrast to the results from the simulations with solid particles and only one organic phase (mass increase of ~39 %). The reason for this is that the ammonium salts are enriched in the particle surface layer, and if no other compounds can dissolve into this phase their uptake is limited. On the other hand if NH_4RCOO is part of a single amorphous organic phase, it will lower the mole fractions of the other compounds and hence increase (at least for ideal conditions) the uptake of them (see Eq. 2). This is the reason why the total SOA mass increase is larger (~270 μg m^{-3}, ~39 %), than the increase explained purely by the carboxylic acids and NH_4RCOO (46+84=130 μg m^{-3}, ~19 %) (see simulation Nr. 4 in Fig. 7a and Fig. 7b). Na et al. (2007) observed a mass increase of 15 % when 1000 ppb NH_3 was added after the α-pinene SOA particle mass formation had ceased. This increase is larger than the modelled increase when considering complete phase separation between NH_4RCOO and the other condensable organic compounds, but substantially smaller than for the simulations with only one organic phase. This indicates that in reality, there will neither be perfect (ideal) mixing between NH_4RCOO and the other condensable organic compounds, nor a complete phase separation.

Figure 8 shows a) the modelled pH, b) the total ammonium mass fraction (free and bonded in ammonium salts), c) the NH_4RCOO mass fraction and d) the carboxylic acid mass fraction ($[RCOO^-]+[RCOOH]$) for a semi-solid SOA particle, at different distances from the particle core. The figure includes results from simulations with initial NH_3(g) concentrations of 50, 100 and 200 ppb, respectively, and at 1 or 6 hours of ageing. A large fraction of the SOA formed early during the experiments are due to condensation of carboxylic acids. This explains the large mass fractions of carboxylic acids and the lower pH in the particle cores (Fig. 8a-b). For the simulations with 200 ppb NH_3, a large fraction of the carboxylic acids and ammonium form salts (Fig. 8c), while when only 50 ppb NH_3 is added, ammonium salts are only present during the early stage of particle formation, when the carboxylic acid mass fraction is large. Because of the assumed relatively rapid mixing of ammonium (e-folding time of a few minutes), the free ammonium concentration (not bound in organic salts) are almost constant in all particle layers. Hence, the differences in the NH_4RCOO concentrations between different layers are largely caused by differences in the carboxylic acid concentrations, which even after 6 hours of ageing are not uniformly mixed.

Form the simulations in this section we can conclude that ADCHAM (with the pure-liquid saturation vapour pressures from SIMPOL and activity coefficients from AIOMFAC), are able to reproduce the observed SOA formation at different concentrations of NH_3(g). With NH_3 present during the formation, reactive uptake of carboxylic acids contributes substantially to the modelled early growth of the particles formed by homogeneous nucleation. However, because of the relatively high concentrations, we cannot conclude whether this mechanism is important in the atmosphere.

3.3 Evaporation of α-pinene SOA

Now we will use ADCHAM to explore which processes are responsible for the slow and size independent evaporation loss rates of α-pinene SOA particles observed by Vaden et al. (2011). α-pinene SOA particles were produced in a 0.1 m^3 Teflon chamber during dark conditions with ~200 ppb α-pinene, ~250 ppm cyclohexane as OH-scavenge and ~500 ppb O_3. The particles were formed by homogeneous nucleation and allowed to age for approximately 1.5 hours until they stopped growing (fresh particles). Alternatively, the particles were aged for 10-15 hours (aged particles). After this, monodisperse aerosol particles were selected with a differential mobility analyser (DMA), the aerosol was then passed through two charcoal denuders (residence time ~2 minutes) before the particles were introduced at low concentration (~10-200 cm^{-3}) into the evaporation chamber described in Sect. 3.1 (Vaden et al., 2011). Vaden et al. also studied the evaporation of α-pinene SOA particles coated with DOP. These particles were formed in the presence of DOP liquid at the bottom of the chamber. For these experiments the SOA and DOP were not mixed and the SOA particles acquired a few nm thick coating of DOP (Vaden et al., 2010).

Vaden et al. (2011) showed that the evaporation rate of the pure α-pinene SOA particles is more than 100 times slower than expected from modelled evaporation rates of liquid-like monomer SOA. The observed evaporation can be divided into two stages. In the first stage (~100 min) a relatively slow evaporation of SOA material occurs (~50 % of particle mass removed). After this a second stage is reached where the SOA mass loss rate is even slower (additionally ~25% of their initial mass are lost after 1 day of ageing). Another interesting finding is that the evaporation rates are almost size-independent. Vaden et al. (2011) concluded that the slow and nearly size independent evaporation loss rates indicate that the SOA particles are not liquid-like. Slow evaporation of α-pinene SOA particles have also been observed by Grieshop et al. (2007). They concluded that the evaporation might be limited by mixing effects, mass transfer limitations and decomposition of weakly bonded oligomers.

Here we use ADCHAM to examine which processes that can be responsible for the slow evaporation rates measured on fresh and aged α-pinene SOA particles (Vaden et al., 2011). It is important to mention that even though we sometimes use a very specific mechanism in ADCHAM (e.g. hemiacetal formation (R3)), we may only conclude about whether this type of mechanism (e.g. oligomerization in general) is important or not. The processes which we will evaluate with ADCHAM are listed below.

1) Vapour pressures of the condensable monomers (pure-liquid saturation vapour pressure method).
2) Slow and non-perfect mixing within the semi-solid amorphous SOA particles.
3) Oligomerization in the surface and particle bulk layers and reversible decomposition back to monomers.
4) Accumulation of low volatility oligomers at the particle surface, creating a coating material which protects the more volatile monomer SOA from evaporating.
5) Non-perfect removal of gas phase compounds in the charcoal denuder evaporation chamber.

We will test three main hypotheses (H1-H3) which possibly can explain the observed evaporation losses:

H1) The observed evaporation rates are controlled by the volatility of the condensing monomer SOA formed in the gas phase in combination with non-perfect mixing within the semi-solid amorphous particle phase. The particle size independent SOA formation can be explained by generally less volatile monomer SOA in the smaller particles caused by the Kelvin effect in combination with a large condensation sink (see e.g. Roldin et al., 2011b).

H2) Formation of small amounts of non-volatile oligomer SOA (a few mass %) which accumulate in the particle surface layer (analogous to the DOP coating found by Vaden et al., 2010) protects the more volatile monomer SOA from evaporation. The initial oligomer surface coating material is formed at the particle surface by a reactive uptake process (e.g. R1b and R2b). When the aerosol is introduced in the evaporation chamber the formation of this coating material stops. The first stage evaporation of the SOA particles is governed by the decomposition of this coating material back to volatile monomer SOA. Upon evaporation more oligomer SOA is added to the surface layer from the bulk phase. This oligomer SOA is more long lived than the initial surface oligomer coating material. The second evaporation stage starts when the initial oligomer coating material has been lost and been replaced by the oligomer from the bulk phase.

H3) A large fraction (~50 %) of the SOA from α-pinene ozonolysis is low-volatility oligomers (see e.g. Gao et al., 2004). During the first evaporation stage the monomer SOA is lost. The relatively slow evaporation during this stage may be explained by oligomer SOA which accumulates in the particle surface layer when the monomer SOA is evaporating. The bulk phase oligomer SOA is less viscous than in H2 and is at least partly mixed by diffusion with the more liquid-like monomer SOA. The second slow evaporation stage starts when almost all monomer SOA has been lost. During the second evaporation stage the evaporation rate is mainly determined by the oligomer decomposition rate, formation rate and how rapidly the oligomer degradation products (monomers) are transported from the bulk to the surface layer.

For all simulations presented in this section the monomer SOA mass accommodation coefficients were assumed to be proportional to the particle surface area not covered by non-volatile oligomer SOA (1- θ_s) (Eq. 18). In the model we used a temperature of 23 °C, an RH of 5 % and a pressure of 1 atm for all simulations. The laminar layer width adjacent to the charcoal denuder in the evaporation chamber was assumed to be 0.1 cm if not otherwise specified (see Sect. 3.1). If not otherwise specified, the pure-liquid saturation vapour pressures were estimated with the SIMPOL model. Particles of different sizes were formed by homogeneous nucleation and were allowed to grow in the presence of each other. After 1.5 hours or 12 hours of ageing (fresh or aged aerosol) 100 cm^{-3} of one particle size was introduced into the modelled charcoal denuder chamber and allowed to evaporate by continuous removal of the gas phase compounds. No wall losses were considered (see discussion in Sect. 3.1 and Sect. 3.4).

3.3.1 Evaporation of pure monomer SOA particles (H1)

We start to model the evaporation loss of pure monomer α-pinene SOA particles. The pure-liquid saturation vapour pressures used in Eq. (2) were derived with the SIMPOL (Pankow and Asher, 2008), Nannoolal et al. (2008) vapour pressure methods or the semi-empirical 7-product model (VBS) parameterization from Pathak et al. (2007). The last method was also used by Vaden et al. (2011). In Sect. 3.2 we showed that the vapour pressure method can have a profound influence on the modelled SOA mass formation from α-pinene ozonolysis (Fig. 6 and Fig. S4 in the supplementary material). Here we evaluate their influence on the modelled evaporation loss rates of two different particle sizes (~150 nm and ~250 nm) (Fig. 9). The model results in Fig. 9 are from simulations with liquid-like SOA ($D_{monomer}=10^{-10}$ cm^2 s^{-1}) or solid-like SOA particles with negligible mixing ($D_{monomer}=0$ cm^2 s^{-1}). In Fig. 9a the results are from simulations with the VBS from Pathak et al. (2007), Fig. 9b shows the results when we use SIMPOL and Fig. 9c results from simulations with the Nannoolal method. In Fig. 9d, we compare the modelled evaporation loss rates (for solid-like amorphous SOA particles with the Nannoolal vapour pressure method) with or without Kelvin effect, with a laminar layer adjacent to the charcoal denuder of 0.1 or 3 cm.

In all model runs except with the Nannoolal method and solid-like amorphous particles the evaporation rates are more than ~100 times faster than the observations. According to the curve fitted to the measurements only ~3 % of the SOA mass is lost during the first 2 minutes. However, in the model runs with almost perfect gas phase removal (Δx = 0.1 cm) 20-80 % are lost, depending on vapour pressure method, the particle size and if the SOA is liquid (l) or solid (s) like.

Another difference is that the observed evaporation loss rate is almost linear for the first 30 minutes while in all model runs with a Δx of 0.1 cm the loss rate is first very rapid and then slows down. This is because (in the model) the formed SOA material is composed of material with different volatility. Hence, the most volatile material is lost first and the less volatile material is enriched in the particle phase. Even if the SOA would be formed from only one or a few compounds with almost the same vapour pressures, the evaporation loss rate would be size dependent (see Sect. 3.1).

The least volatile MCMv3.2 organic compound which contributes to a few mass % of the SOA formation both with the Nannoolal method and SIMPOL is 6-hydroperoxy-1-hydroxy-5-(hydroxymethyl)-6-methylheptane-2,3-dione (in MCMv3.2 called C922OOH). This compound has a vapour pressure as low as 7.5×10^{-8} Pa (at 298 K) when calculated with the Nannoolal et al. method, while with SIMPOL we arrive at a vapour pressure of 2.2×10^{-6} Pa (at 298 K). If the SOA particles are considered to be solid or semi-solid this compound accumulates in the particle surface layer upon evaporation and limits the loss of the other more volatile compounds. Because the vapour pressure of C922OOH is 30 times lower with the Nannoolal method than with the SIMPOL method the evaporation loss rate of solid or semi-solid SOA particles become much slower, even though most of the other SOA mass is less volatile with the SIMPOL method (see Fig. S4 in the supplementary material).

In the chamber experiments and model runs the small and large particles grow by condensation in the presence of each other. Because of the Kelvin effect and the large condensation sink the small particles take up less of the more volatile compounds and thereby contain relatively more of the low-volatility compounds (~4.0 % C922OOH for a 150 nm particle and ~2.8 % C922OOH for a 250 nm particle, with the Nannoolal method). Hence, if not accounting for the Kelvin effect the difference between the modelled evaporation loss rates of a 150 nm and 250 nm particle is approximately twice as big (Fig. 9d).

In Fig. 9d we have also included the modelled evaporation rates of solid-like amorphous SOA particles (~150 and ~250 nm in diameter) when the gas phase removal to the charcoal denuder is less effective (Δx=3.0 cm). For these simulations the modelled first evaporation stage is in better agreement with the measurements, although the evaporation rate depends on the particle size. The second slower evaporation stage is still substantially faster in the model than in the measurements.

From the model simulations of H1 we can conclude that it is unlikely that the observed evaporation rates can be explained purely by incomplete mixing and the vapour pressure controlled evaporation of SOA monomers. We can also conclude that if the amorphous SOA particles are very viscous (as indicated by the resent measurements by Abramson et al. (2013), see Sect. 1) small amounts of low-volatility compounds accumulating in the particle surface (e.g. oligomers) will have large influence on the SOA evaporation loss rate. If these compounds form in the gas phase (e.g. R5) their relative contribution to the SOA mass will be larger in the small particles because of the Kelvin effect.

3.3.2 Evaporation of semi-solid SOA particles with an oligomer coating (H2)

Now we turn to hypothesis 2 where we examine whether the measured slow evaporation loss rate could be governed by the decomposition of a protective surface oligomer monolayer. In contrast to the vapour pressure limited evaporation (H1), this can be a particle size independent process.

Liggio and Li (2006) found that pinonaldehyde (which is relatively volatile) is rapidly taken up on acidic aerosol surfaces due to formation of organosulfates. In the experiments by Vaden et al. (2011) no acid seed aerosol was used. However, uptake of carboxylic acids can still give a weakly acidic environment. Hence, possibly adsorption of pinonaldehyde (or some other gas phase organic compounds) followed by acid catalysed oligomerization could potentially form a low-volatility coating. Alternatively, low-volatility dimers may form in the gas phase (e.g. R5) and then adsorb on the particle surfaces. Such a coating could possibly explain why the evaporation rate during the first evaporation stage is slower in the measurements than for the modelled monomer SOA particles (Fig. 9).

In order to test H2 we decided to model the oligomer surface layer coating by reactive uptake of pinonaldehyde. However, as mentioned above the proposed surface layer oligomer coating may also be formed by other mechanisms. We assume that pinonaldehyde can form oligomer with any organic monomer molecule containing a hydrogen peroxide or aldehyde functional group (R1b and R2b). We also assume that the surface layer oligomer material form a separate organic phase at the particle surface with a relative surface coverage (θ_s). This oligomer coverage decreases the surface mass accommodation coefficient of the monomer SOA compounds and also limits the amount of monomer SOA present at the particle surface. Since the monomer SOA compounds are not condensing on the particle surface area covered with the oligomers and the oligomers are assumed to have a negligible diffusion rate, they will not be incorporated into the particle bulk phase.

Here we simply model the reactive uptake of pinonaldehyde by assuming that the adsorbed pinonaldehyde concentration at the oligomer-free particle surface (1- θ_s) is proportional to the pinonaldehyde gas phase concentration ($c_{PINAL}(g)$). Hence, with the particle surface monolayer concentration of reactive monomers ($c_{m,i}(p.s.)$) in unit molecules cm^{-3} and the gas phase pinonaldehyde concentration in unit molecules cm^{-3}, the reactive uptake rate (surface layer dimer formation rate) is given by Eq. (32).

$$F_f(p.s.) = k_f(p.s.) \cdot c_{m,i}(p.s.) \cdot c_{PINAL}(g) \cdot (1 - \theta_s) \tag{32}$$

The formed particle surface oligomers are decomposed back to monomers using a first order degradation rate constant ($k_d(p.s.)$) (see Eq. 12). The degradation and formation rate constant of surface layer and bulk layer oligomers are unknown parameters which we use to fit the model to the measurements.

The first results which we will present are from simulations where we consider three different oligomerization mechanisms in the particle bulk phase, peroxyhemiacetal formation (R1a), hemiacetal formation (R3) and ester formation (R4). With these three oligomerization mechanisms included almost all SOA monomers can potentially form oligomer SOA. We use the same oligomerization rate constant $k_f(p)$ for all three mechanisms. The relative amount of oligomer SOA is mainly determined by the formation and decomposition rates, the time of ageing, the evaporation of monomer SOA, and to less extent by the monomer composition.

In Fig. 10 we compare the modelled and observed evaporation loss rates of fresh and aged α-pinene SOA particles. The model results are from simulations where the monomer SOA is treated as semi-solid and the oligomer SOA as solid non-mixing material ($D_{0,\mathrm{monomer}}=5\times10^{-17}$ cm^2 s^{-1}, $D_{0,dimer} = 0$ cm^2 s^{-1}).

For the model results presented in Fig. 10 we used a first order decomposition rate of 3/2 h^{-1} for the oligomers formed by the reactive uptake of adsorbed pinonaldehyde (R1b and R2b). The oligomers formed in the bulk particle phase (R1a, R3 and R4) were assumed to be more long lived (k_d = 1/3.2 h^{-1}). The surface layer dimer formation rates in Eq. (32) were set to 3×10^{-15} cm^3 $molecules^{-1}$ and the bulk phase oligomerization rates to 1.2×10^{-27} cm^3 $molecules^{-1}$ (not acid catalysed). With these oligomerization rates the particles acquire almost a complete monolayer thick coverage of dimers (~90 %) at the surface layer and ~3 % of bulk phase oligomer SOA (independent of particle size) at the time when the particles are introduced into the evaporation chamber (see Fig. S6).

Due to the almost complete surface layer dimer coverage only little monomer SOA material needs to evaporate in order for the particle surface layer to be completely covered with dimer SOA. This is the reason why the model (when using SIMPOL) is able to capture the fairly slow initial evaporation loss rate. With the Nannoolal method the model substantially underestimates the initial evaporation rate. The reason for this is the small fraction of low-volatility monomer compounds which accumulates in the particle surface layer (see Sect. 3.3.1). We also performed a simulation with the Nannoolal method and without oligomerization by reactive uptake of adsorbed pinonaldehyde. However, for this simulation 250 nm particles lose ~20 % of their mass within 2 minutes of evaporation, which is not consistent with the measurements (see Fig. S7 in the supplementary material).

Because the gas phase is effectively removed in the evaporation chamber the reactive uptake of pinonaldehyde stops (Eq. 32) and the oligomer SOA is gradually lost during the first evaporation stage. After approximately 2 hours of evaporation almost all short lived oligomer SOA (in the surface layer) has been lost and replaced by the longer lived and continuously formed bulk phase oligomer SOA (see Fig. S7b). This is when the second slow evaporation stage starts. The evaporation rate is now mainly determined by the decomposition rate of the oligomer SOA in the surface layer and hence is almost independent of the particle size (Fig. 10). However, with approximately the same mass fraction of bulk phase oligomer SOA, a larger mass fraction of the small particles needs to evaporate in order for their surface layer to be filled with the longer lived oligomer SOA from the bulk phase. Hence, if the first evaporation stage should be nearly the same independent of particle size the oligomer bulk mass fraction (before evaporation) needs to be larger in the small particles than the large ones. This could be the case if the SOA monomer compounds which form oligomer are more concentrated in the small particles or if the small particles are more acidic than the large ones.

Indeed there are some differences in the modelled chemical composition between the small and large particles formed by homogeneous nucleation (see Fig. 11). A large fraction of the SOA formed early during the homogeneous nucleation experiments are carboxylic acids. Therefore, the large particles contain more carboxylic acids (Fig. 11a). However, there will probably also be some contamination of trace amounts of NH_3 (g) present during the early stage of particle formation (see Kuwata and Martin, 2012). Hence, more ammonium will be dissolved in the large particles as well (Fig. 11c). For the results presented in Fig. 11 we used an initial NH_3(g) concentration of 100 ppt, a SOA monomer diffusion coefficient of $5x10^{-17}$ cm^2 s^{-1} and an ammonium diffusion coefficient of $2x10^{-15}$ cm^2 s^{-1}. We believe that it is reasonable to assume that the small ammonium molecules are mixed more rapidly between the particle layers than the carboxylic acids. However, we do not know how fast the ammonium molecules are mixed. Hence, it is not obvious whether it is the large or small particles which will be most acidic. For the simulation set up used to produce the results presented in Fig. 11 the pH is slightly lower near the particle surface and slightly higher near the particle core in the small particles compared to the larger ones (Fig. 11b). The reason for this is that the ammonium dissolved early during the particle formation event is gradually mixed out into the outermost particle layers (Fig. 11c), while the carboxylic acids stay close to the particle centre. Because of the higher carboxylic acid concentration in the particle core of the large particles, the ester dimer concentration becomes slightly higher in these particles. However, the modelled oligomer concentrations closer to the particle surface (which influence the evaporation loss rates) are almost independent of the particle size (Fig. 11d).

Another substantial difference between the model and the measurements is that the evaporation rates for the modelled aged particles are much slower than for the fresh, which is not seen in the measurements (Fig. 10). In the model the oligomer mass concentrations continue to increase for ~10 hours after the particles are formed (see Fig. S8 in the supplementary material). At 12 hours of ageing the oligomer SOA bulk mass fraction is ~15 % compared to ~3% at 1.5 hours. Hence, (in the model) much less SOA monomer mass needs to evaporate from the aged particles before the particle surface layer is dominated by oligomer SOA. This disagreement between model and measurements could be an indication that only a small fraction of monomer SOA compounds can form oligomer, and that the formation is relatively rapid.

We have now illustrated that if the oligomer mass fraction is approximately the same in small and large semi-solid SOA particles, more monomer SOA is evaporated from the small particles than from the large ones during the first evaporation stage. Hence, in order to explain the observed particle size independent evaporation loss rates, the mass fraction of oligomer SOA may need to be larger in the small particles than the large ones.

In Sect. 3.3.1 we found that that the relative mass fractions of the least volatile condensable compounds increase with decreasing particle size. Hence, if low-volatility dimers are formed in the gas phase (e.g. by peroxy radical termination reactions R5), or if it is the least volatile monomers which preferentially form oligomer SOA in the particle phase, the oligomer SOA mass fraction will increase with decreasing particle size. Low volatility organic compounds generally contain more functional groups which can be involved in different particle phase oligomerization processes. We will now test whether bulk phase oligomerization between the least volatile monomers or dimer formation in the gas phase (R5) potentially could explain the size independent evaporation loss rates measured by Vaden et al. (2011).

In order to accomplish an almost particle age independent evaporation loss rate, we now use a relatively rapid oligomerization formation rate (k_f=10^{-23} cm^{-3} molecules) between the two least volatile MCMv.3.2 α-pinene oxidation products which have a substantial contribution to the SOA formation (C922OOH and C921OOH). Figure S9 in the supplementary material shows the modelled concentrations of these two compounds for two different particle sizes at different distances from the particle centre. The model results in Fig. S9 are from a simulation with $D_{0,\text{monomer}}$=$5\text{x}10^{-17}$ cm^2 s^{-1} and no bulk phase oligomerization. In order to reproduce the second slow evaporation stage we now use an oligomer degradation rate of 1/18 h^{-1}.

Figure 12 shows the modelled evaporation loss of fresh and aged SOA particles with diameters of ~130 nm and ~240 nm, when considering oligomerization between C922OOH and C921OOH, and surface layer oligomerization by reactive uptake of pinonaldehyde (Eq. 32). Now the modelled evaporation loss rates are only slightly larger for the small particles and the ageing has only a moderate influence on the evaporation loss rates. During the first evaporation stage the modelled evaporation loss is slightly smaller than the observations. This may be explained by a slightly too high low-volatility bulk phase oligomer concentration in the modelled particles. The oligomer mass fractions in the different particle layers (for two different particle sizes), at the start and after 1 hour of evaporation is given in Fig. S10 in the supplementary material.

Finally we will also examine whether dimer formation in the gas phase (R5) followed by condensation of these low-volatility compounds could explain the observed slow and size independent evaporation loss rates. The MCMv3.2 α-pinene + cyclohexane gas phase chemistry include 146 different peroxy radicals (RO_2) which react with each other. Because of the large number of peroxy radicals in MCM a simplified approach is needed when considering the reactions between them. In MCMv3.2 each RO_2 is assumed to react with all other peroxy radicals except HO_2 (the peroxy radical pool $\sum RO_2$), at a single collective rate (Jenkin et al., 1997). The reaction between two RO_2 radicals has three possible channels (e.g. Kroll and Seinfeld, 2008 and Ng et al., 2008):

$$\mathrm{RO_2 + RO_2} \quad \rightarrow \mathrm{2RO + O_2} \qquad \text{(R14a)}$$

$$\rightarrow \mathrm{ROH + RCHO + O_2} \qquad \text{(R14b)}$$

$$\rightarrow \mathrm{ROOR + O_2} \qquad \text{(R14c)}$$

In MCMv3.2 only the two first channels are considered (R14a-b). Hence, in order to consider ROOR dimer formation in the gas phase we had to modify the gas phase kinetics and also consider the 3rd reaction channel (R14c). Here we use a simplistic approach and assume that all RO_2 + RO_2 lead to the same fraction of ROOR dimer (f_{ROOR}). f_{ROOR} was varied in order to achieve a ROOR dimer SOA particle mass fraction of a few %. With a f_{ROOR} of 0.4 %, a ROOR decomposition rate of 1/36 h^{-1} in the particle phase, pinonaldehyde surface oligomer formation (Eq. 32), $D_{0,monomer}$=5x10^{-17} cm^2 s^{-1} and $D_{oligomer}$=0 cm^2 s^{-1}, ADCHAM is able to nearly reproduce the observed size independent evaporation loss rates of the fresh SOA particles (Fig. 13).

For the smallest particles (~130 nm in diameter) the evaporation loss rate is even slightly slower than for the largest particles (~240 nm in diameter). However, the intermediate particle size (D_p = 165 nm) lose ~6 % more of its mass than the 130 nm and 240 nm particles during the first evaporation stage. The reason for this is that the Kelvin effect gives an enrichment of ROOR dimer SOA (in the outermost particle layers) primarily in the smallest particles (see Fig. S11 in the supplementary material). For the intermediate particle sizes (165 nm) this effect is less strong and cannot fully compensate for the size dependent vapour pressure driven monomer evaporation loss rates.

Figure 13 also shows the modelled evaporation loss rates for aged particles. These particles even lose slightly more of their mass compared to the fresh particles during the first evaporation stage. The reason for this is that the ROOR dimer mass fraction in the particles slowly decreases because of the decomposition in the particle phase (see Fig. S11). The slow evaporation of monomer SOA during the ageing in the Teflon chamber gives an enrichment of ROOR dimer in the surface layer of the aged particles which partly compensates the decomposition loss of ROOR (see Fig. S11).

From the H2 simulations we can conclude that the model is able to reproduce the main features of the measured evaporation losses of SOA particles from Vaden et al. (2011) if:

1) A relatively weakly bonded oligomer coating material is formed in the particle surface layer before the particles are introduced into the evaporation chamber. This coating material may form either by condensation of dimers formed in the gas phase or by a reactive uptake process on the particle surfaces.
2) A relatively small mass fraction of low-volatility relatively long-lived oligomers, accumulate (because of negligible oligomer diffusion rates) in the particle surface layers upon evaporation. In order to explain the observed relatively small influence of ageing on the SOA particle evaporation loss rates these oligomers need to be formed by a relatively rapid and selective oligomerization mechanism.
3) The oligomer bulk phase mass fraction near the particle surface is higher in the small particles compared to the large ones. As illustrated by the model simulations, this is possible (because of the Kelvin effect) if this oligomer material preferentially is formed from the least-volatile monomer compounds and/or by an oligomerization process in the gas phase (e.g. R5).

3.3.3 Evaporation of particles composed of equal amount of monomer SOA and oligomer SOA (H3).

Finally we evaluate a third possible explanation to the observed slow, particle size independent and almost particle age independent SOA evaporation loss rates. In this hypothesis a relative large mass fraction of the condensing organic monomers (~50 %) reacts relatively rapidly and forms oligomer SOA in the particle phase. During the first evaporation stage the monomer SOA is evaporating and when the second evaporation stage starts the particles are composed almost entirely of oligomer SOA. The second slow evaporation stage is then determined by the decomposition and formation rate of the oligomer SOA, and the diffusion of the monomer SOA from the bulk phase to the surface layer.

In order to test this hypothesis we need to find a group of monomer compounds which can contribute to approximately 50 % of the formed SOA mass if they react with each other and form oligomers in the particle phase. For this purpose we simply decided to use the monomer SOA compounds with $p_0<10^{-3}$ Pa. Without oligomerization these compounds comprises 44 % (247 μg m^{-3}) of the formed SOA mass after 1.5 hours of ageing. Additionally 23 μg m^{-3} of these monomers is at the same time present in the gas phase. Hence, if oligomerization in the particle phase is considered, ~270 μg m^{-3} oligomer SOA could potentially be formed.

The oligomerization rate in the particle phase was set to $1\text{x}10^{-23}$ cm^3 $molecules^{-1}$ and the decomposition rate to 1/12 h^{-1}. The particles were assumed to be semi-solid but substantially less viscous than in H2 ($D_{0,monomer}$=10^{-12} cm^2 s^{-1}, $D_{0,dimer}$=10^{-15} cm^2 s^{-1}). The value of the dimer diffusion coefficient was chosen so that the dimer could be enriched in the particle surface layer but still not completely prevent the monomer SOA from evaporating during the first evaporation stage.

Figure S12 in the supplementary material shows the modelled temporal evolution of the total oligomer SOA and total SOA mass before evaporation. Indeed, the oligomer SOA mass reaches ~270 μg m^{-3}. However, since we assumed that the oligomer and monomer SOA forms separate phases without mixing in-between the dissolution of more volatile monomer compounds ($p_0>10^{-3}$ Pa) is hampered. Hence, with this model set-up the total SOA mass decreases when we consider oligomerization, and the oligomer comprises more than 50 % (~58 %) of the total SOA mass after 1.5 hours of ageing.

Figure 14 shows the modelled evaporation rates for fresh (1.5 h) and aged (12 h) ~150 nm and ~250 nm particles for the H3 set-up. Because the total oligomer mass fraction is larger than 50 % the mass loss during the first evaporation stage is slightly underestimated, both for small and large particles. The first evaporation stage loss rate is mainly governed by the rate at which the monomer SOA is mixed into the surface bulk layers. The small particles have a shorter characteristic time of mass-transport than the large particles (see Sect. 1). This is the reason why the loss rate during the first evaporation stage is overestimated for the 150 nm particles, while it is in good agreement with the measurements for the 250 nm particles. When all monomer SOA mass has been lost the second slow evaporation stage starts. During this stage the evaporation rate is governed by the oligomer degradation rate and the oligomerization rate (cycling between oligomer and monomer SOA) and the mixing of the monomer from the bulk out to the particle surface layer. For this evaporation stage the modelled evaporation rates are nearly size independent, but the in-complete mixing of the monomer SOA still causes slightly faster evaporation losses of the small particles. Because of the rapid oligomerization rate the particle ageing has negligible influence on the particle composition and the evaporation rates.

From the H3 simulations we can conclude that the observed nearly size independent evaporation rates can probably not be explained purely by an initial mass transfer limited evaporation of the monomer SOA, followed by a slow decomposition of the remaining (~50 % by mass) oligomer SOA.

3.4 SOA formation from oxidation of *m*-xylene

Here we model the SOA formation from an *m*-xylene oxidation experiment (Exp. P2 in Nordin et al. 2013). The experiment was conducted in a 6 m^3 Teflon chamber in the Aerosol Laboratory at Lund University. The experiment started with dark conditions by adding $(NH_4)_2SO_4$ seed aerosol into the chamber (~20 ug m^{-3}), followed by ~40 ppb NO and ~240 ppb *m*-xylene. Approximately 30 minutes before the UV-lights were turned on (~90 minutes after the start of the experiment), $(NH_4)_2SO_4$ particles were added a second time in order to achieve the target $(NH_4)_2SO_4$ mass of ~20 ug m^{-3}.

The seed aerosol was formed by nebulizing an $(NH_4)_2SO_4$ – water solution and then drying the droplets. Before the dry $(NH_4)_2SO_4$ particles were introduced into the chamber they were passed through a bi-polar charger in order to achieve a well-defined nearly Boltzmann distributed charge distribution (Wiedensohler et al., 2012). The experiment was performed at a temperature of 22 °C ± 2 °C, dry conditions (RH of 3-5 %) and in the presence of UV-light with an experimentally derived NO_2 photolysis rate of 0.2 min^{-1}. The experimental set-up has been described in detail by Nordin et al. (2012). The measured UV-light spectrum (320-380 nm) is given in the supplementary material to Nordin et al. (2012).

In the model we used a temperature of 21 °C and a RH of 5 %. The photolysis rates were calculated with the recommended cross sections and quantum yields from MCMv3.2 and the measured 1 nm resolution UV-spectrum from Nordin et al. 2013, with a total light intensity of 23 W/m^2 which gives a NO_2 photolysis rate of 0.20 min^{-1}.

3.4.1 Particle deposition loss rates

To be able to quantify the effect of dry deposition on the estimated SOA formation from chamber experiments, the deposition losses of particles to the chamber walls needs to be evaluated. The dry deposition depends both on the friction velocity (u^*), the particle size and charge distributions, the mean electrical field strength ($\bar{E}$) in the chamber, and the chamber surface area to volume ratio (see Sect. 2.2.3). $\bar{E}$ and u^* are commonly not known, but can be estimated by fitting the model to particle number size distribution measurements. For this purpose an experiment with $(NH_4)_2SO_4$ seed particles but without condensable organic compounds was performed.

As the experiments in the chamber processed, the chamber surface area to volume ratio increased because of instrument sampling and leakage out from the chamber due to a small over pressure inside the chamber (see Nordin et al., 2012). We estimate the chamber volume loss rates ($\Delta V/\Delta t$) during the experiments to 0.8±0.2 m^3 h^{-1}.

With a $\Delta V/\Delta t$ of 0.8 m^3 h^{-1}, coagulation and deposition, and a mean electrical field strength of 50 V cm^{-1} and a friction velocity of 0.05 m s^{-1}, ADCHAM is able to nearly reproduce the measured $(NH_4)_2SO_4$ particle number size distributions (Fig. 15a), the temporal evolution of the total particle number (Fig. 15c) and volume concentrations (Fig. 15d). The coagulation has no direct influence on the particle volume concentration but is important for the particle number concentration at the end of the experiment. In the beginning of the experiment the charged smallest particles are rapidly deposited to the chamber walls resulting in a high effective wall deposition loss rate (k_w (s^{-1})) (Fig. 15b). But, as the experiment proceeds the fraction of charged particles (especially the small ones) decreases in the air. At the same time the surface area to volume ratio increases in the chamber, which in turn increases the deposition loss rates of all particle sizes (see the gradual upward displacement of the curves in Fig. 15b). Recharging of particles by collision with air ions was not considered in the model.

After the tuning of the dry deposition loss rates on the pure seed aerosol experiments we used ADCHAM to simulate the SOA formation experiment with *m*-xylene as precursor (Nordin et al. 2013). However, if we use the same $(\Delta V/\Delta t)$, $\bar{E}$ and u^* as in the pure seed particle deposition experiment, the model underestimates the seed aerosol mass loss (especially during the first 2 hours after the UV-lights are turned on), but substantially overestimates the particle number concentration losses before the UV-lights are turned on.

The heating of the air by the UV-lights and the air condition units which blow on the outer chamber walls can produce an increased mixing within the chamber. Therefore, before the UV-lights are turned on u^* may be smaller. By decreasing u^* to 0.01 m s^{-1} before the UV-lights are turned on the model better captures the measured initial particle number concentration losses.

Another important difference between the pure seed particle experiment and the *m*-xylene precursor experiment is that the latter experiment was performed during almost twice as long time (~6 h). Hence, the effect of particle recharging when colliding with air ions may be more important to consider. Furthermore, the chamber volume during the end of the *m*-xylene experiment was substantially smaller (1.5-2 m^3). This might have increased the effective mean electrical field strength within the chamber (see Sect. 2.2.3). In the model we try to account for this by calculating $\overline{E_t}$ (at time t) as the quotient between the initial mean electrical field strength $\overline{E_0}$ (50 V cm^{-1}) and the relative change of the approximate distance between the roof and ceiling (Δh) of the chamber ($\Delta h_t/\Delta h_0$) (which is approximately equal to the relative chamber volume change ($\Delta V_t/\Delta V_0$)) (Eq. 33).

$$\overline{E_t} = \frac{\overline{E_0}}{\Delta h_t/\Delta h_0} \approx \frac{\overline{E_0}}{\Delta V_t/\Delta V_0} \quad (33)$$

Figure S13 in the supplementary material compares the modelled and measured (with AMS and scanning mobility particle sizer (SMPS)) temporal evolution of the sulphate seed particle mass concentration, particle number concentration and the particle number size distribution, and the modelled initial and final effective dry deposition loss rates. The model results are from simulations with, $\overline{E_t}$ = 50 V cm^{-1} and u^*=0.05 m s^{-1} or $\overline{E_t}$ calculated with Eq. 33 and with u^* = 0.01 m s^{-1} before the UV-lights are turned on. With the latter values the model shows substantially better agreement with the measured temporal evolutions of the sulphate seed aerosol mass concentration. However, the model still overestimates the particle number concentration loss rates (especially after the UV-light are turned on). For the model simulations presented below we will use Eq. 33 to estimate $\overline{E_t}$, and u^* = 0.01 m s^{-1} before the UV-lights are turned on and u^* = 0.05 m s^{-1} after the UV-lights are turned on.

3.4.2 Gas - particle partitioning and heterogeneous reactions

Since the *m*-xylene experiment was performed at dry conditions the $(NH_4)_2SO_4$ seed particles will initially be in a solid crystalline phase. Therefore, we assume that no material is mixed between the crystalline solid salt cores and the SOA coating (see e.g. Fig. 1a in Bertram et al., 2011). Hence, in the model there will be no salting-out effect (increase of the nonpolar organic compound activity coefficients caused by NH_4^+, SO_4^{-2} and HSO_4^- from the seed aerosol particles) (see discussion in Sect. 3.2 on possible salting-out effects of NH_4^+).

In total we considered 112 potentially condensable (p_0<1 Pa) non-radical organic MCMv3.2 compounds. The pure-liquid saturation vapour pressures were calculated with either the SIMPOL (Pankow and Asher, 2008) or the method from Nannoolal et al. (2008). We also used a third (semi-empirical) method to model the SOA formation. This method considers in total three oxidation products with vapour pressures and mol based stoichiometric yields (α_i) derived from the parameterizations for low and high NO conditions from Ng et al. (2007). For this we assume that the condensable organic compounds have a molar mass of 200 g mol^{-1}. The two most volatile compounds ($p_{0,1}$ = 6.4x10^{-6} Pa, α_1=0.021 and $p_{0,2}$ = 1.7x10^{-4} Pa, α_2=0.061) represent the volatility distribution of the condensable oxidation products formed through the RO_2 + NO pathway. The third non-volatile product ($p_{0,3}$ = 0 Pa, α_3=0.245) represent the generally less volatile organic compounds formed through the RO_2 + HO_2 pathway. The gas phase was still modelled with the MCMv3.2. The fraction of condensable organic compounds which was formed through the RO_2 + HO_2 pathway (product 3) was derived with the ratio ($k_{RO2+HO2}[HO_2]/(k_{RO2+NO}[NO]+k_{RO2+HO2}[HO_2])$) as proposed by Ng et al. (2007).

The partitioning of the condensable organic compounds to the wall deposited particles and the Teflon walls were modelled according to the procedure described in Sect. 2.2.3. The uptake onto the Teflon film and the particles deposited on the chamber walls depends on the laminar layer width adjacent to the chamber walls (Δx). The uptake (adsorption) on the Teflon film also depends on the first order loss rate from the near wall gas phase to the walls ($k_{g,w}$) and the desorption rate from the Teflon surfaces out to the thin layer next to the chamber walls ($k_{w,g,i}$) (Eq. 4). In Sect. 3.4.4 we test different values of Δx, $k_{g,w}$ and $k_{w,g,i}$ in order to find the best possible agreement between the modelled and the measured SOA formation.

Because coagulation has a considerable influence on the modelled particle number size distribution (see Fig. 15) we will consider this process as well. However, with the current version of ADCHAM coagulation cannot be combined with the complete kinetic multi-layer model (see Sect. 2.2.2). Hence, for the simulations presented in this section the particles were only divided into a solid seed particle core, and a second (well-mixed) bulk layer and a surface monolayer which are composed of the condensable organic compounds. Additionally (if specified) we also consider the adsorption and desorption of O_3 and NO_2, the mass transfer limited diffusion of O_3 and NO_2 from the sorption layer into the particle bulk, and the particle phase reactions between O_3 and unsaturated organic compounds (see Sect. 2.4.2) or between NO_2 and oxidized aromatic compounds (see Sect. 3.4.3).

Table 1 in Sect. 2.4.2 gives the model parameter values used for O_3 uptake. For the simulations presented here the diffusion coefficient of ozone (D_{0,O_3}) was set to values between 10^{-7} and 10^{-8} cm^2 s^{-1} (semi-solid SOA (see e.g. Table 1 in Shiraiwa et al., 2011)), and the reaction rate constants between ozone and the unsaturated (non-aromatic carbon-carbon double bond) organic compounds (k_{O_3}) were varied between 10^{-16} and 10^{-17} cm^3 molecules^{-1} s^{-1}. This can be compared with the measured k_{O_3} of 10^{-16} cm^3 molecules^{-1} s^{-1} for the heterogeneous ozonolysis of oleic and palmitoleic acid (Huff Hartz et al., 2007). The formed particle phase oxidation products were assumed to be non-volatile, which likely is an acceptable assumption if the oxidation products rapidly react and form dimer SOA (see e.g. Maksymiuk et al., 2009). Apart from increasing the SOA mass formation and changing the chemical composition of the SOA these heterogeneous reactions may also serve as an additional ozone sink (which is not accounted for by the MCMv3.2 gas phase chemistry mechanism).

Additionally, we will also test peroxyhemiacetal and hemiacetal dimer formation (R1a and R3) in the particle phase.

3.4.3 Gas phase chemistry and influence from chamber walls and heterogeneous reactions

Bloss et al. (2005a-b) have previously shown that the MCMv3.1 (without particle SOA formation and particle phase chemistry) generally overestimates the ozone concentration and underestimates the OH concentration during oxidation of light aromatic compounds (e.g. xylene and toluene). Hence, for these systems MCM also tends to underestimate the NO and hydrocarbon oxidation (loss) rates. In order to account for the missing OH source Bloss et al. 2005b had to include an artificial OH source of $4x10^8$ molecules cm^{-3} s^{-1} when modelling a toluene oxidation experiment from the EUPHORE chamber.

Conversion of NO_2 to HONO on the organic particle surfaces may partly explain the discrepancy between the modelled and measured particle phase chemistry (Bloss et al., 2005b). These reactions have been observed on diesel exhaust particles (Gutzwiller et al., 2002) and on organic aerosol surfaces e.g. by George et al. (2005). Metzger et al. (2008) instead proposed that the NO_2 primarily is converted to HONO on the Teflon chamber walls.

In this work we will test the heterogeneous NO_2 to HONO conversion mechanism. Bloss et al. (2005b) modelled this mechanism using a constant reaction probability (γ_{HONO}) of 0.025 for the NO_2 molecules which collide with a particle. In this work we model this proposed mechanism in a more detailed way by considering the adsorption, diffusion and reaction of NO_2 with specific organic compounds in the particle phase. NO_2 has approximately the same Henry's law coefficient for dissolution in water (Seinfeld and Pandis, 2006) and molecule size as O_3. Hence, for these simulations, we will use the same parameter values for NO_2 (e.g. Henry's law coefficient and diffusion coefficient) as specified for O_3 in Sect. 3.4.2 and in Table 1.

Gutzwiller et al. (2002) suggested that the organic compounds which react with NO_2 in the particle phase and form HONO are oxygenated aromatics (e.g. 2-methoxyphenol). Hence, we assume that it is only the compounds that contain an aromatic ring which will be oxidized by NO_2 and form HONO. The organic oxidation products formed from these heterogeneous reactions were assumed to be non-volatile.

The NO_2 to HONO conversion mechanism was considered both on the particles deposited on the chamber walls and in the air. We will also test an additional photo-enhanced background reactivity caused by HONO release from the chamber walls (Rohrer et al., 2005). The strength of the HONO emissions (from the walls to the near surface gas phase) in the Lund Teflon chamber (Nordin et al, 2013) was estimated to be $4.6\text{x}10^8$ molecules cm^{-2} s^{-1}. This value is based on the estimated HONO wall production rate of $9.1\text{x}10^6$ molecules cm^{-3} s^{-1} in Metzger et al. (2008) and their chamber volume to surface area characteristics (Paulsen et al., 2005).

Analogous to the MCM light aromatic model simulations by Bloss et al. (2005a-b) we underestimate the OH and overestimate the maximum O_3 concentration, without tuning the MCM gas phase chemistry (Fig. 16). MCMv3.2 also underestimate the initial O_3 formation rate, the amount of reacted *m*-xylene and the rapid NO to NO_2 conversion which starts approximately 20 minutes after the UV-lights were turned on. Therefore, analogous to Bloss et al. (2005b) we decided to include an artificial OH source, in our case with a rate of 10^8 cm^{-3} s^{-1} from 20 minutes after the UV-light were turned on until the end of the experiment. This substantially improves the agreement between the modelled and measured NO, NO_2, O_3 and *m*-xylene concentrations. However, the model still substantially overestimates the maximum O_3 concentration.

The poor agreement between the modelled and measured NO_2 in the latter half of the experiment (Fig. 16b) is because of the interference from peroxy acyl nitrates (PAN), HNO_3, HONO, N_2O_5 and other nitrate containing compounds in the chemiluminescence instrument used (see Nordin et al., 2012 and references there in).

Figure 16 also shows the results from a simulation where we additionally include HONO emissions from the chamber walls. Because the surface area to volume ratio increases during the experiments (~5 times) these emissions have an increasing influence on the modelled gas phase chemistry. With HONO emissions and the OH source, the OH concentration at the end of the model run is 1.5×10^{6} cm^{-3}, while without these emissions but with the OH source the concentration is 7×10^{5} cm^{-3}. Hence, with HONO wall emissions more m-xylene reacts in the simulation than what is indicated by the gas chromatography – mass spectrometry (GC-MS) measurements. Additionally, the model O_3 concentration becomes even higher.

In order to be able to compare the modelled and measured SOA formation during the experiment it is crucial that we are able to accurately simulate both the amount of m-xylene which is consumed and the fraction of RO_2 which reacts with HO_2 and NO, respectively (see e.g. Ng et al., 2007 and Kroll and Seinfeld, 2008). Hence, if not otherwise specified we included the artificial OH source but not any HONO emissions from the chamber walls. With this model set-up, the cumulative fraction of the m-xylene first generation RO_2 oxidation products which have reacted with HO_2 at the end of the experiment is about ~65 %. When we also include HONO wall emissions this value is ~50 % and with the non-tuned MCMv3.2 chemistry we get a value of ~35 % (see Fig. S14 in the supplementary material).

In order to test whether HONO formation from heterogeneous reactions between NO_2 and oxidized aromatic compounds can improve the agreement between the modelled and measured O_3 concentration, we performed a simulation with what we believe are upper estimates of the reaction rates between NO_2 and the oxidized aromatic compounds and the NO_2 diffusion coefficient ($k_{NO_2}=10^{-15}$ cm^{-3} s^{-1} and $D_{0,NO_2}=10^{-7}$ cm^{2} s^{-1}). With these values ~60 % of the aromatic SOA was oxidized by NO_2. The formed (in the model non-volatile) oxidation products comprise 20 % of the total SOA mass in the end of the simulation (Fig. S15a in the supplementary material). Still, this has only a moderate influence on the HONO concentration (Fig. S15b) and the NO_2 and O_3 decrease is equal or less than ~1 % (Fig. S15c-d).

Figure S15d also shows the modelled O_3(g) concentration when including heterogeneous reactions between O_3 and the unsaturated organic compounds ($k_{O_3}=10^{-16}$ cm^{-3} s^{-1} and $D_{0,O_3}=10^{-7}$ cm^{2} s^{-1}). For this simulation ~98 % of the unsaturated organic compounds in the particle phase were oxidized by O_3 and the formed non-volatile SOA products comprise 37 % of the total SOA mass. However, comparable to the heterogeneous NO_2 to HONO conversion this has a very small influence on the modelled O_3(g) (~1% decrease). Hence, we can conclude that it seems unlikely that heterogeneous reactions between NO_2 and oxidized aromatic compounds and/or between O_3 and the unsaturated organic compounds can explain why measurements generally gives much lower O_3(g) concentrations than MCM model. However, as will be shown in Sect. 3.4.4 these heterogeneous reactions can still be important for the amount and type of SOA which is formed.

3.4.4 SOA formation, properties and the potential influence from chamber wall effects and heterogeneous reactions

In Fig. 17 we compare the modelled and measured particle volume concentrations during the *m*-xylene experiment. The model results are from simulations with the SIMPOL vapour pressure method. The desorption of condensable organic compounds from the chamber walls was modelled with $C_w/(M_w \cdot \gamma_{w,i})$ in Eq. 4 equal with 100 μmol m^{-3}. This value is between those measured by Matsunaga and Ziemann (2010) for 2-alcoholes and 2-ketones (see Sect. 2.2.3). For the model results in Fig. 17a we used a Δx of 0.1 cm and $k_{g,w}$ was set to 1/20 s^{-1} while for the results in Fig. 17b we used a Δx of 1.0 cm and $k_{g,w}$ was set to 1/6 s^{-1}. Hence, the model simulation in Fig. 17a represent conditions with only relatively small mass transfer limitations for the gas exchange between the air and the chamber walls and particles on the walls, and a relatively slow uptake of organic compounds directly onto the Teflon walls. The model simulation in Fig. 17b instead represents conditions where the mass transfer limitations between the air and the chamber walls and particles on the walls are substantial while the uptake of gases directly onto the Teflon walls is relatively effective.

The simulations were performed both with and without heterogeneous oxidation of unsaturated organic compounds (k_{O_3}=10^{-16} cm^{-3} s^{-1} and D_{0,O_3}=10^{-8} cm^2 s^{-1}). The oxidation products (ox. prod.) from these reactions were assumed to form one organic semi-solid phase together with the other organic compounds ($D_{0,monomer}$=5x10^{-17} cm^2 s^{-1} and $D_{ox.\,prod.}$=0 cm^2 s^{-1}).

From the model simulations presented in Fig. 17 it is evident that the model is able to capture volume loss rates of the seed aerosol and the onset of the SOA formation in the experiment (~0.5 hours after UV-lights were turned on). However, for all simulations in Fig. 17, ADCHAM underestimates the observed rapid SOA formation between 0.5 and 1.25 hours for the particles suspended in air. Additionally, ADCHAM overestimates the total particle volume loss rates of the suspended particle at the end of the experiments, especially without heterogeneous ozonolysis and relatively rapid uptake of organic compounds onto the Teflon walls (Fig. 17b). For this simulation the particle losses are not only caused by deposition but also evaporation. Heterogeneous ozonolysis or other particle phase reactions allows more gas phase monomers to partition into the particle phase and delay the time when the evaporation and deposition losses dominates over the SOA formation (see Fig. S16 in the supplementary material). Additionally, the SOA formed from these particle phase reactions is less volatile (in the model non-volatile) and will therefore decrease the evaporation loss rates (see Sect. 3.3).

Opposite to the simulation results in Fig. 17b, the maximum particle volume is larger without heterogeneous ozonolysis in Fig. 17a. For these simulations the SOA formation onto the wall deposited particles is more efficient (Δx=0.1 cm) and the gas uptake onto the Teflon walls smaller. The wall deposited particles may not always serve as a sink of SOA but can also become a source of condensable organic compounds from the walls to the air. This is especially the case if the formed SOA is relatively volatile. The more volatile the SOA is, the smaller the SOA fraction found on the wall deposited particles will be. Hence, while the formed total SOA mass (air + walls) is larger with heterogeneous reactions in Fig. 17a, the SOA mass formed on the particles in the air is smaller (see also Fig. S17 in the supplementary material).

Figure S18 in the supplementary material compares the modelled particle volume from simulations with the SIMPOL and Nannoolal vapour pressure method or the semi-empirical two product model parameterization (see Sect. 3.4.2). The model simulations were performed with a Δx of 0.1 cm and $k_{g,w}$=1/20 s^{-1}. For the simulations with the SIMPOL and the Nannoolal method, heterogeneous ozonolysis was also considered (k_{O_3}=10^{-16} cm^{-3} s^{-1} and D_{0,O_3}=10^{-8} cm^{2} s^{-1}). From this figure it is evident that both methods give almost identical SOA mass formation at the end of the experiment. However, with the Nannoolal method the onset of the SOA formation is approximately 15 minutes too late. The reason for this is that the modelled early stage SOA formation is dominated by two MCM oxidation products (MXNCATECH and MXYMUCNO3) (formed through the high NO oxidation pathway (see Sect. 3.4.3 and Fig. S14)). Both of these compounds have higher vapour pressures with the Nannoolal method (3.1×10^{-3} and 1.31×10^{-4} Pa) compared to the SIMPOL method (1.9×10^{-4} and 7.5×10^{-5} Pa).

With the semi-empirical parameterization, derived from experiments in a similar although larger Teflon chamber (28 m^3) (Ng et al., 2007), ADCHAM gives a too early onset of the SOA formation and overestimate the SOA formation when $k_{g,w}$=1/20 s^{-1}. The reason for this is that the three model compounds of this method all have relatively low vapour pressures (see Sect. 3.4.2). Hence, the gas phase is rapidly saturated with respect to all these three compounds and they are effectively taken up by the particles before they are lost to the Teflon wall surfaces. In order to not overestimate the final SOA mass, $k_{g,w}$ need to be much larger ~1 s^{-1}. However, then the model substantially underestimates the early stage SOA formation rate.

We also modelled the SOA formation without losses of condensable organic compounds onto the Teflon wall (see Fig. S19 in the supplementary material). With a Δx of 0.1 cm ADCHAM is now able to capture the rapid early stage SOA formation in the chamber. However, the final particle volume concentration in the air is overestimated with ~40 %. If we instead assume that the gas particle partitioning onto the chamber wall deposited particles is identical to the uptake onto the particles suspended in the air (Δx = 0 cm) (see Sect. 2.2.3 and references there in), the model again substantially underestimates the early stage SOA formation rate, while it gives reasonable particle volume concentrations at the end of the simulation.

Finally we also tested if a relatively rapid oligomerization process in the particle phase could improve the agreement with the modelled and measured SOA formation. For these simulations we again use the SIMPOL vapour pressure method and assume that peroxyhemiacetal and hemiacetal dimers (R1a and R3) form in the particle phase with a reaction rate coefficient of 10^{-22} cm^3 s^{-1}. Additionally, in order to shift the equilibrium toward the particle phase (which might explain the rapid early stage SOA formation seen in the experiment) we assume that the oligomers and monomers form one mixed phase.

Figure 18 shows the modelled particle volume concentrations when considering peroxyhemiacetal and hemiacetal dimer formation and with Δx = 0 or 0.1 cm and $k_{g,w}$ = 0 or 1/15 s^{-1}. Without gas phase losses onto the Teflon walls and ideal uptake onto wall deposited particles (Δx = 0 cm) the model is able to capture the rapid early stage SOA formation seen in the experiment. After this the modelled particle volume concentration in the air continues to increase slowly for additionally ~2 hours, while in the experiment the measured particle volume slowly decreases.

With mass transfer limited diffusion and losses of condensable organic compounds from the near wall gas phase to the Teflon walls ($\Delta x = 0.1$ cm and $k_{g,w} = 1/15$ s^{-1}) the model results are in better agreement with the measurements in the end of the experiment and can nearly reproduce the rapid SOA formation in the beginning of the experiment.

Hence, these simulations indicate that relatively rapid heterogeneous reactions (either oligomerization or oxidation) are required in order to explain the observed rapid SOA formation in the beginning of the *m*-xylene oxidation experiment. Still, the model cannot fully explain the sharp transition between the rapid SOA formation between 0.5 and 1.25 hours after the UV-light is turned on and the slow almost linear volume (mass) loss observed during the latter half of the experiment.

In Fig. 19 we compare the temporal evolution of the modelled SOA formation without wall losses to the chamber walls, with the SIMPOL, Nannoolal or the semi-empirical parameterization method from Ng et al. (2007). The figure also illustrates the influence from heterogeneous ozonolysis (O_3 ox.) of unsaturated organic compounds ($k_{O_3} = 10^{-16}$ cm^{-3} s^{-1} and $D_{0,O_3} = 10^{-8}$ cm^2 s^{-1}) and peroxyhemiacetal and hemiacetal oligomer formation ($k_f = 10^{-22}$ cm^3 s^{-1}). We have also included the measured wall loss corrected SOA mass (SOA mass scaled with the measured relative sulphate loss rate from the time when the UV-lights are turned on) (see Sect. 2.2.3).

The simulation with SIMPOL and no heterogeneous reactions best agreement with the measured final SOA mass formation (70 and 65 μg m^{-3}, respectively). However, this simulation substantially underestimates the SOA formation during the start of the experiment. The best agreement between the model and measurements in the beginning of the experiment is instead reached when we include relatively rapid oligomerization in the particle phase. The results from this simulation also show surprisingly good agreement with the model simulation using the semi-empirical parameterizations from Ng et al. (2007). This again indicates that heterogeneous reactions are likely to be important for the SOA formation. The larger SOA formation from these model simulations compared to the measurements can likely be attributed to substantial gas phase losses directly onto the Teflon walls in the chamber. This effect will be especially pronounced in the end of the experiment when the surface area to volume ratio is large (see Sect. 3.4.1). Hence for this experiment, the model simulations indicate that the wall corrections (which assume continued uptake of condensable organic compounds onto the wall deposited particles) do not give an upper estimate of the actual (atmospheric relevant) SOA formation (see Sect. 2.2.3).

4 Summary and conclusions

We have developed a novel aerosol dynamics, gas- and particle- phase chemistry model for chamber studies (ADCHAM). ADCHAM combines the detailed gas phase chemistry from MCMv3.2, a kinetic multilayer module for diffusion limited transport of compounds between the gas phase, particle surface and particle bulk phase, and an aerosol dynamics and particle phase chemistry module which is based on the ADCHEM model (Roldin et al., 2011a) but with important updates, among others process-based algorithms for: non-ideal interactions (salt effects) between water, organic and inorganic compounds, acidity catalysed oligomerization, and oxidation of organic compounds in the particle phase.

In this work we have illustrated the usefulness of ADCHAM in studying potentially influential but poorly known processes, i.e. different oligomerization mechanisms, organic salt formation, salting-out effects, heterogeneous oxidation reactions and mass transfer limitations between the gas-particle phase, between the particle surface and particle bulk phase, and within the particle bulk phase. All these processes influence the modelled SOA formation and chemical and physical properties (e.g. volatility, phase state, oxidation state and hygroscopicity).

Additionally, we have also shown how ADCHAM can be used to study the influence of the chamber wall effects on the SOA mass formation, particle number size distribution and gas phase chemistry. These effects are important to constrain because current knowledge concerning SOA formation in the atmosphere is to a large extent based on smog chamber experiments, and global climate models and chemistry transport models rely on simplified semi-empirical parameterizations on SOA formation derived from these experiments.

The most important findings from the model simulations performed in this article are:

1) The effect of NH_3(g) on the α-pinene SOA properties and formation depends on: 1) the reactive uptake of carboxylic acids and NH_3(g) from the gas phase, 2) the viscosity of the SOA particles (ammonium and organic compound diffusion rates) and 3) the salting-out effects of NH_4^+. In order to distinguish between these effects we recommend future experiments with AMS, in which the SOA particles are exposed to NH_3 in the absence of gas phase carboxylic acids. In the model simulations the organic salts between ammonium and carboxylic acids are involved in the initial growth of the particles. Hence, these model simulations supports the theory that organic salts e.g. between ammonium or amines and carboxylic acids may be important for the early stage of nanoparticle growth in the atmosphere (Smith et al. 2008, Barsanti et al, 2009 and Smith et al., 2010).
2) Our modelling of the evaporation experiments on SOA particles formed by α-pinene ozonolysis from Vaden et al., (2011) supports the recent experimental findings that these SOA particles are very viscous (tar like amorphous SOA) (see Sect. 1). In these particles low-volatility oligomer SOA can accumulate in the particle surface layer upon evaporation. With the formation of this low-volatility oligomer coating material ADCHAM is able to reproduce the main features of the observed slow evaporation rates. However, in order for the model to resemble the relatively slow and particle size independent first evaporation stage the particle surface layer needs to be covered with some relatively weakly bonded oligomers already before the evaporation starts. Such an oligomer coating may either be formed by condensation of dimers formed in the gas phase or by a reactive uptake mechanism. Additionally the model simulations illustrates that the mass fraction of oligomer SOA in the bulk phase needs to increase with decreasing particle size to explain the nearly size independent evaporation rates. Because of the Kelvin effect, this may be accomplished if a considerable fraction of the low-volatility oligomers compounds is formed in the gas phase or if the oligomer SOA generally is formed from the least volatile monomer compounds.
3) Mass transfer limitations between the smog chamber air volume and the chamber walls because of a thin laminar layer adjacent to the walls have large influence on the uptake of gases onto the wall deposited particles or directly onto the walls. If the formed SOA material is semi-volatile the SOA particles on the chamber walls may even start to evaporate and hence become a source of SOA at the end of smog chamber experiments.

Paradoxically, heterogeneous reactions which give less volatile SOA and generally more SOA mass will increase the fraction of SOA which is found on the chamber walls and can thus even decrease the detectable SOA mass suspended in the chamber air volume.

4) In order to capture the rapid SOA formation observed during the oxidation of *m*-xylene in the Lund University smog chamber we need to consider relatively rapid oligomerization and/or some other heterogeneous reactions (e.g. ozonolysis of unsaturated organic compounds). When considering peroxyhemiacetal and hemiacetal dimer formation in the particle phase, ADCHAM is able to capture both the observed early stage rapid SOA formation in our own *m*-xylene experiment and gives almost identical SOA mass formation as the semi-empirical parameterizations from Ng et al. (2007). This indicates that heterogeneous particle phase reactions are not only important for the SOA properties (e.g. volatility) but also for the amount and formation rates.

Another more general conclusion, which can be drawn from the simulations performed in this work, is that many of the parameters (processes) with large uncertainties (e.g. SOA viscosity, oligomerization rates and mechanisms, pure-liquid saturation vapour pressures, surface tension and chamber wall effects) have large influence on the SOA formation and/or the chemical and physical properties of the SOA. To be able to constrain the uncertainties related to these parameters (processes), the experiments need to be designed where as many variables as possible are varied (e.g. time of ageing, temperature, RH, concentrations, dilution, oxidation agents and light intensities). Apart from evaluating experimental results, ADCHAM can be used as a valuable model tool when planning, designing and selecting which experiments and instrumentation are needed in order to be able to answer specific research questions. The *m*-xylene experiment studied in Sect. 3.4 is part of a larger experiment campaign designed in order to study ageing of anthropogenic SOA precursors and gasoline car exhausts (Nordin et al., 2012). In that paper an early version of ADCHAM was used to study chamber wall effects, gas phase chemistry and SOA formation before the experiments were performed. Currently we are working on an article where ADCHAM is used to study the ageing of gasoline car exhausts. We have also started to implement many of the detailed processes (e.g. the kinetic multilayer model, different oligomerization processes and the detailed MCMv3.2 gas phase chemistry) in the ADCHEM model which we use for detailed atmospheric process studies.

Appendix A

Table A1. List of symbols.

Symbol	Description
α_s	Surface mass accommodation coefficient
$\alpha_{0,s}$	Surface mass accommodation coefficient of surface free from adsorbing material
Γ	Activity coefficient
$\gamma_{w,i}$	Activity coefficient of compound *i* in a Teflon wall film
δ_k	Width of particle layer *k*
Δh	Relative change of the distance between the roof and ceiling of the chamber
Δx	Laminar layer width adjacent to chamber walls or charcoal denuder
θ_s	Relative surface coverage of the adsorbed species
μ	Dynamic viscosity of air
ρ_{air}	Air density
ρ_p	Particle phase density
σ	Surface tension
τ_{d,O_3}	Desorption lifetime of O_3
ω_{O_3}	Mean thermal velocity of O_3
ν_e	Characteristic average deposition velocity due to electrostatic forces
A_k	Area of exchange between particle layer *k*-1 and *k*
$A_{chamber}$	Chamber surface area
c_d	Dimer particle phase concentration
c_{H^+}	Hydrogen ion concentration
c_m	Monomer particle phase concentration
$c_{m,i}(p.s.)$	Particle surface monolayer concentration of reactive monomers
$c_{PINAL}(g)$	Gas phase concentration of pinonaldehyde
C_c	Cunningham slip correction factor
C_k	Kelvin effect
C_∞	Gas phase concentration far from the particle surfaces
C_s	Saturation gas phase concentration at the particle surface
C_w	Effective wall equivalent mass concentration

d_{O_3}	Width of the O_3 sorption layer
d_i	Collision diameter of compound *i*
D_p	Particle diameter
$D_{0,Xi}$	Diffusivity coefficient of compound X_i without obstructing material
D_{Xi}	Diffusion coefficient of compound X_i
e	Elementary charge of a single proton
$\bar{E}$	Mean electrical field strength
$\overline{E_0}$	Initial mean electrical field strength
F	Fuchs-Sutugin correction factor in the transition region
f_p	Particle volume fraction of solid or semi-solid obstructing material
f_{ROOR}	Fraction of RO_2 + RO_2 reactions which give ROOR dimer
$F_f(p)$	Dimer formation rates in the particle phase
$F_f(p.s.)$	Dimer formation rates in the particle surface layer
I	Molar condensation growth rate
J_{ads,O_3}	Adsorption rate of O_3 to the sorption layer
J_{des,O_3}	Desorption rate of O_3 from the sorption layer
k_{charge}	First order deposition loss rate due to charge
k_d	Dimer specific degradation reaction rate constant
k_f	Dimer formation rate constant
$k_{k,k+1,X_i}$	Transport velocity of compound X_i between the layers *k* and layer *k*+1.
k_{Ox}	Oxidation reaction rate constant in the particle phase
k_{so,su,O_3}	Transport velocity of O_3 from the sorption layer to the surface layer
k_{su,so,O_3}	Transport velocity of O_3 from the surface layer to the sorption layer
$k_{g,w}$	First order loss rate from the near wall gas phase to the walls
$k_{w,g}$	Desorption rate from the chamber wall Teflon surfaces
k_w	Effective wall deposition loss rate
K_a	Acid dissociation constant
K_H	Henry's law constant
K_s	Solubility product of salt
K_s^*	Effective solubility product of organic salts

Kn	Non-dimensional Knudsen number
M_i	Molar mass of compound i
M_w	Average molar mass of a Teflon wall film
N	Number of elemental charges of a particle
N_a	Avogadro's number
p_0	Pure-liquid saturation vapour pressure
p_s	Equilibrium vapour pressure
pH	Negative 10-logarithm of the hydrogen ion concentration
pK_a	Negative 10-logarithm of the acid dissociation constant
R	Universal gas constant (8.3145 J K^{-1} mol^{-1})
RH	Relative humidity in %
T	Time
T	Temperature in Kelvin
u^*	Friction velocity
V_k	Volume of particle layer k
$V_{chamber}$	Chamber volume
V_{wall}	Air volume of a thin layer adjacent to the chamber walls
X	mole fractions
x_k	Ratio between the smaller and larger of the two volume fluxes across A_k
X	Condensable organic compound
$[X_{i,g,w}]$	Concentrations of compound X_i in the thin layer adjacent to the chamber walls
$[X_{i,w}]$	Concentration of compound X_i at the chamber wall
Y	Organic compound formed by particle phase oxidation reaction

Acknowledgements

This work was supported by the strategic research area MERGE at Lund University, Swedish Research Council for Environment, Agricultural Sciences and Spatial Planning FORMAS through projects 2007-1205, 2008-1467, 2009-615 and 2010-1678, the Swedish Research Council through project 2006-5940 and by Metalund, the centre for Medicine and Technology for Working Life and Society, a competence centre at Lund University, Sweden, supported by FAS, the Swedish Council for Working Life and Social Research.

The authors would like to thank prof. Gordon McFiggans research group at the University of Manchester, and especially Dr. David Topping, for helpful discussions and for providing the Python script (now a public available function called CompSysProp: http://ratty.cas.manchester.ac.uk/informatics/) to calculate Nannoolal based sub-cooled liquid saturation vapour pressures for all included organic compounds in this paper.

5 References

Abramson, E., Imre, D., Beránek, J., Wilson, J., Zelenyuk, A.: Experimental determination of chemical diffusion within secondary organic aerosol particles, Phys. Chem. Chem. Phys.,15, 2983-2991, 2013

Ammann, M. and Pöschl, U.: Kinetic model framework for aerosol and cloud surface chemistry and gas-particle interactions - Part 2: Exemplary practical applications and numerical simulations, Atmos. Chem. Phys., 7, 6025–6045, 2007.

Barley, M. H. and McFiggans, G.: The critical assessment of vapour pressure estimation methods for use in modelling the formation of atmospheric organic aerosol, Atmos. Chem. Phys., 10, 749-767, doi:10.5194/acp-10-749-2010, 2010.

Barsanti, K. C., McMurry, P. H., and Smith, J. N.: The potential contribution of organic salts to new particle growth, Atmos. Chem. Phys., 9, 2949-2957, doi:10.5194/acp-9-2949-2009, 2009.

Bergström, R., Denier van der Gon, H. A. C., Prévôt, A. S. H., Yttri, K. E., and Simpson, D.: Modelling of organic aerosols over Europe (2002–2007) using a volatility basis set (VBS) framework: application of different assumptions regarding the formation of secondary organic aerosol, Atmos. Chem. Phys., 12, 8499-8527, doi:10.5194/acp-12-8499-2012, 2012.

Bertram, A. K., Martin, S. T., Hanna, S. J., Smith, M. L., Bodsworth, A., Chen, Q., Kuwata, M., Liu, A., You, Y., and Zorn, S. R.: Predicting the relative humidities of liquid-liquid phase separation, efflorescence, and deliquescence of mixed particles of ammonium sulphate, organic material, and water using the organic-to-sulphate mass ratio of the particle and the oxygen-to-carbon elemental ratio of the organic component, Atmos. Chem. Phys., 11, 10995-11006, doi:10.5194/acp-11-10995-2011, 2011.

Bloss, C., Wagner, V., Bonzanini, A., Jenkin, M. E., Wirtz, K., Martin-Reviejo, M., and Pilling, M. J.: Evaluation of detailed aromatic mechanisms (MCMv3 and MCMv3.1) against environmental chamber data, Atmos. Chem. Phys., 5, 623-639, 2005a.

Bloss, C., Wagner, V., Jenkin, M. E., Volkamer, R., Bloss, W. J., Lee, J. D., Heard, D. E., Wirtz, K., Martin-Reviejo, M., Rea, G., Wenger, J. C., and Pilling, M. J.: Development of a detailed chemical mechanism (MCMv3.1) for the atmospheric oxidation of aromatic hydrocarbons, Atmos. Chem. Phys., 5, 641-664, doi:10.5194/acp-5-641-2005, 2005b.

Boy, M., Hellmuth, O., Korhonen, H., Nilsson, E. D., ReVelle, D., Turnipseed, A., Arnold, F., and Kulmala, M.: MALTE – model to predict new aerosol formation in the lower troposphere, Atmos. Chem. Phys., 6, 4499-4517, doi:10.5194/acp-6-4499-2006, 2006.

Camredon, M., Hamilton, J. F., Alam, M. S., Wyche, K. P., Carr, T., White, I. R., Monks, P. S., Rickard, A. R., and Bloss, W. J.: Distribution of gaseous and particulate organic composition during dark α-pinene ozonolysis, Atmos. Chem. Phys., 10, 2893-2917, doi:10.5194/acp-10-2893-2010, 2010.

Chapman, S., and Cowling, T. G.: The Mathematical Theory of Nonuniform Gases, Cambridge University Press, Cambridge, 1970.

Compernolle, S., Ceulemans, K., and Müller, J.-F.: Influence of non-ideality on condensation to aerosol, Atmos. Chem. Phys., 9, 1325–1337, doi:10.5194/acp-9-1325-2009, 2009.

Donahue, N. M., Epstein, S. A., Pandis, S. N., and Robinson, A. L.: A two-dimensional volatility basis set: 1. organic-aerosol mixing thermodynamics, Atmos. Chem. Phys., 11, 3303-3318, doi:10.5194/acp-11-3303-2011, 2011.

Dzepina, K., Volkamer, R. M., Madronich, S., Tulet, P., Ulbrich, I. M., Zhang, Q., Cappa, C. D., Ziemann, P. J., and Jimenez, J. L.: Evaluation of recently-proposed secondary organic aerosol models for a case study in Mexico City, Atmos. Chem. Phys., 9, 5681-5709, doi:10.5194/acp-9-5681-2009, 2009.

Ervens, B. and Volkamer, R.: Glyoxal processing by aerosol multiphase chemistry: towards a kinetic modelling framework of secondary organic aerosol formation in aqueous particles, Atmos. Chem. Phys., 10, 8219-8244, doi:10.5194/acp-10-8219-2010, 2010.

Fuchs, N. A., Sutugin, A. G.: In Topics in Current Aerosol Research, Pergamon Press, 1971.

Gao, S., Keywood, M., Ng, N. L., Surratt, J., Varutbangkul, V., Bahreini, R., Flagan, R. C., and Seinfeld, J. H.: Low-Molecular-Weight and Oligomeric Components in Secondary Organic Aerosol from the Ozonolysis of Cycloalkenes and α-Pinene, J. Phys. Chem. A, 108, 10147-10164, 2004.

George, C., Strekowski, R. S., Kleffmann, J., Stemmler, K., and Ammann, M.: Photoenhanced uptake of gaseous NO2 on solid organic compounds: a photochemical source of HONO?, Faraday Discuss., 130, 195–210, 2005.

Greaves, T. L. and Drummond, C. J.: Protic ionic liquids: Properties and applications, Chem. Rev., 108, 206–237, 2008.

Grieshop, A. P., Donahue, N. M., and Robinson, A. L.: Is the gas-particle partitioning in alpha-pinene secondary organic aerosol reversible?, Geophys. Res. Lett., 34, L14810, doi:10.1029/2007GL029987, 2007.

Griffin, R. J., Cocker III, D. R., Flagan, R. C., and Seinfeld, J. H.: Organic aerosol formation from the oxidation of biogenic hydrocarbons, J. Geophys. Res., 104, 3555–3567, 1999.

Gutzwiller, L., Arens, F., Baltensperger, U., G¨aggeler, H. W., and Ammann, M.: Significance of Semivolatile Diesel Exhaust Organics for Secondary HONO Formation, Environ. Sci. Technol., 36, 677–682, 2002.

Hallquist, M., Wenger, J. C., Baltensperger, U., Rudich, Y., Simpson, D., Claeys, M., Dommen, J., Donahue, N. M., George, C., Goldstein, A. H., Hamilton, J. F., Herrmann, H., Hoffmann, T., Iinuma, Y., Jang, M., Jenkin, M. E., Jimenez, J. L., Kiendler-Scharr, A., Maenhaut, W., McFiggans, G., Mentel, Th. F., Monod, A., Prévôt, A. S. H., Seinfeld, J. H., Surratt, J. D., Szmigielski, R., and Wildt, J.: The formation, properties and impact of secondary organic aerosol: current and emerging issues, Atmos. Chem. Phys., 9, 5155–5236, doi:10.5194/acp-9- 5155-2009, 2009.

Hansen, H. K., Rasmussen, P., Fredenslund, A., Schiller, M., and Gmehling, J.: Vapour–liquid equilibria by UNIFAC group contribution. 5. Revision and extension, Ind. Eng. Chem. Res., 30, 2352–2355, 1991.

Hildebrandt, L., Donahue, N. M. and Pandis, S. N.: High formation of secondary organic aerosol from the photo-oxidation of toluene. Atmos. Chem. Phys. 9, 2973-2986, 2009.

Hoffmann, T., Odum, J. R., Bowman, F., Collins, D., Klockow, D., Flagan, R. C., and Seinfeld, J. H.: Formation of organic aerosols from the oxidation of biogenic hydrocarbons, J. Atmos. Chem., 26, 189–222, 1997.

Hu, D., Tolocka, M., Li, Q., and Kamens, R. M.: A kinetic mechanism for predicting secondary organic aerosol formation from toluene oxidation in the presence of NOx and natural sunlight, Atmos. Environ., 41, 6478–6496, 2007.

Huff Hartz, K. E. H., Weitkamp, E. A., Sage, A. M., Donahue, N. M., and Robinson, A. L.: Laboratory measurements of the oxidation kinetics of organic aerosol mixtures using a relative rate constants approach, J. Geophys. Res.-Atmos., 112, D04204, doi:10.1029/2006jd007526, 2007.

Hyder, M., Genberg, J., Jönsson, J. Å.: Application of hollow fiber liquid phase microextraction for pinic acid and pinonic acid analysis from organic aerosols, Analytica Chimica Acta, 713, 79– 85, 2012.

Iinuma, Y., Böge, O., Gnauk, T., and Herrmann, H.: Aerosolchamber study of the α-pinene/O3 reaction: Influence of particle acidity on aerosol yields and products, Atmos. Environ., 38, 761–773, 2004.

Jacobson, M. Z.: Fundamentals of Atmospheric Modelling (2^{nd} edition), Cambridge University Press, Cambridge, United Kingdom and New York, NY, USA, ISBN: 0 521 54865 9, 2005.

Jenkin, M. E., Saunders, S. M, and Pilling, M. J.: The tropospheric degradation of volatile organic compounds: A protocol for mechanism development, Atmos. Environ., 31, 81-104, 1997.

Jenkin, M. E., Saunders, S. M., Wagner, V., and Pilling, M. J.: Protocol for the development of the Master Chemical Mechanism, MCM v3 (Part B): tropospheric degradation of aromatic volatile organic compounds, Atmos. Chem. Phys., 3, 181-193, doi:10.5194/acp-3-181-2003, 2003.

Jimenez, J. L., Canagaratna, M. R., Donahue, N. M., Prevot, A. S. H., Zhang, Q., Kroll, J. H., DeCarlo, P. F., Allan, J. D., Coe, H., Ng, N. L., Aiken, A. C., Docherty, K. S., Ulbrich, I. M., Grieshop, A. P., Robinson, A. L., Duplissy, J., Smith, J. D., Wilson, K. R., Lanz, V. A., Hueglin, C., Sun, Y. L., Tian, J., Laaksonen, A., Raatikainen, T., Rautiainen, J., Vaattovaara, P., Ehn, M., Kulmala, M., Tomlinson, J. M., Collins, D. R., Cubison, M. J., Dunlea, E. J., Huffman, J. A., Onasch, T. B., Alfarra, M. R., Williams, P. I., Bower, K., Kondo, Y., Schneider, J., Drewnick, F., Borrmann, S., Weimer, S., Demerjian, K., Salcedo, D., Cottrell, L., Griffin, R., Takami, A., Miyoshi, T., Hatakeyama, S., Shimono, A., Sun, J. Y, Zhang, Y. M., Dzepina, K., Kimmel, J. R., Sueper, D., Jayne, J. T., Herndon, S. C., Trimborn, A. M., Williams, L. R., Wood, E. C., Middlebrook, A. M., Kolb, C. E., Baltensperger, U., and Worsnop, D. R.: Evolution of Organic Aerosols in the Atmosphere, Science, 326, 1525-1529, 2009.

Johnson, D., Jenkin, M.E., Wirtz, K., Martin-Reviejo, M.: Simulating the formation of secondary organic aerosol from the photooxidation of aromatic hydrocarbons. Environmental Chemistry 2, 35–48, 2005.

Johnson, D., Utembe, S. R., and Jenkin, M. E.: Simulating the detailed chemical composition of secondary organic aerosol formed on a regional scale during the TORCH 2003 campaign in the southern UK, Atmos. Chem. Phys., 6, 419–431, 2006.

Jonsson, Å. M., Hallquist, M., and Ljungström, E.: The effect of temperature and water on secondary organic aerosol formation from ozonolysis of limonene, Δ^3-carene and α-pinene, Atmos. Chem. Phys., 8, 6541-6549, doi:10.5194/acp-8-6541-2008, 2008.

Kalberer, M., Paulsen, D., Sax, M., Steinbacher, M., Dommen, J., Prévôt, A. S. H., Fisseha, R., Weingartner, E., Frankevich, V., Zenobi, R., and Baltensperger, U.: Identification of polymers as major components of atmospheric organic aerosols, Science, 303, 1659–1662, 2004.

Knopf, D. A., Anthony, L. M., and Bertram, A. K.: Reactive uptake of O3 by multicomponent and multiphase mixtures containing oleic acid, J. Phys. Chem. A, 109, 5579–5589, 2005.

Koop, T., Bookhold, J., Shiraiwa, M., and Pöschl, U.: Glass transition and phase state of organic compounds: dependency on molecular properties and implications for secondary organic aerosols in the atmosphere, Phys. Chem. Chem. Phys., 13, 19238–19255, 2011.

Korhonen, H., Lehtinen, K. E. J., and Kulmala, M.: Multicomponent aerosol dynamics model UHMA: modle development and validation, Atmos. Chem. Phys., 4, 471–506, 2004.

Kroll, J., and Seinfeld, J. H.: Chemistry of secondary organic aerosol: Formation and evolution of low-volatility organics in the atmosphere, Atmos. Env., 42, 3593–3624, 2008.

Kuwata, M., and Martin, S., T.: Phase of atmospheric secondary organic material affects its reactivity, PNAS, 109, 17354-17359, doi/10.1073/pnas.1209071109, 2012.

Lai, A. and Nazaroff, W.W.: Modelling indoor particle deposition from turbulent flow onto smooth surfaces, J. Aerosol Sci., 31, 463-476, 2000.

Li, Q., Hu, D., Leungsakul, S., and Kamens, R. M.: Large outdoor chamber experiments and computer simulations: (I) Secondary organic aerosol formation from the oxidation of a mixture of d- limonene and α-pinene, Atmos. Environ., 41(40), 9341–9352, 2007.

Lide, D. R. (Ed.): CRC Handbook of chemistry and physics, Taylor and Francis Group, Boca Raton, FL, USA, 88th Edition, 2008.

Liggio, J. and Li, S.-M.: Organosulfate formation during the uptake of pinonaldehyde in acidic sulphate aerosols, Geophys. Res. Lett., 33, L13808, doi:10.1029/2006GL026079, 2006.

Loza, C. L., Chhabra, P. S., Yee, L. D., Craven, J. S., Flagan, R. C., and Seinfeld, J. H.: Chemical aging of *m*-xylene secondary organic aerosol: laboratory chamber study, Atmos. Chem. Phys., 12, 151-167, doi:10.5194/acp-12-151-2012, 2012.

Maksymiuk, C. S., Gayahtri, C., Gil, R. R., and Donahue, N. M.: Secondary organic aerosol formation from multiphase oxidation of limonene by ozone: mechanistic constraints via two-dimensional heteronuclear NMR spectroscopy. Phys. Chem. Chem. Phys., 2009, 11, 7810–7818, 2009.

Marcolli, C. and Peter, T.: Water activity in polyol/water systems: new UNIFAC parameterization, Atmos. Chem. Phys., 5, 1545–1555, 2005.

Matsunaga, A., and Ziemann, P.J.: Gas-Wall Partitioning of Organic Compounds in a Teflon Film Chamber and Potential Effects on Reaction Product and Aerosol Yield Measurements, Aerosol Sci. Technol., 44, 881-892, 2010.

McFiggans, G., Topping, D. O., and Barley, M. H.: The sensitivity of secondary organic aerosol component partitioning to the predictions of component properties – Part 1: A systematic evaluation of some available estimation techniques, Atmos. Chem. Phys., 10, 10255–10272, 2010.

McMurry, P. H. and Rader, D. J.: Aerosol wall losses in electrically charged chambers. Aerosol Sci. Technol., 4, 249-268, 1985.

Metzger, A., Dommen, J., Gaeggeler, K., Duplissy, J., Prévôt, A. S. H., Kleffmann, J., Elshorbany, Y., Wisthaler, A., and Baltensperger, U.: Evaluation of 1,3,5 trimethylbenzene degradation in the detailed tropospheric chemistry mechanism, MCMv3.1, using environmental chamber data, Atmos. Chem. Phys., 8, 6453–6468, 2008.

Na, K., Song, C., Switzer, C., and Cocker, D.: Effect of Ammonia on Secondary Organic Aerosol Formation from α-Pinene Ozonolysis in Dry and Humid Conditions. Environ. Sci. Technol., 41, 6096-6102, 2007.

Nannoolal, J., Rarey, J., Ramjugernath, D.: Estimation of pure component properties Part 3. Estimation of the vapour pressure of non-electrolyte organic compounds via group contributions and group interactions Fuild Phase Equilibria, 269, 117-133, 2008.

Nash, D. G., Tolocka, M. P., and Baer, T.: The uptake of O_3 by myristic acid-oleic acid mixed particles: evidence for solid surface layers, Phys. Chem. Chem. Phys., 8, 4468–4475, doi:10.1039/b609855j, 2006.

Ng, N. L., Kroll, J. H., Chan, A. W. H., Chhabra, P. S., Flagan, R. C., and Seinfeld, J. H.: Secondary organic aerosol formation from *m*-xylene, toluene, and benzene, Atmos. Chem. Phys., 7, 3909–3922, 2007.

Ng, N. L., Kwan, A. J., Surratt, J. D., Chan, A. W. H., Chhabra, P. S., Sorooshian, A., Pye, H. O. T., Crounse, J. D., Wennberg, P. O., Flagan, R. C., and Seinfeld, J. H.: Secondary organic aerosol (SOA) formation from reaction of isoprene with nitrate radicals (NO3), Atmos. Chem. Phys., 8, 4117–4140, 2008.

Nordin, E. Z., Eriksson, A. C., Roldin, P., Nilsson, P. T., Carlsson, J. E., Kajos, M. K., Hellen´, H., Wittbom, C., Rissler, J., Löndahl, J., Swietlicki, E., Svenningsson, B., Bohgard, M., Kulmala, M., Hallquist, M. and Pagels, J.: Secondary organic aerosol formation from gasoline passenger vehicle emissions investigated in a smog chamber, Atmos. Chem. Phys. Discuss., 12, 31725–31765, 2012.

Odum, J. R., Hoffmann, T., Bowman, F., Collins, D., Flagan, R. C., and Seinfeld, J. H.: Gas/particle partitioning and secondary organic aerosol yields, Environ. Sci. Technol., 30, 2580–2585, 1996.

Pankow, J. F.: An absorption-model of the gas aerosol partitioning involved in the formation of secondary organic aerosol, Atmos. Environ., 28, 189–193, 1994.

Pankow, J. F. & Asher, W. E.: SIMPOL.1: a simple group contribution method for predicting vapour pressures and enthalpies of vaporization of multifunctional organic compounds, Atmos. Chem. Phys., 8, 2773–2796, 2008.

Pathak, R. K., Presto, A. A., Lane, T. E., Stanier, C. O., Donahue, N. M., and Pandis, S. N.: Ozonolysis of α-pinene: parameterization of secondary organic aerosol mass fraction, Atmos. Chem. Phys., 7, 3811-3821, doi:10.5194/acp-7-3811-2007, 2007.

Paulsen, D., Dommen, J., Kalberer, M., Prevot, A. S. H., Richter, R., Sax, M., Steinbacher, M.,Weingartner, E., and Baltensperger, U.: Secondary organic aerosol formation by irradiation of 1,3,5-trimethylbenzene-NOx-H2O in a new reaction chamber for atmospheric chemistry and physics, Environ. Sci. Technol., 39, 2668–2678, 2005.

Pfrang, C., Shiraiwa, M., and Pöschl, U.: Chemical ageing and transformation of diffusivity in semi-solid multi-component organic aerosol particles, Atmos. Chem. Phys., 11, 7343-7354, doi:10.5194/acp-11-7343-2011, 2011.

Pierce, J. R., Engelhart, G. J., Hildebrandt, L., Weitkamp, E. A., Pathak, R. K., Donahue, N. M., Robinson, A. L., Adams, P. J., and Pandis, S. N.: Constraining Particle Evolution from Wall Losses, Coagulation, and Condensation-Evaporation in Smog-Chamber Experiments: Optimal Estimation Based on Size Distribution Measurements, Aerosol Sci. Technol., 42:12, 1001-1015, 2008.

Pun, B. K. and Seigneur, C.: Investigative modelling of new pathways for secondary organic aerosol formation, Atmos. Chem. Phys., 7, 2199-2216, doi:10.5194/acp-7-2199-2007, 2007.

Pöschl, U., Rudich, Y., and Ammann, M.: Kinetic model framework for aerosol and cloud surface chemistry and gas-particle interactions – Part 1: General equations, parameters, and terminology, Atmos. Chem. Phys., 7, 5989–6023, 2007.

Pöschl, U.: Gas–particle interactions of tropospheric aerosols: Kinetic and thermodynamic perspectives of multiphase chemical reactions, amorphous organic substances, and the activation of cloud condensation nuclei, Atmos. Res. 101, 562–573, 2011.

Rader, D. J., McMurry, P. H. and Smith, S.: Evaporation Rates of Monodisperse Organic Aerosols in the 0.02- to 0.2-μm-Diameter Range, Aerosol Sci. Technol., 6,247-260, 1987.

Ray, A. K, Lee, J., and Tilley, H. L.: Direct Measurements of Evaporation Rates of Single Droplets at Large Knudsen Numbers, Langmuir, 4, 631-637, 1988.

Rickard, A. R., Wyche, K.P., Metzger, A., Monks, P.S., Ellis, A.M., Dommenc, J., Baltensperger, U., Jenkin, M.E., Pilling, M.J.: Gas phase precursors to anthropogenic secondary organic aerosol: Using the Master Chemical Mechanism to probe detailed observations of 1,3,5-trimethylbenzene photo-oxidation, Atmos. Env. 44, 5423–5433, 2010.

Riipinen, I., Pierce, J. R., Donahue, N. M, Pandis, S. N.: Equilibration time scales of organic aerosol inside thermodenuders: Evaporation kinetics versus thermodynamics. Atmos Environ 44:597–607, 2010.

Rohrer, F., Bohn, B., Brauers, T., Bruning, D., Johnen, F. J., Wahner, A., and Kleffmann, J.: Characterisation of the photolytic HONO-source in the atmosphere simulation chamber SAPHIR, Atmos. Chem. Phys., 5, 2189–2201, 2005.

Roldin, P., Swietlicki, E., Schurgers, G., Arneth, A., Lehtinen, K. E. J., Boy, M., & Kulmala, M.: Development and evaluation of the aerosol dynamics and gas phase chemistry model ADCHEM, Atmos. Chem. Phys., 11, 5867-5896, 2011a.

Roldin, P., Swietlicki, E., Massling, A., Kristensson, A., Löndahl, J., Eriksson, A., Pagels, J., and Gustafsson, S.: Aerosol ageing in an urban plume – implication for climate, Atmos. Chem. Phys., 11, 5897–5915, 2011b.

Rudich, Y., Donahue, N. M., and Mentel, T. F.: Aging of organic aerosol: Bridging the gap between laboratory and field studies, Annu. Rev. Phys. Chem., 58, 321–352, 2007.

Saukko, E., Lambe, A. T., Massoli, P., Koop, T., Wright, J. P., Croasdale, D. R., Pedernera, D. A., Onasch, T. B., Laaksonen, A., Davidovits, P., Worsnop, D. R., and Virtanen, A.: Humidity-dependent phase state of SOA particles from biogenic and anthropogenic precursors, Atmos. Chem. Phys., 12, 7517-7529, doi:10.5194/acp-12-7517-2012, 2012.

Saunders, S. M., Jenkin, M. E., Derwent, R. G., and Pilling, M. J.: Protocol for the development of the Master Chemical Mechanism, MCM v3 (Part A): tropospheric degradation of non-aromatic volatile organic compounds, Atmos. Chem. Phys., 3, 161-180, doi:10.5194/acp-3-161-2003, 2003.

Seinfeld, J. H., and Pandis, S. N.: Atmospheric Chemistry and Physics: From Air Pollution to Climate Change, (2nd edition), Wiley, New Jersey, ISBN: 0-471-72018-6, 2006.

Shiraiwa, M., Pfrang, C., and Pöschl, U.: Kinetic multi-layer model of aerosol surface and bulk chemistry (KM-SUB): the influence of interfacial transport and bulk diffusion on the oxidation of oleic acid by ozone, Atmos. Chem. Phys., 10, 3673-3691, doi:10.5194/acp-10-3673-2010, 2010.

Shiraiwa, M., Ammann, M., Koop, T., Pöschl, U.: Gas uptake and chemical aging of semisolid organic aerosol particles, Proc. Natl Acad. Sci., 108, 11003-11008 doi:10.1073/pnas.1103045108, 2011.

Shiraiwa, M., Pfrang, C., Koop, T., and Pöschl, U.: Kinetic multi-layer model of gas-particle interactions in aerosols and clouds (KM-GAP): linking condensation, evaporation and chemical reactions of organics, oxidants and water, Atmos. Chem. Phys., 12, 2777–2794, 2012.

Smith, J. N., Dunn, M. J., VanReken, T. M., Iida, K., Stolzenburg, M. R., McMurry, P. H., and Huey, L. G.: Chemical composition of atmospheric nanoparticles formed from nucleation in Tecamac, Mexico: Evidence for an important role for organic species in nanoparticle growth, Geophys. Res. Lett., 35, L04808, doi:10.1029/2007gl032523, 2008.

Smith, J. N., Barsanti, K. C, Friedli, H. R., Ehn, M., Kulmala, M., Collins, D. R., Scheckman, J. H., Williams, B. J., and McMurry, P. H.: Observations of aminium salts in atmospheric nanoparticles and possible climatic implications, Proc. Natl Acad. Sci. 107, 6634–6639, 2010.

Smith, M. L., Kuwata, M., and Martin, S. T.: Secondary Organic Material Produced by the Dark Ozonolysis of α-Pinene Minimally Affects the Deliquescence and Efflorescence of Ammonium Sulphate, Aerosol Sci. Technol., 45, 244–261, doi:10.1080/02786826.2010.532178, http://dx.doi.org/10.1080/02786826.2010.532178, 2011.

Stroeve, P.: On the Diffusion of Gases in Protein Solutions, Ind. Eng. Chem. Fund., 14, 140-141, 1975.

Surratt, J. D., Kroll, J. H., Kleindienst, T. E., Edney, E. O., Claeys, M., Sorooshian, A., Ng, N. L., Offenberg, J. H., Lewandowski, M., Jaoui, M., Flagan, R. C., and Seinfeld, J. H.: Evidence for organosulfates in secondary organic aerosol, Environ. Sci. Technol., 41, 517–527, 2007.

Svenningsson, B., Rissler, J., Swietlicki, E., Mircea, M., Bilde, M., Facchini, M. C., Decesari, S., Fuzzi, S., Zhou, J., Mønster, J., and Rosenørn, T.: Hygroscopic growth and critical supersaturations for mixed aerosol particles of inorganic and organic compounds of atmospheric relevance, Atmos. Chem. Phys., 6, 1937-1952, doi:10.5194/acp-6-1937-2006, 2006.

Tolocka, M. P., Jang, M., Ginter, J. M., Cox, F. J., Kamens R. M., and Johnston, M. V.: Formation of Oligomers in Secondary Organic Aerosol, Environ. Sci. Technol., 38, 1428-1434, 2004.

Vaden, T. D., Song, C., Zaveri, R. A., Imre, D., Zelenyuk, A.: Morphology of mixed primary and secondary organic particles and the adsorption of spectator organic gases during aerosol formation, Proc. Natl. Acad. Sci,, 107, 6658–6663, 2010.

Vaden, T. D., Imreb, D., Beráneka, J., Shrivastavaa, M., and Zelenyuka, A.: Evaporation kinetics and phase of laboratory and ambient secondary organic aerosol, Proc. Natl. Acad. Sci., 108, 2190-2195, 2011.

Valorso, R., Aumont, B., Camredon, M., Raventos-Duran, T., Mouchel-Vallon, C., Ng, N. L., Seinfeld, J. H., Lee-Taylor, J., and Madronich, S.: Explicit modelling of SOA formation from α-pinene photooxidation: sensitivity to vapour pressure estimation. Atmos. Chem. Phys., 11, 6895–6910, 2011.

Vesterinen, M., Lehtinen, K. E. J., Kulmala, M., and Laaksonen, A.: Effect of particle phase oligomer formation on aerosol growth, Atmos. Environ., 41, 1768–1776, 2007.

Virtanen, A., Joutsensaari, J., Koop, T., Yli-Pirilä, P., Leskinen, J., Mäkelä, J. M., Holopainen, J. K., Pöschl, U., Kulmala, M., Worsnop, D. R. and Laaksonen, A.: An amorphous solid state of biogenic secondary organic aerosol particles, Nature, 467, 824-827, 2010.

Wiedensohler, A., Birmili, W., Nowak, A., Sonntag, A., Weinhold, K., Merkel, M., Wehner, B., Tuch, T., Pfeifer, S., Fiebig, M., Fjäraa, A. M., Asmi, E., Sellegri, K., Depuy, R., Venzac, H., Villani, P., Laj, P., Aalto, P., Ogren, J. A., Swietlicki, E., Williams, P., Roldin, P., Quincey, P., Hüglin, C., Fierz-Schmidhauser, R., Gysel, M., Weingartner, E., Riccobono, F., Santos, S., Grüning, C., Faloon, K., Beddows, D., Harrison, R., Monahan, C., Jennings, S. G., O'Dowd, C. D., Marinoni, A., Horn, H.-G., Keck, L., Jiang, J., Scheckman, J., McMurry, P. H., Deng, Z., Zhao, C. S., Moerman, M., Henzing, B., de Leeuw, G., Löschau, G., and Bastian, S.: Mobility particle size spectrometers: harmonization of technical standards and data structure to facilitate high quality long-term observations of atmospheric particle number size distributions, Atmos. Meas. Tech., 5, 657-685, doi:10.5194/amt-5-657-2012, 2012.

Yli-Juuti, T., Barsanti, K., Hildebrandt Ruiz, L., Kieloaho, A.-J., Makkonen, U., Petäjä, T., Ruuskanen, T., Kulmala, M. and Riipinen, I.: Model for acid-base chemistry in nanoparticle growth (MABNAG), Atms. Chem. Phys. Discuss., 13, 7175-7222, 2013

Zhang, S-H., Seifeld, J. H., and Flagan, R. C.: Determination of Particle Vapour Pressures Using the Tandem Differential Mobility Analyzer, Aerosol Sci. Technol., 19,3-14, 1993.

Zobrist, B., Soonsin, V., Luo, B. P., Krieger, U. K., Marcolli, C., Peter, T., and Koop, T.: Ultra-slow water diffusion in aqueous sucrose glasses, Phys. Chem. Chem. Phys., 13, 3514–3526, doi:10.1039/c0cp01273d, 2011.

Zuend, A., Marcolli, C., Luo, B. P., and Peter, T.: A thermodynamic model of mixed organic-inorganic aerosols to predict activity coefficients, Atmos. Chem. Phys., 8, 4559–4593, doi:10.5194/acp-8-4559-2008, 2008.

Zuend, A., Marcolli, C., Peter, T., and Seinfeld, J. H.: Computation of liquid-liquid equilibria and phase stabilities: implications for RH-dependent gas/particle partitioning of organic-inorganic aerosols, Atmos. Chem. Phys., 10, 7795-7820, doi:10.5194/acp-10-7795-2010, 2010.

Zuend, A., Marcolli C., Booth , A. M., Lienhard, D. M., Soonsin, V., Krieger, U. K., Topping, D. O., McFiggans G., Peter, T., and Seinfeld, J. H.: New and extended parameterization of the thermodynamic model AIOMFAC: calculation of activity coefficients for organic-inorganic mixtures containing carboxyl, hydroxyl, carbonyl, ether, ester, alkenyl, alkyl, and aromatic functional groups., Atmos. Chem. Phys., 11, 9155–9206, 2011.

Zuend, A. and Seinfeld, J. H.: Modelling the gas-particle partitioning of secondary organic aerosol: the importance of liquid-liquid phase separation, Atmos. Chem. Phys., 12, 3857-3882, doi:10.5194/acp-12-3857-2012, 2012.

Table 1. Model parameters used in the multilayer module for O_3 uptake, diffusion and reactions in the particle phase.

Parameter	Definition	Value
$\alpha_{s,0,O3}$	Surface accommodation coefficient of O_3 on a free substrate	1^a
$\tau_{d,O3}$ (s)	O_3 desorption lifetime	$10^{-9\ a}$
K_{H,O_3} (mol m^3 Pa^{-1})	Henry's law coefficient of O_3	$4.7x10^{-3a*}$
D_{0,O_3} (cm^2 s^{-1})	Bulk diffusion coefficient O_3 without obstruction	Variable
ω_{O_3} (cm s^{-1})	Mean thermal velocity O_3	$3.6x10^{4a}$
d_{O_3} (nm)	Effective diameter cross section O_3	0.4^a
k_{O_3} (cm^3 $molec^{-1}$ s^{-1})	Reaction rate constant between O_3 and organic comp.	Variable

[a] Values from Pfrang et al. (2011), [*]Different unit than in Pfrang et al. (2011)

Table 2. Base case model set-up values for the simulation of organic salt formation between carboxylic acids and dissolved ammonium ions.

Parameter	Definition	Value[a]
$pK_{a,COOH}$	Logarithm of carboxylic acid dissociation constant	4.6
$pK_{a,NH3}$	Logarithm of NH_4^+ dissociation constant	9.25^b
K_s^* (mol^2 m^{-6})	Effective solubility product (see Eq. 31)	0.1
K_H (mol m^{-3} atm^{-1})	Henry's law coefficient for NH_3	57.6^c
$p_{0,i}$	Pure-liquid saturation vapour pressure comp. *i*	SIMPOL
γ_i	Activity coefficient for compound *i*	AIOMFAC
$D_{0,monomer,SOA}$ (cm^2 s^{-1})	Diffusion coefficient for SOA monomers	$5x10^{-17d}$
$D_{0,ammonium}$ (cm^2 s^{-1})	Diffusion coefficient for NH_3/NH_4^+	$1.3x10^{-16d}$
$D_{NH4RCOO}$ (cm^2 s^{-1})	Diffusion coefficient of organic salts	0

[a]Base case simulation value. [b]Lide, 2008 (CRC Handbook of Chemistry and Physics) at 298 K. [c] Jacobson, 2005. [d]Based on the Stoke-Einstein relationship and a SOA viscosity of 10^8 Pa s (Abramson et al., 2013).

Table 3. Initial conditions and results from the α-pinene – O_3 – NH_3 – CO experiments (Na et al., 2007) and base case model simulations.

Date	Initial [α-pin.] exp. (ppb)	Initial NH_3 (ppb)	Δ[O_3] exp. (ppb)	Δ[α-pin.] exp.	Yield exp. (%)	Initial [α-pin.] model (ppb)	Δ[O_3] model (ppb)	Δ[α-pin.] model (ppb)	Yield model. (%)
01/25/05	221		130	218	**54.3**	222	149	216	**57.5**
01/11/05	221	50	150	203	**60.3**	222	149	216	**63.6**
01/10/05	223	100	150	206	**64.0**	222	149	216	**65.4**
01/06/05	224	200	151	220	**65.3**	222	149	216	**67.0**

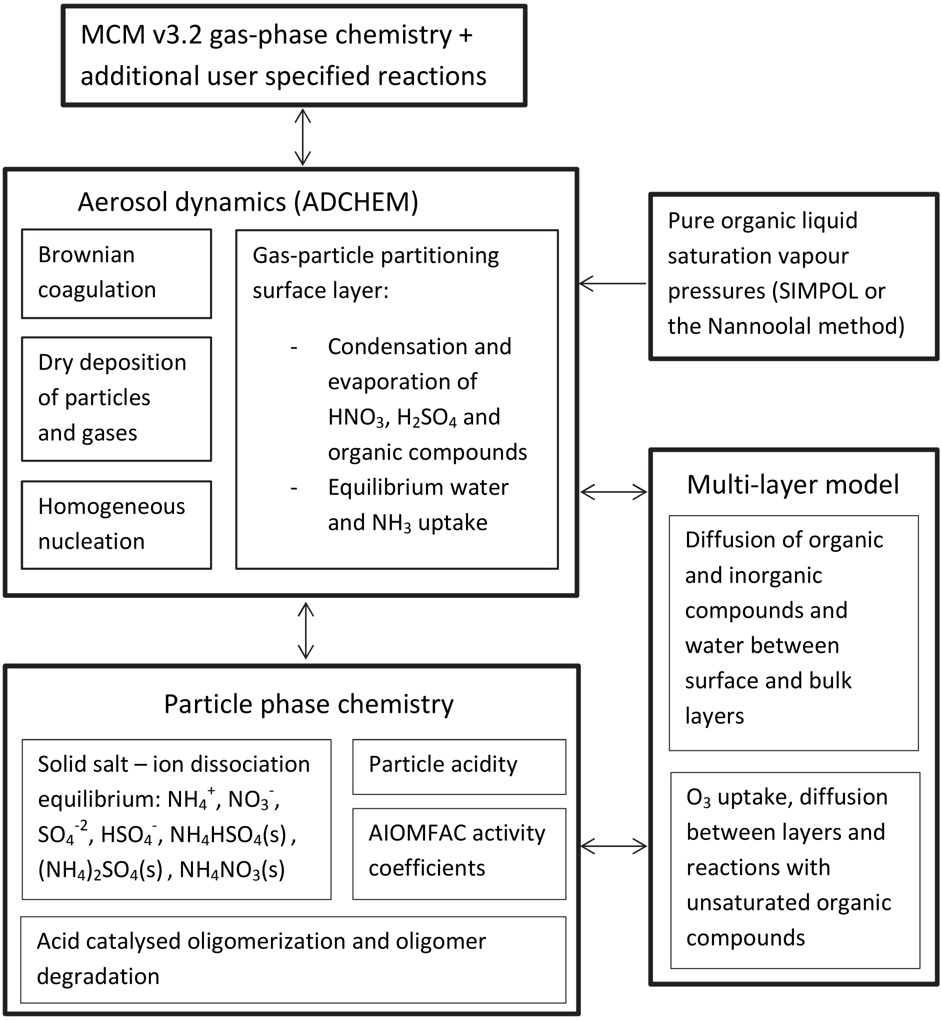

Figure 1. Schematic picture of the ADCHAM model structure.

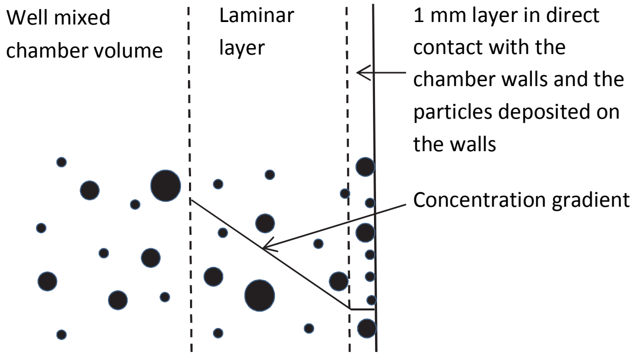

Figure 2. Schematic figure which illustrates how ADCHAM treat the diffusion limited mass transfer of gas phase compounds across a laminar layer next to the chamber walls. The thin (1 mm thick) air layer next to the chamber walls is treated as a separate volume which exchange gas phase compounds with the well mixed chamber and the walls + wall deposited particles.

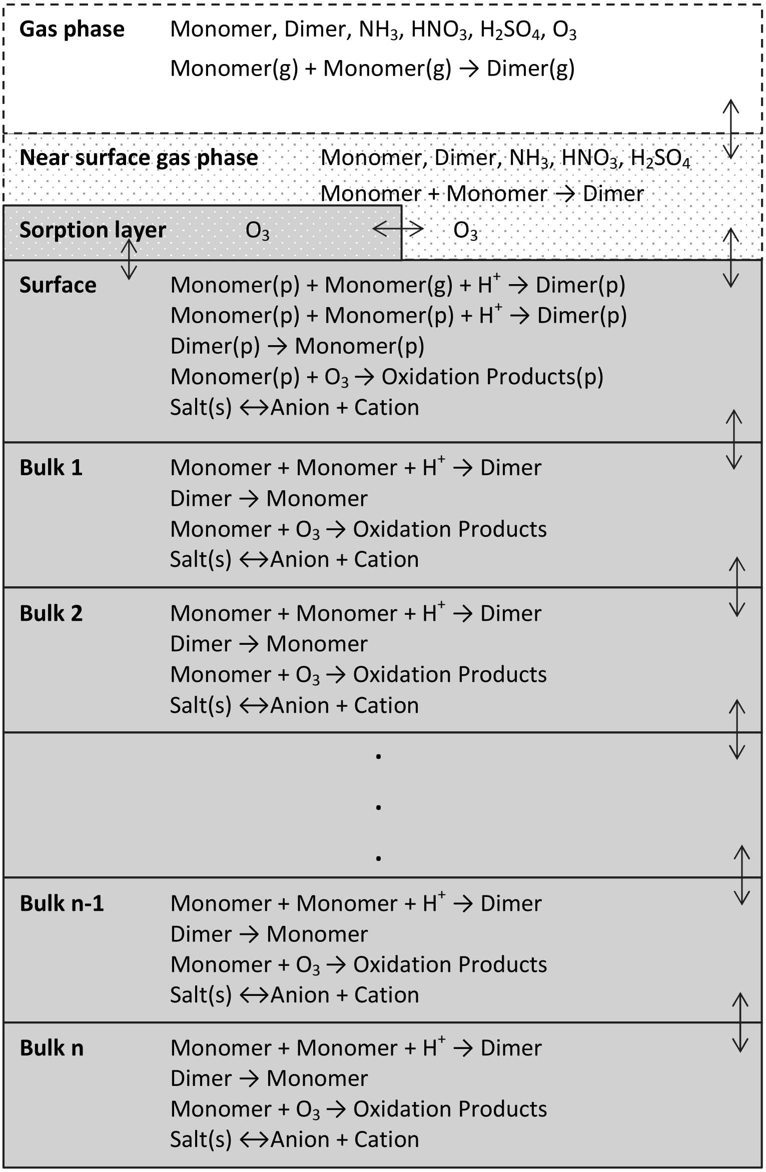

Figure 3. Schematic picture which illustrates the model structure and processes included in the kinetic multilayer model in ADCHAM.

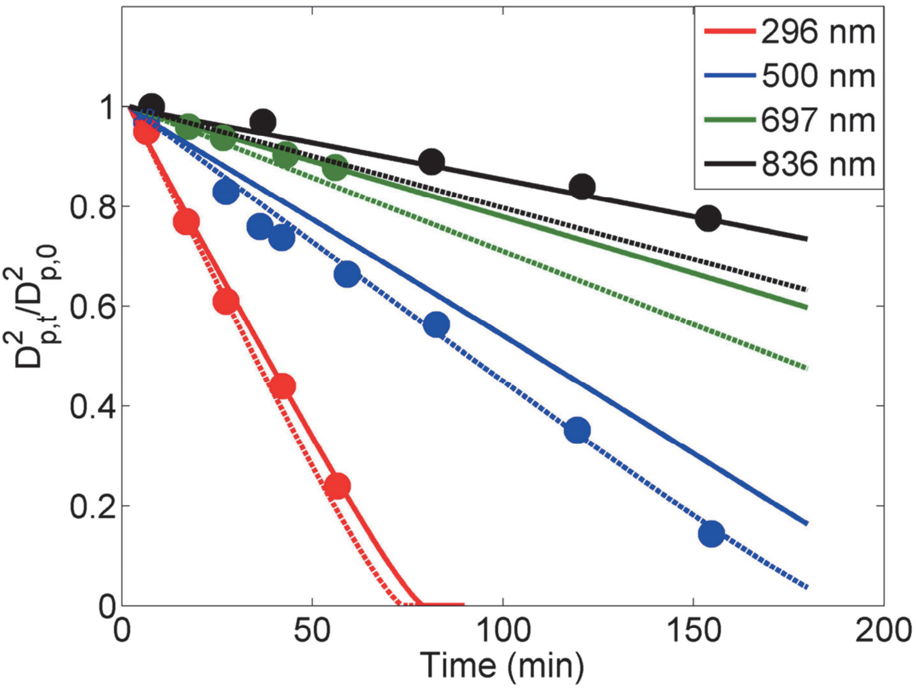

Figure 4. Comparison of measured (dots) (approximate values taken from Vaden et al., 2011) and modelled (lines) evaporation loss rates of DOP particles of different sizes. All model simulations were performed with unity mass accommodation coefficient and a diffusion coefficient of 1.5×10^{-2} cm^2 s^{-1} calculated with Eq. 30. Solid lines show the model simulations with a 3 cm thick laminar layer adjacent to the charcoal and dashed lines are for simulations with a 0.1 cm thick laminar layer. The values on the y-axis is the ratio between the squared particle diameter at time t ($D_{p,t}$) and squared initial particle diameter ($D_{p,0}$).

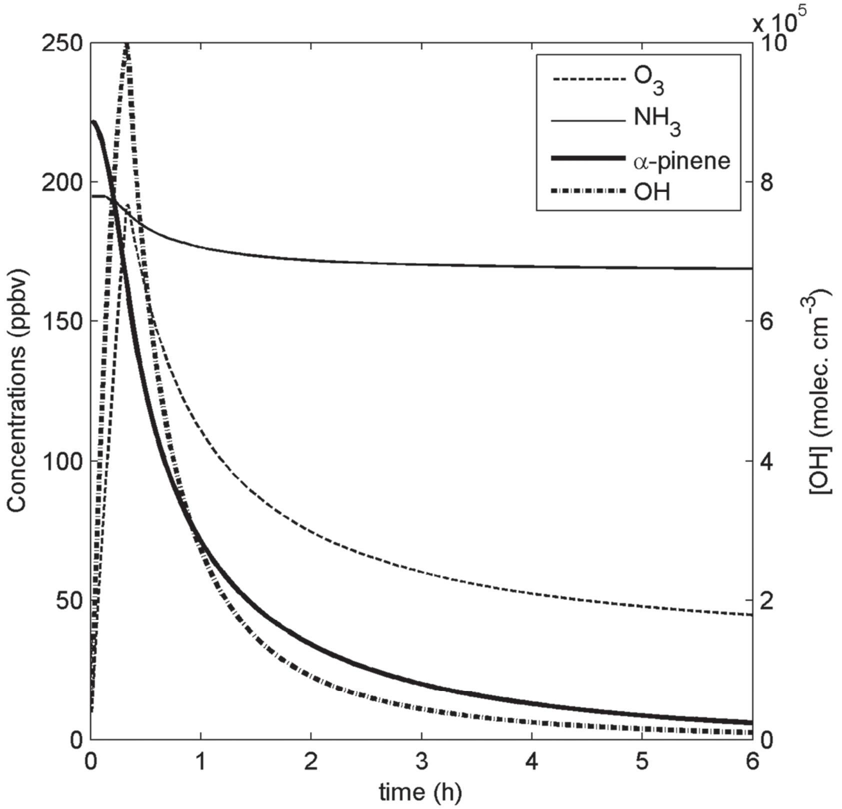

Figure 5. Modelled NH_3(g), O_3(g), α-pinene(g) and OH(g) concentrations for the α-pinene oxidation experiments by Na et al. (2007).

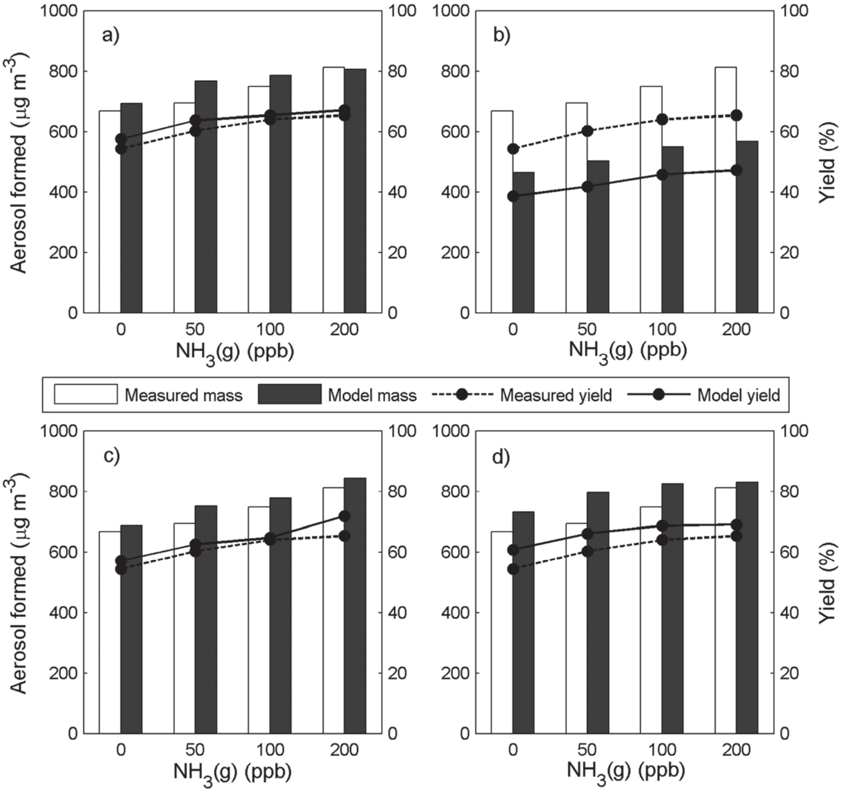

Figure 6. Comparison of modelled and measured SOA mass and mass yields at different initial levels of $NH_3(g)$. In Fig. a) the model results are from simulations with vapour pressures from SIMPOL, activity coefficients from AIOMFAC and very slow mixing between the particle layers (base case), in Fig. b) the results are from simulations with vapour pressures from Nannoolal et al. (2008), activity coefficients from AIOMFAC and very slow mixing between particle layers, in Fig. c) the results are from simulations with vapour pressures from SIMPOL, unity activity coefficients (ideal solution) and very slow mixing between the particle layers, and in Fig. d) the model results are from simulations with vapour pressures from SIMPOL, activity coefficients from AIOMFAC and semi-solid less viscous particles with $D_{0,monomer,SOA}=10^{-15}$ cm^2 s^{-1}, $D_{0,ammonium}=10^{-13}$ cm^2 s^{-1} and $D_{0,NH4RCOO}=0$ cm^2 s^{-1}.

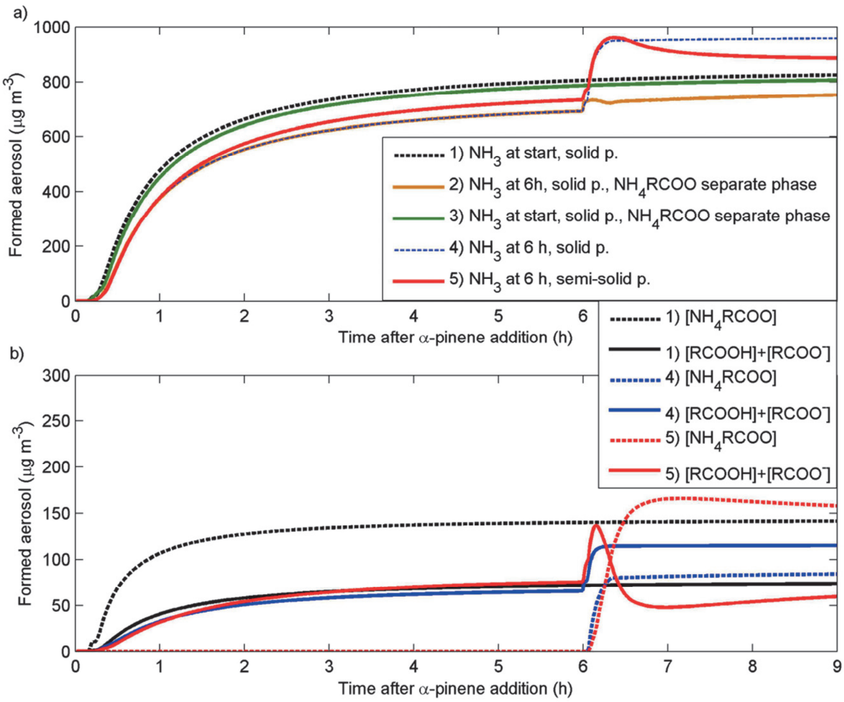

Figure 7. Modelled SOA mass formation for α-pinene – O_3 – NH_3 – CO experiments with 200 ppb NH_3 added at the start or after 6 hours of ageing. For all simulations SIMPOL was used to estimate the vapour pressures of the organic compounds. The SOA particles were either treated as completely solid (no mixing between particle layers) (simulation 1-4) or semi-solid with $D_{0,monomer,SOA}=10^{-15}$ cm^2 s^{-1}, $D_{0,ammonium}=10^{-13}$ cm^2 s^{-1} and $D_{0,NH4RCOO}=0$ cm^2 s^{-1} (simulation 5). For simulation 2 and 3 we assume that the NH_4RCOO salts form a separate phase which other organic compounds cannot dissolved into.

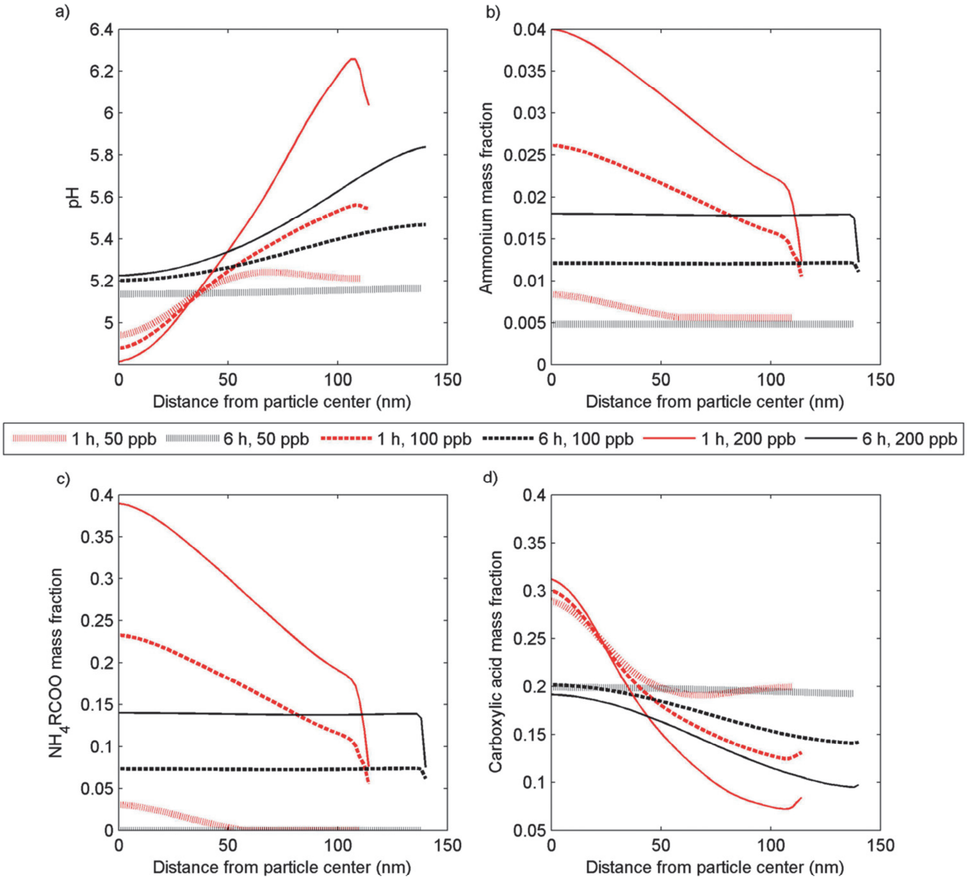

Figure 8. Modelled a) pH, b) Ammonium (NH_4^+ + NH_3(l) + NH_4 in NH_4RCOO) mass fractions, c) NH_4RCOO mass fractions and d) Carboxylic acid (COOH + COO^-) mass fractions at different distances from the particle core, for α-pinene SOA particles with a diameter of approximately 240 nm after 1 hour and 280 nm after 6 hours of ageing. The model results are from three different simulations with an initial [NH_3(g)] of 50, 100 or 200 ppb. The SOA particles were assumed to be semi-solid with $D_{0,monomer,SOA}=10^{-15}$ cm^2 s^{-1}, $D_{0,ammonium}=10^{-13}$ cm^2 s^{-1} and $D_{0,NH4RCOO}=0$ cm^2 s^{-1}.

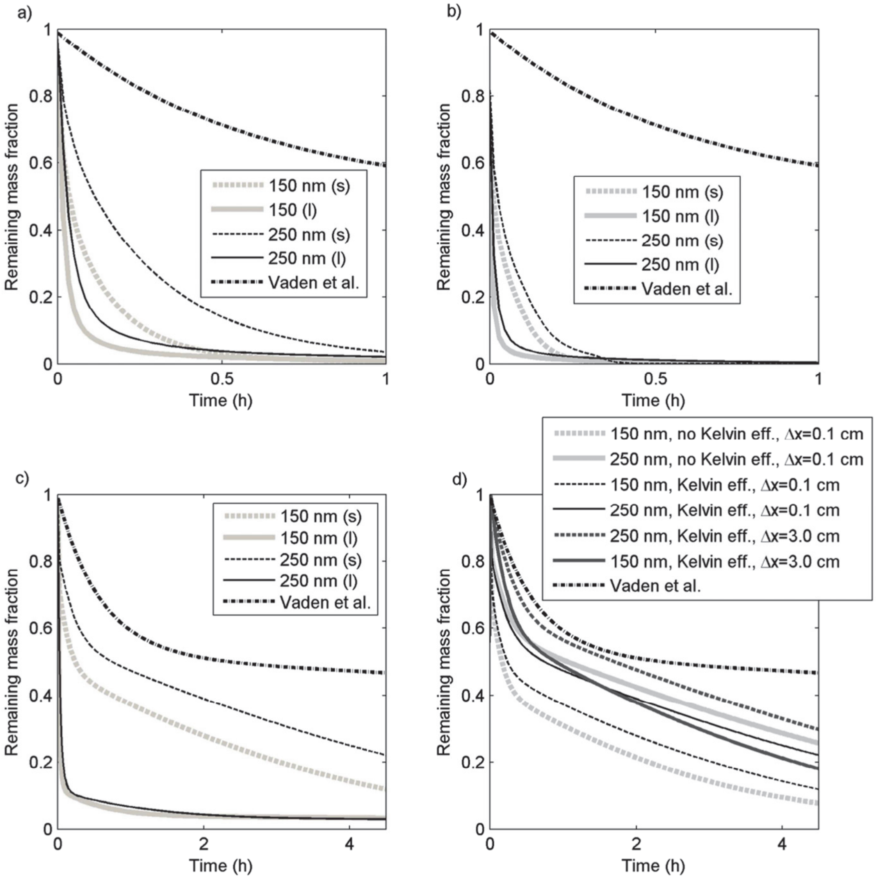

Figure 9. Modelled and measured evaporation rates of fresh α-pinene SOA particles. The measured evaporation rates are from Vaden et al. (2011). In Fig. 9a the model results are from SOA particles with volatility according to the VBS parameterization from Pathak et al. (2007), in Fig. 9b the model results are from simulations when the vapour pressures of the MCMv3.2 compounds were estimated with SIMPOL and in Fig. 9c-d the vapour pressures were estimated with the Nannoolal method. Fig. 9a-c shows the evaporation loss rates of particles with a diameter of 150 and 250 nm, when either treated as liquid (l) or solid (s) like SOA (no diffusion between the particle layers). In Fig. 9d the results are from simulations where the particles are assumed to be solid, with or without Kelvin effect and with a laminar layer (Δx) of 0.1 or 3.0 cm adjacent to the charcoal denuder in the evaporation chamber.

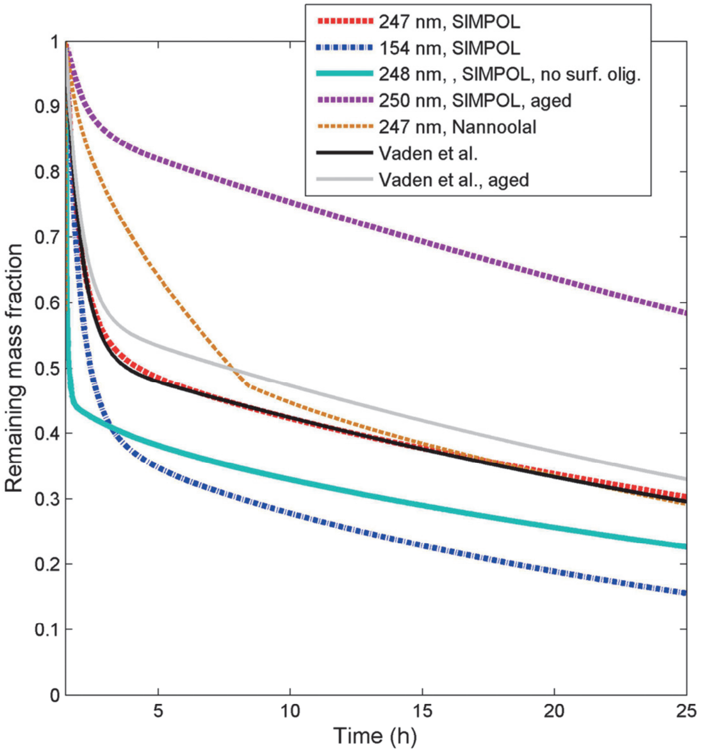

Figure 10. Modelled and measured (Vaden et al., 2011) evaporation of α-pinene SOA particles. For the model simulations we considered three different bulk phase oligomerization mechanisms: peroxyhemiacetal formation (R1a), hemiacetal formation (R3) and ester formation (R4) (k_f = $1.2\text{x}10^{-27}$ cm^3 molecules^{-1} and k_d = 1/3.2 h^{-1}). We also considered surface layer oligomers formed by the reactive uptake of adsorbed pinonaldehyde (R1b, R2b and Eq. 32) (k_f = $3\text{x}10^{-15}$ cm^3 molecules^{-1} k_d = 3/2 h^{-1}). SOA was treated as semi-solid and the oligomer SOA as solid non mixing material ($D_{0,\text{monomer}}$=$5\text{x}10^{-17}$ cm^2 s^{-1}, $D_{0,dimer}$ =0 cm^2 s^{-1}). The figure shows the modelled remaining particle mass fraction for particles with an initial diameter of 154 or ~250 nm, respectively. The results are from simulations with the SIMPOL or Nannoolal vapour pressure method, fresh or aged SOA particles, and with or without surface layer oligomer formation by the reactive uptake of adsorbed pinonaldehyde.

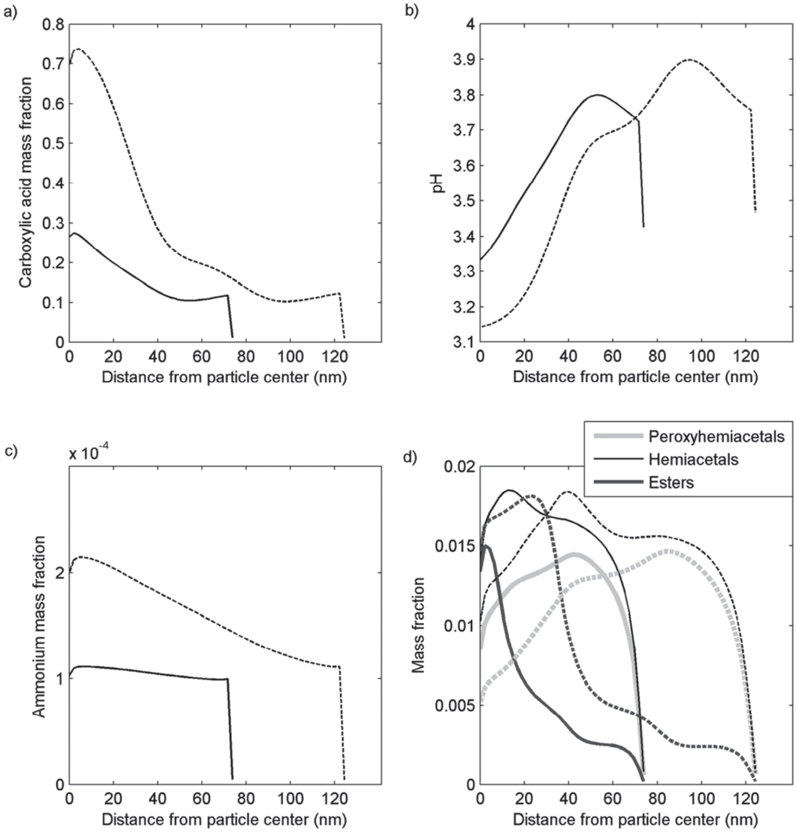

Figure 11. Modelled α-pinene SOA single particle composition, as a function of the distance from the particle centre. The results are from fresh SOA particles. We used an initial NH_3(g) concentration of 100 ppt, a SOA monomer diffusion coefficient of $5x10^{-17}$ cm^2 s^{-1} and an ammonium diffusion coefficient of $2x10^{-15}$ cm^2 s^{-1}. Three different bulk phase oligomerization mechanisms were considered: peroxyhemiacetal (R1a), hemiacetal (R3) and ester formation (R4) ($k_f = 1.2x10^{-27}$ cm^3 $molecules^{-1}$ and $k_d = 1/3.2$ h^{-1}). We also considered surface layer oligomers formed by the reactive uptake of adsorbed pinonaldehyde (R1b, R2b and Eq. 32) ($k_f = 3x10^{-15}$ cm^3 $molecules^{-1}$ and $k_d = 3/2$ h^{-1}). The chemical composition is given for two particle sizes (D_p≈150 (solid lines) and 250 nm (dashed lines)). Figure a) shows the modelled carboxylic acids mass fractions, b) the pH, c) the ammonium mass fraction and d) the different bulk phase oligomer mass fractions.

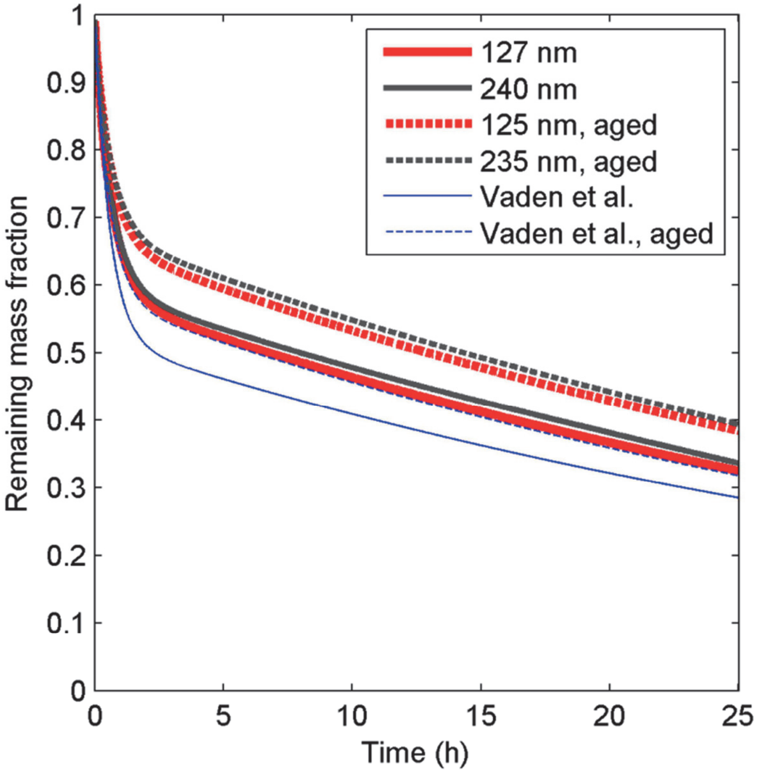

Figure 12. Modelled and measured (Vaden et al., 2011) evaporation loss rates for semi-solid particles ($D_{0,monomer}$=5x10^{-17} cm^2 s^{-1} and $D_{oligomer}$=0 cm^2 s^{-1}). In the model we included oligomerization by reactive uptake of pinonaldehyde in the particle surface layer (R1b, R2b and Eq. 32) (k_f = 3x10^{-15} cm^3 molecules^{-1} and k_d = 3/2 h^{-1}) and bulk phase oligomerization between C922OOH and C921OOH (k_f = 10^{-23} cm^3 molecules^{-1} and k_d = 1/18 h^{-1}).

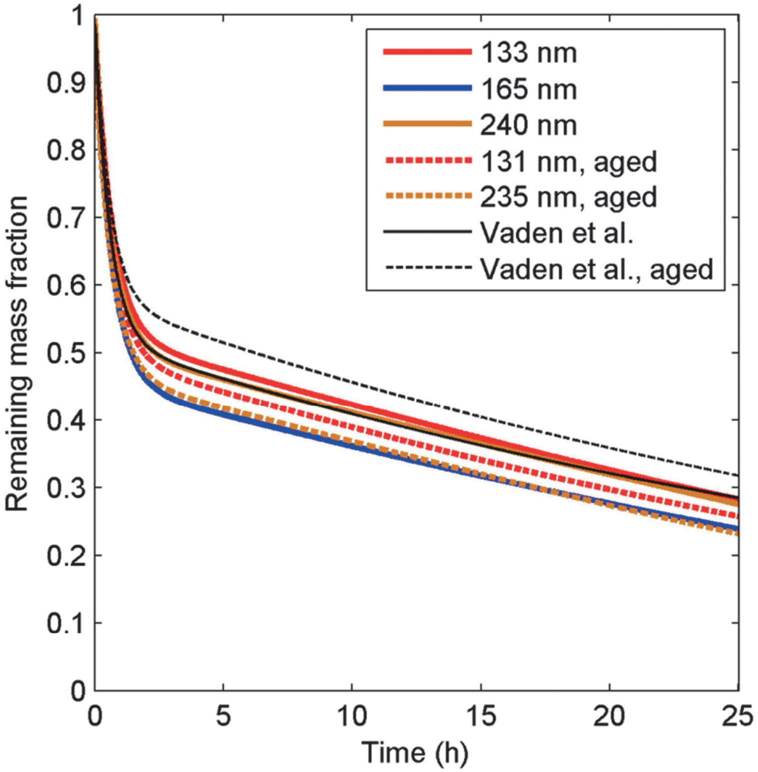

Figure 13. Modelled and measured (Vaden et al., 2011) evaporation loss rates for semi-solid particles ($D_{0,monomer}$=5x10^{-17} cm^2 s^{-1} and $D_{oligomer}$=0 cm^2 s^{-1}). For the simulations we considered oligomerization by reactive uptake of pinonaldehyde in the particle surface layer (R1b, R2b and Eq. 32) (k_f = 3x10^{-15} cm^3 molecules^{-1} and k_d = 3/2 h^{-1}) and condensation of ROOR type oligomers from the gas phase (f_{ROOR} = 0.4 %, k_d = 1/36 h^{-1}).

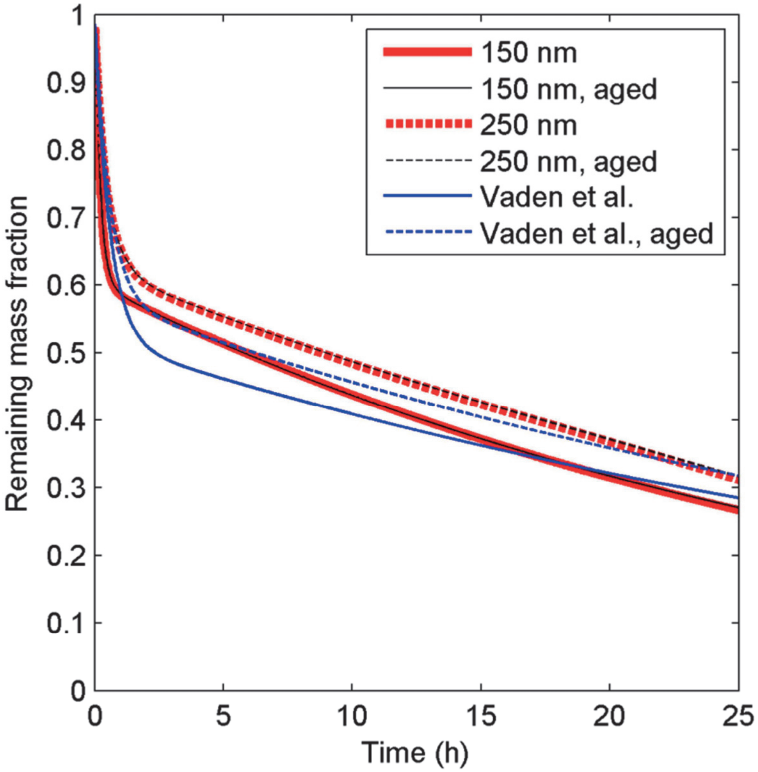

Figure 14. Modelled and measured (Vaden et al., 2011) evaporation losses for H3 (Sect. 3.3.3). The results are given both for fresh and aged particles with a diameter of ~150 nm and ~250 nm, respectively.

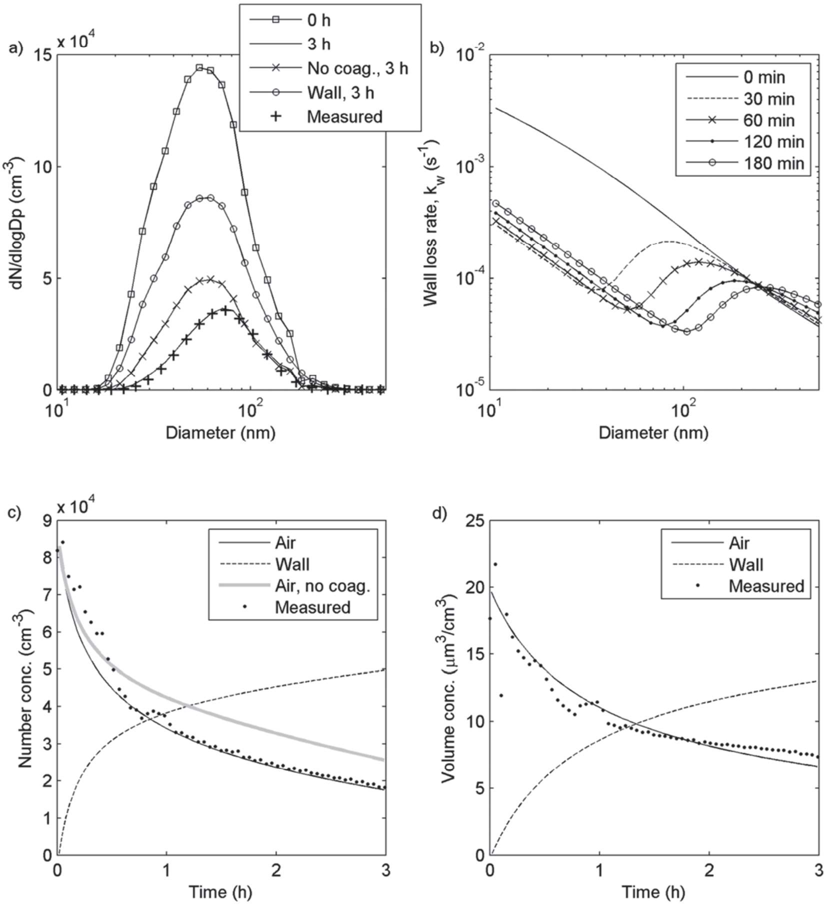

Figure 15. Modelled dry deposition and coagulation losses of $(NH_4)_2SO_4$ seed aerosol particles in the Lund University 6 m^3 Teflon chamber. We used a friction velocity of 0.05 m/s and a mean electrical field strength of 50 V cm^{-1}. The chamber volume loss rate was set to 0.8 m^3 h^{-1}. The model results gives both the particle concentrations in the air (with or without coagulation) and on the particle walls. Figure a) shows the modelled and measured particle number size distributions, b) effective wall loss rates (modelled), c) number concentration and d) volume concentration.

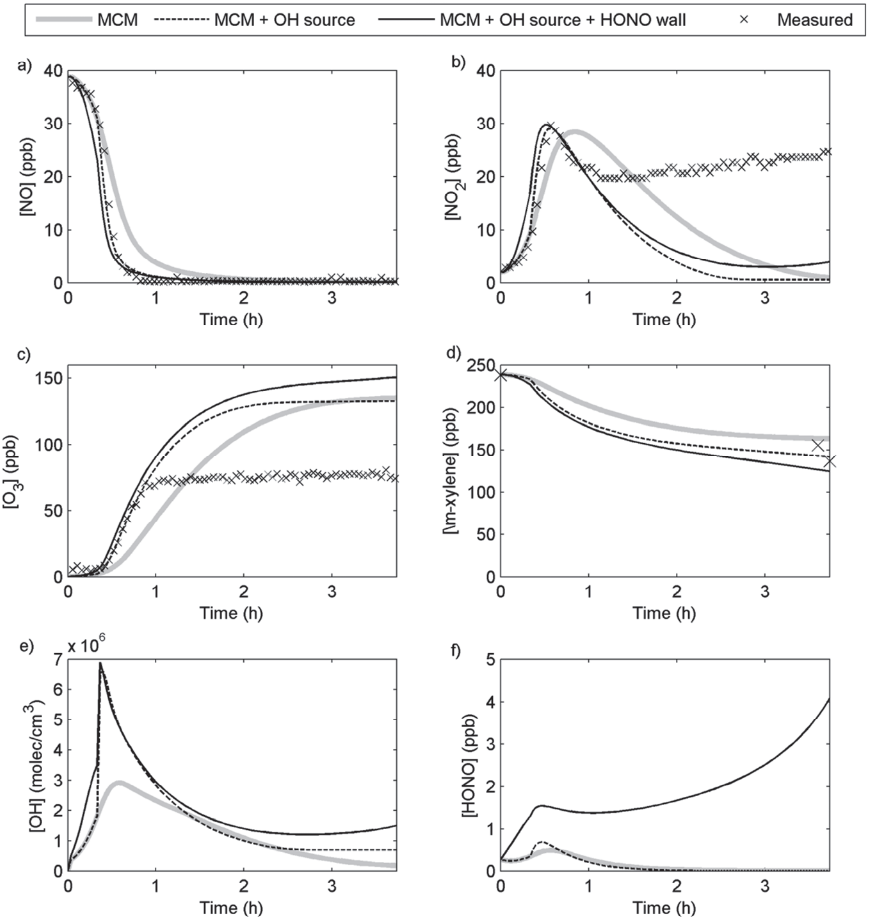

Figure 16. Modelled and measured gas phase concentrations from the *m*-xylene oxidation experiment from Nordin et al. (2012). Figure 16a-d gives the modelled and measured NO, NO_2, O_3 and *m*-xylene concentration, respectively. Figure 16e-f shows the modelled OH and HONO concentrations. The model results are from simulations with: 1) the original MCMv3.2 gas phase chemistry, 2) with MCMv3.2 gas phase chemistry and an artificial OH source of 10^8 cm^3 s^{-1}, and 3) with MCMv3.2 gas phase chemistry, the artificial OH source and wall emissions of HONO.

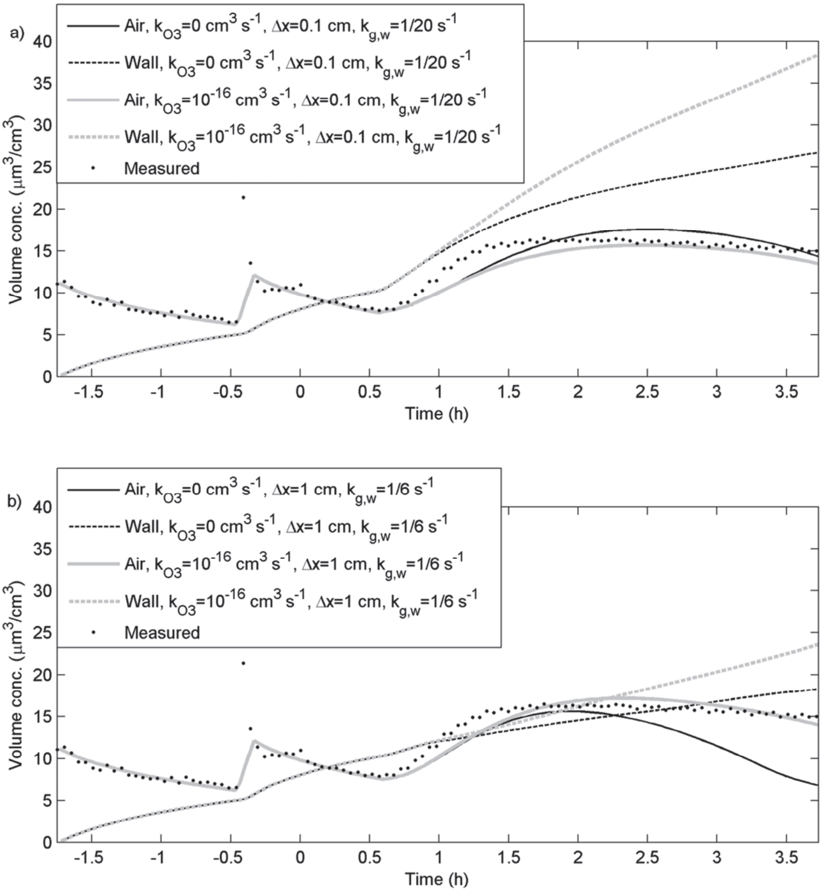

Figure 17. Modelled and measured volume concentrations of (seed aerosol + SOA coating) during the *m*-xylene oxidation experiment by Nordin et al. (2012). The model results are given both for the particles in the air and for those that have deposited on the chamber walls. The results in (a) are from simulations with a laminar layer width (Δx) of 0.1 cm adjacent to the chamber walls and a first order loss rate from the near wall gas phase to the walls ($k_{g,w}$) of 1/20 s^{-1}. The results in (b) are from simulations with a Δx of 1.0 cm and a $k_{g,w}$ of 1/6 s^{-1}. The figures show both the results from simulations without or with heterogeneous reactions between O_3 and unsaturated organic compounds ($k_{O_3}=10^{-16}$ cm^{-3} s^{-1} and $D_{0,O_3}=10^{-8}$ cm^2 s^{-1}).

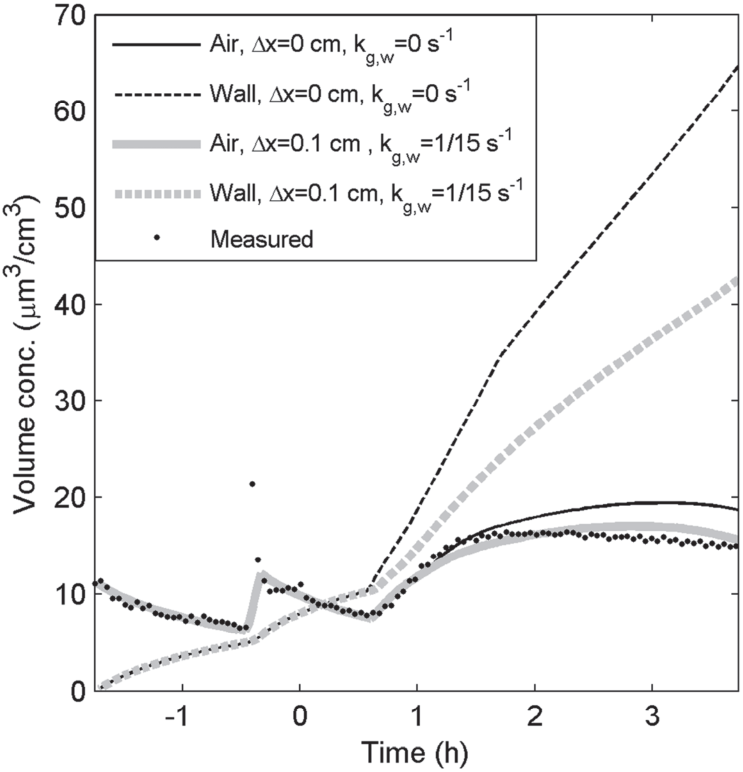

Figure 18. Modelled and measured volume concentrations (seed aerosol + SOA coating) during the *m*-xylene oxidation experiment from Nordin et al. (2012). The model results are from simulations with relative rapid ($k_f = 10^{-22}$ cm^3 s^{-1}) peroxyhemiacetal (R1) and hemiacetal (R3) formation, Δx = 0 or 0.1 cm and $k_{g,w}$ = 0 or 1/15 s^{-1}. The model results are given both for the particles in the air and the particles deposited on the chamber walls.

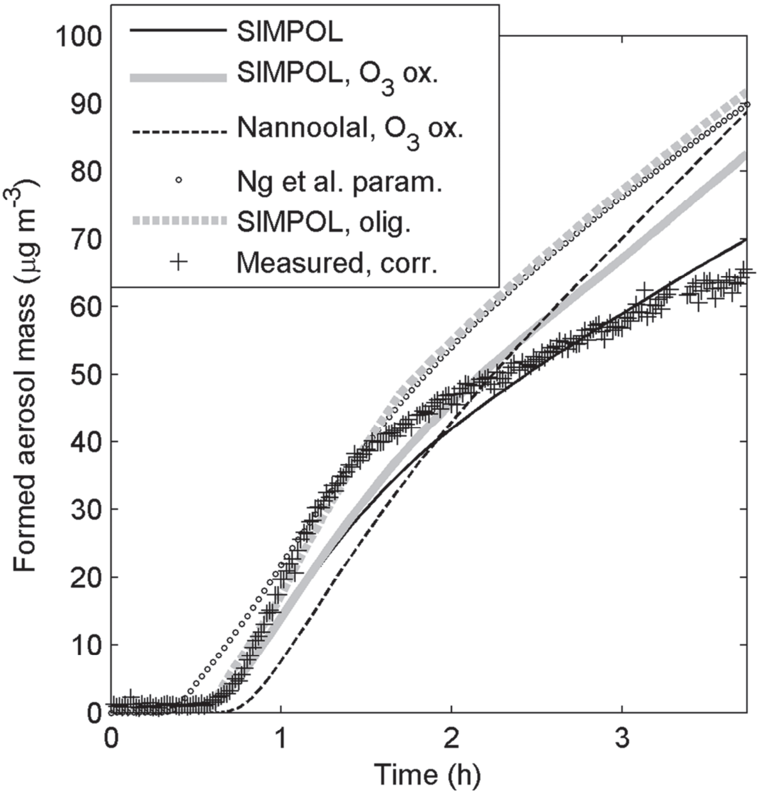

Figure 19. Modelled and measured (wall loss corrected) SOA mass during the *m*-xylene oxidation experiment by Nordin et al. (2012). The model results are from simulations without wall losses to the chamber walls. The simulations were performed with the SIMPOL vapour pressure method without or with heterogeneous reactions between O_3 and the unsaturated organic compounds (k_{O_3} =10^{-16} cm^{-3} s^{-1} and D_{0,O_3}=10^{-8} cm^2 s^{-1}), the Nannoolal vapour pressure method and heterogeneous reactions between O_3 and the unsaturated organic compounds, the semi-empirical parameterizations from Ng et al. (2007), and the SIMPOL vapour pressure method and peroxyhemiacetal (R1) and hemiacetal (R3) dimer formation (k_f =10^{-22} cm^3 s^{-1}).

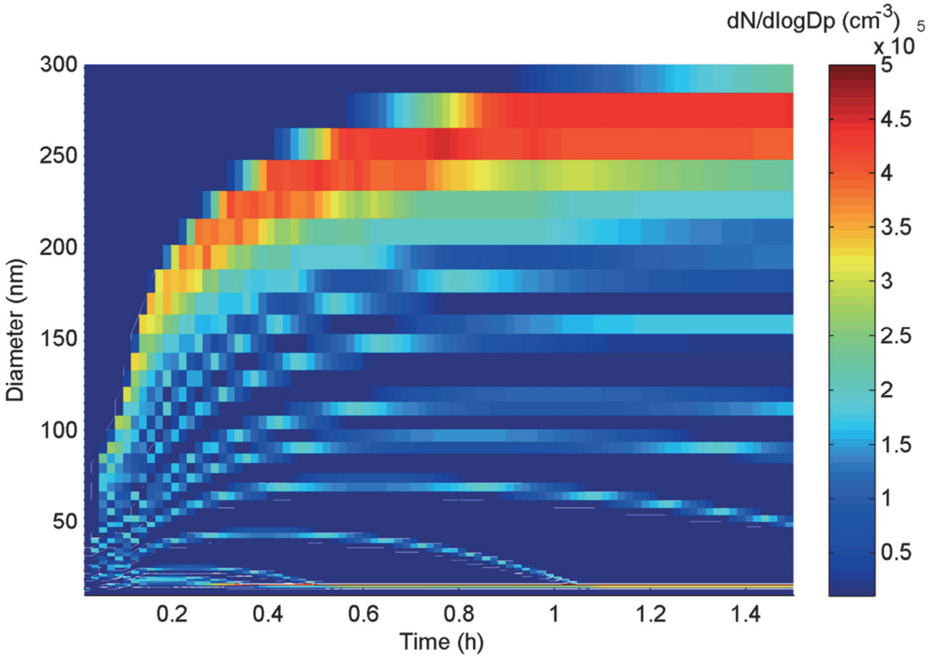

Figure S1. Modelled temporal evolution of the particle number size distribution. The results presented in this figure are from a simulation with initially 200 ppb α-pinene, 500 ppb O_3 and 250 ppm cyclohexane as OH-scavenger, semi-solid particles, no oligomerization and with pure-liquid saturation vapour pressures from the SIMPOL method. The condensational growth of the particles was modelled with the full moving method (Sect. 2.2.4). However, the particle number size distribution was converted to a fixed diameter grid for the plot.

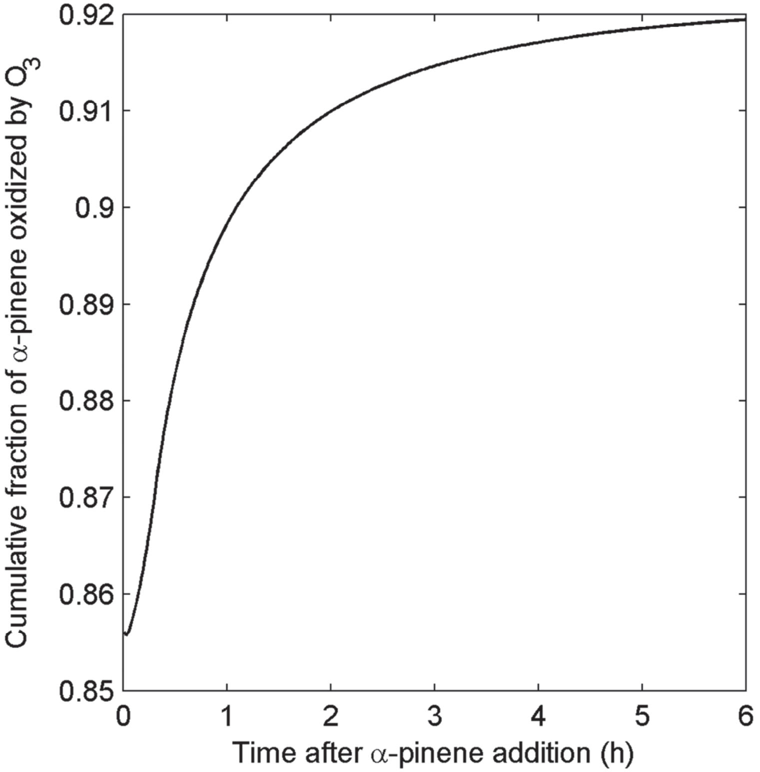

Figure S2. Cumulative fraction of α-pinene oxidized by O_3 for the modelled experiments from Na et al. (2007).

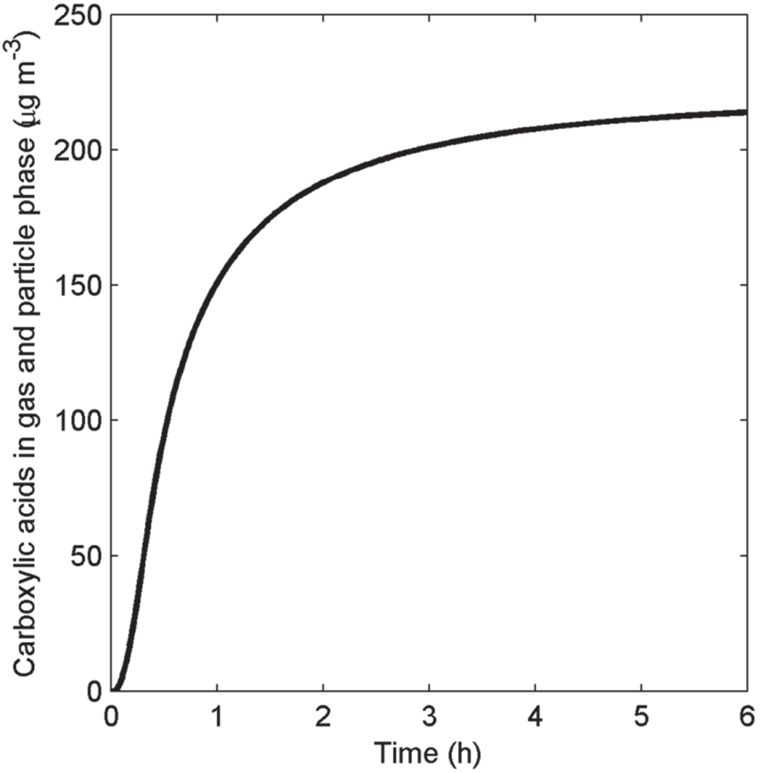

Figure S3. Modelled total carboxylic acids concentration in the gas and particle phase during the α-pinene oxidation experiments from Na et al. (2007).

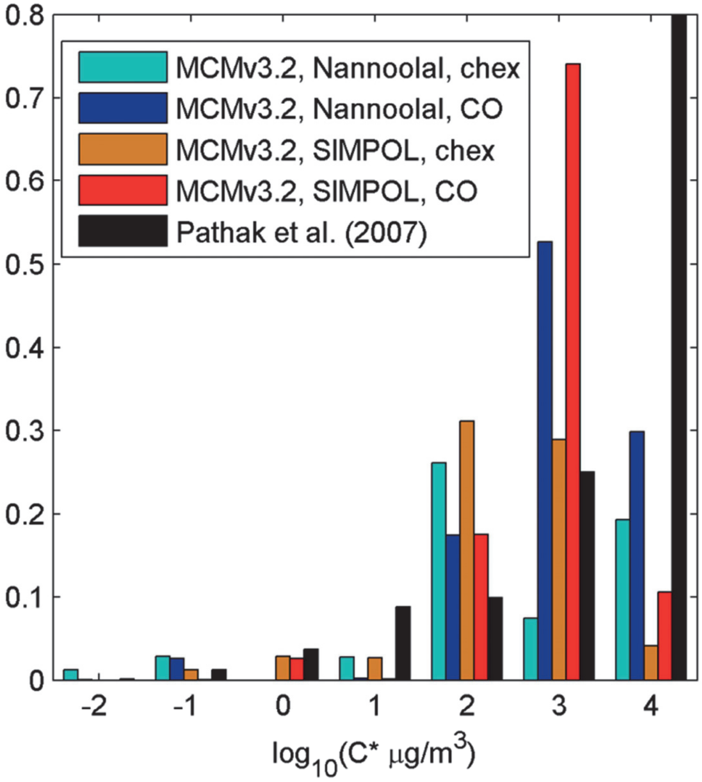

Figure S4. Derived VBS from the simulated α-pinene oxidation experiments from Na et al. (2007) with CO as OH scavenger, and from Vaden et al. (2011) with cyclohexane as OH scavenger. The VBS parameterizations were derived with the pure-liquid saturation vapour pressure method from Nannoolal et al. (2008) and SIMPOL (Pankow and Asher, 2008). Given is also the experimentally derived VBS parameterization from Pathak et al. (2007).

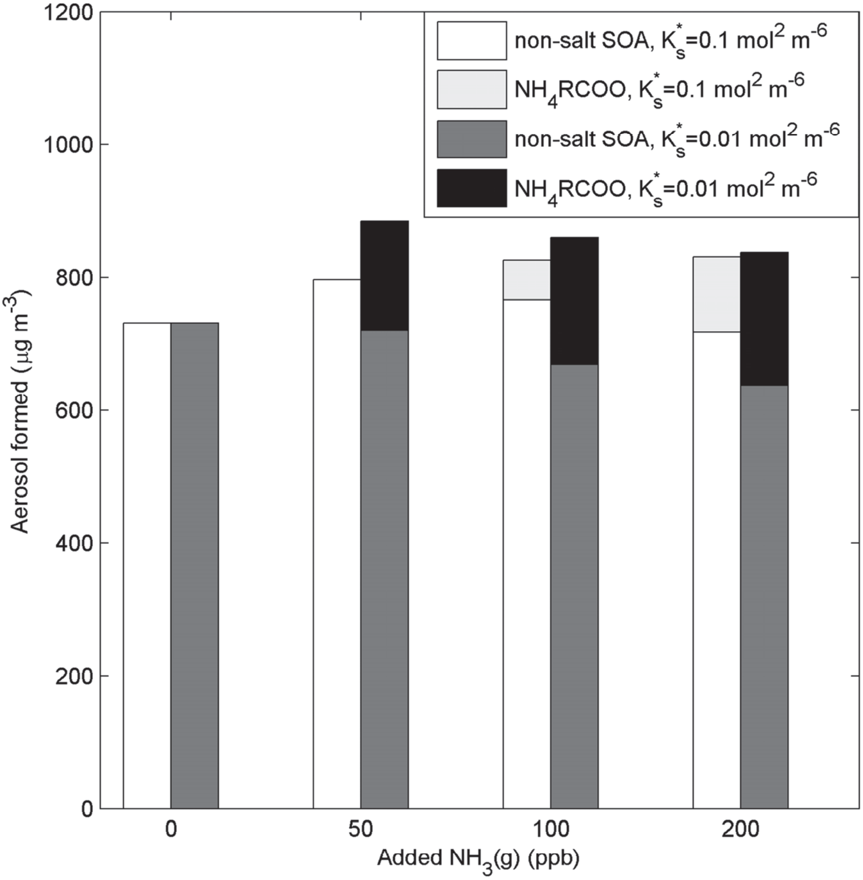

Figure S5. Comparison of modelled SOA mass formation with an effective solubility product (K_s^*) of 0.01 or 0.1 mol^2 m^{-6} (Eq. 31) for the organic salts of carboxylic acids and ammonium (NH_4RCOO). The total aerosol mass is divided into the fraction composed of non-salt SOA and NH_4RCOO.

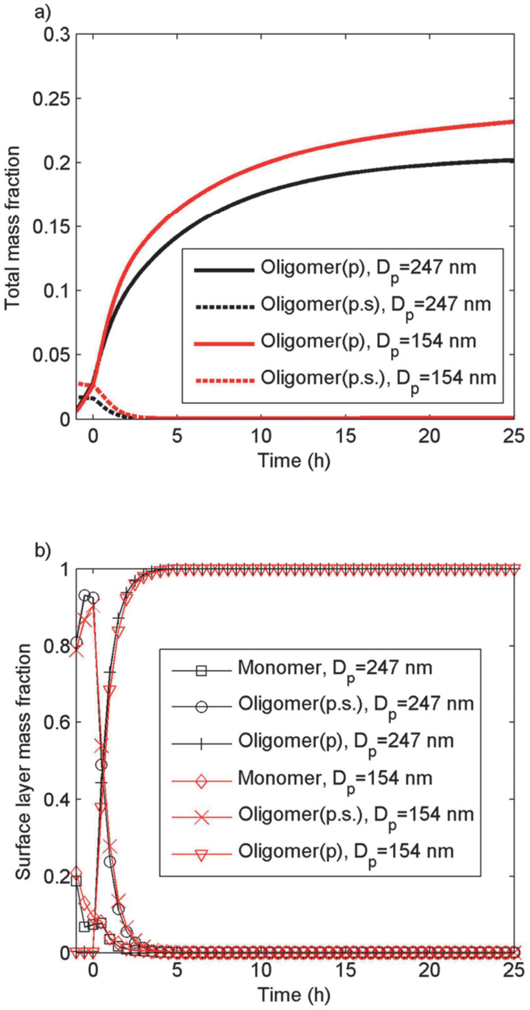

Figure S6. Modelled total oligomer mass fraction (a) and surface layer oligomer and monomer mass fraction (b) for particles with a diameter of 154 and 247 nm. The results are from a simulation with three different bulk phase oligomerization mechanisms: peroxyhemiacetal (R1a), hemiacetal (R3) and ester formation (R4) ($k_f = 1.2\text{x}10^{-27}$ cm^3 molecules^{-1} and k_d = 1/3.2 h^{-1}), and surface layer oligomer formation by the reactive uptake of adsorbed pinonaldehyde (R1b, R2b and Eq. 32) ($k_f = 3\text{x}10^{-15}$ cm^3 molecules^{-1} k_d = 3/2 h^{-1}).

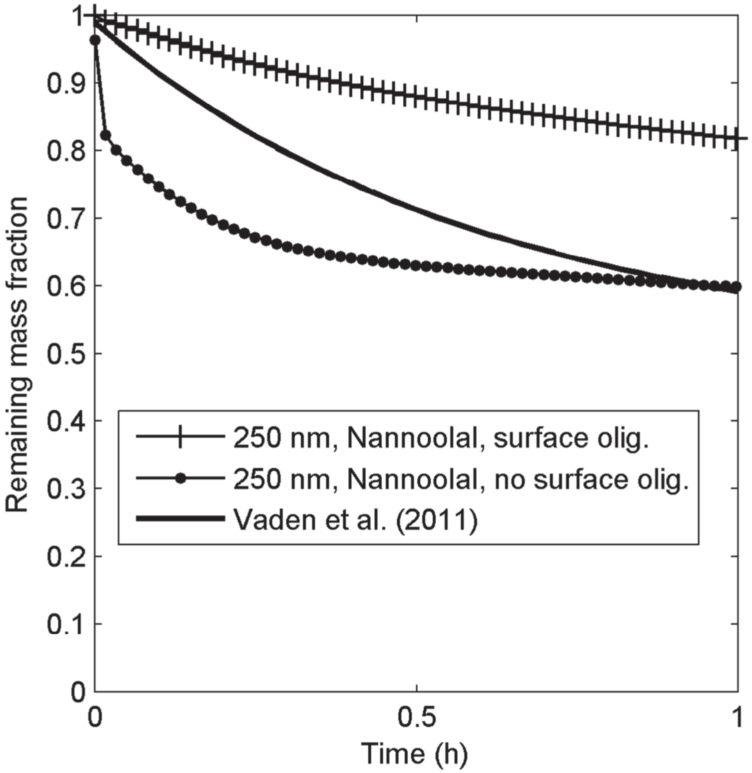

Figure S7. Modelled and measured (Vaden et al., 2011) remaining mass fractions during α-pinene SOA particle evaporation. The model results are from simulations with the vapour pressure method from Nannoolal et al. (2008) and with or without oligomer formation in the surface layer by the reactive uptake of adsorbed pinonaldehyde (R1b, R2b and Eq. 32) (k_f = 3x10^{-15} cm^3 molecules^{-1} k_d = 3/2 h^{-1}).

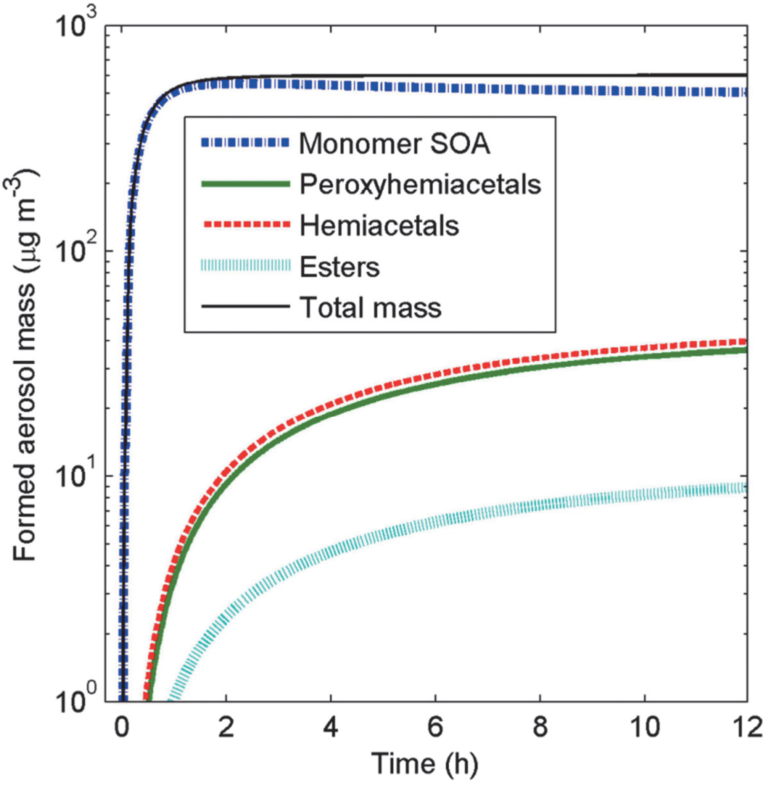

Figure S8. Modelled SOA composition when considering three different particle bulk phase oligomerization mechanisms: peroxyhemiacetal formation (R1a), hemiacetal formation (R3) and ester formation (R4) (k_f= 1.2x10^{-27} cm^3 molecules^{-1} and k_d = 1/3.2 h^{-1}).

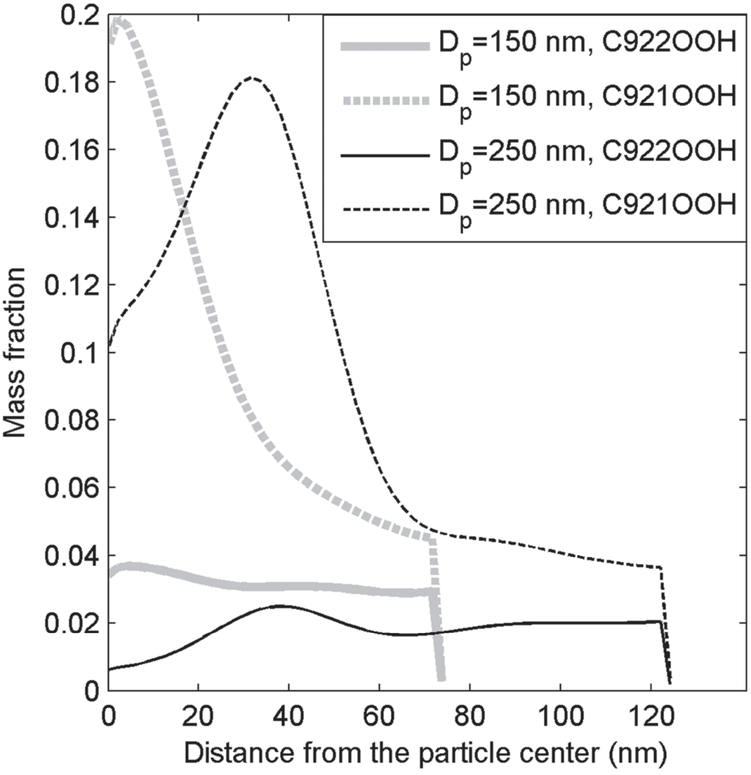

Figure S9. Modelled single particle mass fractions of two of the least volatile MCMv.3.2 α-pinene oxidation products (C922OOH and C921OOH), as a function of the distance from the particle centre (core). The results are given for two different particle sizes (D_p≈150 and 250 nm, respectively).

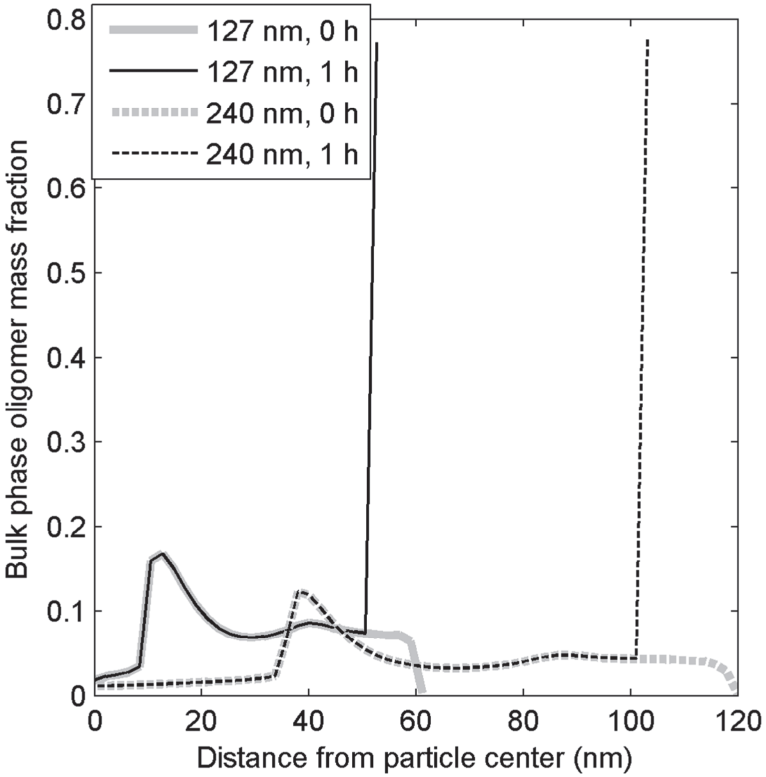

Figure S10. Modelled bulk phase oligomer mass fractions in the different particle layers at different distances from the particle centre at the start and after 1 hour of evaporation. The results are given for two particle sizes (D_p=127 and 240 nm, respectively). The oligomer SOA was assumed to be formed by a reaction between two of the least volatile MCMv.3.2 α-pinene oxidation products (C922OOH and C921OOH) ($k_f = 10^{-23}$ cm^3 molecules^{-1} and k_d = 1/18 h^{-1}).

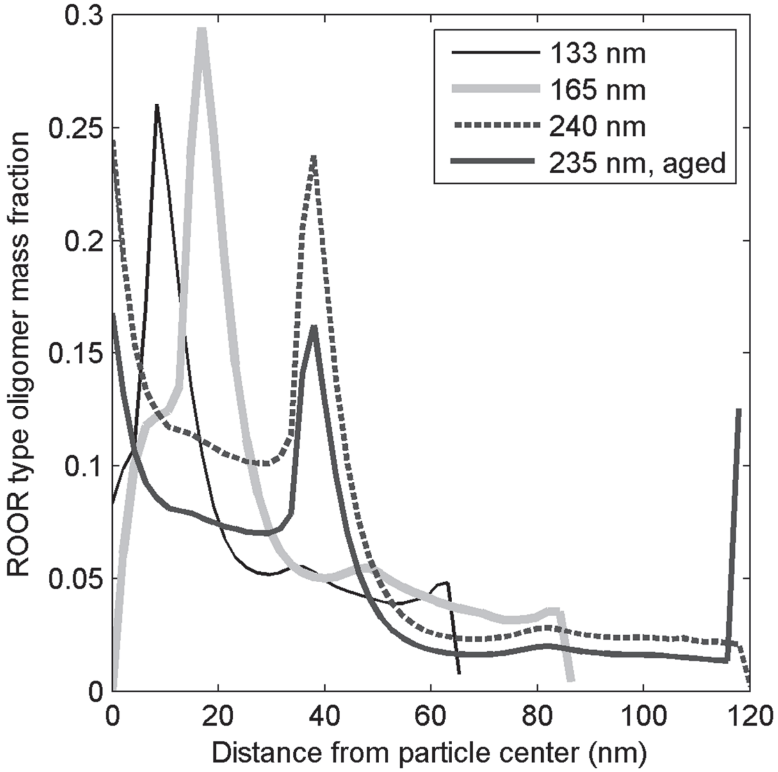

Figure S11. Modelled ROOR type oligomer mass fractions (f_{ROOR} = 0.4 %, k_d = 1/36 h^{-1}), as a function of the distance from the particle centre, in particles with different diameters. The results are given both for a fresh and an aged particle, before evaporation.

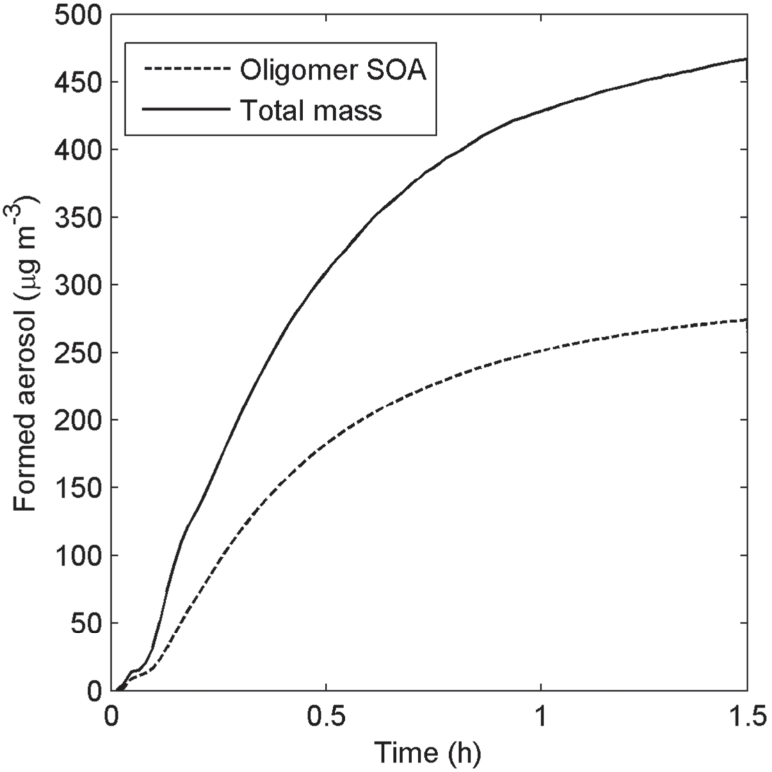

Figure S12. Modelled oligomer and total SOA mass for H3 (Sect. 3.3.3).

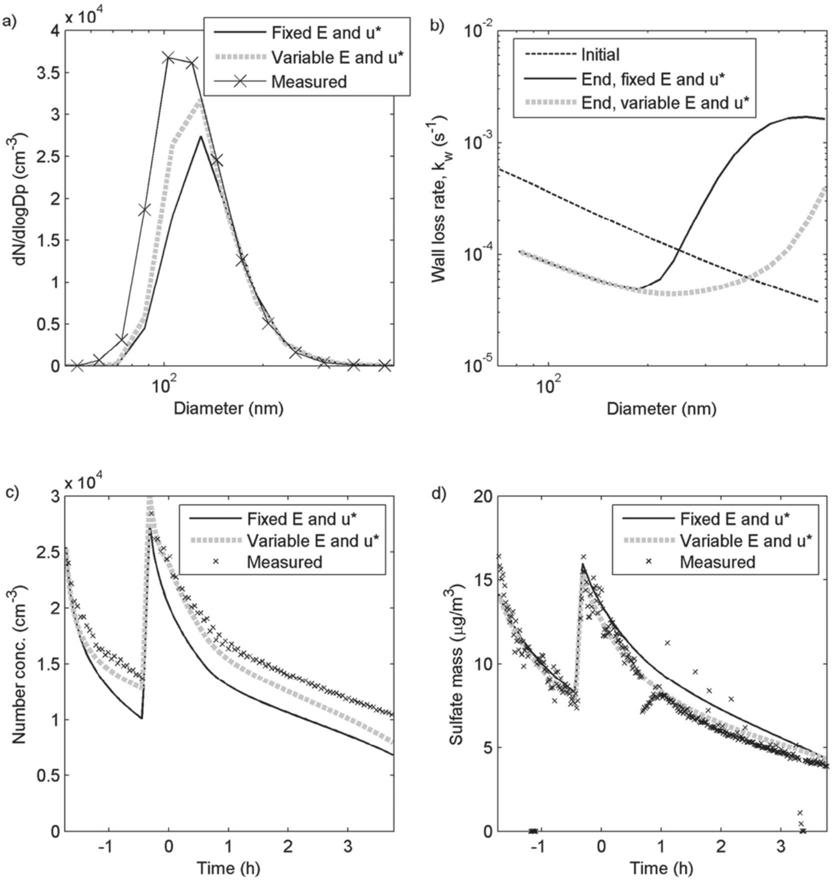

Figure S13. Modelled and measured a) particle number size distribution at the end of the *m*-xylene experiment, b) initial and final effective wall deposition loss rates (modelled), c) number concentration and d) sulphate seed aerosol mass concentration. The model results are from a simulation with a fixed $\overline{E_t}$ of 50 V cm^{-1} and a u^* of 0.05 m s^{-1} or variable $\overline{E_t}$ calculated with Eq. 33 and u^* = 0.01 m s^{-1} before the UV-lights are turned on and u^* = 0.05 m s^{-1} after the UV-lights are turned on.

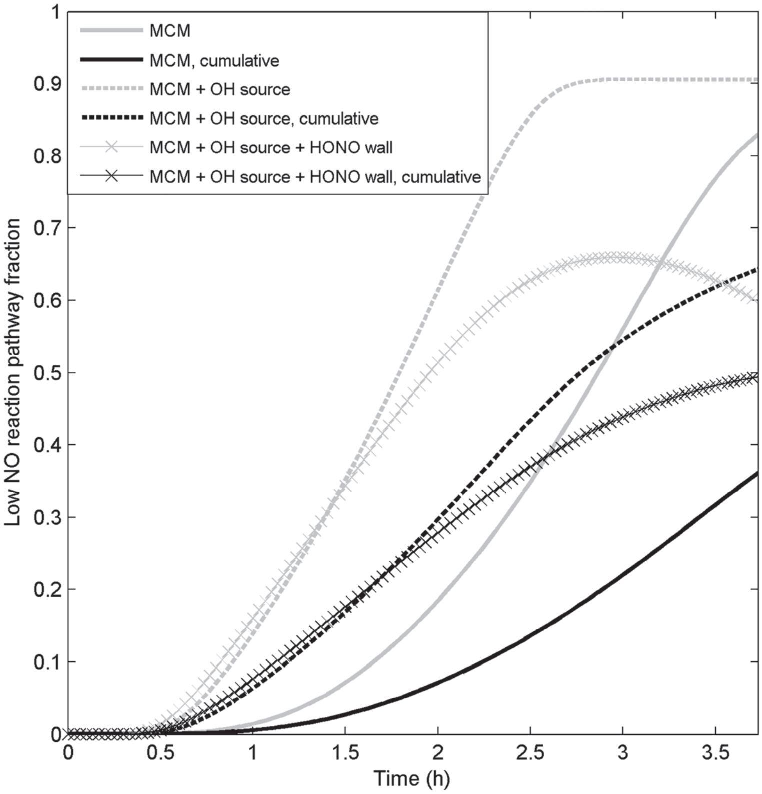

Figure S14. Modelled current time step and cumulative fraction of the *m*-xylene first generation RO_2 products that react (have reacted) with HO_2 instead of NO. The results are given for simulations with the original MCMv3.2 gas phase chemistry, with MCMv3.2 gas phase chemistry and an artificial OH source of 10^8 cm^3 s^{-1}, and with MCMv3.2 gas phase chemistry, the artificial OH source and wall emissions of HONO.

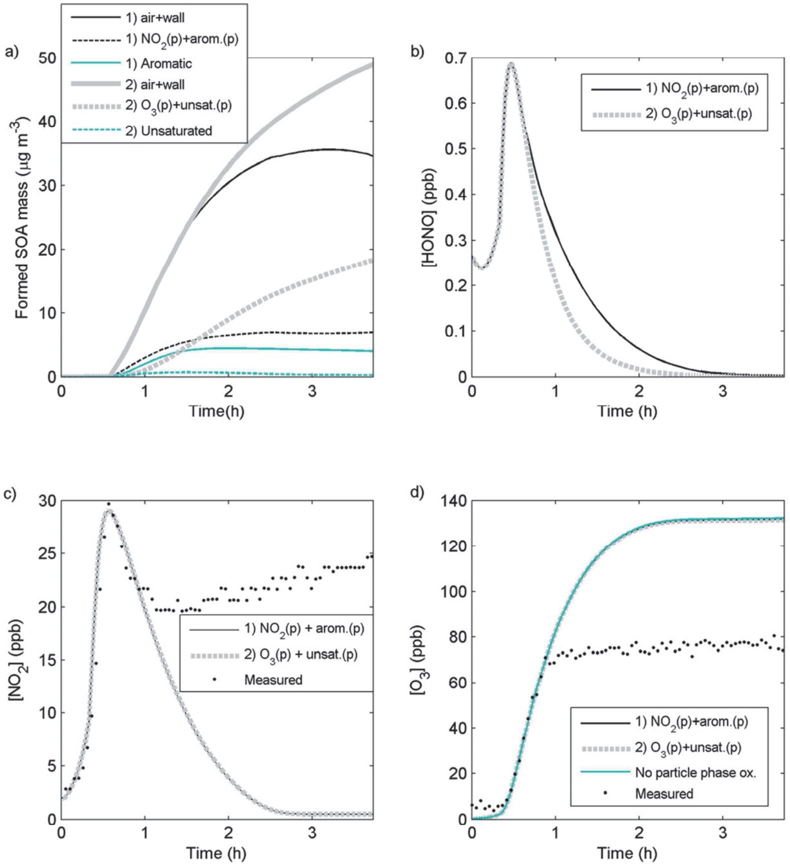

Figure S15. Results from simulations of the *m*-xylene oxidation experiment by Nordin et al. (2012) when considering 1) HONO formation from heterogeneous reactions ($k_{NO_2}=10^{-15}$ cm^{-3} s^{-1} and $D_{0,NO_2}=10^{-7}$ cm^2 s^{-1}) or 2) heterogeneous reactions of O_3 ($k_{O_3}=10^{-16}$ cm^{-3} s^{-1} and $D_{0,O_3}=10^{-7}$ cm^2 s^{-1}). For simulation Nr. 1 Fig. 15a shows the total SOA mass (air + wall), SOA mass of formed oxidation products from the reaction between the aromatic compounds and NO_2, and the remaining non reacted aromatic SOA mass. For simulation Nr. 2 Fig. 15a shows the total SOA mass, SOA mass of formed oxidation products from the heterogeneous O_3 reactions, and the remaining non reacted unsaturated organic SOA mass. Figure 15b shows the modelled HONO concentration, c) the NO_2 concentration and d) the O_3 concentration. In Figure 15d we also included the results from a simulation without heterogeneous oxidation reactions.

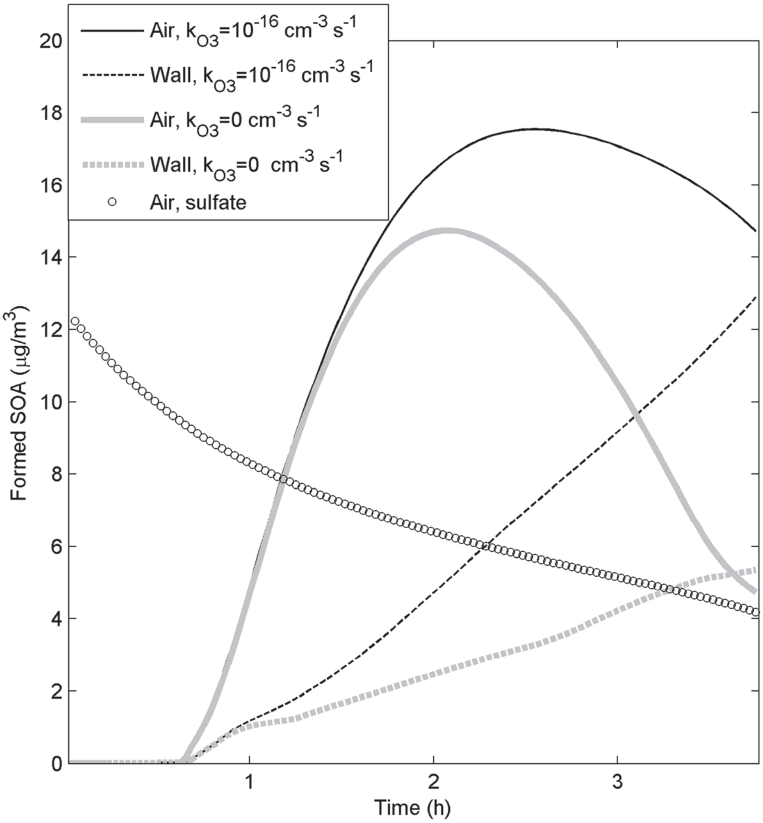

Figure S16. Modelled SOA mass formation in the air and on the wall deposited particles during the *m*-xylene oxidation experiment by Nordin et al. (2012). The results are from simulations with a laminar layer width (Δx) of 1.0 cm adjacent to the chamber walls and a first order loss rate from the near wall gas phase to the walls ($k_{g,w}$) of 1/6 s^{-1}. ADCHAM was either run without or with heterogeneous reactions between O_3 and the unsaturated organic compounds ($k_{O_3}=10^{-16}$ cm^{-3} s^{-1} and $D_{0,O_3}=10^{-8}$ cm^2 s^{-1}).

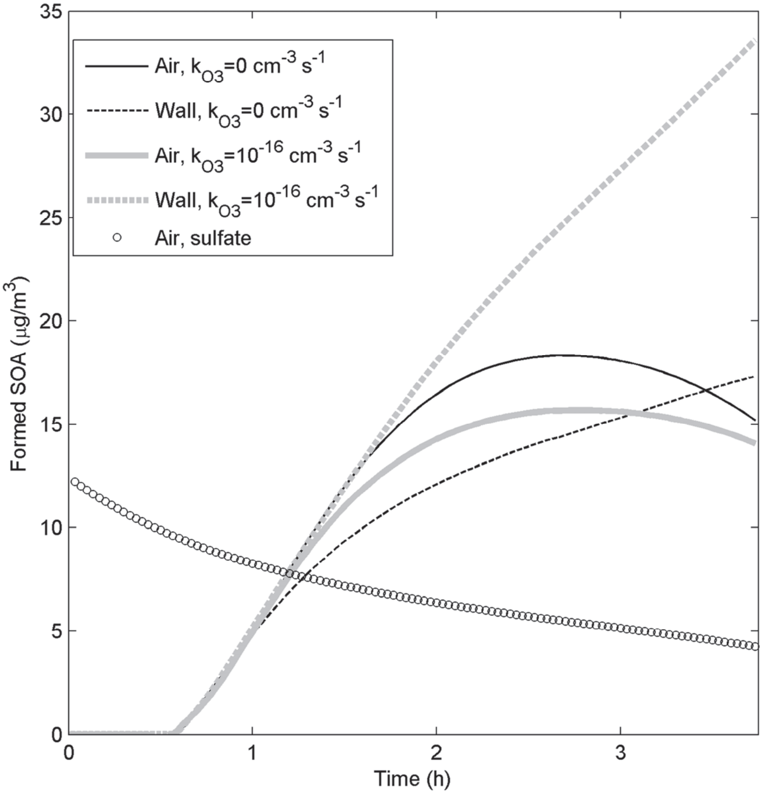

Figure S17. Modelled SOA mass formation in the air and on the wall deposited particles during the *m*-xylene oxidation experiment by Nordin et al. (2012). The results are from simulations with a laminar layer width (Δx) of 0.1 cm adjacent to the chamber walls and a first order loss rate from the near wall gas phase to the walls ($k_{g,w}$) of 1/20 s^{-1}. ADCHAM was either run without or with heterogeneous reactions between O_3 and the unsaturated organic compounds (k_{O_3} =10^{-16} cm^{-3} s^{-1} and D_{0,O_3}=10^{-8} cm^2 s^{-1}).

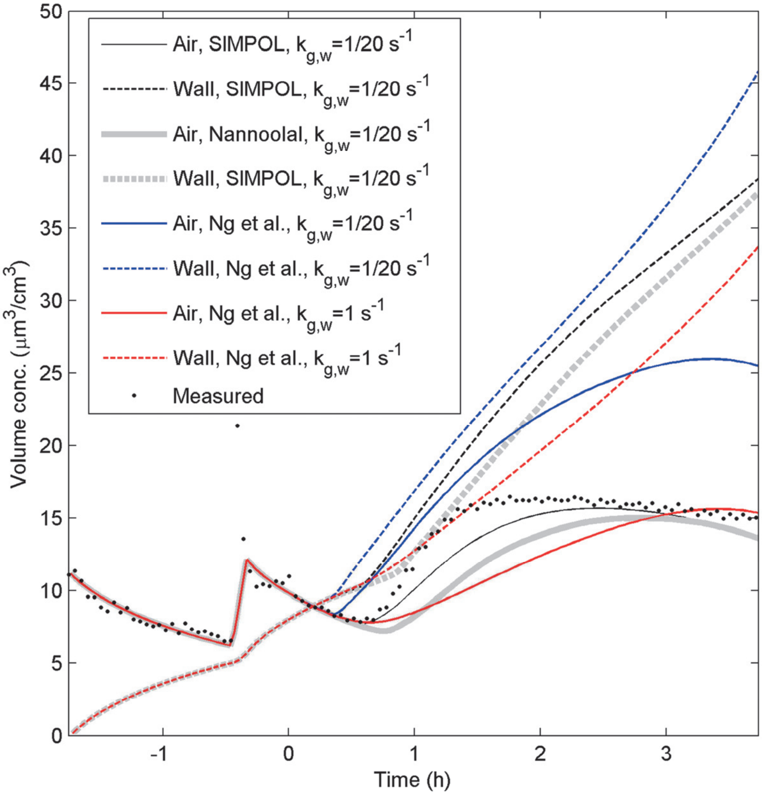

Figure S18. Modelled and measured volume concentrations (seed aerosol + SOA coating) during the *m*-xylene oxidation experiment by Nordin et al. (2012). The model results are from siumations with the SIMPOL (Pankow and Asher, 2008), Nannoolal et al. (2008) vapour pressure method or the semi-empirical parameterizations from Ng et al. (2007). The figure shows both the modelled particle volume concentrations in the air and on the walls.

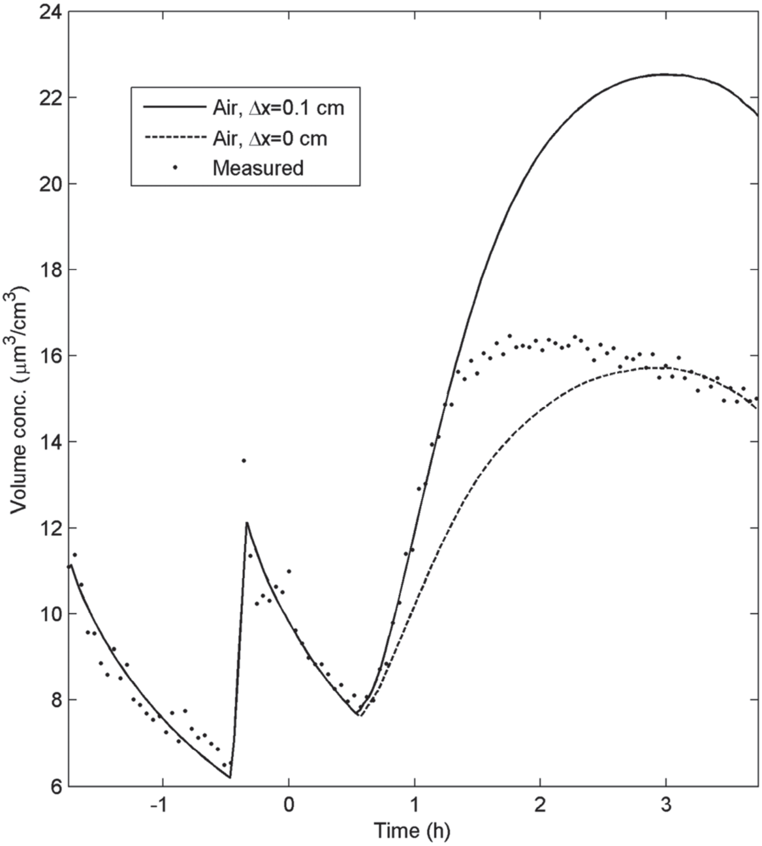

Figure S19. Modelled and measured particle volume concentrations in the air from the *m*-xylene oxidation experiment by Nordin et al. (2012). The model results are from simulations with a laminar layer of 0 or 0.1 cm adjacent to the chamber walls and without uptake of organic compounds directly onto the Teflon walls.

Paper IV

Atmos. Chem. Phys. Discuss., 12, 31725–31765, 2012
www.atmos-chem-phys-discuss.net/12/31725/2012/
doi:10.5194/acpd-12-31725-2012

Atmospheric Chemistry and Physics Discussions

Secondary organic aerosol formation from gasoline passenger vehicle emissions investigated in a smog chamber

E. Z. Nordin[1], A. C. Eriksson[2], P. Roldin[2], P. T. Nilsson[1], J. E. Carlsson[1], M. K. Kajos[3], H. Hellén[4], C. Wittbom[2], J. Rissler[1], J. Löndahl[1], E. Swietlicki[2], B. Svenningsson[2], M. Bohgard[1], M. Kulmala[2,3], M. Hallquist[5], and J. Pagels[1]

[1]Ergonomics and Aerosol Technology, Lund University, P.O. Box 118, 221 00 Lund, Sweden
[2]Division of Nuclear Physics, Lund University, P.O. Box 118, 221 00 Lund, Sweden
[3]Department of Physics, University of Helsinki, P.O. Box 64, 00014 Helsinki, Finland
[4]Finnish Meteorological Institute, P.O. Box 503, 00101 Helsinki, Finland
[5]Department of Chemistry, Atmospheric Science, University of Gothenburg,
412 96 Gothenburg, Sweden

Received: 14 November 2012 – Accepted: 28 November 2012
– Published: 11 December 2012

Correspondence to: E. Z. Nordin (erik.nordin@design.lth.se)

Published by Copernicus Publications on behalf of the European Geosciences Union.

Abstract

Gasoline vehicles have elevated emissions of volatile organic compounds during cold starts and idling and have recently been pointed out as potentially the main source of anthropogenic secondary organic aerosol (SOA) in megacities. However, there is a lack of laboratory studies to systematically investigate SOA formation in real-world exhaust. In this study, SOA formation from pure aromatic precursors, idling and cold start gasoline exhaust from one Euro II, one Euro III and one Euro IV passenger vehicles were investigated using photo-oxidation experiments in a 6 m^3 smog chamber. The experiments were carried out at atmospherically relevant organic aerosol mass concentrations. The characterization methods included a high resolution aerosol mass spectrometer and a proton transfer mass spectrometer. It was found that gasoline exhaust readily forms SOA with a signature aerosol mass spectrum similar to the oxidized organic aerosol that commonly dominates the organic aerosol mass spectra downwind urban areas. After 4 h aging the formed SOA was 1–2 orders of magnitude higher than the Primary OA emissions. The SOA mass spectrum from a relevant mixture of traditional light aromatic precursors gave $f43$ (mass fraction at $m/z = 43$) approximately two times higher than to the gasoline SOA. However O : C and H : C ratios were similar for the two cases. Classical C_6–C_9 light aromatic precursors were responsible for up to 60 % of the formed SOA, which is significantly higher than for diesel exhaust. Important candidates for additional precursors are higher order aromatic compounds such as C_{10}, C_{11} light aromatics, naphthalene and methyl-naphthalenes.

1 Introduction

The formation mechanisms, magnitude and chemical composition of secondary organic aerosol (SOA) are of importance for predicting future climate scenarios (Monks et al., 2009; Hallquist et al., 2009). SOA is formed from low vapor pressure reaction products, which originate from gas phase oxidation of volatile organic compounds

(VOCs). De Gouw and Jimenez (2009) suggested that SOA from urban sources may be the dominating source of organic aerosol globally between the 30th and 50th latitude.

Traditionally the VOCs responsible for the majority of urban SOA formation have been assumed to be light aromatic hydrocarbons, which are hydrocarbons with one benzene ring, often with one or more alkyl groups (methyl, ethyl or propyl), i.e. benzene (C_6), toluene (C_7), xylenes and ethyl benzene (C_8), C_9 and C_{10} aromatics (Odum et al., 1997).

Robinson et al. (2007) recognized intermediate volatility organic compounds (IVOCs) and semi volatility organic compounds (SVOCs) as important sources for production of ambient organic aerosol. Photo-oxidation experiments of exhaust from a diesel generator indicated that only a small fraction of the SOA formed originated from light aromatic precursors (Weitkamp et al., 2007). They also suggested that IVOCs such as long chain and branched alkanes could be responsible for a large fraction of the SOA produced from diesel exhaust. However, recent smog chamber studies suggest that the SOA formation from modern diesel vehicles with functioning oxidation catalysts is very low (Chirico et al., 2010; Samy and Zielinska, 2010).

Less attention has been paid to SOA formation from gasoline exhaust, although VOC emissions can be high during cold starts, increasing with decreasing ambient temperature. At ambient temperatures below 0 °C the VOC emissions from the startup-phase can be equivalent to thousands of driven kilometers (Weilenmann et al., 2009). This is due to fuel condensing on the inner surface of the cylinder when the engine temperature is low, causing a fuel rich incomplete combustion but also because the operation temperature of the oxidation catalyst is below its optimum range (Schifter et al., 2010). The emissions from passenger gasoline vehicles may also contain ammonia which is formed as a reaction product when NO is reduced on catalytic surfaces in catalytic converters (Heeb et al., 2006; Kean et al., 2009). Gasoline exhaust contains a complex mixture of VOCs, nitrogen oxides (NO_x), ammonia and particulate matter (PM) emissions. However, primary PM emissions are typically lower than for diesel exhaust.

There is currently a debate of the relative proportions of gasoline and diesel exhaust SOA production in the atmosphere. In a recent study in the Los Angeles, California Basin, Bahreini et al. (2012) noted that diesel consumption was roughly halved on weekends and they found a corresponding reduction in primary organic aerosol (POA) and NO_x but no decrease in SOA that originated from fossil fuel combustion. They concluded that gasoline exhaust is the main source of fossil SOA in the Los Angeles Basin. This suggests that diesel exhaust may dominate the emissions of soot particles in urban areas and gasoline exhaust may dominate the SOA formation. On the contrary, Gentner et al. (2012) characterized the organic aerosol formation potential of emissions from diesel and gasoline vehicles, they concluded that diesel vehicles are responsible for the majority of vehicle SOA but recognized both sources as important. Thus there is a need for more studies especially on the gasoline SOA properties and production rates. Gasoline SOA may also be an important contributor to the early stages of atmospheric transformation of diesel soot. Aging of soot agglomerates strongly alters the optical and hygroscopic properties of soot particles (Zhang et al., 2008; Pagels et al., 2009a).

Odum et al. (1997) investigated the SOA formation from vaporized gasoline and a large number of light aromatic hydrocarbons occurring in reformulated gasoline. They showed that the SOA formation from vaporized whole gasoline can be well approximated by the sum of the SOA formed from the single light aromatic precursors. However, the composition of real-world gasoline exhaust differs from that of vaporized gasoline. For example, the fraction of light aromatics was found to be 21 % by mass in vaporized un-combusted gasoline and 13 % by mass in gasoline exhaust (Schauer et al., 2002). Important classes of compounds with relevance for SOA formation present in gasoline exhaust but not in vaporized gasoline are aldehydes and the complex unresolved mixture of IVOCs not quantified with the gas chromatography – mass spectrometry (GC-MS) techniques typically used (Schauer et al., 2002). Finally, benzene and naphthalene are enriched in the exhaust relative to the fuel (Elghawi et al., 2010).

Kleindienst et al. (2002) performed smog chamber experiments using a gasoline exhaust surrogate mixture made from gasoline fuel and organic additives relevant for the gasoline exhaust. From filter based techniques they concluded that 75–85 % of the SOA could be explained by C_6–C_9 light aromatic compounds and suggested that the remaining fraction was due to higher order aromatics and cyclic and long chain alkenes.

There is a need for investigations of the role of C_6–C_9 light aromatics and additional precursors have in the formation of gasoline SOA in real-world vehicles, particularly in the early aging of gasoline exhaust where IVOCs may be of importance, as has been found for diesel generators (Weitkamp et al., 2007) and wood smoke (Grieshop et al., 2009). There is also a need to define source signatures of gasoline SOA for example in terms of high resolution aerosol mass spectra that can be used for source apportionments studies in ambient air.

In this study, SOA formation of gasoline exhaust emissions from in-use Euro II, Euro III and Euro IV passenger vehicles was investigated in a smog chamber set-up. The aim of this study was: (1) to determine the fraction of the SOA from gasoline exhaust that can be explained by classical C_6–C_9 light aromatics precursors and (2) to investigate whether the chemical composition of the secondary aerosol from gasoline vehicle exhaust can be simulated using only light aromatic precursors. Better understanding of the magnitude and chemical composition of SOA from anthropogenic sources, like gasoline vehicles, will give valuable information to climate modelers and also improve the knowledge of health risks that are linked with air pollution in urban environments.

2 Methods

2.1 Experimental setup

The photo-oxidation experiments were carried out in a 6 m^3 ($W \times L \times H, 2.1 \times 1.5 \times 1.8$ m) DuPont fluorinated ethylene propylene (FEP) Teflon chamber (Welch Fluorocarbon,

USA), with a wall thickness of 125 µm, a smog chamber setup of similar size is presented in Miracolo et al. (2010). For sampling and air exchange three of the vertical sides were each equipped with three 1/4″ and one 3/4″ Kynar fittings. The Teflon chamber was suspended inside a 22 m^3 air conditioned steel chamber. The steel chamber has been described previously by Pagels et al. (2009b).

Four banks positioned on opposite sides of the smog chamber, each consisting of five 100 W fluorescent blacklights (Cleo performance 100-R, Phillips, Netherlands) were used to simulate the spectrum of the UV-band in solar irradiation. The light spectrum ranged from 320 nm to 380 nm, peaking at about 350 nm, which is similar to spectra from several other smog chamber setups (Carter et al., 2005; Presto et al., 2005). The UV spectrum is shown in Fig. S1 in the Supplement. The transmission of FEP at wavelengths between 290 and 800 nm has been reported to be more than 90 % (Paulsen et al., 2005). To enhance the radiation uniformity and intensity in the chamber, the walls of the enclosing steel chamber were coated with reflective aluminum foil. The NO_2-photolysis rate during these experiments was determined to 0.2 min^{-1}, by irradiating a mixture of NO_2 and O_3.

The temperature inside the steel chamber was controlled by a water based cooling unit (model 602D 9.43 kW, CIAT, France). This unit gave the means to control the temperature at 22 °C with a stability of ±2 °C. The temperature was monitored at the midpoint of the Teflon chamber as well as in the space between the smog chamber and the outer steel chamber. A schematic representation of the smog chamber setup and inlet system is shown in Fig. 1.

Gasoline exhaust was injected to the smog chamber through a heated inlet system using an ejector diluter (DI-1000, Dekati Ltd Finland) with an inlet nozzle modified to achieve a primary dilution ratio of 4–5. The ejector was supplied with pressurized air that was preheated to 140 °C and filtered by gas absorbing (NO_x, SO_x, O_3, organic acids) pellets (Triple blend makeup air media, Purafil, USA) and multiple sets of activated carbon and nano particle filters (CLEARPOINT®, Beko, Germany). This filter configuration was used for all pressurized air applications to the chamber. The heated exhaust inlet system and cleaning and conditioning of the smog chamber are further described in the Supplement.

Before each experiment the particle number concentration was $< 100\,\mathrm{cm^{-3}}$ and the particle volume concentration was $< 0.1\,\mathrm{\mu m^3\,cm^{-3}}$. Blank UV exposure experiments where filtered air was passed through the heated inlet with no exhaust or precursors added to the chamber were performed to make sure that the cleaning procedure worked properly. The formation of secondary organic aerosol was $< 0.1\,\mathrm{\mu g\,m^{-3}}$ and the formation of nitrate $< 0.01\,\mathrm{\mu g\,m^{-3}}$ during a typical 2 h blank experiment.

The pressure difference between the inside of the smog chamber and the surrounding steel chamber was monitored by a differential pressure sensor (ASP1400, Sensirion, Switzerland), to ensure that an overpressure was maintained and leaks into the chamber were avoided. The scanning mobility particle sizer (SMPS) data, NO, NO_2, O_3, CO, chamber RH, temperature and differential pressure were logged using a custom made LabVIEW™ (National Instruments, USA) program.

2.2 Vehicles

Three gasoline powered passenger vehicles were used in this study, one Euro II, one Euro III and one Euro IV vehicle, see Supplement Table S1 for more information about the vehicles. All vehicles were driven in normal use in between the experiments. The vehicles were fueled with Swedish standard MK1 gasoline fuel with an octane rating of 95 ("sulfur free" $< 10\,\mathrm{mg\,kg^{-1}}$). The fuel composition was analyzed with Gas Chromatography-Mass Spectrometry (GC-MS) in a similar way to the exhaust VOC samples as described in Sect. 2.3.3. The mass fraction of C_6–C_9 light aromatics was 30 %. The major oxidative additives used in this fuel were ethanol (5 % by volume) and MTBE 1.2 % by weight. The result of the fuel analysis is given in Table S3.

2.3 Instrumentation

2.3.1 Particle characterization instruments

A custom built SMPS-system (Löndahl et al., 2008) consisting of a Vienna-type ($L = 0.28\,\mathrm{m}$, $R_1 = 0.025\,\mathrm{m}$, $R_2 = 0.0335\,\mathrm{m}$) differential mobility analyzer (DMA) and a condensation particle counter (CPC model 3010, TSI Inc., USA), was used to monitor the size resolved number concentrations. A sheath flow/aerosol flow relationship of $4.9/0.7\,\mathrm{dm^3\,min^{-1}}$ was used for the measurements and the used size range was 10 to 600 nm. The particle volume concentration determined from the SMPS data was used as the volume standard and as a reference value for determination of the collection efficiency of the aerosol mass spectrometer (AMS). The SMPS and AMS were size calibrated with polystyrene latex (PSL)-spheres (80, 100, 240 and 350 nm, Duke Scientific Corp., USA) during the campaign.

The particle chemical composition was measured online by means of a High-Resolution Time of Flight Aerosol Mass Spectrometer (HR-ToF-AMS, Aerodyne research Inc., USA). The instrument was equipped with a laser vaporizer to allow detection of refractory black carbon (rBC; soot), a configuration known as the Soot-Particle Aerosol Mass Spectrometer (SP-AMS). The HR-ToF AMS and SP-AMS are described in detail elsewhere (DeCarlo et al., 2006; Onasch et al., 2012) and briefly below. The aerosol is sampled through an aerodynamic lens, which focuses sub-micrometer particles into a tight beam. The particle beam is modulated to obtain particle size resolved information using the Particle Time of Flight (PToF) mode. After impaction on a heated (600 °C) tungsten vaporizer plate, under low pressure ($\sim 10\,\mathrm{\mu Pa}$), the operationally defined non-refractory particulate mass (NR-PM) is vaporized and ionized using electron ionization (70 eV). The ions are subsequently analyzed though time of flight mass spectrometry. In these experiments NR-PM is expected to include all PM components except rBC. The instrument was operated in dual vaporizer mode, i.e. both laser and tungsten vaporizers were present. The laser vaporizer was turned on in 5 min periods every hour in most experiments, in order to probe rBC without interfering significantly with the tungsten vaporizer data set. Data analysis was performed with IGOR pro 6 (Wavemetrics, USA), SQUIRREL 1.51 and PIKA 1.1. Elemental analysis (EA) was performed on V-mode data. The fragmentation pattern and calibration factors suggested by Aiken et al. (2008) were used. Nitrate fragments were excluded from the elemental analysis.

2.3.2 Measurement of inorganic gases

The O_3 concentration was monitored using a UV spectrophotometer (model 49i ozone analyzer, Thermo Scientific, USA). The NO and NO_2 (NO_y–NO) concentrations were monitored by a NO_x-monitor (model CLD 700 AL, Eco Physics, USA). The NO_x-instrument uses two measurement chambers which gives a direct measurement of NO and an indirect NO_2 measurement. The principle for measurement of NO_2 is converting NO_2 to NO by a molybdenum converter at high temperature (375 °C); the converter may also convert peroxy acyl nitrates (PAN) and nitric acid (HNO_3) to NO. This gives an interference of the NO_2 signal (Gerboles et al., 2003). The monitoring of O_3 and NO_x were continuous throughout the experiment.

CO, NO_x and O_2 were measured in the raw exhaust by a gas analyzer (model 350 XL, Testo, Germany) in selected experiments. The CO mixing ratio in the smog chamber was typically below 1 ppm for the cold idling experiments and about 8 ppm in the cold start experiment.

2.3.3 Measurement of organic gas-phase compounds

The concentration of light aromatic compounds and other selected VOCs were monitored using a Proton Transfer Reaction Mass Spectrometer (PTR-MS, Ionicon Analytik GmbH, Austria), which allows real time measurements of concentrations down to the ppt range. Since the quadrupole version of the PTR-MS instrument measures only with a unity resolution, different compounds with same nominal mass cannot be distinguished. A detailed description of the PTR-MS technique is given by (Lindinger et al.,

1998; de Gouw and Warneke, 2007). The used volume mixing ratio calculations and calibration procedures are described by Taipale et al. (2008).

VOC samples were collected on adsorbent tubes filled with Tenax-TA and Carbopack-B and were analyzed in the laboratory with GC-MS, using a thermal desorption instrument (Perkin-Elmer TurboMatrix 650, Waltham, USA) attached to a gas-chromatograph (Perkin-Elmer Clarus 600, Waltham, USA) with DB-5MS (60 m, 0.25 mm, 1 µm) column and a mass selective detector (Perkin-Elmer Clarus 600T, Waltham, USA). Typically, duplicate adsorbent tube samples were collected before the UV-lights were turned on and at the end of the experiment. Thirteen C_6–C_9 light aromatic compounds and selected alkanes were quantified.

GC-MS was the standard method for determining the mass concentration of C_6–C_9 light aromatic hydrocarbons. The PTR-MS was available in four experiments (I1, I2, S1 and P1) and was used for monitoring of time resolved VOC concentrations. The VOC levels showed good agreement between the methods, see Supplement for comparison Fig. S3.

Initial C_{10}, C_{11} light aromatics and naphthalene concentrations were estimated from the PTR-MS channels m/z 135, 149 and 129 respectively in experiments when the PTR-MS was available, similar measurements have previously been performed by Jobson et al. (2010).

Cumulative OH exposures were estimated to allow investigation of the effect of processing on the aerosol MS composition data. The decay curves of C_8 and C_9 aromatics from PTR-MS and 1,2,4 TMB from GC-MS were fitted using a simple model to derive the OH concentration as a function of time. In the case of using the PTR-MS data, average OH reactivities based on the speciated GC-MS data were used.

2.4 Experimental procedure

Before the experiments, the smog chamber was filled with clean dry pressurized air (relative humidity 3–5 %). A nebulized water (Pro Analysi, Merck, Germany) solution of ammonium sulfate (1 $g\,dm^{-3}$) (Merck, Germany), was utilized as condensation seeds to collect the formed low vapor pressure reaction products. The nebulizer (Collison type, Topas Gmbh, Germany) was operated by filtered pressurized air (3 bar). The aerosol particles were dried using a silica diffusion drier and passed through a ^{63}Ni bi-polar charger before introduced to the smog chamber. The salt seeds were injected for about 20–30 min until a concentration of 15–20 $\mu g\, m^{-3}$ was accomplished, corresponding to an initial number concentration of 20 000–25 000 particles cm^{-3}.

Two different idling cases were defined: (1) cold start; the vehicle was started on site (after cold soaking for > 3 h) and the exhaust was injected to the smog chamber from first ignition. (2) Cold idling; the vehicles were driven for about 3 min on a standardized circuit before injection, until an engine temperature of 55 ± 5 °C was established. The ambient temperature was between −5 and +3 °C during the campaign (Table S2 Supplement).

In the precursor experiments, *m*-xylene or a mixture of three selected precursors were injected through evaporation from a glass flask purged with pressurized air. The precursors used were: toluene (> 99.5 % Merck, Germany) *m*-xylene (> 99 %, Sigma-Aldrich, USA) and 1,2,4-trimethylbenzene (> 98 %, Alfa Aesar, Germany). 1,2,4-trimethylbenzene was chosen because it is often the most abundant C_9-aromatic in idling gasoline exhaust (Table S3 in Supplement and Schauer et al., 2002).

The target VOC concentration in the chamber for each gasoline exhaust experiment was established using PTR-MS (raw spectrum intensities of m/z 93, 107, 121) sampling from the smog chamber and a flame ionization detector (FID, Model RS 53-T, Ratfisch, Germany), sampling from the raw exhaust. The total VOC concentration (FID) was between 1 and 2.5 ppm in the gasoline exhaust experiments. The length of the exhaust injection period was typically 5–15 min for cold idling and 60 s for cold start. Including the dilution in the Teflon chamber a total dilution ratio for the cold idling experiments of 30–120 was achieved, depending on the injection time of the exhaust. Additional NO typically had to be added after the exhaust injection to achieve a desired ratio between light aromatics (LA) and NO_x (ppbC/ppb). In four gasoline exhaust experiments and the two precursor experiments (Table 2) a light aromatic to NO_x ratio of

around 50 was used. In experiments I3 and I4 lower LA to NO_x ratios of 13 and 7, respectively were used. In experiment I4 O_3 was added to convert a major fraction of the emitted NO into NO_2. The level of NO at the start of the experiments was 35–107 ppb. O_3 was produced by a modified spark discharge ozone generator (AM 3000-2, Ozone Technology, Sweden) using pure O_2 (medical grade, Air Liquid).

After exhaust injection and addition of NO or O_3 there was a period of 30 to 60 min to allow mixing in the chamber and for characterization of the fresh exhaust composition. After this the UV-lights were lit, which is referred to as time $t = 0$ throughout the paper. The length of the experiments was 3–4 h.

2.5 Data analysis

2.5.1 Wall loss corrections

Aerosol particles suspended in a Teflon chamber may deposit to the chamber walls (McMurry and Rader, 1985), due to electrostatic forces and other deposition mechanisms, such as sedimentation and diffusion. To be able to quantify the SOA formation, wall losses have to be accounted for. In this work, a wall loss correction method based on AMS data was used (Hildebrandt et al., 2009). An assumption is made that VOCs do not condense on the chamber walls but are rather in equilibrium with particles deposited on the walls. The particulate sulfate seed is then conserved by the chamber system. The organic aerosol mass concentration ($C_{OA}(t)$) as a function of time is calculated by Eq. (1), by multiplying the mass concentration of seed aerosol at the time when UV-light was initiated ($C_{seed}^{sus}(t=0)$) with the ratio between organic aerosol ($C_{OA}^{sus}(t)$) and ammonium sulfate seed concentrations ($C_{seed}^{sus}(t)$) derived from AMS-data. $C_{seed}^{sus}(t=0)$ is derived from SMPS measurements, using a ρ_{seed} of 1.769 $g\, cm^{-3}$.

$$C_{OA}(t) = \frac{C_{OA}^{sus}(t)}{C_{seed}^{sus}(t)} C_{seed}^{sus}(t=0) \tag{1}$$

Secondary sulfates may also form in the chamber from oxidation of SO_2. However, the sulfur content of European gasoline fuel is extremely low ($< 10\,\mathrm{mg\,kg^{-1}}$). To make sure that secondary sulfates did not bias the measurements, we carried out several nucleation experiments with gasoline exhaust under conditions similar to the seeded experiments. It was found that secondary sulfate formation was 0.1–0.3 $\mu\mathrm{g\,m^{-3}}$. The resulting influence of the wall loss corrected SOA concentration is therefore less than 5 % in every experiment.

The half-life of ammonium sulfate mass concentration in experiments with no or negligible SOA formation was found to be ~ 3 h for the period starting when the UV-lights were turned on, which makes quantitative experiments meaningful up to about 4 h after UV on.

2.5.2 Aerosol mass yield

The aerosol mass yield Y at time $= t$ is defined as the ratio between the wall-loss corrected formed organic mass concentration divided by the mass concentration of reacted VOCs (ΔHC), at time = t (Eq. 2) (Odum et al., 1997).

$$Y = \frac{C_{\mathrm{SOA}}}{\Delta \mathrm{HC}} \tag{2}$$

In the calculations presented in this paper t exclusively refers to the end of the experiment. For the gasoline experiments an apparent mass yield was calculated taking into account only C_6–C_9 alkyl substituted light aromatics and benzene, thus the ΔHC term only consists of these compounds. These apparent mass yields can then be compared with true mass yields from the pure precursor experiments carried out at similar conditions in our chamber, to gain insight into the fraction of formed SOA that originated from C_6–C_9 light aromatics.

2.5.3 Primary exhaust particles and subtraction of primary organic aerosol

Upon exhaust injection an immediate increase in OA was observed in each experiment, after which a plateau was reached. This fraction of OA is referred to as Primary Organic Aerosol (POA). The ratio of POA to sulfate seed was assumed to be constant throughout the experiments. The estimated POA concentration at the end of the experiment was subtracted from the wall-loss corrected organic concentrations to determine C_{SOA}. The POA and particulate nitrates observed in these experiments will be treated in more detail in future publications.

The primary emissions from the Euro II vehicle were investigated in a separate experiment without condensation seeds. The emissions of primary particles were less than 50 particles $\mathrm{cm^{-3}}$ in the smog chamber at a dilution ratio of 1 : 36 for the cold idling gasoline emissions, indicating that the concentration of primary particles (such as soot cores) were negligible compared to the seed aerosol (~ 20 000–25 000 $\mathrm{cm^{-3}}$). Only in the cold start experiment (S1), there was a noticeable increase in the number concentration (about 2000 $\mathrm{cm^{-3}}$) upon adding the exhaust to the chamber. Similarly, only in the cold start experiment there was a noticeable signal of rBC (soot) detected with the SP-AMS. The mass concentration of rBC was estimated to 1.5 $\mu\mathrm{g\,m^{-3}}$ and $< 0.3\,\mu\mathrm{g\,m^{-3}}$ in the cold start and cold idling experiments, respectively.

3 Results and discussion

A summary of the results and conditions from six gasoline exhaust experiments and two precursor experiments is presented in Table 2. Photo-oxidation of gaseous gasoline exhaust forms SOA and ammonium nitrate. At the end of the experiments the formed SOA is 9–500 times higher than the emitted POA, which is in sharp contrast to diesel exhaust where the contribution of primary PM often dominates over secondary PM (Chirico et al., 2010). Experiment I1 had the highest contribution of POA corresponding to 12 % of the OA in the chamber at the end of the photo-oxidation experiment, while in experiments I2 and I3 the POA contribution was less than 0.5 %. The POA most likely originates from organic compounds with volatility low enough to condense onto the seed particles when the exhaust is cooled down after injection in the smog chamber. The aerosol mass spectra of these primary emissions were similar to diesel exhaust POA and the hydrocarbon-like organic aerosol (HOA) found in urban areas.

3.1 VOC composition and emissions

The classical light aromatic precursors (C_6–C_9) constituted 30 % of the fuel by mass but only 10–15 % of the total VOC emissions in the gasoline exhaust, where the latter figure includes methane (Table 1).

In Fig. 2 it is shown that the distribution of light aromatic SOA precursors depends on both vehicle type and operation mode. In the cold start with the Euro IV vehicle, the distribution of the light aromatics is similar to the distribution in the fuel. In the cold start experiment it is expected that the VOC-emissions may be well represented by vaporized fuel, due to the low temperatures of the engine and the oxidation catalyst (Schifter et al., 2010). A more detailed analysis of the light aromatic content in the fuel and gasoline exhaust is presented in Table S3 in the Supplement.

The distribution of light aromatics from the Euro II vehicle was fairly repeatable under cold idling conditions (Fig. 2) and shows an even distribution between the C_6–C_9 light aromatics. The Euro III and Euro IV vehicles when used under cold idling showed a trend towards decreasing concentration with increasing molecular size. The benzene concentration is strongly elevated in these cold idling experiments compared to the fuel content (benzene is regulated to < 1 % by volume in gasoline in Europe), most likely due to formation of benzene from other light aromatic compounds in the catalyst (Bruehlmann et al., 2007). The enrichment of benzene in the exhaust is also found in road tunnel emission measurements (Legreid et al., 2007). The distribution of light aromatics from the cold idling case reasonably well represents the road tunnel data.

The concentration of C_{10} and C_{11} light aromatics and naphthalene were assessed from the corresponding PTR-MS channels: $m/z = 135$, 149 and 129. This was done

for the Euro II vehicle at cold idling (I1 and I2 experiments) and the cold start experiment (S1) with the Euro IV vehicle. The contribution in percent to the summed initial mixing ratio (ppb) of C_6–C_{11} light aromatics and naphthalene was as follows 4.6; 0.4 % (C10), 0.8; < 0.1 % (C11) and 1.1; < 0.1 % (naphthalene) for cold idling (I1 and I2) and cold start respectively. As it can be seen the C_{10}, C_{11} and naphthalene fraction is significantly higher at cold idling compared to the cold start.

3.2 Formation of gasoline SOA

Figure 3a, b compares the temporal evolution for one representative gasoline experiment (I2) and an experiment with a precursor mixture (P1) containing three of the most important C_7–C_9 light aromatic precursors. The upper panels show the mixing ratios of NO, NO_2 and O_3 (left y-axis) and the ratio of nitrate and OA to sulfate seed (right y-axis). The middle panels show the mixing ratios for the most important light aromatic precursors and one photochemical gas-phase reaction product, obtained by PTR-MS. The PTR-MS channels correspond to toluene (C_7 $m/z = 93$), C_8 ($m/z = 107$), C_9 ($m/z = 121$), C_{10} ($m/z = 135$) aromatics and acetaldehyde ($m/z = 45$). In the P1 experiment (Fig. 3b) toluene, *m*-xylene (C_8) and 1,2,4 trimethylbenzene (C_9) were used as precursors. The lower panels show the H : C and O : C elemental ratios of the formed SOA, derived from AMS data.

The SOA formation is delayed 30–45 min after the lights are turned on corresponding to the time required to initiate photochemistry and for NO to be converted to NO_2 (Fig. 3). The NO to NO_2 conversion, and thereby the formation of ozone and HO_x occurs slightly faster in the gasoline exhaust experiment compared to the pure precursor experiment. The delay between ozone and SOA formation is shorter and the SOA formation starts at a higher NO level in the idling gasoline exhaust experiment compared to the precursor experiment. These differences are attributed to the large group of additional VOCs (in addition to C_6–C_9 light aromatics) present in the gasoline exhaust compared to the pure precursor experiment.

The initial concentrations of C_7–C_9-aromatics are all at a similar level in the cold idling gasoline exhaust, while the C_{10}-aromatics are present in much lower concentrations. The reactivity typically increases with increasing carbon number. For example *m*-xylene and 1,2,4-trimethylbenzene are much more reactive than toluene. The sum of the concentration of reacted light aromatics (C_6–C_9) is used for mass yield calculations, although the reacted fraction of benzene is small under the prevailing (atmospherically relevant) OH-radical concentrations ($1–3 \times 10^6\,cm^{-3}$), due to its low reactivity with the OH-radical.

The O : C and H : C ratios were both similar for the gasoline exhaust and the precursor experiment (~ 0.4 and ~ 1.4, respectively). Figure 4 shows the wall loss corrected mass concentration of SOA, nitrate and excess ammonium for experiment I2 (a), I3 (b) and P1 (c), the ammonium sulfate seed mass has been subtracted. The reacted mass concentration of C_6–C_9 light aromatics were about two times higher for the precursor experiment compared to the gasoline exhaust experiments. Still, the wall loss corrected SOA mass concentration was similar (Table 2).

Formation of nitrate occurs only to a limited extent in the precursor experiments (about 4 % of the total organics). The nitrate formation in the precursor experiment is attributed to formation of particle phase organic nitrates, while the formation of nitrate in the gasoline experiments can be attributed to a mixture of ammonium nitrate and organic nitrates that varies strongly between experiments. Information on the occurrence of organic and ammonium nitrate can be obtained from the NO / NO_2 ion fragment ratio in the AMS. The NO / NO_2 ratio is substantially higher for SOA from light aromatic precursors compared to ammonium nitrate (Sato et al., 2010). This analysis will be reported separately.

The ammonium nitrate is most likely formed by reactions of ammonia from the car exhaust and HNO_3 formed by reactions in the smog chamber (originating from NO_x). SOA from passenger vehicle emissions co-condenses with ammonia and nitric acid as can be expected during atmospheric processing of pollutants. The ammonium nitrate

formation increased with increasing initial NO_x level and thus in experiment I3 the aerosol was dominated by nitrate.

3.3 Mass yield of gasoline exhaust and precursors

The apparent mass yield, *Y* is defined here as the ratio between the mass concentration of formed secondary organic aerosol, C_{SOA} and the mass concentration of reacted light aromatic compounds (C_6–C_9), ΔHC (Eq. 2). By comparing the apparent mass yields with the yields from the precursor experiments at a given C_{SOA} we can infer the contribution from additional SOA precursors. The apparent mass yield from C_6–C_9 light aromatics in the gasoline exhaust SOA increases with increasing concentration of organic aerosol in the smog chamber as has been shown in several previous studies for yields of single precursor systems (Cocker et al., 2001; Song et al., 2005; Ng et al., 2007; Hildebrandt et al., 2009). A two-product fit (Odum et al., 1997) to the cold idling data is shown in Fig. 5.

Our precursor data agree well with *m*-xylene data from Song et al. (2005) carried out at similar conditions (so called classical photo-oxidation experiments), therefore we used their fit to extend the comparison between our precursor and gasoline exhaust data towards lower mass concentrations. The mass yield for experiment P1 and P2 is lower than some pure precursor experiment presented in the literature (Hildebrandt et al., 2009; Ng et al., 2007). Those experiments with significantly higher yield were often performed in the "low-NO_x regime" using H_2O_2 as OH-precursor. The experiments presented in this paper were performed without added OH-precursors and do all start in the "high NO_x regime" and as the NO concentration goes towards zero the experiment moves towards the "low NO_x regime". The VOCs which reacted in the "high NO_x" regime, are likely to form products that is too volatile to end up in the particle phase, when oxidized at the OH radial concentration used here (Ng et al., 2007).

According to the fits, the apparent mass yield of the gasoline exhaust from intermediate idling is about 1.7 times higher than the yield of the pure precursors under the conditions in this study. Thus, about 1.7 times more C_6–C_9 light aromatics have been reacted in the precursor experiments to form the same mass concentration of SOA (Eq. 2). If we assume that the reacted C_6–C_9 aromatic precursors form the same amount of SOA in the complex mixture in the gasoline exhaust as they do in the pure precursor experiments this would indicate that about 60 % of the SOA in the gasoline exhaust originates from C_6–C_9 precursors and 40 % from additional precursors (Fig. 5). The cold start experiment was an exception as it falls essentially on the fit of the yield of pure precursors.

By percentage, the reacted light aromatic compounds in the cold idling gasoline exhaust were on average 0.9 % benzene, 9.3 % toluene, 29.1 % C_8, 41.5 % C_9, 17.2 % C_{10}, and 2.0 % C_{11}. Assuming that the C_{10} and C_{11} light aromatics have similar yields as the C_8–C_9 aromatics, C_{10} and C_{11} aromatics would be responsible for about 11 % and 1 % respectively of the SOA formed. Additional candidates as SOA precursors will be discussed in Sect. 3.4.

The fraction of emitted C_{10} and C_{11} light aromatics and naphthalene were all substantially lower in the cold start experiment which is consistent with the classical C_6–C_9 aromatics being responsible for a larger fraction of the formed SOA in this case. Thus, SOA-formation from cold start emissions but not from cold idling could be well described by only including the C_6–C_9 light aromatics.

3.4 Chemical composition

High-resolution SOA mass spectra from experiment I2 and P1 are shown in Fig. 6. The AMS ion fragments have been grouped into four families based on their carbon, hydrogen and oxygen content. The dominating organic m/z peaks in SOA from gasoline exhaust are m/z 44 followed by m/z 43 (Fig. 6a), while the reverse trend was found in the precursor experiments (Fig. 6b).

The peaks at m/z 43 and 44 were dominated by $C_2H_3O^+$ and CO_2^+ fragments respectively, for both the gasoline exhaust and the precursor experiments. These two are the most abundant fragments in ambient oxygenated organic aerosol (OOA). CO_2^+ is

typically the main fragment for low volatility OOA (LV-OOA) while in semi-volatile OOA (SV-OOA) CO_2^+ and $C_2H_3O^+$ are of similar magnitude (Ng et al., 2010).

The gasoline SOA mass spectrum (Fig. 6a) shows strong similarities to atmospheric observations of fresh OOA detected in and downwind urban areas and gasoline SOA may thus be an important contributor to SOA in these locations as recently hypothesized from ambient data (Bahreini et al., 2012). Although SOA from many different sources show similarities, a few differences compared to diesel exhaust SOA should be pointed out. For example, diesel SOA (Chirico et al., 2010) has significant contributions from hydrocarbon fragments in the C_nH_{2n+1} series (for example $C_3H_7^+$ and $C_4H_9^+$). The main hydrocarbon fragments in the gasoline SOA are instead $C_3H_3^+$ and $C_3H_5^+$ consistent with aromatic (and potentially also alkene) precursors that have a H/C ratio closer to 1.

The organic mass fraction detected at m/z 43 ($f43$) and m/z 44 ($f44$) from the AMS measurements at the end of each experiment is shown in Fig. 7a. The figure also features the triangular boundary of atmospheric OOA observations introduced by Ng et al. (2010). Photochemical aging in the atmosphere typically increases the $f44$ in the organic spectra; a relatively high $f44$ indicates that the atmospheric aging process is more progressed.

The concept of the triangular space is formulated for atmospheric measurements of aged aerosols from multiple precursors and sources. Since gasoline exhaust SOA is a more complex mixture than SOA from pure precursors, it can be expected that gasoline SOA resembles atmospheric observations better than SOA from pure precursors. It is also apparent that SOA from a relevant mixture of light aromatics are not able to adequately simulate the composition of the SOA from early ageing of gasoline exhaust.

For one cold idling and one precursor experiment we have plotted the $f43$ vs. $f44$ relationship as a function of cumulative OH exposure. A cumulative OH exposure of $9 \times 10^6\,\mathrm{cm^{-3}}\,\mathrm{h}$ corresponds to 9 h of aging at a 24 h mean OH concentration of $1 \times 10^6\,\mathrm{cm^{-3}}$. For the cold idling experiment there is an increase in both $f43$ and $f44$ with increasing OH exposure, while for the precursor mixture the $f43$, $f44$ relationship is little influenced.

A van Krevelen diagram, showing the hydrogen to carbon (H : C) and oxygen to carbon (O : C) ratios is shown in Fig. 7b. The diagram depicts the molar ratios at the end of each experiment. The H : C ratio varies between 1.2 and 1.55 and the O : C ratio 0.36 to 0.43 for the set of experiments and there is no systematic difference between gasoline exhaust and pure precursor experiments in this aspect. A higher O : C and lower H : C ratio represents a higher oxidation state. Average carbon oxidation (OS_C) states can be estimated from O : C and H : C (Kroll et al., 2011). The SOA produced in these experiments have OS_C ranging from −0.8 to −0.4, similar to SV-OOA in the atmosphere. The diagonal red lines indicate oxidation states −1, −0.5 and 0.

An important observation is that the cold idling gasoline exhaust and pure precursor experiments are clearly separated in terms of their $f43/f44$ relationship but not in terms of their O : C vs H : C relationship and the division of ions into four different families dependent on their composition. This is not contradictory since m/z 44 and 43 only represent a fraction of the organic MS while the atomic ratios are calculated from the full spectra. A higher abundance of $C_2H_3O^+$ (the main fragment at m/z 43 in these data) pulls the O : C ratio towards 0.5 and the H : C ratio towards 1.5. The remaining fraction of the precursor SOA MS compensates this effect.

The $f43$, $f44$ values from this study are compared with literature data for light aromatic precursors in Fig. 8. The precursor experiments reported here are in general agreement with previous studies of SOA from pure *m*-xylene and 1,3,5-TMB (Ng et al., 2010) both positioned to the right of the triangular plot.

From known literature values of the fragmentation patterns of the dominating C_6–C_9 light aromatic compounds we calculated the theoretically expected fragmentation pattern of the gasoline exhaust assuming that only the C_6–C_9 light aromatic compounds were contributing to the SOA. It was assumed that the fragmentation pattern of the mixed SOA could be determined as the weighted sum of the fragmentation patterns of

SOA from the individual precursors. The procedure and the in-data to this calculation are shown in more detail in the Supplement.

It is found (Fig. 8.) that the expected $f43$ calculated, as described above, is slightly lower for the actual gasoline exhaust experiments than for the pure precursor experiments, but still substantially higher than that experimentally found in the cold idling experiments. The small difference compared to the three component precursor mixture used in our experiment is due to the low $f43$ of ethyl benzene and slightly higher toluene content in the gasoline exhaust compared to experiment P1. From this analysis we can put constraints on the magnitude and composition of SOA from the additional precursors discussed above.

If we subtract the expected $f43$ and $f44$ fractions based on only C_6–C_9 aromatics from the mass spectra at the end of each gasoline exhaust experiment, it can be shown that a maximum 50–60 % of the mass would come from light aromatics, (S4 in the Supplement). At higher fractions of light aromatic precursors, the $f43$ fraction of the unknown additional precursors would become below 0. In contrast, for the cold start experiment, the $f43/f44$ relationship assuming only C_6–C_9 precursors is almost identical to the experimentally found value, again supporting that the cold start emissions can be explained from essentially C_6 to C_9 light aromatics only.

This indicates that the additional precursors are likely to produce SOA with low $f43$, to the left of the triangle in Fig. 8. Possible precursors for the non-light aromatic SOA that do produce SOA with low $f43$ are 2-ring PAHs such as naphthalene (Fig. 8), which has been identified as an important SOA precursor in aging of diesel exhaust (Chan et al., 2009).

Naphthalene have also previously been quantified in gasoline exhaust at similar proportions compared to the sum of C_6–C_9 light aromatics (Schauer et al., 2002) as was found in the cold idling experiments here. The mass yield from two-ring PAHs in low-NO_x and high-NO_x photooxidation experiments (Chan et al., 2009) is about two and four times greater respectively, than the mass yield from similar experiments (Ng et al.,

2007) with *m*-xylene as precursor. This implies that relatively low concentrations of PAHs can give a significant contribution to SOA formation.

We used our measured initial naphthalene concentration and the known OH reactivity to estimate the reacted concentration of naphthalene, and assumed that the mass yield for naphthalene is three times higher than the yield for *m*-xylene in our chamber under the conditions studied. We found that naphthalene could contribute with around 5 % of the SOA mass in experiment I1 and I2. Results from Schauer et al. (2002) suggested that the summed concentration of 1- and 2-methyl naphthalene could be up to 150 % of the naphthalene concentration in gasoline exhaust, but those were not measured in our experiments. If and when methyl-naphthalenes are present in such significant concentrations, they would have to be considered as important SOA precursors in the early aging of gasoline exhaust due to their high yield and OH-reactivity (Chan et al., 2009). The result of superposition of SOA from light aromatic and naphthalene precursors in the "Ng-triangle" would decrease the discrepancy in composition between expected and measured values for gasoline exhaust.

As discussed above, we also estimated that C_{10} and C_{11} aromatics could contribute to about 12 % of the SOA in experiment I1 and I2. If the experiments would have proceeded to a higher cumulative OH exposure it is likely that a larger fraction of the formed SOA would originate from C_6 to C_9 aromatics, since they occur in higher concentration but have a lower OH-reactivity than the larger aromatic molecules, The shift towards higher $f43$ and $f44$ with increasing cumulative OH exposure shown for experiment I3 is consistent with naphthalenes being a major contributor in the early phase of SOA formation in gasoline exhaust.

In addition to the C_{10} and C_{11} light aromatics and naphthalenes a minor part of the remaining SOA may possibly be formed by other IVOCs such as phenols (that also produce low $f43$ SOA Chhabra et al., 2011), aromatic aldehydes, long chain and branched alkanes and alkenes and highly reactive compounds (such as styrene). Finally, an additional potentially important effect could be that photo-oxidation of light aromatics in a more complex mixture, like gasoline exhaust, results in more complex

reaction products and SOA with different composition, and an altered SOA yield compared to pure precursor experiments (Song et al., 2007).

3.5 SOA production factors

SOA production factors (PF) ($\mathrm{g\,kg^{-1}}$) are calculated using Eq. (3), where the numerator is the SOA concentration ($\mathrm{\mu g\,m^{-3}}$) and the denominator is the concentration of total combusted carbon ($\mathrm{\mu g\,m^{-3}}$). ω_c is the carbon content in fuel which is 0.85 (Kirchstetter et al., 1999). HC is the total hydrocarbons in the raw exhaust, BC is the black carbon emitted and we assume that all organic carbon is emitted in gas phase.

$$\mathrm{PF} = 10^3 \left([\mathrm{SOA}]/([\mathrm{CO_2}]+[\mathrm{CO}]+[\mathrm{HC}]+[\mathrm{BC}])\right)\omega_c \tag{3}$$

The SOA production factors ranged between 0.005 and 0.09 $\mathrm{g\,kg^{-1}}$ for the cold idling experiments, the PF for the cold start experiment was 0.48 $\mathrm{g\,kg^{-1}}$. Compared to emission factors from diesel passenger vehicles reported by Chirico et al. (2010), the PF from the cold start is in the same range as the PF from diesel vehicles with deactivated oxidation catalyst (0.254 to 0.461 $\mathrm{g\,kg^{-1}}$). The PF from cold idling gasoline vehicles is similar to or higher than that for diesel vehicles with functioning catalyst (0.012–0.020 $\mathrm{g\,kg^{-1}}$) (Chirico et al., 2010). Platt et al. (2012) have reported a SOA emission factor of 0.345 for a gasoline vehicle undergoing a complete driving cycle.

4 Conclusions

VOC emissions from gasoline vehicles when the engine and catalyst have not yet reached their operating temperature are substantial. Since the driving pattern in urban environments includes idling and shorter driving stints, which may hinder the engine and catalyst from reaching its optimum operating temperature, gasoline vehicles may significantly contribute to the VOC emissions to urban air. The gasoline fuel and VOC emissions have a substantial contribution of C_6–C_9 light aromatic compounds that are known SOA precursors. As shown in this study gasoline exhaust readily forms secondary organic aerosol with a signature aerosol mass spectrum with similarities to the oxidized organic aerosol that commonly dominates the OA mass spectra in and downwind urban areas. This substantiates recent claims that gasoline SOA is a dominating source to SOA in and downwind large metropolitan areas (Bahreini et al., 2012). Evidence for additional SOA precursors that are responsible for 40 % or more of the formed gasoline SOA during cold idling has been shown using two independent approaches. These were based on (1): the difference in apparent mass yield and (2): the difference in chemical composition between SOA from gasoline exhaust and that of pure precursors. Important candidate contributors are higher order aromatic compounds such as C_{10}, C_{11} light aromatics, naphthalenes and methyl-naphthalenes. In contrast, during a cold start experiment, the distribution of light aromatics was consistent with vaporized fuel and the apparent mass yield and the aerosol mass spectra were both consistent with C_6–C_9 light aromatics being responsible for more than 90 % of the SOA formation.

Supplementary material related to this article is available online at: http://www.atmos-chem-phys-discuss.net/12/31725/2012/acpd-12-31725-2012-supplement.pdf.

Acknowledgements. This work was supported by the Swedish Research Council for Environment, Agricultural Sciences and Spatial Planning FORMAS through projects 2007-1205, 2008-1467, 2009-615 and 2010-1678, the Swedish Research Council through project 2006-5940 and by Metalund, the centre for Medicine and Technology for Working Life and Society, a competence centre at Lund University, Sweden, supported by FAS, the Swedish Council for Working Life and Social Research.

References

Aiken, A. C., Decarlo, P. F., Kroll, J. H., Worsnop, D. R., Huffman, J. A., Docherty, K. S., Ulbrich, I. M., Mohr, C., Kimmel, J. R., Sueper, D., Sun, Y., Zhang, Q., Trimborn, A., Northway, M., Ziemann, P. J., Canagaratna, M. R., Onasch, T. B., Alfarra, M. R., Prevot, A. S. H., Dommen, J., Duplissy, J., Metzger, A., Baltensperger, U., and Jimenez, J. L.: O/C and OM/OC ratios of primary, secondary, and ambient organic aerosols with high-resolution time-of-flight aerosol mass spectrometry, Environ. Sci. Technol., 42, 4478–4485, 2008.

Bahreini, R., Middlebrook, A. M., de Gouw, J. A., Warneke, C., Trainer, M., Brock, C. A., Stark, H., Brown, S. S., Dube, W. P., Gilman, J. B., Hall, K., Holloway, J. S., Kuster, W. C., Perring, A. E., Prevot, A. S. H., Schwarz, J. P., Spackman, J. R., Szidat, S., Wagner, N. L., Weber, R. J., Zotter, P., and Parrish, D. D.: Gasoline emissions dominate over diesel in formation of secondary organic aerosol mass, Geophys. Res. Lett. 39, L06805, doi:10.1029/2011GL050718, 2012.

Bruehlmann, S., Novak, P., Lienemann, P., Trottmann, M., Gfeller, U., Zwicky, C. N., Bommer, B., Huber, H., Wolfensberger, M., and Heeb, N. V.: Three-way-catalyst induced benzene formation: a precursor study, Appl. Catal. B-Environ. 70, 276–283, 2007.

Carter, W. P. L., Cocker, D. R., Fitz, D. R., Malkina, I. L., Bumiller, K., Sauer, C. G., Pisano, J. T., Bufalino, C., and Song, C.: A new environmental chamber for evaluation of gas-phase chemical mechanisms and secondary aerosol formation, Atmos. Environ. 39, 7768–7788, 2005.

Chan, A. W. H., Kautzman, K. E., Chhabra, P. S., Surratt, J. D., Chan, M. N., Crounse, J. D., Kürten, A., Wennberg, P. O., Flagan, R. C., and Seinfeld, J. H.: Secondary organic aerosol formation from photooxidation of naphthalene and alkylnaphthalenes: implications for oxidation of intermediate volatility organic compounds (IVOCs), Atmos. Chem. Phys., 9, 3049–3060, doi:10.5194/acp-9-3049-2009, 2009.

Chhabra, P. S., Ng, N. L., Canagaratna, M. R., Corrigan, A. L., Russell, L. M., Worsnop, D. R., Flagan, R. C., and Seinfeld, J. H.: Elemental composition and oxidation of chamber organic aerosol, Atmos. Chem. Phys., 11, 8827–8845, doi:10.5194/acp-11-8827-2011, 2011.

Chirico, R., DeCarlo, P. F., Heringa, M. F., Tritscher, T., Richter, R., Prévôt, A. S. H., Dommen, J., Weingartner, E., Wehrle, G., Gysel, M., Laborde, M., and Baltensperger, U.: Impact of aftertreatment devices on primary emissions and secondary organic aerosol formation potential from in-use diesel vehicles: results from smog chamber experiments, Atmos. Chem. Phys., 10, 11545–11563, doi:10.5194/acp-10-11545-2010, 2010.

Cocker, D. R., Mader, B. T., Kalberer, M., Flagan, R. C., and Seinfeld, J. H.: The effect of water on gas-particle partitioning of secondary organic aerosol: II. *m*-xylene and 1,3,5-trimethylbenzene photooxidation systems, Atmos. Environ., 35, 6073–6085, 2001.

de Gouw, J. and Jimenez, J. L.: Organic aerosols in the Earth's Atmosphere, Environ. Sci. Technol., 43, 7614–7618, 2009.

de Gouw, J. and Warneke, C.: Measurements of volatile organic compounds in the earths atmosphere using proton-transfer-reaction mass spectrometry, Mass Spectrom. Rev., 26, 223–257, 2007.

DeCarlo, P. F., Kimmel, J. R., Trimborn, A., Northway, M. J., Jayne, J. T., Aiken, A. C., Gonin, M., Fuhrer, K., Horvath, T., Docherty, K. S., Worsnop, D. R., and Jimenez, J. L.: Field-deployable, high-resolution, time-of-flight aerosol mass spectrometer, Anal. Chem., 78, 8281–8289, 2007.

Elghawi, U. M., Mayouf, A., Tsolakis, A., and Wyszynski, M. L.: Vapour-phase and particulate-bound PAHs profile generated by a (SI/HCCI) engine from a winter grade commercial gasoline fuel, Fuel, 89, 2019–2025, 2010.

Gentner, D. R., Isaacman, G., Worton, D. R., Chan, A. W. H., Dallmann, T. R., Davis, L., Liu, S., Day, D. A., Russell, L. M., Wilson, K. R., Weber, R., Guha, A., Harley, R. A., and Goldstein, A. H.: Elucidating secondary organic aerosol from diesel and gasoline vehicles through detailed characterization of organic carbon emissions, P. Natl. Acad. Sci., 109, 18318–18323, 2012.

Gerboles, M., Lagler, F., Rembges, D., and Brun, C.: Assessment of uncertainty of NO_2 measurements by the chemiluminescence method and discussion of the quality objective of the NO_2 European Directive, J. Environ. Monitor., 5, 529–540, 2003.

Grieshop, A. P., Donahue, N. M., and Robinson, A. L.: Laboratory investigation of photochemical oxidation of organic aerosol from wood fires 2: analysis of aerosol mass spectrometer data, Atmos. Chem. Phys., 9, 2227–2240, doi:10.5194/acp-9-2227-2009, 2009.

Hallquist, M., Wenger, J. C., Baltensperger, U., Rudich, Y., Simpson, D., Claeys, M., Dommen, J., Donahue, N. M., George, C., Goldstein, A. H., Hamilton, J. F., Herrmann, H., Hoffmann, T., Iinuma, Y., Jang, M., Jenkin, M. E., Jimenez, J. L., Kiendler-Scharr, A., Maenhaut, W., McFiggans, G., Mentel, Th. F., Monod, A., Prévôt, A. S. H., Seinfeld, J. H., Surratt, J. D., Szmigielski, R., and Wildt, J.: The formation, properties and impact of secondary organic aerosol: current and emerging issues, Atmos. Chem. Phys., 9, 5155–5236, doi:10.5194/acp-9-5155-2009, 2009.

Heeb, N. V., Forss, A. M., Bruhlmann, S., Luscher, R., Saxer, C. J., and Hug, P.: Three-way catalyst-induced formation of ammonia-velocity- and acceleration-dependent emission factors, Atmos. Environ., 40, 5986–5997, 2006.

Hildebrandt, L., Donahue, N. M., and Pandis, S. N.: High formation of secondary organic aerosol from the photo-oxidation of toluene, Atmos. Chem. Phys., 9, 2973–2986, doi:10.5194/acp-9-2973-2009, 2009.

Jobson, B. T., Volkamer, R. A., Velasco, E., Allwine, G., Westberg, H., Lamb, B. K., Alexander, M. L., Berkowitz, C. M., and Molina, L. T.: Comparison of aromatic hydrocarbon measurements made by PTR-MS, DOAS and GC-FID during the MCMA 2003 Field Experiment, Atmos. Chem. Phys., 10, 1989–2005, doi:10.5194/acp-10-1989-2010, 2010.

Kean, A. J., Littlejohn, D., Ban-Weiss, G. A., Harley, R. A., Kirchstetter, T. W., and Lunden, M. M.: Trends in on-road vehicle emissions of ammonia, Atmos. Environ., 43, 1565–1570, 2009.

Kirchstetter, T. W., Harley, R. A., Kreisberg, N. M., Stolzenburg, M. R., and Hering, S. V.: On-road measurement of fine particle and nitrogen oxide emissions from light- and heavy-duty motor vehicles, Atmos. Environ., 33, 2955–2968, 1999.

Kleindienst, T. E., Corse, E. W., Li, W., McIver, C. D., Conver, T. S., Edney, E. O., Driscoll, D. J., Speer, R. E., Weathers, W. S., and Tejada, S. B.: Secondary organic aerosol formation from the irradiation of simulated automobile exhaust. J. Air Waste Manage., 52, 259–272, 2002.

Kroll, J. H., Donahue, N. M., Jimenez, J. L., Kessler, S. H., Canagaratna, M. R., Wilson, K. R., Altieri, K. E., Mazzoleni, L. R., Wozniak, A. S., Bluhm, H., Mysak, E. R., Smith, J. D., Kolb, C. E., and Worsnop, D. R.: Carbon oxidation state as a metric for describing the chemistry of atmospheric organic aerosol, Nat. Chem., 3, 133–139, 2011.

Legreid, G., Reimann, S., Steinbacher, M., Staehelin, J., Young, D., and Stemmler, K.: Measurements of OVOCs and NMHCs in a swiss highway tunnel for estimation of road transport emissions, Environ. Sci. Technol., 41, 7060–7066, 2007.

Lindinger, W., Hansel, A., and Jordan, A.: On-line monitoring of volatile organic compounds at pptv levels by means of proton-transfer-reaction mass spectrometry (PTR-MS) – medical applications, food control and environmental research, Int. J. Mass Spectrom., 173, 191–241, 1998.

Löndahl, J., Pagels, J., Boman, C., Swietlicki, E., Massling, A., Rissler, J., Blomberg, A., Bohgard, M., and Sandstrom, T.: Deposition of biomass combustion aerosol particles in the human respiratory tract, Inhal. Toxicol., 20, 923–933, 2008.

McMurry, P. H. and Rader, D. J.: Aerosol wall losses in electrically charged chambers, Aerosol Sci. Tech., 4, 249–268, 1985.

Miracolo, M. A., Hennigan, C. J., Ranjan, M., Nguyen, N. T., Gordon, T. D., Lipsky, E. M., Presto, A. A., Donahue, N. M., and Robinson, A. L.: Secondary aerosol formation from photochemical aging of aircraft exhaust in a smog chamber, Atmos. Chem. Phys., 11, 4135–4147, doi:10.5194/acp-11-4135-2011, 2011.

Monks, P. S., Granier, C., Fuzzi, S., Stohl, A., Williams, M. L., Akimoto, H., Amann, M., Baklanov, A., Baltensperger, U., Bey, I., Blake, N., Blake, R. S., Carslaw, K., Cooper, O. R., Dentener, F., Fowler, D., Fragkou, E., Frost, G. J., Generoso, S., Ginoux, P., Grewe, V., Guenther, A., Hansson, H. C., Henne, S., Hjorth, J., Hofzumahaus, A., Huntrieser, H., Isaksen, I. S. A., Jenkin, M. E., Kaiser, J., Kanakidou, M., Klimont, Z., Kulmala, M., Laj, P., Lawrence, M. G., Lee, J. D., Liousse, C., Maione, M., McFiggans, G., Metzger, A., Mieville, A., Moussiopoulos, N., Orlando, J. J., O'Dowd, C. D., Palmer, P. I., Parrish, D. D., Petzold, A., Platt, U., Poschl, U., Prevot, A. S. H., Reeves, C. E., Reimann, S., Rudich, Y., Sellegri, K., Steinbrecher, R., Simpson, D., ten Brink, H., Theloke, J., van der Werf, G. R., Vautard, R., Vestreng, V., Vlachokostas, C., and von Glasow, R.: Atmospheric composition change – global and regional air quality, Atmos. Environ., 43, 5268–5350, 2009.

Ng, N. L., Kroll, J. H., Chan, A. W. H., Chhabra, P. S., Flagan, R. C., and Seinfeld, J. H.: Secondary organic aerosol formation from *m*-xylene, toluene, and benzene, Atmos. Chem. Phys., 7, 3909–3922, doi:10.5194/acp-7-3909-2007, 2007.

Ng, N. L., Canagaratna, M. R., Zhang, Q., Jimenez, J. L., Tian, J., Ulbrich, I. M., Kroll, J. H., Docherty, K. S., Chhabra, P. S., Bahreini, R., Murphy, S. M., Seinfeld, J. H., Hildebrandt, L., Donahue, N. M., DeCarlo, P. F., Lanz, V. A., Prévôt, A. S. H., Dinar, E., Rudich, Y., and Worsnop, D. R.: Organic aerosol components observed in Northern Hemispheric datasets from Aerosol Mass Spectrometry, Atmos. Chem. Phys., 10, 4625–4641, doi:10.5194/acp-10-4625-2010, 2010.

Odum, J. R., Jungkamp, T. P. W., Griffin, R. J., Forstner, H. J. L., Flagan, R. C., and Seinfeld, J. H.: Aromatics, reformulated gasoline, and atmospheric organic aerosol formation, Environ. Sci. Technol., 31, 1890–1897, 1997.

Onasch, T. B., Trimborn, A., Fortner, E. C., Jayne, J. T., Kok, G. L., Williams, L. R., Davidovits, P., and Worsnop, D. R.: Soot particle aerosol mass spectrometer: development, validation, and initial application, Aerosol. Sci. Tech., 46, 804–817, 2012.

Pagels, J., Khalizov, A. F., McMurry, P. H., and Zhang, R. Y.: Processing of soot by controlled sulphuric acid and water condensation mass and mobility relationship, Aerosol. Sci. Tech., 43, 629–640, 2009a.

Pagels, J., Wierbicka, A., Nilsson, E., Isaxon, C., Dahl, A., Gudmundsson, A., Swietlicki, E., and Bohgard, M.: Chemical composition and mass emission factors of candle smoke particles, J. Aerosol. Sci., 40, 193–208, 2009b.

Paulsen, D., Dommen, J., Kalberer, M., Prevot, A. S. H., Richter, R., Sax, M., Steinbacher, M., Weingartner, E., and Baltensperger, U.: Secondary organic aerosol formation by irradiation of 1,3,5-trimethylbenzene-NO_x-H_2O in a new reaction chamber for atmospheric chemistry and physics, Environ. Sci. Technol., 39, 2668–2678, 2005.

Platt, S. M., El Haddad, I., Zardini, A. A., Clairotte, M., Astorga, C., Wolf, R., Slowik, J. G., Temime-Roussel, B., Marchand, N., Ježek, I., Drinovec, L., Močnik, G., Möhler, O., Richter, R., Barmet, P., Bianchi, F., Baltensperger, U., and Prévôt, A. S. H.: Secondary organic aerosol formation from gasoline vehicle emissions in a new mobile environmental reaction chamber, Atmos. Chem. Phys. Discuss., 12, 28343–28383, doi:10.5194/acpd-12-28343-2012, 2012.

Presto, A. A., Hartz, K. E. H., and Donahue, N. M.: Secondary organic aerosol production from terpene ozonolysis. 1. effect of UV radiation, Environ. Sci. Technol., 39, 7036–7045, 2005.

Robinson, A. L., Donahue, N. M., Shrivastava, M. K., Weitkamp, E. A., Sage, A. M., Grieshop, A. P., Lane, T. E., Pierce, J. R., and Pandis, S. N.: Rethinking organic aerosols: semivolatile emissions and photochemical aging, Science, 315, 1259–1262, 2007.

Samy, S. and Zielinska, B.: Secondary organic aerosol production from modern diesel engine emissions, Atmos. Chem. Phys., 10, 609–625, doi:10.5194/acp-10-609-2010, 2010.

Sato, K., Takami, A., Isozaki, T., Hikida, T., Shimono, A., and Imamura, T.: Mass spectrometric study of secondary organic aerosol formed from the photo-oxidation of aromatic hydrocarbons, Atmos. Environ., 44, 1080–1087, 2010.

Schauer, J. J., Kleeman, M. J., Cass, G. R., and Simoneit, B. R. T.: Measurement of emissions from air pollution sources, 5. C-1-C-32 organic compounds from gasoline-powered motor vehicles, Environ. Sci. Technol., 36, 1169–1180, 2002.

Schifter, I., Diaz, L., and Rodriguez, R.: Cold-start and chemical characterization of emissions from mobile sources in Mexico, Environ. Technol., 31, 1241–1253, 2010.

Song, C., Na, K. S., and Cocker, D. R.: Impact of the hydrocarbon to NO_x ratio on secondary organic aerosol formation, Environ. Sci. Technol., 39, 3143–3149, 2005.

Song, C., Na, K., Warren, B., Malloy, Q., and Cocker, D. R.: Impact of propene on secondary organic aerosol formation from *m*-xylene, Environ. Sci. Technol., 41, 6990–6995, 2007.

Taipale, R., Ruuskanen, T. M., Rinne, J., Kajos, M. K., Hakola, H., Pohja, T., and Kulmala, M.: Technical Note: Quantitative long-term measurements of VOC concentrations by PTR-MS – measurement, calibration, and volume mixing ratio calculation methods, Atmos. Chem. Phys., 8, 6681–6698, doi:10.5194/acp-8-6681-2008, 2008.

Weilenmann, M., Favez, J. Y., and Alvarez, R.: Cold-start emissions of modern passenger cars at different low ambient temperatures and their evolution over vehicle legislation categories, Atmos. Environ., 43, 2419–2429, 2009.

Weitkamp, E. A., Sage, A. M., Pierce, J. R., Donahue, N. M., and Robinson, A. L.: Organic aerosol formation from photochemical oxidation of diesel exhaust in a smog chamber, Environ. Sci. Technol., 41, 6969–6975, 2007.

Zhang, R. Y., Khalizov, A. F., Pagels, J., Zhang, D., Xue, H. X., and McMurry, P. H.: Variability in morphology, hygroscopicity, and optical properties of soot aerosols during atmospheric processing, P. Natl. Acad. Sci. USA, 105, 10291–10296, 2008.

Table 1. Initial experimental conditions.

Exp -ID	Type	Source	Initial C_6–C_9 light aromatics (ppb)	Initial NO (ppb)	Initial $(NH_4)_2SO_4$ ($\mu g\,m^{-3}$)	Total hydrocarbons (ppm)*
I1	Cold idling	Euro II	303	33	10	2.4
I2	Cold idling	Euro II	317	47	18	2.5
I3	Cold idling	Euro II	197	107	13	2.2
I4	Cold idling	Euro III	123	20**	15	1.0
I5	Cold idling	Euro IV	289	35	22	2.2
S1	Cold start	Euro IV	402	47	6	~ 1
P1	Precursor	tol., m-xyl., 1,2,4-tmb	288	43	18	–
P2	Precursor	m-xyl.	250	38	19	–

* Measured with the FID.

** The given NO value is after addition of O_3 to convert NO to NO_2, the initial NO concentration prior to addition of O_3 was 125 ppb.

Table 2. Summary of the results and experimental conditions.

Exp. -ID	Initial LA to NO_x ratio (ppbC/ppbN)	Formed ozone (ppb)	Reacted LA (C_6–C_9) ($\mu g m^{-3}$)	Emitted POA ($\mu g m^{-3}$)	Formed SOA ($\mu g m^{-3}$)	Apparent Mass Yield Y	Formed NO_3 ($\mu g m^{-3}$)
I1	55	111	138	2.9	21	0.15	9
I2	45	118	198	0.2	44	0.22	24
I3	13	156	264	0.1	51	0.19	71
I4	7	72	97	0.1	9	0.09	91
I5	53	102	62	0.2	5	0.09	4
S1	64	98	205	0.6	12	0.06	< 1
P1	49	86	462	–	53	0.12	2
P2	49	72	435	–	59	0.14	2

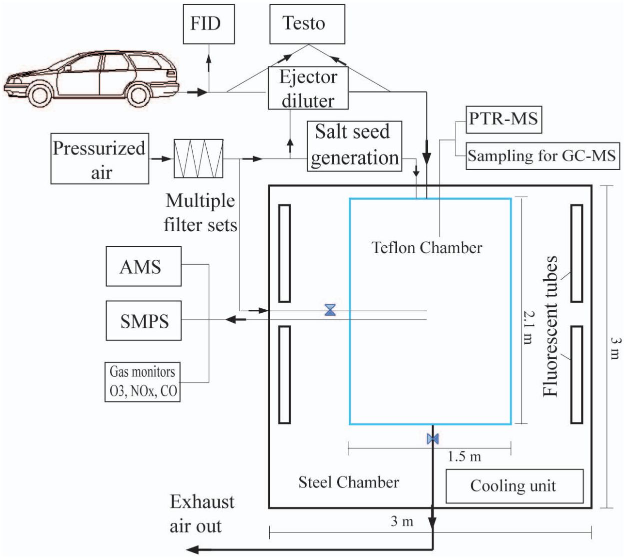

Fig. 1. Schematic representation of the smog chamber and dilution system, seen from above.

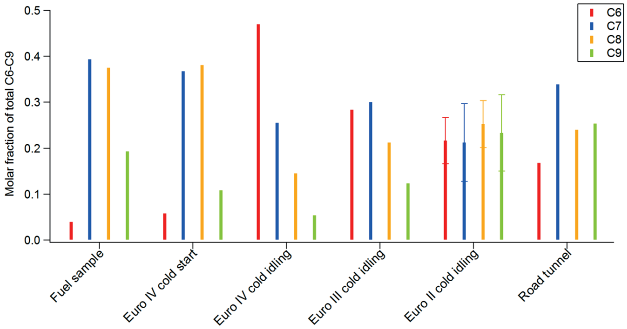

Fig. 2. The molar fraction of C_6–C_9 light aromatics (GC-MS) in the exhaust, a sample of the gasoline fuel used in the measurement campaign and VOC measurements in a road tunnel (Legreid et al., 2007). The whiskers indicate ±1 standard deviation (σ) of repeated measurements. Legreid et al. (2007) only measured 1,2,4-TMB, the total C_9 concentration is estimated from that number and the fraction of 1,2,4-TMB of total C_9 in our exhaust measurements.

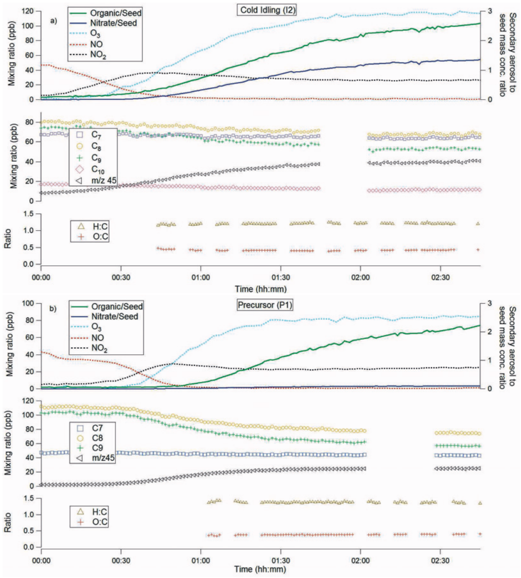

Fig. 3. Time resolved data from experiment I2 **(a)** and P1 **(b)**. The upper panels show the mixing ratios of NO, NO_2 and O_3 (left y-axis) and the mass concentration ratio between SOA, nitrate and seed aerosol on the right y-axis. The middle panels represent the mixing ratio of light aromatics (m/z 93: toluene, m/z 107: xylenes, m/z 121: C_9-aromatics, m/z 135: C_{10}-aromatics) and acetaldehyde (m/z 45). The lower graphs feature the H : C and O : C ratios extracted from elemental analysis of organic aerosol in high-resolution AMS data. The UV lights were turned on at Time = 00:00. Missing data points are either due to internal calibration (PTR-MS), thermodenuder measurements (AMS) or omitted on account of low mass loadings.

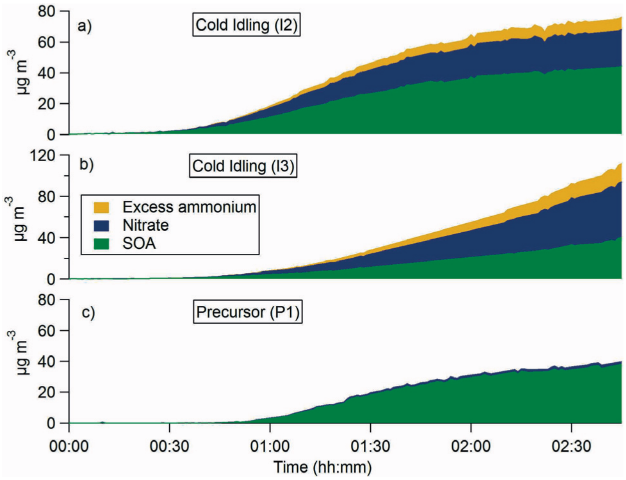

Fig. 4. Chemically resolved wall loss corrected mass concentration (µg m^{-3}) from AMS data from experiment I2 **(a)**, I3 **(b)** and P1 **(c)**. The ammonium sulfate seed has been subtracted. The reported ammonia is excess ammonia not bound to sulfate, thus indicative of ammonium nitrate formation. Time = 00:00 indicates the start of the UV radiation.

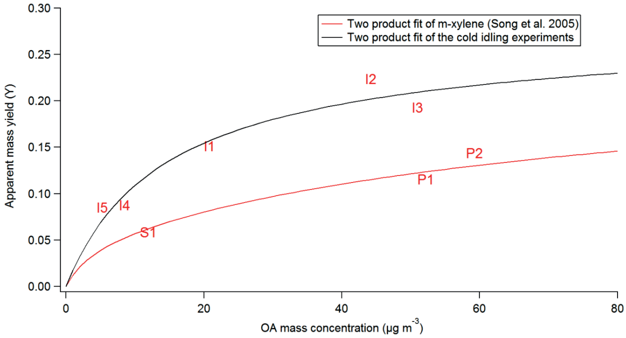

Fig. 5. The apparent mass yield (Eq. 2) from the gasoline experiments plotted against the concentration of organic aerosol mass. The black line represents a two product fit, $\left(Y = C_{\mathrm{OA}} \cdot \left[\left(a_1 \cdot k_1/(1 + k_1 \cdot C_{\mathrm{OA}})\right) + \left(a_2 \cdot k_2/(1 + k_2 \cdot C_{\mathrm{OA}})\right)\right]\right.$, where $a_1 = 0.254$, $a_2 = 0.048$, $k_1 = 0.072$ and $k_2 = 0.005$) to the apparent mass yield for experiment I1–I5. The red line is a two product fit to the m-xylene yield from Song et al. (2005), (scaled by 0.88 and assuming a density of 1.4 g cm^{-3}) to fit the precursor experiments carried out in this study. I1–I5 represents cold idling, S1 cold start and P1–P2 the precursor experiments.

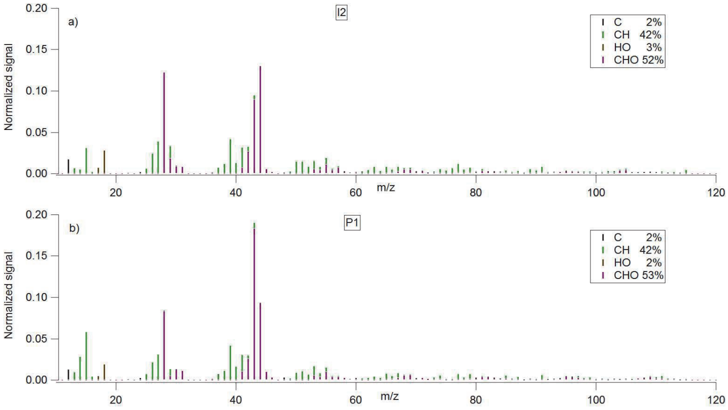

Fig. 6. Normalized high resolution MS of OA at the end of gasoline exhaust experiment I2 **(a)** and precursor mixture experiment P1 **(b)** (toluene, *m*-xylene, 1,2,4 TMB). The ion fragments detected have been grouped into four families; C containing only carbon; CH containing only carbon and hydrogen; HO containing only oxygen and hydrogen; and CHO containing carbon, hydrogen and oxygen (with the exception of CO_2^+ which dominates at m/z 44). The POA contribution in experiment I2 was < 0.5 %.

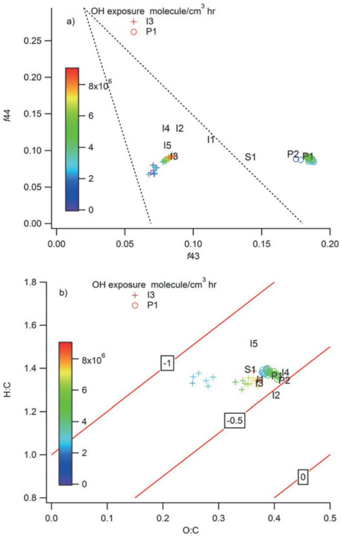

Fig. 7. **(a)** The mass fraction of organic signal at m/z 44 ($f44$) vs m/z 43 ($f43$) at the end of each experiment, **(b)** H : C vs O : C of the OA at the end of each experiment. The triangular space in **(a)** indicates the range which covers the majority of atmospheric OOA observations (Ng et al., 2010). The diagonal lines in **(b)** indicate estimated average carbon oxidation states −1, −0.5 and 0 (Kroll et al., 2011). For experiments I3 (+) and P1 (o) time resolved data are shown colored by OH exposure. The cumulative OH exposure was 8.5×10^6 molecule cm^{-3} h in I3 and 6.4×10^6 molecule cm^{-3} h in P1.

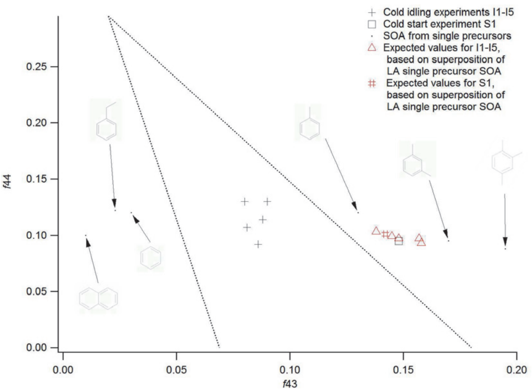

Fig. 8. The *f*43, *f*44 for experiments I1–I5 (+) and for SOA formed from single precursors; LA and naphthalene plotted together with the triangle from Ng et al. (2010). Also plotted are expected values for I1–I5 if only LA contribute to SOA formation, assuming superposition of single precursor SOA. For experiment I1 and S1 which had non negligible POA contribution to OA, the SOA values have been calculated from the total OA assuming non-volatile POA with a constant composition through the whole experiment. The *f*44 to *f*43 of SOA from precursors featured in the figure are retrieved from the following sources: benzene (Ng et al., 2010), toluene (Chhabra et al., 2011), ethylbenzene (Sato et al., 2010) *m*-xylene (experiment P2, this study), 1,2,4-trimethylbenzene (derived from exp. P1) naphthalene (Chhabra et al., 2011). The results suggest no more than 60 % of SOA in I1–I5 were due to C_6–C_9 LA precursors, assuming that the MS of gasoline exhaust SOA can be estimated as a weighted mean of the MS of SOA from single precursors. See Table S4 (Supplement) for more details about these calculations.